Circularly Polarized multi-beam Antenna System for High-Altitude-Platforms

PAR

Marco LETIZIA

ÉCOLE POLYTECHNIQUE
FÉDÉRALE DE LAUSANNE

Suisse
2013

[...] fatti non foste a viver come bruti,
ma per seguir virtute e canoscenza

Dante, Commedia, Inferno, Canto XXVI

Abstract

High Altitude Platform Stations (HAPS) are unmanned platforms positioned at stratospheric altitude, aiming to provide mainly telecommunication services as broadcasting repeaters. Communication services delivered by HAPS require the use of high gain circularly polarized multi-beam antennas. Multiple beams allow switching between different antenna footprints while increasing the capacity of the communication channel. On the other hand, circular polarization is the standard solution to overcome misalignments between transmitter and receiver and to mitigate multipath problems.

In this context, the objective of this thesis is to contribute to the development of solutions for HAPS antenna subsystems. From the frequency point of view, the migration towards higher frequencies, providing larger bandwidths and hence higher channels capacities, is a continuous trend. Nowadays, the Ka-band (around 30 GHz) is considered very promising for this type of application. At these frequencies, one of the most useful implementations of the antenna subsystem is probably the use of a dielectric lens fed by several feeds. Taking into account a wide range of technical concerns, we have designed, prototyped and measured a multibeam dielectric lens antenna suitable for typical HAPS scenarios. In this type of antenna subsystem, the circular polarization can be obtained essentially in two ways: either the elementary radiators feeding the lens are already circularly polarized or they are linearly polarized and circular polarization is generated after the lens, with the help of an external polarizer. In the former situation, a polarizer has been optimized numerically, whereas in the second one, we have implemented a design procedure based on the combination of transmission line models with unit cell full wave analysis including periodic boundary conditions. Thus, we propose two effective designs, highlighting advantages and drawbacks of each one of these solutions. Our investigations are validated by prototype measurements in agreement with the predicted values.

When a multibeam antenna system is mounted on platforms flying above Earth, the shape of the ground footprints has to be carefully controlled for different elevation angles. In this thesis, we propose a Ka-band multi-beam dielectric lens antenna design in which the beam symmetry is perturbed by acting on the lens shape, with the goal of generating circular footprints in the entire covered area. Such radiation characteristics are useful not only for HAPS, but for any scenario where the antenna system is mounted on platforms flying above Earth and, in general, for any application where the shape of the footprints has to be carefully controlled for different elevation angles. The new ellipsoidal shape is obtained with a set of simple analytical design equations, eventually enhanced by full-wave optimizations. Radiation pattern measurements show that such a lens minimizes the natural beam footprint

elongation unavoidable with traditional spherical lenses and confirm the validity of the proposed system.

All the above results pave the way for future research oriented to the development of a complete on-board antenna payload for HAPS.

Sintesi

High Altitude Platform Stations (HAPS) sono piattaforme che sono posizionate nella Stratosfera, al fine di fornire servizi principalemnte di telecomunicazione in qualità di ripetitori di radiodiffusione. Servizi di comunicazione forniti da HAPS richiedono l'uso di un elevato guadagno e antenne multifascio circolarmente polarizzate. Fasci multipli permettono infatti di riconfigurare dinamicamente le performances dell'antenna, aumentando la capacità del canale di comunicazione. Inoltre, la polarizzazione circolare è una soluzione molto usata per superare effetti indesiderati dovuti a disallineamenti tra il trasmettitore e il ricevitore e per attenuare i problemi inerenti al multipath.

In questo contesto, l'obiettivo di questa tesi è quello di contribuire allo sviluppo di soluzioni per antenne in grado di operare su HAPS. Dal punto di vista della frequenza, la migrazione verso le alte frequenze, fornendo grandi larghezze di banda e, quindi, capacità di canale, è una tendenza continua e rappresenta una necessità. Oggi, la banda Ka (circa 30 GHz) è considerata molto promettente per questo tipo di applicazioni e, probabilmente, una delle implementazioni più utili a questa frequenza è la l'uso di una lente dielettrica opportunamente illuminata da diverse sorgenti elettromagnetiche primarie. Prendendo in considerazione una vasta gamma di considerazioni tecniche, abbiamo progettato, costruito e misurato un'antenna multi fascio basata sull'uso di una lente dielettrica per operare nello scenario d'interesse. In questo tipo di sistema di antenna, la polarizzazione circolare può essere ottenuta essenzialmente in due modi: i) i radiatori elementari che alimentano la lente sono già circolarmente polarizzati o ii) sono polarizzati linearmente e la polarizzazione circolare viene generata dopo la lente con l'aiuto di un polarizzatore esterno. Per il primo caso, un polarizzatore è stato ottimizzato numericamente, mentre per il secondo caso, abbiamo implementato una procedura di progettazione basata sulla combinazione di modello a linee di trasmissione e unit-cell analysis. Pertanto, abbiamo proposto due soluzioni, evidenziando vantaggi e inconvenienti per ciascuna di queste. Le nostre indagini sono convalidate da prototipi e misure.

Quando un sistema di antenna a fasci multipli è montato su piattaforme operanti sopra la Terra, le forme dell'impronta ricevuta a terra devono essere attentamente controllati specialemnte per elevati angoli di elevazione. Noi proponiamo una antenna a lente in cui la simmetria del fascio viene perturbata agendo sulla forma della lente, con l'obiettivo di generare impronte circolari in tutta l'area coperta. Caratteristiche di radiazioni di questo tipo sono utili non solo per gli HAPS, ma più in generale in scenari in cui il l'antenna è montata su piattaforme nell'atmsofera o nello Spazio e, in generale, in applicazioni in cui la forma delle impronte deve essere attentamente controllata per angoli di elevazione elevati.

La nuova forma ellissoidale è ottenuta con un insieme di semplici equazioni di progetto e l'analisi, puo' essere eventualmente arricchita mediante ottimizzazioni numeriche. Misure effettuate sulla radiazione dell'antenna validano il sistema proposto.

Crediamo che i nostri risultati aprono la strada per la ricerca futura orientata alla realizzazione di sistemi di antenna per HAPS.

Parole chiave: antenne multifascio, polarizzazione circolare, polarizzatore, HAPS, banda KA, lente dielettrica, lente ellipsoidale, controllo forma del beam.

Acknowledgements

The completion of this thesis is a joyful occasion to remember the colleagues, friends and family who have helped and supported me along this road.

First and foremost, I wish to thank my thesis advisor Prof. Juan R. Mosig for his invaluable scientific help and extraordinary human quality; for his trust, inspiration and precious support over these years. His true passion for electromagnetism was a great motivation for this work, and the scientific discussions we shared were a unique experience. Thank you Juan.

My appreciation goes to the committee members Prof. Antonije Djordjevic, from the University of Belgrade, Prof. Andrzej A. Kucharski from Wroclaw University of Technology and Prof. Farhad Rachidi-Haeri from EPFL for having accepted to examine this work and for all their useful remarks which contributed to improve the value of this thesis; I would also like to thank Prof. Rachid Cherkaoui for charing this Jury Commission.

Thanks to all the permanent members of LEMA: Prof. Anja Skrivervik and Dr. Michael Mattes for their support and professional advice. I would like to deeply acknowledge the contribution of J.-F. Zürcher for having taught me many "secrets" about antenna prototyping and measurements as well as for his availability and professionalism during the characterization of the antenna system. A particular thank you to Eulalia for flawlessly running the most delicate matters ans for solving many practical issue.
Huge thanks to the LEMA guys. To Gabriele, my office-mate and the best triathlete: abbiamo passato sempre bei momenti. Thanks to my LEMA Post-Doc: Benjamin and Roberto for their incommensurable help and patience. To the Greek-Docs: Ioannis and Apostolos, unforgivable friends; to David, Marc, Jovanche, Nuno, Madda, Ruzica, Gabriela, Eduardo, Anton, Michele, Baptiste, my past and present office mates Mohsen, Laleh and Sergio: guys you really made these four years a great experience. Likewise, my students Vladimir, Arthur, Fabio, Shima, Christelle, Baptiste, Carlos and Ivan who have given me opportunities to learn more.

Thanks to the StratXX team, Kamal Alavi, Daniel Gautschi and Sergio Lopez for the very rewarding collaboration during the FEASANT project and CHAPS, and for proposals we prepared together. Thanks to the OFCOM project manager Markus Riederer for all his support and help.

Away from the sit-down job, I would like to offer my fondest regards to the EPFL cycling team: Matthew, Paolo and Gabriele. I will never forget the hardest time following your

Table of Contents

1. Introduction

Contents

The global telecommunications industry continues its evolution in improving network services and architectures [1]. The considerable increasing of high capacity services pushes the technologies to more complex and efficient solutions [2, 3]. In modern communication systems, the infrastructure is essentially based in two strategies. On one hand, the transport of the information is ensured by optical networks that can provide long and extremely high capacity links. But these architectures are fixed and not directly accessible by users. On the other hand, wireless technologies allow mobile users dynamical access to the network, with portable devices. Moreover, they deliver 'last mile' communication services efficiently.

As the demand grows for broadband communication services (such as high speed Internet, TV broadcasting, and real-time applications) efficient wireless solutions are becoming more and more important [4–8]. However, delivering high-capacity services by wireless presents a challenge since the radio resources (bandwidth and frequency spectrum allocation) are limited. Hence, frequency re-use techniques are implemented to provide enough bandwidth to a large number of users. This strategy is based on the use of cellular structures, in which a group of frequencies is re-used considering many factors, such as the dimension of the cells and the propagation environment [9–14].

The frequency spectrum allocation is congested due to other existing applications and the continuous growing of spectrum demands leads to a move towards higher frequency bands (e.g. Ka-band) where the spectrum is less populated [15, 16]. However, at mm-waves, the interaction with obstacles, heavily impacts on the propagation of the signal due to strong attenuation experimented after each reflection [17, 18]; therefore, the use of Ka-band waves implies line-of-sight propagation [19–21]. To overcome such propagation issues, a solution might be a very tall base station in line-of-sight with the users. Of course, installing hundred meters height towers dedicated to this purpose everywhere is neither economically nor

environmentally acceptable.

Broadband services delivered from geostationary (GEO) satellites can provide line-of-sight communication to many users and in the recent years a significant market has been going in that direction. However, the free space path loss (FSPL) for extremely long distance communications in considerable. When GEO satellites are exploited, the distance between the transmitting (Tx) and receiving (Rx) antenna is around 36 000 km, yielding a FSPL in the order of 200 dB. Expensive transceiver front ends must be employed to handle such propagation constraint and the user terminals may be inaccessible due to untenable costs. A further drawback is the propagation delay over a geostationary link (around 250 ms), which may cause problems with some communication protocols [22, 23].

Low earth orbit (LEO) satellites may obviate some of these propagation issues, but suffer from complexity of constellation architectures, network protocols and maintenance [24].

An innovative solution to deliver wireless services, providing line-of-sight communication type and modest FSPL lies in aerial platforms [25]. These platforms may be airplanes or airships and may be manned or unmanned with the capability of flying in the stratosphere at the altitude of up to 21 km with a telecommunication payload. Such a payload can be a transparent transceiver or a more complex base station [26–31].

In recent years, increased emphasis has been placed on systems that can provide communications and surveillance support from such altitude [32] although many aspects introduced by these new solutions constitute a challenge in many research domains. Many energetic, aerodynamic and system control issues [33–35] rise when considering an aerial platform mission in the stratosphere. From the communication payload point of view, an antenna system that provides broadband communication services from aerial platforms operating at nearly 21 km from the ground is not available on the market and it needs to be fully developed [36].

Within this framework, StratXX [37](a Swiss company which is also the main stratospheric platforms developer in Europe) has launched a project aiming to investigate the feasibility of a Ka-band antenna payload for broadband communications delivered from stratospheric platforms. The FEASANT (Feasibility study for HAPS antenna, 2009-2010) project was funded by the Commission for Technology and Innovation (CTI) [38] and by StratXX under contract number 19301.1 (PFNM-NM) and apart from StratXX also involved the research institute Centre Suisse d'Electronique et Microtechnique SA (CSEM) [39] and the Laboratory of Electromagnetics and Acoustics (EPFL-LEMA) [40]. Most achievements of this thesis were strongly driven by the activities that EPFL-LEMA developed in FEASANT project.

1.1. The FEASANT project

1.1.1. Project goal

The FEASANT project was devoted to the feasibility study of a broadband communication link between an aerial platform operating in the stratosphere and ground terminals situated in the area below the platform. The on-board antenna is indeed the most challenging element of an aerial platform-based communication system that aims to deliver high capacity (similar to that available from terrestrial system [41–43]) and wide coverage (similar to that available from satellite [44]). With this idea, the aerial platform would be able to provide rapid coverage and high capacity while being capable of serving both densely populated cities and suburban & rural/remote areas, where wireless communications are poor. This communication system has the potential to work as a complement of the existing telecommunication infrastructure or as a provisory solution for areas struck by natural calamities [45–51]. These are the scientific and technological objectives of the FEASANT project, as epitomized by the typical application scenario depicted in Fig. 1.1 [52–56].

1.1.2. Project overview

A key element to achieve the FEASANT goals is a high quality Tx-Rx antenna subsystem. Rather than using or adapting existing equipment, the idea is to develop a proprietary antenna subsystem, well adapted to the aerial platform environment (compact, light) and working at mm-wave frequencies, allowing faster and easy transmission of multimedia signals. In addition, a stabilized platform is needed for proper operation of the antennas and this requires the selection of adequate gimbals and stabilizer mechanisms for the antenna subsystems.
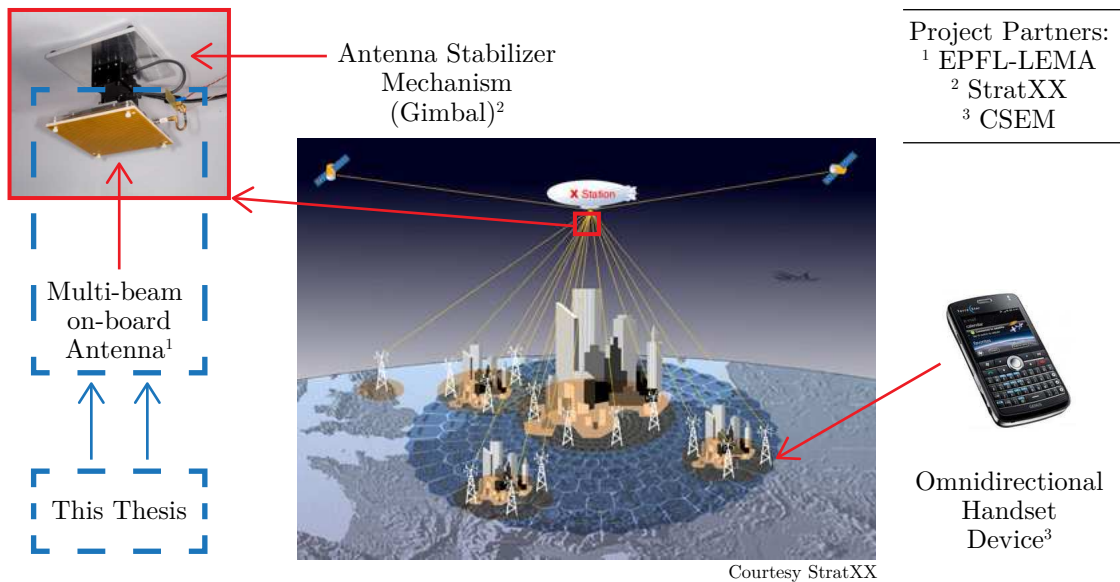
Figure 1.1.: FEASANT typical application scenario.

More specifically, the scientific target of the project partners were as follows:

- **EPFL-LEMA** aims to satisfy the scenario requirements with a Tx on-board antenna design based on adeguate technologies as well as to characterize the proposed antenna system. Emphasis is placed on antenna solutions that are as compact, efficient and as low power as possible.

- **StratXX** aims to identify the requirements for the antenna stabilization system and perform a design suitable for long stratospheric missions.

- **CSEM** aims to provide a Rx antenna design suitable for mobile handset devices. Emphasis is placed on antenna solutions that are omnidirectional, lightweight and primarily low cost.

1.1.3. Specifications

Scenario requirements.
In a cellular system, each cell uses a different set of frequencies from neighboring cells, to avoid interference and to provide guaranteed services within each cell. This enables a large number of mobile users to communicate with each other and with fixed users anywhere in the network, via base stations. The cell shape can be hexagonal, square, circular or some other regular shapes, although hexagonal cells are preferred since this shape maximizes the overall system performances [11, 47, 52, 54, 57, 58]. The density of active users and the complexity of the base station transceiver determine the dimension of the cells. In cities, each cell site may have a range of up to approximately 2 km, while in rural areas, the range could be as much as 8 km. When joined together, these cells provide radio coverage over a wide geographic area. Large geographic areas, adequately divided into smaller cells, can be covered by high altitude platforms, keeping low power level on the ground.

Cellular networks offer a number of advantages over alternative solutions:

- reduced interference from other signals

- increased capacity

- reduced power use

- larger coverage area

Within this context, the scenario specifications for high altitude platform communications were derived by StratXX as part of their business plan. They are listed in Table 1.1.

Table 1.1.: *Scenario specifications*

Parameter	Requirement
Station Altitude	≈ 21 km
Coverage type	Uniform coverage
Adjacent beam-overlap level	$\approx$-4 dB
Cluster type	Hexagonal multi-cells
Number of cells	19
Nominal cell radius	≈ 2.5 km
Cell ellipticity	$\leq 5\%$
Cell surface	18.0 km^2 - 21.2 km^2
Distance adjacent cell centers	≈ 4.33 km

This scenario for requirements determines in turn the initial technical specifications of the 3 main parts of the communications system: Tx on-board antenna, stabilizer platform (gimbal) and Rx handset antenna. But, other circumstances also contribute to fix the final specifications of these components, as determined here below.

On-board antenna specifications. Aerospace industry is strongly driven by high performance as well as by demanding aerodynamics and mechanical criteria. This implies an on-board antenna design that is, on one hand, compatible with typical electromagnetic standards for terrestrial broadband communications, and, on the other hand, qualified for stratosphere and near-space applications. It is within this context that one should interpret the performance requirements specified in Tables 1.2 for the on-board antenna.

Table 1.2.: *On-board antenna specifications*

Parameter	Requirement
Frequency band	27.5 to 31.3 GHz
Bandwidth (S_{11}@ -10 dB)	3.8 GHz ($\approx$13%)
Return loss	$\geq$ 10 dB
Coupling between adjacent feeds	$\leq$ -20 dB
Number of beams	19
Power handling	$\geq$ 100 W/beam
Half-power beam-width	11.8° - 12.2°
Beam feed of view	13.4° - 13.8°
Sidelobe levels	$\leq$-14 dB
Polarization	Circular
Axial ratio	$\leq$ 3 dB
Aperture size	$\leq$ 30 cm
Max antenna sizes	30 cm ×30 cm × 30 cm
Weight	$\leq$ 30 kg

Performance parameters where required values are not explicitly determined
from system calculations are estimated from typical expectations.

Stabilizer platform system (gimbal) specifications.

In aerospace navigation, a gimbal is a mechanical device that measures the rotation of an object in three dimensions and controls that rotation. Gimbals used in spacecraft have three sets of three gyroscopes in the inertial measurement unit, one for each axis (x, y and z). A three-axis gimbal may allow an object mounted on it to remain in a horizontal plane regardless of the motion of its support [59, 60].

Aerospace and automation industries are characterized by high performance-to-cost ratios as well as demanding aerodynamics and mechanical constraints. This implies that the stabilizer platform designed for the FEASANT project should be compatible with typical aerial platform communication scenarios, enabling the proper antenna positioning while being simultaneously as robust and compact as possible. All this leads to the performance requirements specified in Tables 1.3 for the stabilizer platform system.

Table 1.3.: *Stabilizer platform system specifications.*

	Parameter	Requirement
Payload	Payload description	RF payload (antenna)
	Weight	≤ 100 kg
	Max dimensions	70 cm $\times$ 70 cm $\times$ 50 cm
	Inertia	8 kgm^2
Performance	Max Slew Rate (Azimuth and elevation)	12°/s
	Acceleration	$\geq 200°/s^2$
	Positional resolution	0.1°
	Pointing accuracy	$\leq 1°$
	Repeatability	0.2°
	Azimuth travel range	360°Continuous
	Elevation travel range	$\pm 20°$
	Duty cycle	100%
Power	Input voltage available	24 V
	Maximum power available	2 kW
Gimbal dimensions	Dimensional space limits	$\oslash : 400$ mm; H:400 mm
	Weight	≤ 20 kg
	Others	Low aerodynamic drag
Operating environment	Temperature	-20 °C/50 °C
	Weather (Indoor/Outdoor)	Outdoor
	Dust sand	IP 55

Omnidirectional handset antenna specifications.
The consumer handset market is strongly driven by low-cost, size, weight and aesthetics criteria [61–63]. This implies that the handset antenna should be essentially compatible with standard mass production techniques, to enable a convenient reduction of cost through production volume [60, 64–69]. The handset antenna requirements, as originally requested by StratXX, are summarized in Table 1.4.

Table 1.4.: *Handset antenna specifications*

Parameter	Requirement
Pattern type	Quasi omni-directional
Frequency band	27.5 to 31.2 GHz
Bandwidth (S_{11}@ -6 dB)	3.8 GHz ($\approx$13%)
Return loss	$\geq$ 6 dB
Max Power handling	2 W
Polarization	Circular
Axial ratio	$\leq$ 3 dB
Max antenna sizes	5 cm $\times$ 5 cm $\times$ 2 cm
Weight	$\leq$ 30 g

Performance parameters where required values are not explicitly determined
from system calculations are estimated from typical expectations.

1.2. Objectives of this thesis

This thesis deals with the characterization at the pre-industrial level of a Tx aerial platform on-board antenna system that fulfills the scenario requirements and meets the technical specifications. At the time of writing, no commercial antennas performing similar functions are available on the market. Hence, the development of the targeted system would give the industrial partner a competitive edge in the domain of antennas for high altitude platform communications.

As partner of the FEASANT project, EPFL-LEMA has contributed throughout all its phases, from the conception up to the implementation and experimental verification of the first on-board antenna prototypes. This section is an overview of some of the main topics addressed during the development of the FEASANT project and covered in this thesis.

An important point of this research work was the choice made at the very beginning for the antenna technology. The antenna requirements present indeed several challenges both from the electromagnetic and from the mechanical points of view. From the first, the coexistence of strict specifications on broadband, multi-beams and polarization behavior calls for an antenna design that has electrically large dimensions. From the second, antenna for space and near-space applications must be as compact as possible. Therefore, several antenna types were compared during the project and final agreement fell upon a lens antenna that can provide several beams with a single aperture, thus resulting in a very compact and efficient design.

A first, obvious, issue to be considered concerns circular polarization. Traditional lens antenna design envisages the use of a lens to focus the radiation of elementary radiators (also called feeds) placed adequately in the lens proximity. Broadband circularly polarized beams can be achieved with lens antennas by two strategies. Either the EM wave impinging on the lens and generated by the feeds is already circularly polarized (the polarizer is inside the feed and is called "internal") or the EM wave crosses the lenses with a linear polarization and transformed into a circularly polarized wave by a polarizer located just after the lens ("external" polarizer). The two different solutions have been characterized and compared. For the second, which was considered more interesting, a mathematical model has been developed for the evaluation of the polarizer performances.

The second issue concerns the shape of the power footprints generated on the ground by the on-board antenna beams. If used on altitude platforms, traditional symmetric beams generate elliptical ground footprints, producing a degradation of the communication performance which is proportional to the experienced elongation of the footprint. An important goal was to fully characterize a new lens topology suitable to overcome this problem.

Globally, the objective of the present PhD memoir is to provide a reasoned outline of this complete design process and of its results, while performing a comprehensive analysis of the

structures selected in the project.

1.3. Outline and original contributions

This section summarizes the layout and the contents of the thesis chapters and provides some comments on the original contributions, linked with each chapter.

Chapter 1 presents the context in which the thesis is carried out and defines the goals of this research. Essentially, these goals are related to the development of an on-board antenna system for high altitude platform communications within the framework of the Swiss CTI project FEASANT. This chapter also provides the summary of the thesis and outlines the contents of the present memoir.

Chapter 2 provides an overview of high altitude platforms as well as a comprehensive state-of-the art on antenna technology suitable for such platforms. It covers various aspects, from the history of stratospheric missions and the current state of the worldwide research in high altitude platforms to a survey of the most advanced antenna technology suitable for such applications.

The selection of the Ka-band for these antenna results in a strong innovation contents. An original contribution here resides in the identification and description of the antenna types suitable for stratospheric missions.

Chapter 3 describes the criteria that will guide the design of the on-board antenna system and explains the selected solution. The proposed antenna design depends critically on the polarizer which is embedded into the antenna feeds. In this design, a number of different microwave sub-systems are investigated. The theoretical aspects related to such sub-systems are reviewed, to understand their principle of operation, and their suitability for the purpose of aerial platform antennas.

Although the antenna solution investigated in this chapter is based on microwave concepts available in literature, a circularly polarized multi-beam antenna design for aerial platform communications is not available in literature and, to the best of our knowledge, constitutes a novelty in this domain. Furthermore, this chapter brings new contributions to the various addressed topics, such as (i) the design of a very compact circularly polarized feed array at Ka-band, (ii) the study of the interaction between the circularly polarized waves generated by these feeds and the lens, (iii) the study of the mutual coupling between different feeds including the different configurations of polarization status of each feed, and (iv) the evaluation of the impact of each antenna element in the overall antenna system performances.

Chapter 4 describes the on-board antenna design based on the use of an external polarizer to achieve circularly polarized beams. The antenna concept remains essentially the

one studied in chapter 3, but the use of an external polarizer constitutes a different solution to achieve multiple circularly polarized beams. The antenna sub-system is fully characterized and the performances of the design obtained in this chapter are compared with the antenna performances presented in chapter 3.

An innovative procedure to design external polarizers has been investigated in this chapter. The proposed procedure is based on transmission line circuit theory and on full-wave unit cell analysis in frequency domain. The hybrid combination of those two techniques paves the way for the polarizer complete design process, while avoiding heavy full-wave optimizations. Such procedure also allows an efficient sensitivity analysis, useful to give a quantitative insight on the effect of any tolerance on the optimal working condition of the polarizers.

Chapter 5 introduces a novel lens antenna geometry. The concept investigated in this chapter has allowed the correction and optimization of the ground power footprints generated by the antenna beams. Such correction is extremely important in broadband antenna systems, where the interference produced in each cell strongly influences its neighbors. Antenna design and prototypes as well as measurements made on the complete Ka-band lens antenna system are shown in this chapter.

Chapter 6 concludes this thesis with a summary and a general assessment the work perceived in this thesis while also discussing possible future research directions.

Appendix An appendix is provided reporting the mechanical design of the antenna parts discussed in Chapter 3.

References

[1] A. Aragón-Zavala, J. Cuevas-Ruíz, and J. Delgado-Penín, *High-altitude platforms for wireless communications.* Wiley, 2008.

[2] D. A. Baker and Scientific American, *Inventions from Outer Space: Everyday Uses for NASA Technology / David Baker.* Universal International, Gordon, N.S.W., 2000.

[3] S. J. Dick and R. D. Launius, Eds., *Societal impact of spaceflight.* Washington DC: NASA Office of External Relations, History Division, 2007. [Online]. Available: http://permanent.access.gpo.gov/lps115997/

[4] F. Hules, G. Streelman, and H. Yen, "A direct broadcast satellite reception system for automotive OEMs," in *IEEE Antennas and Propagation Society International Symposium*, vol. vol. 1B, 2005, pp. 80–83.

[5] G. L. Charvat, L. C. Kempel, E. J. Rothwell, C. M. Coleman, and E. L. Mokole, "An ultrawideband (UWB) switched-antenna-array radar imaging system," *presented at IEEE Int. Symp. on Phased Array Systems and Technology (ARRAY)*, pp. 543-550, Oct 2010.

[6] E. Carrasco, M. Arrebola, J. A. Encinar, and M. Barba, "Demonstration of a shaped beam reflectarray using aperture-coupled delay lines for LMDS central station antenna," *IEEE Trans. Antennas Propagat.*, vol. AP-56, pp. 3103-3111, Oct 2008.

[7] R. Baggen, S. Vaccaro, and D. Llorens, "Design considerations for compact mobile Ku-band satellite terminals," in *proc. EuCAP 2007, 2nd International Conference on Antennas and Propagation*, Nov. 2007.

[8] R. Baggen, S. Vaccaro, and D. L. del Río, "Mobile Ku-band satellite terminal for low-cost applications," in *International URSI Commission B. Electromagnetic Theory Symposium*, Ottawa, ON, Canada, Jul. 2007, pp. 80–83.

[9] J. Thornton and D. Grace, "Effect of lateral displacement of a high-altitude platform on cellular interference and handover," *IEEE Transaction Wireless Communications*, vol. 4, no. 4, pp. 1483–1490, July 2005.

[10] R. Tafazolli and A. K. Widiawan, "High altitude platform station (HAPS): a review of new infrastructure development for future wireless communications," *International Journal on Wireless Personal Communications*, vol. 42, no. 3, pp. 387–404, 2007.

[11] T. Morisaki, "Overview of regulatory issues and technical standards on high altitude platform stations," *Proceedings of the International Workshop on High Altitude Platforms Systems, WHAPS 05*, Athens, Sept. 2005.

[12] "Document 8-1/307-e: Revised technical and operational parameters for typical imt-2000 terrestrial systems using high altitude platformstations and cdma radio transmission technologies," *International Telecommunication Union*, Geneva, 1999.

[13] J. Delgado-Penín, H. Carrasco, F. Ulloa, and E. Bertran, "Space-time coding and processing to improve radio communication coverage from high altitude platforms (HAPs)-an approach," *Proceedings of Data Systems in Aerospace Conference (DASIA'01)*, Nice, June 2001.

[14] F. Daneshgaran and M. Laddomada, "Optimized prunable single cycle interleavers for turbo codes," *IEEE Transactions on Communications*, vol. 52, no. 6, pp. 899–909, June 2004.

[15] "IRIG Telemetry standard RCC. Doc.106-07, September 2007. URL: http://www.irig.org."

[16] "Document/2/049-E: Operational and Technical Characteristics for a Terrestrial IMT-2000 System using High Altitude Platform Stations (Technical Information Document)," *International Telecommunication Union*, Geneva, 1998.

[17] "Resolution 122 (Rev. WRC-07): Use of the Bands 47.2-47.5 GHz and 47.9-48.2 GHz by High Altitude Platform Stations in the Fixed Service and by Other Services," Geneva, 2007.

[18] "World Radio communications Conference, Resolution 145 (Rev. WRC-07): Use of the Bands 27.9-28.2 GHz and 31-31.3 GHz by High Altitude Platform Stations in the Fixed Service," Geneva, 2007.

[19] "Mobile, radio determination, amateur and related satellite services recommendation m. 1456: Minimum performance characteristics and operational conditions for high altitude platform stations providing imt-2000 in the bands 1885-1980 mhz, 2010-2025 mhz and 2110-2170 mhz in regions 1 and 3, and 1885-1980 mhz and 2110-2160 mhz in region 2," *International Telecommunication Union*, 1-21, Geneva, 2000.

[20] "Itu-r propagation recommendation p.681-6: Propagation data required for the design of earth-space land mobile telecommunication systems," *International Telecommunication Union*, Geneva, 2003.

[21] "Resolution221: Use of high altitude platform stations providing imt-2000 in the bands 1885-1980 mhz, 2010-2025 mhz the bands 27.5-28.35 ghz and 31-31.3 ghz," *International Telecommunication Union*, Geneva, 1999.

[22] H. Lee, "Ku-bandlink budget analysis of UAV with atmospheric losses," *25th Digital Avionics Systems Conference, 2006 IEEE/AIAA*, 1-8, Oct. 2006.

[23] S. Rao, M. Tang, C.-C. Hsu, and J. Wang, "Advanced antenna technologies for satellite communication payloads," *1st European Conference on Antennas and Propagation*, 2006.

[24] F. Averty, A. Louzir, J. F. Pintos, P. Chambelin, C. Person, G. Landrac, and J. P. Coupez, "Cost effective antenna for LEO-satellites communication system using a homogeneous lens," *Antennas and Propagation Society International Symp., 2004 IEEE*, vol.1, pp. 671-674, June 2004.

[25] M. Oodo, H. Tsuji, R. Miura, M. Maruyama, M. Suzuki, Y. Nishi, and H. Sasamoto, "Experiments on IMT-2000 using unmanned solar powered aircraft at an altitude of 20 km," *IEEE Transactions Vehicular Technology*, vol. 54, no. 4, pp. 1278–1294, May 2005.

[26] "ITU Internet Report, Birth of Broadband," *International Telecommunication Union*, 1-200, Geneva, September, 2003.

[27] "High Altitude Platform Stations: An Opportunity to Close the Information Gap," *Question 9/2*, Report on ITU, Geneva, 1998.

[28] "Fixed Service Recommendation F.1399-1, Vocabulary of Terms for Wireless Access," *International Telecommunication Union*, 1-14, Geneva, 2001.

[29] "Resolution 122: Whereby HAPS is allowed to operate within the fixed service in the band 47.2-47.5 GHz and 47.9-48.2 GHz," *World Radio Communications Conference*, 1997.

[30] J. D. Laurier, B. Gagnon, J. Wong, R. Williams, and C. Hayball, "Research on the technology of an airplane concept for a Stationary High Altitude Relay Platform (SHARP)," *32nd Annual General Meeting of the Canadian Aeronautics and Space Institute*, Montreal, Canada, May 1985.

[31] "Fixed Service Recommendation F.592-3, Vocabulary of terms for the fixed service," *International Telecommunication Union*, 1-10, Geneva, 2002.

[32] C. Oestges and D. Vanhoenacker-Janvier, "Coverage analysis of a stratospheric communication system," *IET Proceedings on Microwave, Antennas and Propagation*, vol. 148, no. 1, pp. 45–49, May 2001.

[33] M. A. Dornheim, "Special fuel cells: key to months-long night," *Aviation Week and SpaceTechnology*, February 2000.

[34] W. Knaupp and E. Mundschau, "Photovoltaic-hydrogen energy systems for stratospheric platforms," *Proceedings 3rd World Conference on Photovoltaic Energy Conversion*, 2003.

[35] Lavagno and R. Gerboni, "Energy subsystem for HeliNet: hydrogen as stratospheric application propellant," *Proceedings of the 14th World Hydrogen Energy Conference*, Montreal, Canada, June 2002.

[36] F. Pinkney, "UAV communications payload development," *Proceedings MILCOM '97*, Nov. 1997.

[37] "http://www.stratxx.com/," StratXX Near Space Technology AG, Bahnhof 11, 6056 Kaegiswil.

[38] "http://www.kti.admin.ch," Swiss CTI.

[39] "http://www.csem.ch/site/," CH-2002 Neuchâtel.

[40] "http://lema.epfl.ch/," CH-1015 Lausanne.

[41] "Fixed service recommendation f1245-1: Mathematical model of average radiation patterns for line-of-sight point-to-point radio-relaysystem antennas for use in certain coordination studies and interference assessment in thefrequency range from 1 to about 70 ghz," *International Telecommunication Union*, Geneva, 2000.

[42] "Fixed service. recommendation f. 1500: Preferred characteristics of systems in the fixed service using high altitude platforms operating in the bands 47.2-47.5 ghz and 47.9-48.2," *International Telecommunication Union*, 1-14, Geneva, 2000.

[43] "Fixed service. recommendation f. 1569:technical and operational characteristics for the fixed service using high altitude platformstations in the bands 27.5-28.35 ghz and 31-31.3 ghz," *International Telecommunication Union*, Geneva, 2002.

[44] "Satellite service recommendation 672-4:satellite antenna radiation pattern for use as a design objective in the fixed-satellite service employing geostationary satellites," *International Telecommunication Union*, Geneva, 1997.

[45] G. M. Djuknic, J. Freidenfelds, and Y. Okunev, "Establishing wireless communications services via high-altitude aeronautical platforms: a concept whose time has come?" *IEEE Communications Magazine*, pp. 128–135, Sept. 1997.

[46] J. Gavan and M. Haridim, "Stratospheric quasi-stationary platforms: can they replace communication satellite systems?" *Telecommunications and Space Journal*, vol. 4, pp. 275–282, 1997.

[47] D. Grace, M. Mohorčič, M. H. Capstick, M. Bobbio-Pallavicini, and M. Fitch, "Integrating users into the wider broadband network via high altitude platforms," *IEEE Transactions on Wireless Communications*, vol. 12, no. 1, pp. 98–105, May 2005.

[48] "High Altitude Platforms for Communications and Other Services," COST 297, URL:http://www.hapcos.org, 2005.

[49] Y. Hase, R. Miura, and S. Ohmor, "A novel broadband all-wireless access network using stratospheric radio platform," *IEEE Vehicular Technology Conference*, vol. 98, pp. 98–105, May Ottawa, Canada, May 1998.

[50] S. Karapantazis and F. N. Pavlidou, "The role of high altitude platforms in beyond 3G Networks," *IEEE Wireless Communications*, pp. 33–41, 2005.

[51] M. Pent, T. C. Tozer, and J. A. Delgado-Penín, "HAPs for telecommunications and surveillance applications," *32nd European Microwave Conference, EMS'02*, pp. 24–26, Milan, Italy, Sept. 2002.

[52] F. Akyildiz, X. Wangand, and N. Colella, "HALO (High Altitude Long Operation):a broadband wireless metropolitan area network," *MOMUC '99*, pp. 271–277, 1999.

[53] D. Avagnina, "Wireless networks based on high platforms for the provision of integrated navigation/communication services," *IEEE Communications Magazine*, vol. 40, no. 2, pp. 119–125, 2002.

[54] "European Union contract FP6-IST-2003-506745, Communications from aerial plat-form networks delivering broadband communications for all," *6th Framework Programme, Priority 2, Information Society Technologies, Annex*, pp. 1–27, December 2003.

[55] "European Union contract FP6-IST-2003-506745, Communications from aerial plat-form networks delivering broadband communications for all," *6th Framework Programme, Publish-able Executive Summary*, pp. –6, Mar. 2007.

[56] S. Karapantazis and F. N. Pavlidou, "Broadband communications via high-altitude plat-forms: a survey," *IEEE Communications Surveys & Tutorialsn*, vol. 7, no. 1, pp. 2–31, 2005.

[57] D. Grace, J. Thornton, G. P. Whire, C. Spillard, D. A. J. Pearce, M. Mohorčič, T. Javornik, E. Falleti, J. A. Delgado-Penín, and E. Bertran, "The European HeliNet broadband communications application - an update on progress," *The 4th Stratospheric Platform Systems Workshop*, Tokyo, Japan, 2003.

[58] D. Grace, N. E. Daly, T. C. Tozer, and A. G. Burr, "LMDS from high altitude aeronautical platforms," *Proceedings IEEE GLOBECOM*, vol. 99, pp. 2625–2629, 1999.

[59] T. Wierzbanowski, "Unmanned aircraft systems will provide access to the strato-sphere," *RF Design*, pp. 12–16, Feb. 2006.

[60] NATALIA consortium. Submitted by IMST, "Appendix 1 to ESA ITT AO/1-4482/03/NL/US. Patch Antenna for Mobile Receive Only Terminals," Statement of Work, Sep. 2003.

[61] J. Huang, "Microstrip antennas for commercial applications," in *Microstrip Antennas. The Analysis and Design of Microstrip Antennas and Arrays*, D. M. Pozar and D. H. Schaubert, Eds. New York: IEEE Press., 1995, pp. pp. 371–379.

[62] A. Henderson and J. James, "Improved microstrip flat-plate array for domestic DBS reception," in *Antennas and Propagation Society International Symposium*, vol. 24, Jun. 1986, pp. 565–568.

[63] ——, "Low-cost flat-plate array with squinted beam for DBS reception," *Microwaves, Antennas and Propagation, IEE Proceedings H*, vol. 134, no. 6, pp. 509–514, 1987.

[64] R. Azadegan, "A Ku-band planar antenna array for mobile satellite TV reception with linear polarization," *IEEE Trans. Antennas Propagat.*, vol. 58, no. 6, pp. 2097 –2101, 2010.

[65] (2008, Feb.) MotoSAT Product Information Sheet. MotoSAT Systems. [Online]. Available: http://www.motosat.com/

[66] (2008, Feb.) Datron Product Information Sheet. Datron Advanced Technologies Inc. [Online]. Available: http://www.turbosurf.com/CruiseTV-STS.html

[67] (2008, Feb.) Satellites in Motion(R) catalog. Satellites in Motion(R). [Online]. Available: http://www.satellitesinmotion.com/

[68] R. Baggen, S. Vaccaro, and D. L. del Río, "Mobile Ku-band satellite terminal for low-cost applications," in *International URSI Commission B. Electromagnetic Theory Symposium*, Ottawa, ON, Canada, Jul. 2007, pp. 80–83.

[69] M. Bourry, F. Tiezzi, and S. Vaccaro, "Omni-directional antenna for mobile satellite broadcasting applications," Patent US 20 090 027 294, January 29, 2009.

2. The High Altitude Platform Stations

Contents

2.1. Introduction

High Altitude Platforms Station (HAPS) are considered a very interesting alternative to the broadcasting services provided by satellites [1–4].

The aim of this chapter is to provide the state of the art for HAPS communications as well as a review of the knowledge required for the design of an on-board antenna system for these applications. In particular the two main goals of this chapter are:

1. to discuss the advantages and issues that occur when using aerial platforms to establish communication links from the *stratosphere*.

2. to describe the technologies and requirements for HAPS antennas.

The analysis presented in this chapter serves as a common base for all the investigations and results presented later on. The theoretical aspects presented in Section 2.7 are useful in the design of on-board antenna parts in Chapters 3 and 5. The considerations made in Section 2.8 find their applications in the design of the radiating elements of the on-board antenna in Chapters 4. The introductory topics presented in Sections 2.2, 2.5 and 2.6 are essential to guide the choices made in the rest of this thesis.

2.2. The HAPS concept

A High Altitude Platform Station (HAPS) is a very simple concept [5], with a great deal of potential. These platforms are positioned at stratospheric altitude, typically at 20-25 km approximately [6]. HAPS aim to provide mainly telecommunications services acting as broadcasting repeaters [2]. The motivation in using such a solution to serve large number of users, dates back to the 60s when wireless communication systems became interesting, not only for military use, but also for civilian applications. Since then, researchers have seen HAPS as a potential solution to improve communications systems in general and such platforms have been considered for many other applications such as remote sensing, traffic control, surveillance and weather forecast. [1, 3, 4, 7, 8].

2.3. The stratosphere

The *stratosphere* is one of the layers that transitionally compose the Earth's atmosphere. The lowest atmospheric layer is the *troposphere*. It extends from the Earth's surface to the *tropopause* about 10 to 18 km in altitude, depending on the season and on the geographical position. In the *troposphere*, the air temperature generally decreases with the altitude. The air pressure decreases from about 1000 hPa at sea level to about 100 hPa at the *tropopause* altitude. Approximately 80% of the total air mass and almost all weather phenomena reside here. Wind speed is very high at the altitude of 12-15 km.

The *stratosphere* is the next layer, extending from the *tropopause* to the *stratopause* at about 50 km from the ground. The ozone layer resides here and more than 99% of the total air mass is concentrated in the first 40 km from the Earth's surface. The *stratosphere* is characterized by a high kinematic stability associated to the increase of temperature with height. The pressure decreases to reach about 1 hPa at the *stratopause* and the wind speed ranges from few m/s at 20 km of altitude to 40-59 m/s in the high *stratosphere*.

The *mesosphere* extends from the *stratopause* to the *mesopause* at about 90 km, where the pressure is 0.01 to 0.001 hPa. Most of meteors burn up in the *mesosphere* as a result of collisions with gas particles there. The temperature in this layer constantly decreases up to -100 °C, as well as pressure that reaches 10^{-3} hPa at the *thermopause*. The wind speed ranges from 10 to 60 m/s in this layer.

The *thermosphere* is located higher, up to 300 km. Here, aurora phenomena occur. The *exosphere*, located above the *thermosphere*, is the most distant atmospheric region, a transitional zone between the Earth's atmosphere and interplanetary space.

Figure 2.1, 2.2 and 2.3 show the temperature, pressure and average wind speed profile in the atmosphere, respectively. These parameters vary according to the season, geographic position and the temperature gradient.

From the HAPS point of view, one of the most critical factors is the wind speed, directly related to the platform positional stability. At altitudes of about 20 km, the air masses are relatively stationary, with very slow winds only. This contrasts heavily with the maximum values observed for wind speed at the altitudes of conventional aviation (10-12 km). HAPS can thus operate in this altitude being at a relatively close distance to Earth surface. That is why most of stationary high altitude platforms have to be located at the altitude of about 20 km.
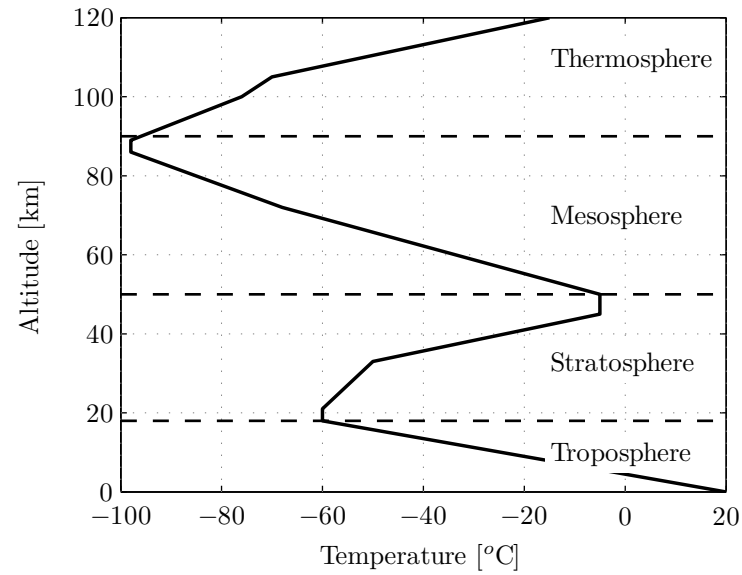
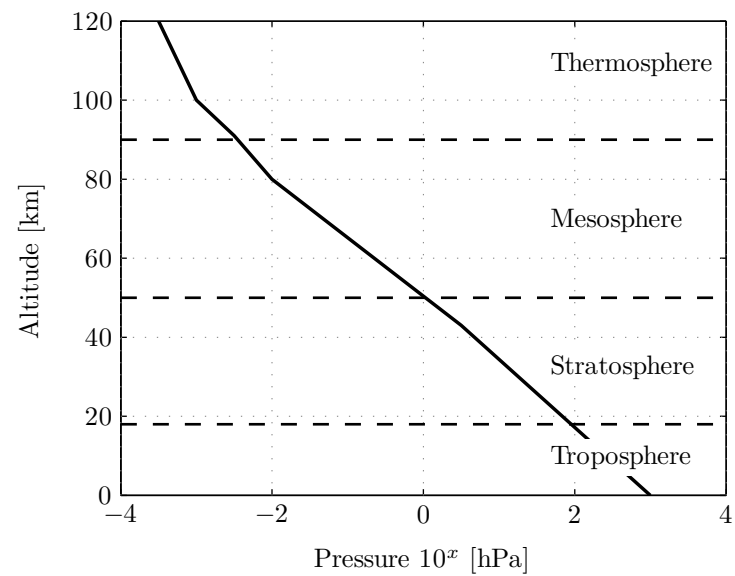**Figure 2.1.:** Temperature profile in Earth atmosphere.

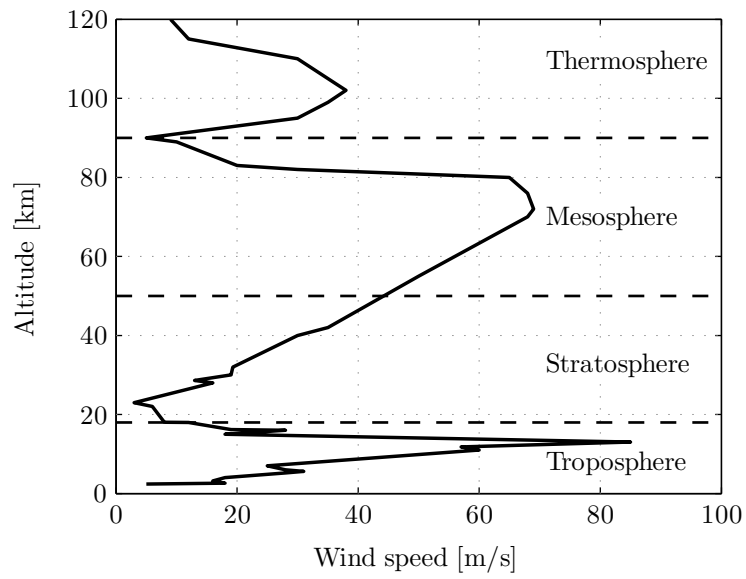**Figure 2.2.:** Pressure profile in Earth atmosphere.

Figure 2.3.: Wind speed profile in Earth atmosphere.

2.4. HAPS history

Data regarding HAPS history is not easy to obtain, as it is frequently hidden due to commercial and strategic reasons. However as the succinct description here below proves, HAPS have been around for more than 30 years and quite intensively used [9].

The SHARP activity [10, 11]

In 1980, SHARP was the first project conceived for civil high-altitude-platform stations. It was developed by the Communication Research Center in Canada. The SHARP station (see Fig. 2.4), called *wingspan* flew at an altitude of 21 km providing surveillance, monitoring services, and establishing a simple communication link with the ground station.

http://www.friendsofcrc.ca/Projects/ SHARP/sharp.html

(a)   (b)

Figure 2.4.: *Wingspan*: the first civilian aerial station. (a) Preliminary prototype carried out in 1982. (b) Final prototype carried out in 1987.

The SKY station [9]

Immediately after the successful flight of *Wingspan*, a North American project was launched: Sky Station International planned a high-altitude platforms mission aiming at worldwide coverage. This station was able to safely maintain a geo-stationary position at the altitude of 21 km in the *stratosphere*. The *Sky Station* platform (see Fig. 2.5.a) was powered by solar panels, non-polluting fuel cells hence was environmentally friendly. With a length of 200 m and a diameter of 60 m, *Sky Station* was equipped with a telecommunication payload, delivering a variety of wireless communication services. A single station could provide a broadband wireless link (2 Mb/s uplink and 10 Mb/s downlink) over an urban area using mm-wave frequencies. Similar services were achieved also by the airplane *Pathfinder* (see Fig. 2.5.b), realized by AeroVironment Co. in the early 1980s [12].
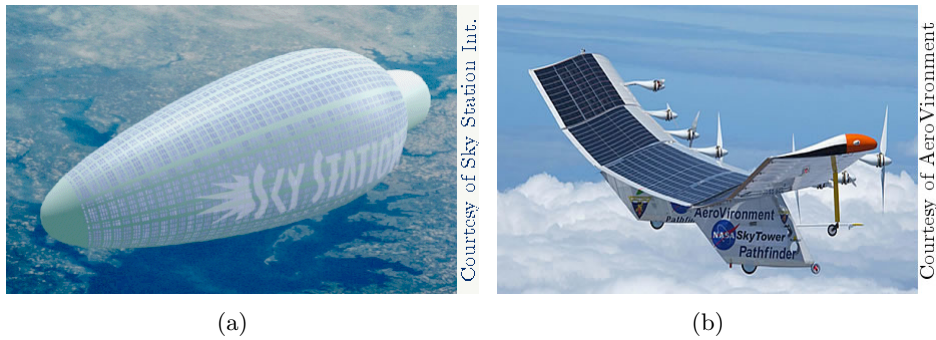
(a)   (b)

Figure 2.5.: (a) The *Sky Station* platform and (b) the Sky Tower *Pathfinder*.

The HALO project [13, 14]

The Angel Technology Corporation [15] developed the first communication network in USA employing high altitude platforms. In the project HALO, Angel Technology Corporation aimed to provide long operation missions flying continuously at the altitude of about 21 km with many platforms. Each platform (see Fig.2.6) was used as *hub* of the network, guaranteeing up to 100 Gb/s of throughput over an area of 100 km diameter. Operating in Ka-band, the antenna mounted on-board covered such an area with 121 spot-beams.

(a)   (b)

Figure 2.6.: The first long operation mission platform: *Proteus* (the Angel Technology Corporation platform) with communication payload.

The ERAST program

ERAST was a program started by NASA in 1994. A variety of unmanned platforms, propelled with solar power, were tested with several flights demonstrating that such light stations can independently take off, reach the *stratosphere* for a long scientific mission and land. Among these platforms, *HELIOS* was able to maintain safely the altitude of 21 km for 6 months.

HAPS in Europe

In Europe, the European Space Agency (ESA) and the European Commission (EC) have been involved in HAPS research activities for a long time. The former, with HALE and STRATOS, was the first institution in Europe to promoted research on HAPS [16–20]. The latter investigated the possibility of creating networks based on stratospheric platforms. CAPANINA [21] and HeliNet [22] were the two main projects supported by the EC.

The HALE and STRATOS activity

HALE was a project addressed to the feasibility study of aerostatic platforms. The idea was to use HAPS as an alternative solution or in synergy with satellites and terrestrial networks. The airship (see Fig. 2.7) was studied to keep a stationary position in the *stratosphere* by using turbines to move into the wind. With 600 kg of payload, the HALE station was supposed to provide broadband communication services, meteo forecast and surveillance services.
 In 2005, together with STRATOS, ESA investigated the performances of a hypothetic HAPS
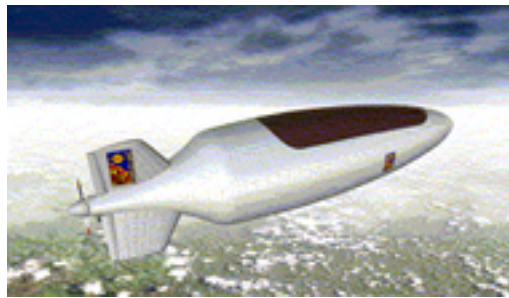
Courtesy of ESA

Figure 2.7.: Aerostatic platform of the HALE project.

for the best suited stratospheric station concept answering the needs of future telecommunications markets. These platforms were considered essential elements to boost the existing satellite-terrestrial infrastructure, for many services. From the point of view of the design, two configurations were considered. The first solution was based on static platform (baloon) whereas the second was based on an aerodynamic light airplane. Both solutions would be solar powered and unmanned.

The HELINET project

HeliNet (Network of Stratospheric Platform for Traffic Monitoring, Environmental Surveillance and Broadband Services) was a research project in which Switzerland was also involved [23]. It lasted four years starting from 1999. The aim of HeliNet was to prototype an unmanned stratospheric platform (see a model in Fig. 2.8) to fly above Europe, while providing different services [2, 24, 25]. In this project, a telecommunication network protocol was also standardized for different configuration of HAPS elements flying above a certain area.
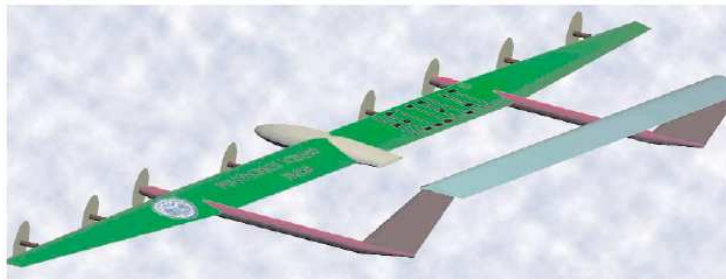
www.helinet.polito.it

Figure 2.8.: HeliNet airplane.

The CAPANINA project [21]

The CAPANINA (Communications from Aerial Platform Networks delivering broadband Communications for All) objective was to investigate a system and a network (see examples in Fig. 2.9) capable of delivering wireless communications by using HAPS to all, meaning developed and undeveloped countries, to areas momentarily involved in natural calamities, to users geographically marginalized and moving vehicles. One of the goals of CAPANINA was to deliver high data rate (up to 120 MB/s) anywhere within an area of 60 km of radius from a stratospheric platform. Ka-band was the selected frequency band for the RF up-down links [6, 26]. CAPANINA was performed by an international partnership involving companies, research institutes and universities of Switzerland, Spain, Italy, Germany, Japan, UK, Hungary and Slovenia. With intensive test campaigns, among which we highlight the successful HAPS missions in the UK (2004), Sweden (2005) and the USA (2007), the HAPS concept was asserted as a valid solution to deliver multiple communication services.
CAPANINA proved credibility in the use of HAPS to deliver broadband services. For this, three launches were completed successfully. The first launch was conducted in the UK in 2004 using a tethered airship platform (balloon) at 300 m altitude. The second launch was conducted and completed in Sweden in 2005 using a free-floating stratospheric balloon that was capable of reaching 25 km altitude. The last CAPANINA launch was conducted in the USA in 2007. For this test, a free-flight stratospheric balloon delivered broadband services such as web services, video download, and back haul communications with both a 1.25 Gb/s free-space optical link and a RF link at 11Mb/s. The project also aimed to develop a business model both for the station and for the network architecture and a radio regulatory strategy to allocate the spectral resources for this HAPS communications.

The same partners of the Helinet and CAPANINA projects promoted the European COST Action HAPCOS (High Altitude Platforms for Communications and Other Services [27]) in 2005 to continue the HAPS research activity initiated with former programs.

Although research and development in HAPS have been performed for many years, only recently technologies and materials reached a stage that allows sustainable commercial operations. At the same time, the technological development of payload equipment has reached a level of performance and precision that makes the use of HAPS more efficient [28–32]. In particular, the first phase of the Swiss project FEASANT (FEASANT, CTI 9301.1, 2008-2010) mentioned in Chapter 1 clearly demonstrated the feasibility and potential advantages of a communication system for HAPS based on high frequency (Ka-band) antennas.

(a)
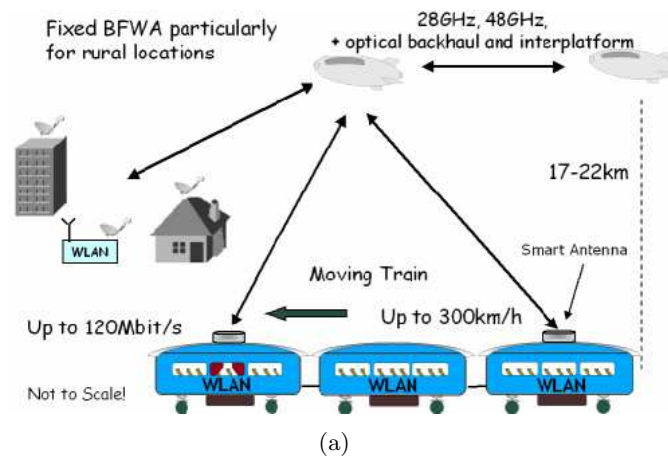
Courtesy of CAPANINA

(b)

Figure 2.9.: Scenarios of a possible HAPS network.

2.5. Overview of communication systems based on HAPS. Applications and services

Fig. 2.9 depicts the CAPANINA-inspired HAPS communications scenario that has been selected in this thesis. Services can be provided from a single HAPS with up- and down-links to the user terminals, together with backhaul links as required into the fiber backbone. Links between stations may serve to connect a network of HAPS, while links may also be established via satellite directly from the HAPS [4, 22]. The coverage region served by a HAPS is essentially determined by the line-of-sight propagation (at least at the higher frequency bands) and by the minimum zenith angle at the ground terminal. There is then the opportunity to subdivide this area into a large number of smaller coverage zones, or cells, to provide large overall capacity optimized through frequency reuse plans [33, 34]. The size, the number and the shape of these cells determine the design of the on-board antenna. Such HAPS architectures allow for adaptive resource allocation techniques, which can provide efficient usage of bandwidth and maximize capacity [8, 35, 36].

HAPS, specially if arranged in networks, can offer applications to facilitate services such as:

- navigation and positioning;
- traffic monitoring;
- security & surveillance;
- telecommunications services.

All communication services delivered from HAPS can be classified as:

- individual services (voice, file transfert, etc.);
- symmetrical and asymmetrical (up-link/down-link data transfert and broadcasting);
- real-time and non real-time services;
- distribution services (radio, TV, etc.);
- narrow-band and broadband.

According to the standard recommendation for HAPS (ITU-R), a communication is defined broadband when there is enough bandwidth to allow simultaneous transmission of voice and video and when the bit-rate is higher than 2.0 Mb/s. Therefore, narrowband transmissions are limited to 2.0 Mb/s. Examples of broadband services are voice and video telephony, TV-broadcasting and Web. Examples of narrowband services are voice, medical telemetry, navigation and positioning, traffic monitoring and surveillance [10, 37–41].

2.6. A comparison of terrestrial, satellite and stratospheric communication systems

There are three telecommunication infrastructures which can provide both narrowband and broadband services to users: satellites (geo-stationary or not), terrestrial repeaters and HAPS. HAPS are considered hybrid intermediate infrastructures, having similarities to both satellites and terrestrial base stations for communications. For instance, in terms of power constraints and network architecture, HAPS have similarities to satellites. On the other hand, many HAPS protocols are inspired by typical wireless ground communication systems on Earth. Both at atmospheric and stratospheric level, HAPS can offer new and competitive services, where they can either replace or complement satellites, aircraft and terrestrial systems [2, 42, 43].

There are several important differences between satellite communication and terrestrial communication. Furthermore, the concept of delivering communication services via HAPS has many of the advantages of both terrestrial and satellite systems, while at the same time avoiding many of their drawbacks. This solution also brings advantages of its own, not available in current satellite and terrestrial systems as shown here below [44–46]:

Performances

Space architectures perform very well in providing enough bandwidth whenever required, but they cannot provide the same capacity as terrestrial networks. Satellites are unmatched for broadcast applications like television. Terrestrial networks are superior for mobile communications in very populated areas. Holding power, bandwidth and other link parameters, the capacity of a telecommunication system directly depends on the number of spot beams that the antenna can generate in a certain area. The number of spot beams in urban areas depends directly on the distance of the repeaters and the coverage area of each repeater. Terrestrial systems generate thousands of spot beams in a certain area (i.e city of 50 km diameter), a HAPS can generate around one-hundred beams in the same zone whereas a non-geostationary satellite operating at an altitude of 500 km can generate only five or six.

A communication system based on HAPS will offer an excellent signal quality to the receiver, since the communication is most of the time in line of sight. HAPS based systems suffer less from multipath and shadowing effects with respect to ground communication systems because, as with satellites, the HAPS zenith angle is higher than for traditional ground base stations. HAPS can operate as unique infrastructure or as complementary infrastructure for an existing communication system. In both cases, HAPS can deliver high capacity similar to that available from terrestrial systems and wide coverage similar to that available from satellites.

Availability of services

Communication satellites cover all Earth land masses and there is growing capacity to serve maritime and even aeronautical markets. The satellite infrastructure is very helpful for people in rural and remote areas. Satellite can operate independently from terrestrial network. The satellite communication services are very helpful when terrestrial outages occur from natural events, since satellite links remain operational. The propagation of the signal can be an issue in satellite communications since the satellite link is extremely sensitive to atmospheric conditions.
Depending on the energy available on board, HAPS missions can last days, weeks or months. Availability of HAPS services mainly depends on the duration of the mission and on the strategy adopted to turn-over the platforms. One HAPS station can cover hundreds of km^2 during its operations, including both rural areas and densely populated cities.

Versatility and system upgrading

Satellite solutions are highly flexible and can operate independently or as part of a larger network. On the other hand, the cell cluster of a terrestrial network can be sub-divided in order to enhance the communication resources. In both cases, to increase the capacity or the coverage, a new station must be installed.
HAPS can be brought down relatively readily for maintenance or upgrading of the payload. Moreover, the failure of a component is less critical in HAPS systems, for the same reason.

Deployment

Satellites take several years from initial requirements until the launch, with the payload often obsolete by the time it is launched. Similarly, the deployment of terrestrial networks may involve time-consuming planning procedures and civil works.
It is possible to install and deploy a new HAPS-based service relatively quickly. HAPS-ground link composed of only one platform and one terrestrial base station, can be deployed much faster than a terrestrial network, and much quicker than a satellite system. This facilitates their use in emergency scenarios (e.g. natural disasters, restoration where a terrestrial network experiences failure, overload due to a large concentration of users, etc.).

Security

The satellite communication services are very helpful for the defense department, where people involved in operations cannot always use wired services every time. Also, for such people, it is very important to keep their missions and secrets undisclosed due to national security reasons. Satellite communication services fulfill this purpose since none of the calls or any other communication made through the satellite communication can be tracked by the common services. Hence, the satellite communication is a must for the defense and for the security

of the nation. The security in terrestrial network reaches an excellent level although the communications are traceable by national authorities.

HAPS and constellations of HAPS can operate independently or used to extend the existing ground network. In both cases, the use of communication protocols as for terrestrial networks ensures an excellent level of security.

Cost

The cost of satellite capacity does not depend on the number of ground users, nor on the distance between communication points. Whether crossing continents or staying local, the satellite connection cost is distance insensitive. However, the initial costs of a satellite mission (space segment and launch) are higher than the ground station installation.

Regarding costs, HAPS occupies an intermediate position between satellites and terrestrial systems. Indeed, the infrastructure itself includes the telecommunication payload and a relative simple platform to reach and keep a stationary position in the *stratosphere*. This infrastructure is indeed slightly more complex than ground base stations and much simpler than satellites.

Resources

The frequencies and orbits available for satellite communications are congested. The location selected to install a ground base station constitutes a minor issue.

The choice of frequency band at which HAPS can operate is determined by two technical factors. First, some frequencies are strongly affected by atmospheric losses in the *stratosphere*. Indeed, the choice of the frequency of communication should minimize the cost of transmission and maximize the information carrying rate. The second factor is the congestion of the spectrum allocation which forces the use of determined frequency bands, not to interfere with existing systems.

Environment aspects

A satellite mission (including launch and satellite recovery) is surely more pollutant than a base station installation, maintenance and disposal.

HAPS represent environmentally friendly reusable crafts, especially when they rely upon sunlight for their power and do not require launch vehicles with their associated fuel implications.

2.6.1. HAPS issues

Currently, the most critical issues are related to the platform itself and to the offered services. From the point of view of the platform, its stability and its positioning still have to be improved enhancing aspects as cost efficiency and flight security. From the point of view of the services, the availability of RF power on-board probably constitutes the most critical issue since this directly affects the quality of the communication link.

There are also some communications issues that will need to be addressed, such as the design and implementation of the required multibeam on-board antenna and the propagation characterization of the HAPS-ground channel.

Platform station-keeping

The ability of HAPS to maintain the position independently from the atmospheric conditions is a major challenge and will critically affect the viability of communication services. HAPS positioning is determined as a certain statistical probability of remaining within a particular volume, e.g. a location cylinder. Stratospheric flights have recently been performed with 99% and 99.9% platform availability within specified location limits, and despite this really large availability such parameters are still a long way from providing communication services having traditional 'four nines' availability, 99.99%.

Stability

Inevitably turbulence in the *stratosphere* produces roll, pitch and yaw on the platform (see their intuitive explanation in Fig. 2.10). The antenna pointing must be maintained either through the use of a mechanically stabilized sub-system, or through the use of electronically steered array antenna. This latter technique offers considerable potential, but is also technologically demanding, especially at the mm-wave bands, where the steering network losses are quite sizable.
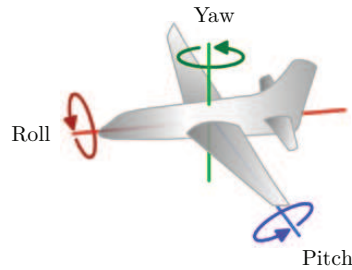
Figure 2.10.: The three possible rotations of a veichle.

Antennas

Antenna technology will be critical for broadband communication from HAPS. A large number of spot beams will be required. Section 2.7 details all the antenna aspects for HAPS applications.

Propagation and diversity

The International Communication Union (ITU) has allocated services from HAPS in the mm-wave bands, at Ka-band. Propagation from HAPS is not fully characterized at these higher frequencies. There is a need to develop rainfall attenuation and scattering statistics. This will allow appropriate margins to be included in the link budget and highlights any problems with frequency reuse plans developed at the system level. An important objective is to determine the most appropriate diversity techniques (e.g. space, time or frequency) for each traffic type.

Payload power

Available power at 20 km altitude might be a limitation. Thus the achievable downlink RF power has to be constrained and used efficiently. Compared with a satellite, HAPS require a higher proportion of power to charge the batteries (fuel cells) and not to stop working during long periods of darkness each night.

An important distinction between the different types of HAPS is the power available to the payload. Typically an airship may have 20 kW available for the payload, due to the large surface area on which to deploy solar cells. On the other hand, solar powered planes (e.g. HeliPlat) may have significantly less available payload power.

Table 2.1 summarizes a comparison of satellite, HAPS and terrestrial systems [9].

Conclusion

Providing a wider coverage than traditional terrestrial networks and higher capacity than satellite systems, HAPS can integrate the service provided by both satellite systems and terrestrial networks, in areas where the communication infrastructure is already developed. On the other hand, in areas where the telecommunication architecture is poor, HAPS can be quickly deployed and provide a valid communication infrastructure. Last but not least, HAPS represent the most efficient solution in case of emergency scenarios.

Table 2.1.: *Comparison of satellite, HAPS and terrestrial systems.*

Issue	Satellite	HAPS	Terrestrial
RF channel quality	Distance limits the spectrum efficiency. Ricean fading	Distance similar to terrestrial. Line of sight propagation in Ka-band	Good signal quality. Rayleigh fading
Cell diameter	500 km for GEO, 100 km for LEO	$\leq$ 10km	1 km
Propagation delay	Large delay	Low delay	Low delay
Complexity	Moving LEO satellites is complicated	The platform needs to be re-fueled	Operating in rural area is more complicated than for HAPS
Technology risk	Fairly new technology for LEO satellites. Technologies for GEO are mature	Some innovations are expected in antennas, and energy supply systems for the stations	Mature technology
Deployment timing	The entire system (many times the entire satellite constellation) needs to be built to operate	HAPS based systems needs just one platform to initiate operations	Initial build-out is needed to provide coverage
System growth	Capacity is increased by adding satellites. Hardware upgrading is an issue	Capacity is increased by adding platforms. Hardware upgrading is easy	It is relatively easy to increase the number of base stations in terrestrial systems

2.6.2. Frequency allocation for HAPS services: why Ka-band

The Ka band is a part of the K band of the electromagnetic spectrum. The Ka symbol refers to "Kurtz-abov" and indicates the band directly above the Kurtz (K)-band. The formal spectrum allocation for Ka-band is from 26.5 to 40GHz.

The interest behind the rapid adoption of Ka-band is mainly due to the growing demand for broadband which is quickly exhausting the available capacity of existing L-band (1.4-1.6 GHz), C-band (4-8 GHz), X-band (8-12 GHz) and Ku-band (10.75-14.5 GHz) satellites. Furthermore, C-band spectrum is highly attractive to terrestrial fixed wireless systems due to the superior building penetration that this frequency band offers, and satellite applications at X-band are also suffering from encroachment of terrestrial wireless systems.

The main obstacle to a deep market penetration of these systems is the high cost of the aerial station capacity due to the limited bandwidth available from L-Band to Ku-Band. In particular, L-Band systems can offer only few MHz of frequency band resulting in an extremely high cost of the capacity, which restricts the usage of such systems only to professional airborne or shipborne users.

The next logical band to develop for satellite and aerial platform services is Ka-band, and there is now an increasing number of dedicated Ka-band systems in the planning stages.

Ka-band offers huge potential in a range of market segments, including retail, hospital, and government initiatives such as emergency communications, rural broadband, telemedicine, and distance education. In addition, capabilities such as bandwidth-on-demand, constant bit services, and dish-to-dish networking enable more advanced applications. The technology also holds considerable promises for airline, railroad, military, and other mobile applications [4].

The possibility to perform mobile broadband in Ka-band would allow drastically reduction in the exploitation costs, thus permitting a deeper penetration in the different markets of satellite communications. In particular, for airborne traffic monitoring, Ka-band would support the large amount of data that would be generated by daily flights at a fraction of the cost of the actual Ku-Band services. Nowadays, no antenna solutions are available for mobile broadband at Ka-band and the available solutions only operate in Ku-Band [37–39, 41].

Ka-band systems offer up to 100 times more capacity than the presently available ones at lower frequencies. Such a large capacity of a single broadcaster results in an extremely low price per Megabit, enabling a new set of applications which has not been possible up to now. The high bandwidth available in the Ka spectrum and frequency re-use capabilities across multiple beams enable the delivery of more capacity at higher speeds to several users, opening the door to upgraded services at lower costs.

The reason why Ka-band was not commercially viable up to now was that the technology was not mature enough. Ka-band, which operates at the 25.5-40 GHz range, is susceptible to weather interference, but now techniques exist to counter this drawback, hence greatly improving the reliability.

Propagation aspects at Ka-band

The troposphere is composed of particles (essentially, raindrops and gas molecules), which have a wide range of sizes and characteristics. The total loss resulting from an electromagnetic wave passing through such a medium is composed of two additive contributions: absorption and scattering [47].

Absorption results from the conversion of RF energy into thermal energy within molecules of gas or raindrops. In normal atmospheric conditions, only water and oxygen molecules contribute significantly to absorption. On one hand, an electric field applied to water molecules produces alignments of their oppositely charged ends. Since the electric field in the wave changes in direction twice per period, realignment of such molecules occurs continuously, so a significant loss may result. At higher frequencies this realignment happens faster, so the absorption loss has an overall tendency to increase with frequency. On the other hand, non-polar molecules, such as oxygen, may also absorb electromagnetic energy due to the existence of magnetic moments. The main resonance peaks of oxygen molecules are at 60 and 118 GHz, whereas those of water molecules are at 22, 183 and 323 GHz (see Figs. 2.11 and 2.12), preventing the use of such frequencies for satellite and HAPS communications. Ka-band constitutes a window in the frequency spectrum where the atmospheric absorption phenomena allow long communication links between aerial platforms and ground stations.
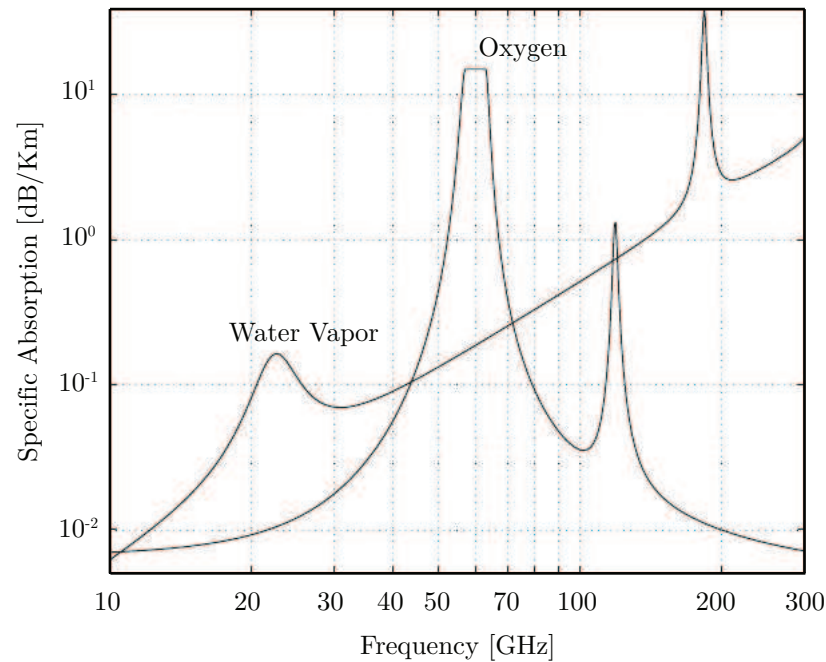
Figure 2.11.: Specific attenuation for water vapour and oxygen (pressure = 1013 mb, temperature = 14°C, water vapour content = 7.5 g/m^3) calculated using equations from [48].

One of the most attractive features of a HAPS based wireless system is its very favorable
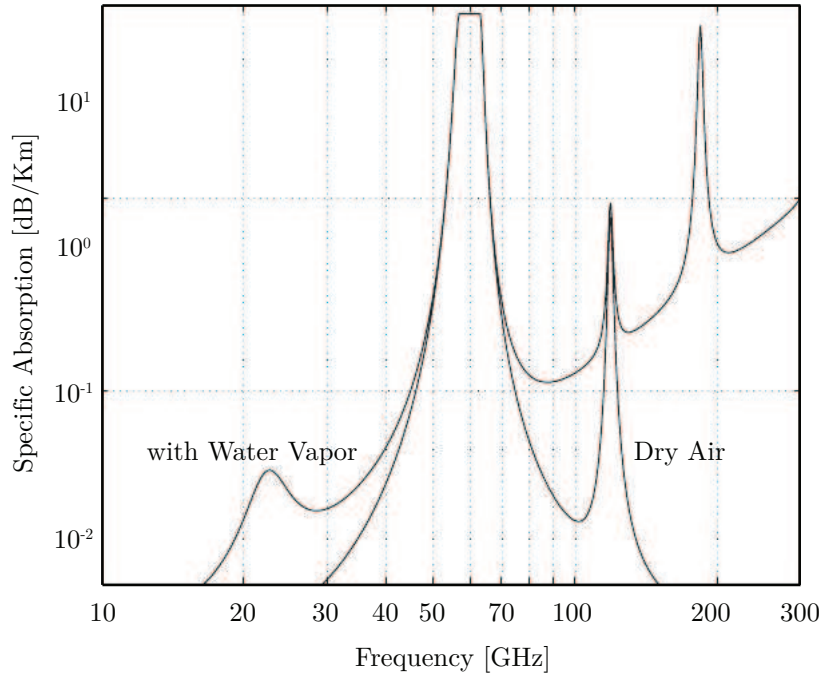
Figure 2.12.: Total attenuation in dry air including water vapour calculated using equations from [48].

path-loss characteristic relative to either terrestrial or satellite systems. For satellite systems, the path loss is inversely proportional to the square of the distance, $1/r^2$, whereas in terrestrial systems it is most commonly assumed as $1/r^4$ [49]. The HAPS-to-Earth channel type at mm-waves can be assumed as the satellites (line-of-sight propagation and with $1/r^2$ path-loss type). Indeed, at the ground level, the propagation of Ka-band microwave signals is strictly line-of-sight since trees, as well as buildings, vehicles and terrain, normally cause non-acceptable path loss at these frequencies. With this kind of propagation characteristics, HAPS distances cause path losses comparable to those, in a relatively small terrestrial system cell with approximately 2 km radius. As a result, the system can operate with conventional cellular handsets technology (adequately adapted to the new mm-wave band) and relatively simple on-board equipment.

2.7. Antenna requirements for HAPS

In general, antennas are designed to couple the electromagnetic energy transported by a transmission-line into free space. HAPS are supposed to provide a variety of communication services for different kinds of users and special antenna requirements need to be addressed, depending on the application targeted for the system. Indeed, the antenna characteristics have to match different, and often opposite, properties/requirements of the applications. For instance, on-board operating radars require narrow-beams and broadband antennas, whereas broadcasting payloads need relatively wide beams and narrowband antennas. Last but not least, the HAPS payload needs to reconfigure the antenna radiated power to respond both to changing of channel requirements (rain, need for capacity increasing,...) and to undesired movement of the station (roll, pitch, yaw,...). Thus the on-board antenna is considered a key element of the HAPS system.

A typical on-board antenna design would seek low power consumption, high reliability, and minimum weight and size. This would lead to an architecture which places most of the communication sub-system on the ground in order to limit the station components only to a multichannel transponder, associated antenna and interfaces.

For communications delivered from HAPS, a consistent number of spot beams will be required, and these may be produced either by an ensemble of horn antennas or some form of phased arrays. Sidelobe performance is an important issue, which will affect inter-cell interference and system capacity. At Ka-band, this is a demanding challenge both for the HAPS antenna and also for ground terminals.

Different types of antennas can be used in Ka-Band mobile user terminals, from fully active phased arrays (see Fig. 2.19) to gimbaled dish reflectors (see Fig. 2.15). Each of them has a different level of development complexity and market potential. A particular category of antennas that appears to be especially interesting for Ka-Band user terminals is the medium profile mechanical antenna as illustrated in Fig. 2.14 [50–52]. Such antenna solutions are constituted by a low profile aperture (typically 20 cm of height by 60 cm of width). The aperture is mounted on a mechanical positioner that rotates the antenna in azimuth and sets the aperture in elevation in order to track the HAPS aircraft while the vehicle is moving.

In this section we review the most typical antenna parameters used in HAPS-based systems and we show the requirements needed for each of them.

2.7.1. Physical requirements

One of the challenging tasks for an antenna designer is to find the best trade-off between performances, physical dimensions and cost of the antenna. In many ground applications, antennas are designed to minimize visual impact on users (e.g. antenna for mobile phones, wearable antennas, etc.). Much effort has been made over the last few years to minimize size and weight for these antennas. For aerial platforms, the constraints on physical dimensions are even more demanding. Heavy and bulky antennas become a prohibitive solution on board, since this represents an issue for the platform stabilization and imposes severe limitations on the platform design. The two antenna systems shown in Fig. 2.13 have to be mounted on unmanned aerial platform underneath the wing. The antenna space and the shape of the radome was quite constrained. A steerable antenna system based on a parabolic reflector [50, 52, 53] is shown in Fig. 2.14. The maintenance of this kind of antenna is an issue, since the steering mechanism often needs to be re-visioned.
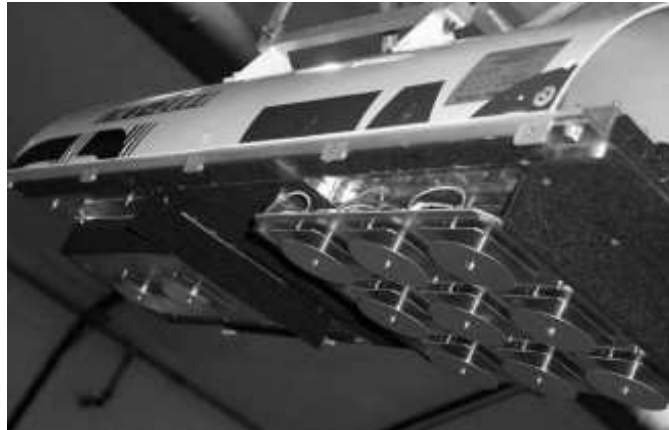
(a)

(b)

Figure 2.13.: HAPS antenna system mounted underneath the wing, with the antenna plane parallel to the ground. Figures taken from [30].

Figure 2.14.: Paraboloidal reflector for HAPS telecommunication systems.

2.7.2. Frequency band of operation

An antenna is usually designed to work at a specific frequency, denoted as **central frequency** or, more generally, in a frequency range constituting its operational **bandwidth**. The bandwidth of an antenna determines the frequency spectrum where the antenna is matched and the maximum accepted radiated power of the antenna. In this bandwidth, the main radiative characteristics of the antenna are supposed to satisfy specified criteria (usually in terms of reflection coefficient, polarization and pattern). The bandwidth is usually identified by the reflection coefficient $|S_{11}(f)|$. For electrically small antennas the bandwidth is defined as to the frequency range of the spectrum in which this reflection coefficient is lower than -6 dB. For Space and Near-Space applications this level is more constrained and the bandwidth is taken at -10 dB of the reflection coefficient.

The antenna frequency of operation is strictly linked with the antenna dimensions and, theoretically, any antenna design can be adequately rescaled to be matched in different bandwidths. In practical antenna designs, the operating frequency band delimits the antenna technologies which can be used. Indeed, an antenna design performing well in a certain frequency band can not be often rescaled adequately and provide the same good performances at other frequencies. At mm-wave frequencies, due to high losses in dielectric substrates, printed arrays become less efficient and classical radiation pattern synthesis techniques can hardly be implemented. Also directivity requirements, sidelobes and losses reduction represent challenge tasks to be overcome by the designer at these frequency bands. On the other hand at low frequency, aperture antenna designs (i.e. based on reflectors, lenses, horns)

are extremely bulky and heavy and printed technology is the best choice.

Antennas are frequently classified according to their bandwidth into narrowband, broadband and frequency-independent antennas. The former are used when the requirements ask for a stable long range communication, (e.g. in satellite communications). The second are used when it is important to transmit information over a large bandwidth and to allow high values of range resolution (e.g. for medium and short range wireless communication [54] and high resolution and radars [55]). The last category of antennas is mainly used as feeds for reflectors for surveillance of the frequency spectrum. Typically, both narrow and broadband antennas are present on HAPS based communication stations.

2.7.3. Antenna radiation pattern

The following specific definitions, taken from standard antenna theory [56] are particularly relevant for the HAPS scenario discussed in this thesis.

In a given direction (θ, ϕ), the **radiation intensity** $U(\theta, \phi)$ is the power radiated from an antenna per unit solid angle and it is related to the far field intensity of the antenna $\mathbf{E}(r, \theta, \phi)$ by [56]:

$$U(\theta, \phi) = \frac{r^2}{2Z_C} \left| \mathbf{E}(r, \theta, \phi) \right|^2 \tag{2.1}$$

where $\mathbf{E}(r, \theta, \phi)$ is the peak complex value of the field and Z_C is the intrinsic or characteristic impedance of the medium. The total radiated power is obtained by integrating the radiation intensity over the entire solid angle 4π:

$$P_{rad} = \oiint_\Omega U \, d\Omega = \int_0^{2\pi} \int_0^{\pi} U \sin\theta \, d\theta \, d\phi \tag{2.2}$$

The **directivity** D of an antenna is defined as the ratio of the radiation intensity of the antenna in a given direction over that of an isotropic source:

$$D(\theta, \phi) = \frac{4\pi U(\theta, \phi)}{P_{rad}} \tag{2.3}$$

The directivity is used to compare the radiation intensity in a given direction to the average radiation intensity and this does not include the power losses in the antenna materials [57–59]. Gain includes these losses, and it is defined in a similar manner to the directivity, except that the total input accepted power (P_{acc}) to the antenna (rather than the total radiated power) is used as the reference:

$$G(\theta, \phi) = 4\pi \frac{U(\theta, \phi)}{P_{acc}} \tag{2.4}$$

The total radiated power is related to the total input accepted power by:

$$P_{rad} = \eta \, P_{acc} \Rightarrow G = \eta D \tag{2.5}$$

where η is the antenna radiation **efficiency** and it takes into account the losses in the antenna material.

The gain of an antenna is often used to compute the **effective isotropic radiated power** (EIRP), which is the product of the input power and the maxim gain. It is also defined as as the amount of power that a theoretical isotropic antenna would emit to produce the peak power density observed in the direction of maximum antenna radiation.

The **half-power beamwidth** HPBW is defined in a plane containing the direction of the maximum of the beam and it is the angle between the two directions in which the radiation intensity is one-half the maximum value of the beam. For many practical antennas the maximum gain is related to the beam solid angle Ω_A an thus to the HPBW by [56]:

$$G_0 \simeq \frac{30\,000}{\Omega_A \mid_{(degrees)}} = \frac{30\,000}{\Theta_{1d}\,\Theta_{2d}} \tag{2.6}$$

where Θ_{1d} and Θ_{2d} are the half-power beam angles in two orthogonal planes in degrees.

The **effective aperture area** A_e of an antenna describes the power capturing characteristics of the antenna when a wave impinges on it. This parameter is related to the maximum directivity D_0 of the antenna by:

$$A_e = \frac{\lambda^2}{4\pi} D_0 \tag{2.7}$$

In general, A_e is not related at all to the physical area $A_A P$ of the antenna. But for aperture-based antennas, the upper bound of A_e is usually given by the physical area $A_A P$ and the aperture efficency ε_{AP} is defined as:

$$\varepsilon_{AP} = \frac{A_e}{A_A P} \tag{2.8}$$

The antenna patterns have to be differentiated depending on the applications. In HAPS based communications, the patterns of on-board and ground terminal antennas are quite different. On one hand, the on-board antenna pattern must be either directive or moderatively directive depending on the purpose. Indeed, in point to point communications (i.e. links between flying stations, between HAPS and ground repeaters or between HAPS and satellites), the gain is a parameter that needs to be maximized, especially in Ka-band applications, where the free-space path-loss has a severe impact on the power link budget. An example of high directive antenna for HAPS is given in Fig. 2.15. On the contrary, for cellular coverage, the on-board antenna beams should illuminate a very specific area in the

region of interest delimiting in such a way the cell boundaries. It is evident in this case that the beam aperture drives the radiating element design and the absolute gain does not represent a constraint. An example of antenna for cellular coverage is given in Fig. 2.16. On the other hand, ground terminal antennas must be either moderately directive or omni-directional [60–62]. Indeed, for high-speed mobile users, steerable medium gain antennas can be used to allow dynamic allocation of large capacity and tracking capability. Medium-gain antenna beams are also used to provide bi-directional broadband wireless communications for quasi-static ground users. In order to receive mobile services delivered from stratospheric platforms, low-gain, low-directivity antenna patterns are definitely good candidates.

One final word must be mentioned about the efficiency of the antenna, since very high gain antennas become useless if a low efficiency is achieved. The efficiency, indeed, represents an additional parameter in the power link budget that might be determinant.

Courtesy of ERA Ltd.

Figure 2.15.: Plastic dual-reflector antenna for HAPS.

(a)   (b)

Figure 2.16.: Lens-corrected horn antennas for HAPS. Each horn radiates one beam in Ka-band. The beam aperture at -3dB is around 5°. Figures taken from [63]

2.7.4. Area covered by the antenna radiation

For cellular systems served by HAPS, the on-board antenna needs to illuminate a specific coverage area to satisfy the system requirements. Typically, the on-board antenna is fixed for these applications. From basic theory of cellular communication systems [49], the ground area covered by the on-board antenna radiation determines the capacity of the communication system. For a given density of population, the wider this areas is, the higher the capacity. At mm-wave frequencies, the ground coverage is highly determined by the HAPS antenna characteristics, since the terrain multipath is negligible. The dimension of such area is the parameter that most impacts on the on-board antenna design [64–70]. Controlling the beam patterns of a multi-beam antenna system is often a key issue of the design since the link budget and the geographic coverage are strongly influenced by the gain, the aperture, and the shape of the beams [49]. The previous paragraph (eqns. 2.6 and 2.7) shows the relation between antenna dimensions, directivity and the aperture of the beam that illuminates the ground area under the HAPS has been given.

On the other hand, for ground terminal antennas where the communication between high-speed ground vehicles and HAPS needs to be established, steerable beams are used to maintain a line-of-sight communication between transmitter and receiver. In such cases, the antenna points the sky and the scan angle range defines the portion of the sky traceable by the beam. The scan angle range is defined as the maximum sweep angle which is intended to be covered by the steerable beam antenna to follow the target. For HAPS communication systems requiring steerable beams, this angle is estimated to be 150°.

2.7.5. Shape of the ground footprint

In HAPS communications based on cellular systems the boundary of each cell and its shape are determined by the beam pattern. Circular footprints in such systems present many advantages [71]: geographic coverage is better and the link budget across the coverage area is more uniform. If used on an aerial station, circular and symmetric multi-beams produce a circular footprint in the area just below the antenna and elliptical footprints in the remaining area (see the example in Fig. 2.17). The elongation of such footprints increases with the zenith/polar angle degrading the performance of the communication system [72, 73]. The desired footprint can be achieved by a proper design of the HAPS antenna. For equal and circular footprints served by an aerial station, asymmetric antenna spot-beams are the sole solution. This issue is fully addressed in chapter 5.

Ground Power Footprint, $10\log(P_r\,(x,y)/P_{max})$[dB]

(a)

Ground Power Footprint, $10\log(P_r\,(x,y)/P_{max})$[dB]
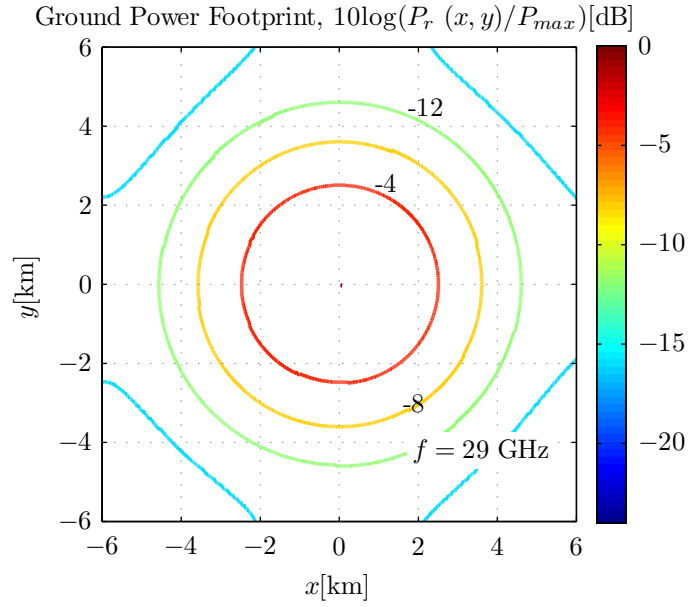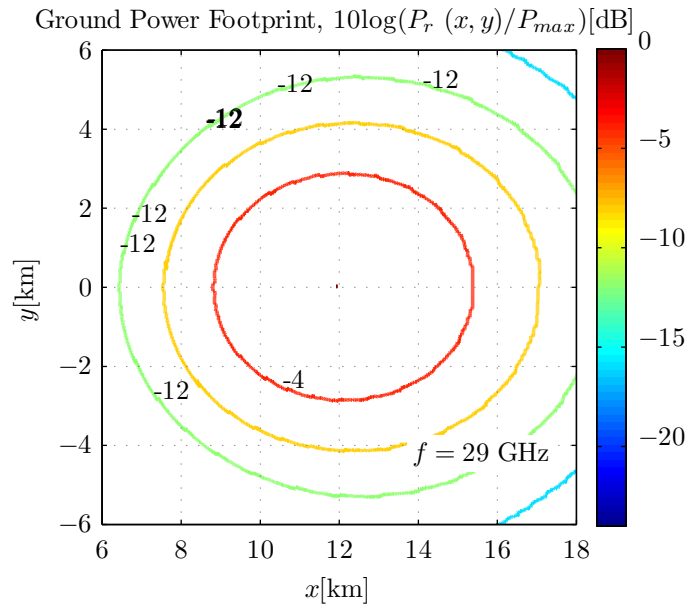
(b)

Figure 2.17.: Footprint generated by the beams shown in Fig. 2.18 from a HAPS flying at 21 km altitude. (a) Circular footprint of the cell below the station (Nadir direction). (b) The cell is center at 12 km from the center of the cluster and presents an elongated footprint.

2.7.6. Sidelobe levels

Although spectral reuse schemes are adopted to reduce the co-channel interference, in cellular system communications delivered from HAPS, a high level of sidelobes of the on-board antenna might cause two undesired effects. When spot beams are required to provide a cluster of footprints, the power of each beam has to be confined in the cell boundary. Beams with important side lobe level cause interference to neighbor cells. At each point of the ground, the effect of the interferences can be evaluated by computing the signal-to-noise ratio (SNR) between the power of the desired signal ($P_{r,1}$) and the noise power (P_N). Noise power here includes interference phenomena and is the sum of the thermal noise (P_T) and the power ($P_{r,i}$) of all the neighbor beams i that are using the same frequency of the desired signal. Thus,

$$SNR = \frac{P_{r,1}}{P_N} = \frac{P_{r,1}}{P_T + \sum_i^{N_f} P_{r,i}} \tag{2.9}$$

where N_f is the number of neighbors that share the same frequency with the desired signal. Cellular systems are limited by the interference of neighbors and the thermal noise can often be neglected in Eqn. 2.9. Furthermore, the frequency scheme usually prevents the reuse of the same frequency for neighbor cells, and the cells using the same frequency are far enough to consider the power of an interfering signal as

$$P_{r,i} = P_{r,1} \times SLL \tag{2.10}$$

yielding

$$SNR = \frac{P_{r,1}}{P_N} \simeq \frac{P_{r,1}}{N_f \times P_{r,i}} \simeq \frac{1}{N_f \times SLL} \tag{2.11}$$

Eqn. 2.11 demonstrates the importance of the side lobe level of the on-board antenna on the system performances.

An additional negative effect might occur in multiple HAPS constellations when the direction of the sidelobes creates interference to contiguous stations. Such a case has been fully addressed by [33], and it is not of interest in this work since only one station is considered in the scenario.
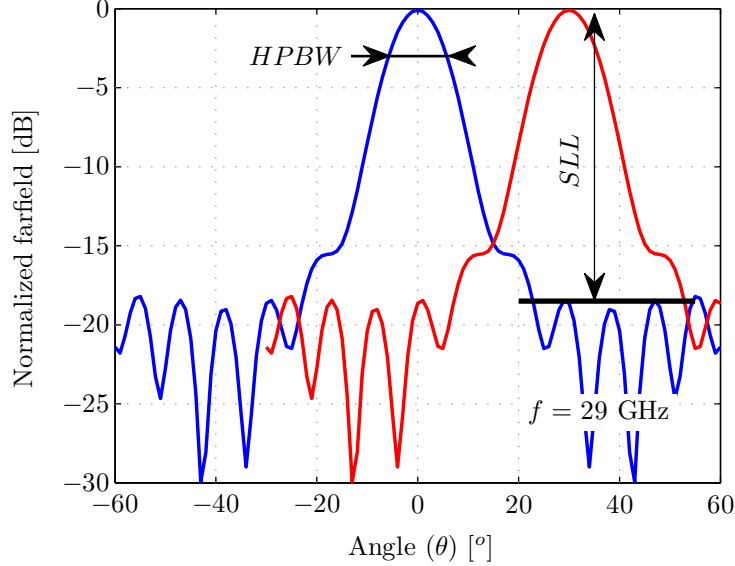
Figure 2.18.: Radiation pattern of two beams of a multi-beam antenna system for HAPS.

2.7.7. Polarization

Circularly polarized antennas where quality is traditionally measured by its axial ratio AR [56] are essential in altitude stations. Although an efficient stabilizer system is supposed to act on the HAPS antenna orientation to compensate the undesired perturbation of the optimal station position with respect to ground, a circularly polarized on-board antenna helps in reducing the effect of undesired movements of the station induced by the atmospheric conditions on the communication link. This perturbation of the station position, indeed, may lead to negative effects in the HAPS performances especially with regards to the SNR of the communication channels negatively influenced by the presence of fading in the received signal. In stratospheric communication applications, the use of circularly polarized waveforms is a smart solution to both overcome the problems of alignment between the on-board antenna and the user antenna and to mitigate the effects of undesired reflections. Furthermore, circularly polarized antennas make it possible to increase the capacity of a HAPS-link by combining adequately frequency and polarization reuse schemes in the cluster [74–76].

2.8. Antenna technologies for HAPS

This section describes the antenna technologies most suitable for HAPS communications systems. The section is not intended to be a review of antenna theory, for which the reader should refer to [56, 77, 78]; here only the the antenna aspects that constitute a challenge for HAPS systems are addressed.

2.8.1. Phased array antennas

Most antenna arrays are either linear or planar. While a linear array makes it possible to obtain a conical beam (a 2D pencil beam in a plane containing the array axis), planar arrays allow to produce a pencil beam [79, 80]. Linear arrays are suitable for HAPS antennas where an omni-directional pattern has to be synthesized in one plane. In some applications, the amplitude and phase of its elements are electronically controlled, to allow beam steering in the other plane, without involving mechanisms to move the antenna mechanically. In planar arrays, the amplitude-phase law can be adjusted in the x-y plane in order to control the sidelobes (amplitude level and direction) or to steer the beam. Antenna arrays (see Fig. 2.19) have been designed for HAPS [63].

Advantages: Phased arrays have some advantages and they are used in HAPS applications where the following features need to be addressed [81, 82]:

- electronic beam steering;

- fast scanning over wide angles;

- reduction of sidelobes in a certain angular region;

- low cost and easy manufacturability of the antenna prototypes (using printed array);

- conformal antenna layout (using printed array).

Drawbacks: However, phased arrays have some disadvantages that make this technology unsuitable for some HAPS antenna applications:

- when they are used to implement electronic beam steering, the shape of the beam degrades sensibly with increasing scan angles. The grating lobes also affect the radiation pattern, especially for high value of the scan angle. This problem could be mitigated using (if the application allows it) a combination of mechanical and electronic steerings, where one of the axis is mechanically steered, minimizing in such a way, the number of active elements (phase shifters) in the array;

- for the same beam aperture the sidelobe level is generally higher than in alternative antenna technology (reflectors or lenses based antennas);

- feeding network complexity [83–88].

Moreover, in the case of planar arrays made using printed techniques, other disadvantages have to be mentioned:

- the antenna efficiency strongly decreases at mm-wave frequency (in general above 18-20 GHz) due to the presence of losses in the dielectric substrate [55, 89–96];

- the relatively low antenna power handling becomes an issue for many applications [60, 61, 97].

(a) (b)
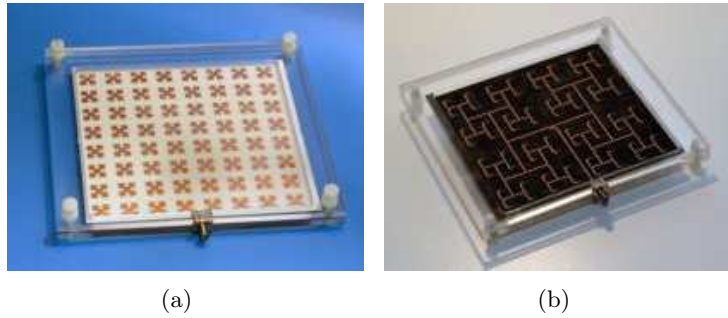
Figure 2.19.: Prototype of a 64 elements array generating a directive beam for the on-board HAPS antenna. The gain and the sidelobe level values are 30 dB and -11 dB respectively. Figures taken from [63].

2.8.2. Reflectors

Reflector antennas rely on the application of the image theory. If an electromagnetic source is placed in the focus of a perfect conducting paraboloid surface, then the combined system has the same field (on the side of the focus) as if infinite images of the source were present on the opposite side of the focus. The location of these images is such to produce a parallel beam from the reflector.

A parabolic reflector is a frequent choice for space communications, where high directivity is required. Good efficiency characterizes parabolic reflectors also at mm-wave frequency. However, a tapered illumination (achieved typically with corrugate horn feeds) is the only solution that makes it possible to keep the sidelobe level reasonably low. The radiation of the reflector might be disturbed by the presence of the primary feed and so, in many reflector antenna systems, the primary feed is off-set to avoid aperture blockage [98–100].

Advantages: For HAPS, parabolic reflectors could be advantageous because of the following properties:

- high power handling;

- high efficiency (also in Ka-band);

- design mechanically robust;

- high gain and low sidelobe level can be achieved;

- with only one aperture and several primary feeds, the design of a multi-beam antenna system is relatively compact;

Drawbacks: However, reflectors have some disadvantages for some HAPS antenna applications:

- aperture blockage is an issue for on-board multi-beam antennas;

- the design can not be easily integrated below the the station body (conformal design for aerodynamic purpose is practically unfeasible).

Nevertheless in HAPS communications, parabolic antennas provide a good solution for fixed ground terminal users.

2.8.3. Lens antennas

A microwave lens is capable of changing a spherical waves to a plane waves. A lens antenna operates on this principle. The lens antennas can be classified essentially as delay lenses and fast lenses. In the former, the electrical path is increased by the lens, whereas in the latter the electrical path is decreased by the lens. Other classifications have been addressed in literature depending on the lens shape [101–107]. Spherical dielectric lenses are used as antennas because their symmetry allows beam shaping in any direction. An effective spherical lens is the Luneberg lens (see the working principle in Fig. 2.21 (b)), in which any plane wave incident in the lens surface is directed to a point called focus. This is achieved by smoothly changing the dielectric permittivity of the lens as function of the radius. Different Luneberg lenses are possible where different laws of permittivity variation are used; for example, the focal surface may be made inside or outside the lens. Spherical lenses are very interesting for HAPS communications, since this geometry allows multi-beams capabilities by placing several feeds around the lens surface.

While parabolic reflectors use the laws of reflection to produce a collimate beam, lenses are based on the EM refraction laws to straighten the waveforms. Although the nature of the radiator is different (material and shape) these two types of antennas share many similar aspects when they are used for HAPS communications.

Advantages: For HAPS, lens antennas could be advantageous because of the following properties [108]:

- high power handling if proper feeds (i.e. waveguides, horns) are used;

- high efficiency (also in Ka-band);

- design mechanically robust;

- high gain and low sidelobe level can be achieved;

- with only one aperture and several primary feeds, the design of a multi-beam antenna system is relatively compact;

- aperture blockage is not an issue since the beams are shaped on the opposite side of the lens with respect to the feeds;

- by using multi-layered lenses, the antenna volume, the feed arrangement and the radiation performances are controllable.

Drawbacks: However, lens antennas have some disadvantages for some HAPS antenna applications:

- The weight and the volume of the lens constitute a problem for low frequency applications.

(a)   (b)
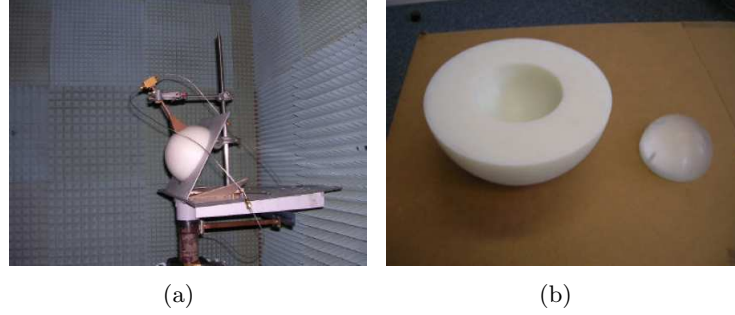
Figure 2.20.: 2.1 GHz prototype of hemispherical dielectric lens for HAPS. (a) homogeneous lens with one feed and (b) 2 layers-lens. Figures taken from [63].

Aberrations - With the notation shown in Fig. 2.22 and with the focus on the lens surface, aberrations (phase error) are found by computing the differences between the electrical path length l_D and $l_B + l_C$:

$$\Delta = l_D \cdot \sqrt{\varepsilon_r} - (l_B \cdot \sqrt{\varepsilon_r} + l_C) \tag{2.12}$$

The aberration is a phenomenon which is sufficiently small to be be negligible for all practical applications. Fig. 2.21 (a) depicts an homogeneous lens and shows how rays are directed to the focus. Considering the geometry and normalizing with respect to the lens diameter D in wavelengths D/λ, we have:

$$\frac{\Delta/\lambda}{D/\lambda} = \sqrt{\varepsilon_r}\left(1 - \cos\theta\right) - \frac{1}{2}\left(1 - \cos 2\theta\right) = 2\sqrt{\varepsilon_r}\sin^2\frac{\theta}{2} - \sin^2\theta \tag{2.13}$$

and

$$\frac{l_Y}{D} = \frac{1}{2}\sin 2\theta \tag{2.14}$$

Fig. 2.23 shows the aberration of the lens aperture as function of the relative permittivity. Due to the lens geometry, only spherical aberrations are present. Eqn. 2.13 shows that this phenomenon is less important for materials characterized by a dielectric permittivity ε_r within the range [3 ÷ 4]. Typically, for practical applications that envisage low aberrations when aberration needs to be reduced, ε_r=3.5 is chosen as good compromise. If the aberration is not an issue, a lower permittivity material is chosen to avoid reflections from the lens surface.

Reflection at the surface - Depending on the lens design and material, another phenomenon named complete internal reflection may reduce the available aperture diameter of the lens, since rays emitted by the source with an angle greater than arcsin $\frac{1}{\sqrt{\varepsilon_r}}$ are not radiated by the lens. Indeed, with regards to Fig. 2.22, complete internal reflection occurs

when

$$\sin \theta \geq \frac{1}{\sqrt{\varepsilon_r}} \tag{2.15}$$

This phenomenon can be reduced by choosing a lens material with low permittivity or by surrounding the lens surface with a dielectric matching layer, to reduce the reflection coefficient at the surface.

Focal distance - If the relative permittivity of the homogeneous lens is greater than 3.5 then the focus of an incident plane wave will be inside the lens. The relative permittivity is reduced from 3.5 the focus progressively moves externally away from the surface. Ray tracing techniques and experiments have proved [109, 110] that the focal distance F of a homogeneous lens is related with its radius R by

$$F/R = \frac{1}{\sqrt{2}} \frac{\sqrt{\varepsilon_r}}{\sqrt{\varepsilon_r} - 1} \tag{2.16}$$

Eqn. 2.16 differs from the general optical equation for thick lenses,

$$F_{thick}/R = \frac{1}{2} \frac{\sqrt{\varepsilon_r}}{\sqrt{\varepsilon_r} - 1} \tag{2.17}$$

and take into account that the optimum relative permittivity for spherical lens is 3.5 rather than 4. Fig. 2.24 shows graphically eqn. 2.16.

Teflon is an adequate material to build a homogeneous lens. It is a relatively low cost and mechanically robust. From the EM point of view, the relative dielectric constant of Teflon (ε_r=2.2) allows negligible aberration effects, low reflection at the lens surface and a focus which is externally away from the lens surface. Dielectric losses in teflon lens are acceptable for Ka-band antennas [110].

Approximately
plane phase front

Plane phase front

Focus

Focus

R

r

$$\epsilon_r = 3.5$$

$$\epsilon_r = 2 - \left(\frac{r}{R}\right)^2$$

(a)

(b)
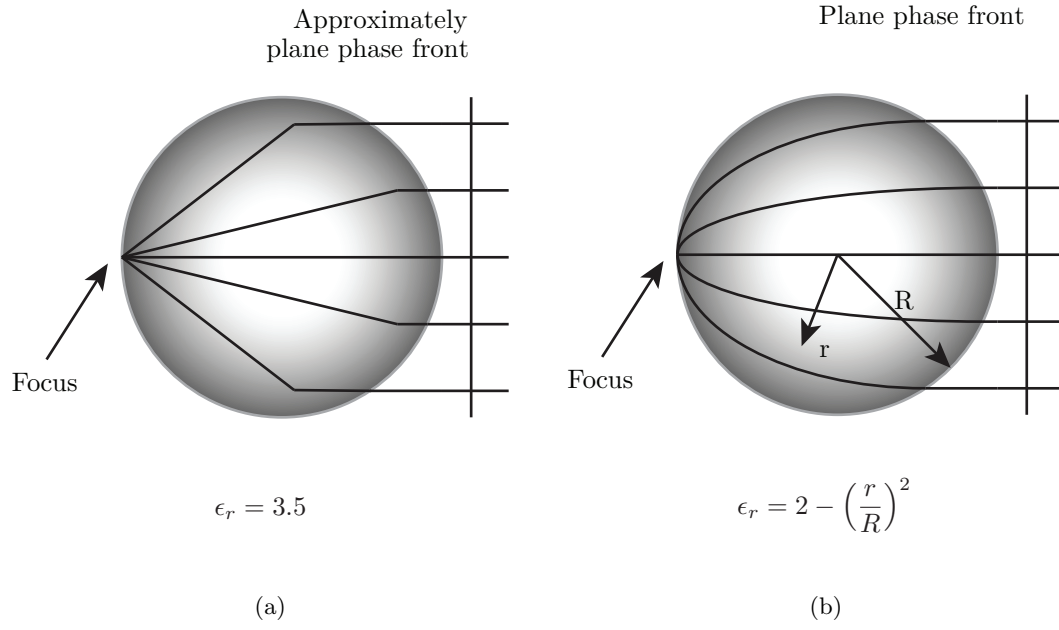
Figure 2.21.: Spherical lens model. (a) Homogeneous Lens. (b) Luneberg lens

Ideal constant
phase front

l_C

θ

l_B

l_Y

l_D

Focus

$$R = \frac{D}{2} = \frac{l_D}{2}$$

$$\epsilon_r = 3.5$$
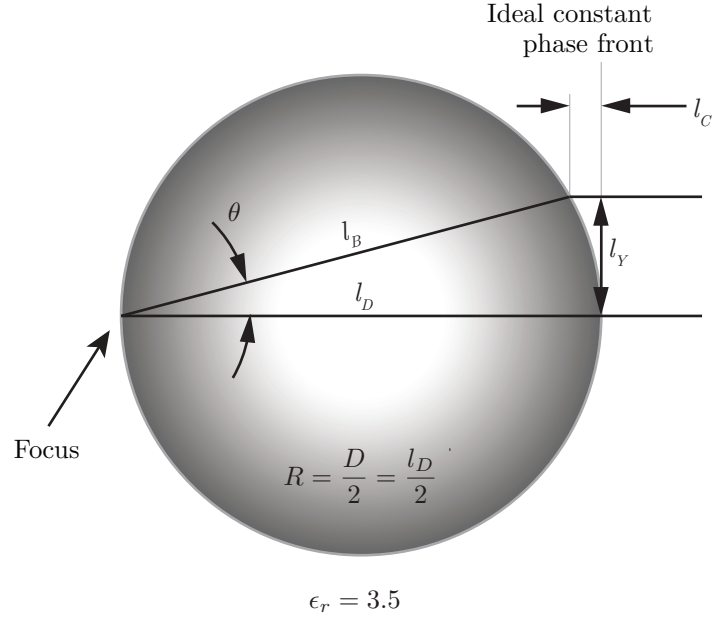
Figure 2.22.: Geometry of spherical lens with uniform permittivity.
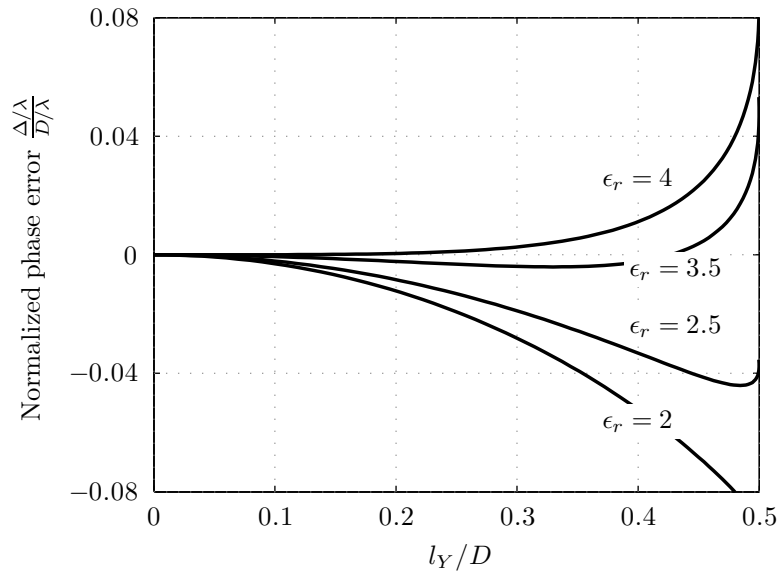
Figure 2.23.: Aberrations from a homogeneous lens with feed at the surface.
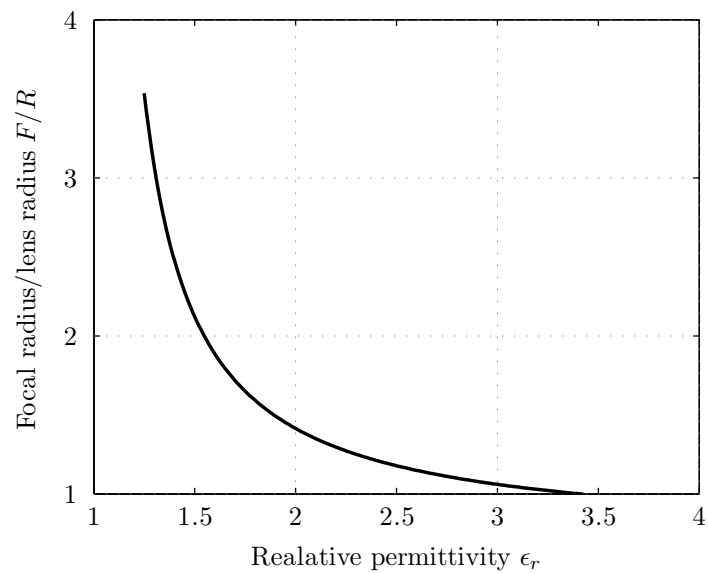
Figure 2.24.: Focus as function of the lens relative permittivity.

Luneburg lenses

A homogeneous-dielectric electrical lens is easy to fabricate, but suffers from non-exact focus-
ing and reflection loss. Another type of spherical lens is the Luneburg lens [111]. This kind of
lens focuses an incident plane wave at a point which is ideally located on the lens surface. Its
spherical geometry make it possible to easily achieve multiple beams by using multiple feeds
placed adequately around the lens [112]. This concept makes Luneburg lenses very attractive
for a HAPS payload.

The Luneburg lens requires a continuous radial variation of dielectric constant as follows
[113–115]:

$$\varepsilon_r = 2 - \left(\frac{r}{R}\right)^2 \tag{2.18}$$

where r is the radius within the lens, and R is the outer radius. Hence, the variation of
dielectric constant from the edge to the center of the antenna without reflection loss due to a
brupt transitions is:

$$1 \leq \varepsilon_r \leq 2 \tag{2.19}$$
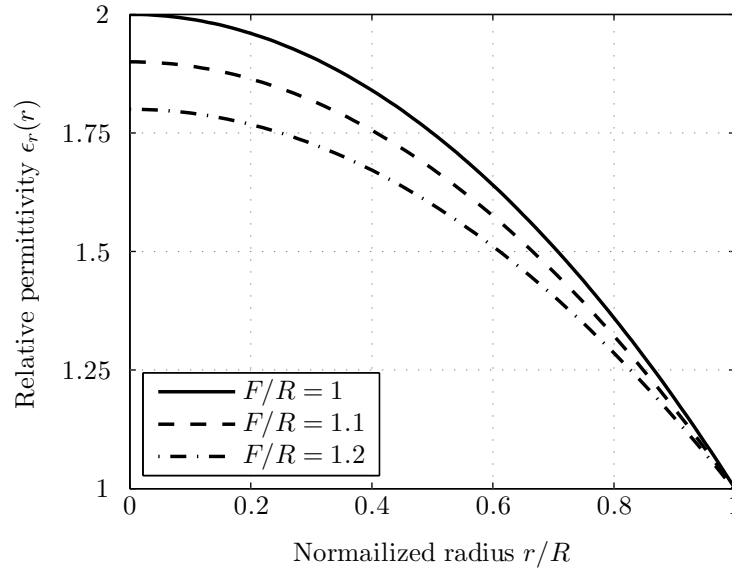
Figure 2.25.: Permittivity as a function of the radius

Figure 2.25 shows the relationship between the relative permittivity of the dielectric shells
and the lens radius for three different focusing radii. F the focal radius of the lens [116]. The
solid curve ($F/R = 1.0$) is the permittivity variation of the standard Luneburg lens described

by equation 2.19. Since R_f equals R_0, a lens with this permittivity variation will focus to a point on its outer surface. Each of the remaining curves in Fig. 2.25 describes a permittivity variation for a lens which focuses some distance away from its surface [111, 117, 118].

The aperture efficiency is very good, but unfortunately such a lens cannot be practically constructed [119–121]. However, a finite number of concentic dielectric shells can approximate the continuous variation of dielectric constant seen in a true Luneburg lens.

Since the lens does not have the continuous variation in dielectric constant of the ideal Luneburg lens, it does suffer some focusing errors and small efficiency degradation [122–124]. These focusing errors are a function of the number of shells used to make up the lens [125], and the method of incrementing the shells [122, 126–128]. The quantization also causes a reflection at each material interface. These reflections do not occur in a Luneberg lens because of its continuous variation of dielectric constant. The amount of reflection decreases as the number of shells increases [129–132].

A number of different quantization methods [132–139] are available for selecting the radii and dielectric constants of the shells. Table 2.2 lists a parameter set of a discretized Luneberg lens which is composed of layered dielectric spherical shells [140]. Such layers are typically made out of foam based materials. The density of foam can be chosen to control the permittivity of the material.

Table 2.2.: Characteristic of an N-shell Luneburg lens

N	Shell normalized radii: r_i	Shell relative permettivity: $\varepsilon_{r,i}$
1	0.82	1.67
2	0.63 0.89	1.80 1.4
3	0.53 0.75 0.93	1.86 1.57 1.28
4	0.47 0.67 0.82 0.94	1.88 1.67 1.44 1.22
5	0.43 0.60 0.74 0.85 0.95	1.91 1.73 1.55 1.36 1.18
6	0.39 0.56 0.68 0.78 0.88 0.96	1.93 1.77 1.61 1.46 1.31 1.16
7	0.37 0.52 0.63 0.73 0.82 0.89 0.97	1.93 1.80 1.67 1.53 1.40 1.27 1.13
8	0.34 0.49 0.59 0.69 0.77 0.84 0.91 0.97	1.94 1.82 1.71 1.59 1.47 1.35 1.24 1.12

It is obvious that by increasing the number of shells, the lens behavior gets closer to the ideal one (see Fig. 2.26) and therefore, theoretically, the performances of the lens improve. However, there is a kind of threshold effect, and that above a given, and quite small, number of shells both the directivity and side lobe levels no longer improve. Figure 2.27 shows that a two-shells design can give almost the same performance of a Luneberg lens.

Moreover, with a large number of shells, the manufacturing difficulty is important [141, 141–143] and then the air gap effects can significantly alter the lens antenna performances. Furthermore, homogeneous spherical lenses focusing properties are very similar to those of Luneberg lenses [109, 110, 144, 145], except that small aberrations might occur. A compromise between performances and facility of manufacturing is necessary.
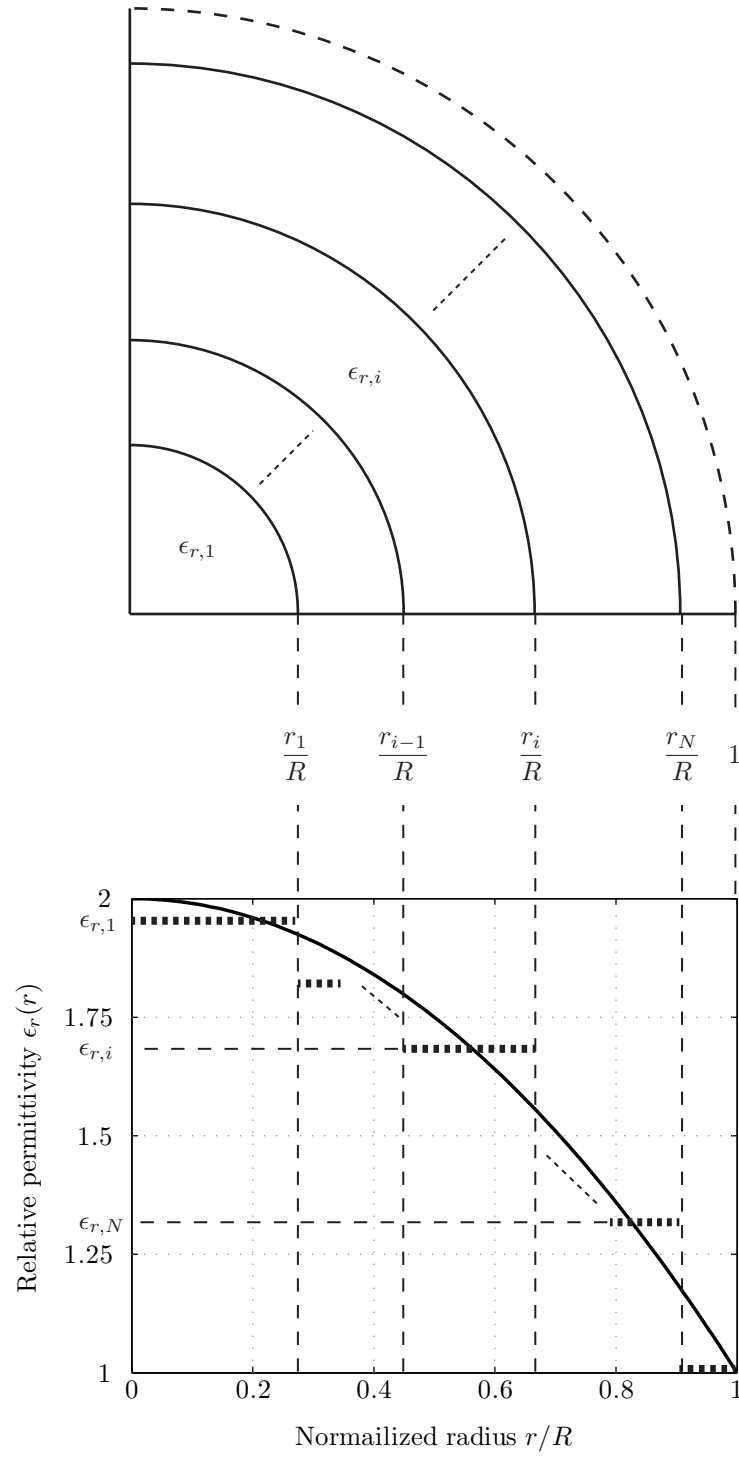
Figure 2.26.: Cut view of a quarter of a N-shell Luneburg lens and the fictive air shell. Representation of the theoretical and reconstructed permittivity law (Formula 2.19)
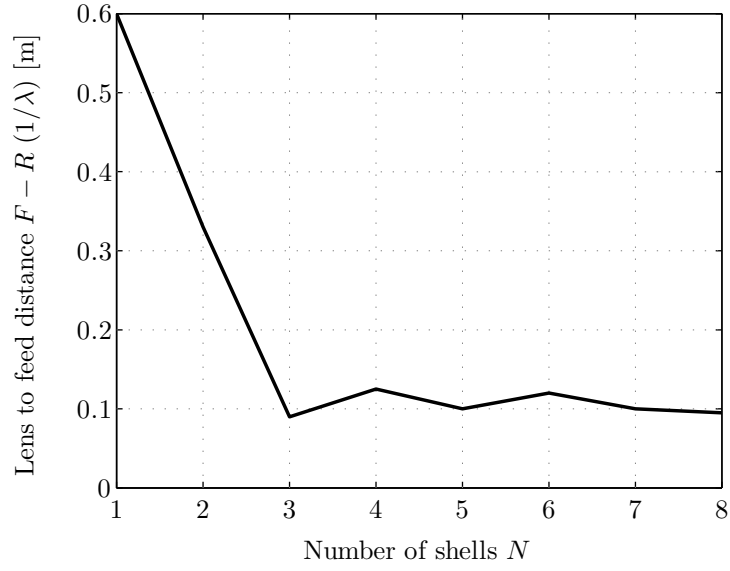
(a)
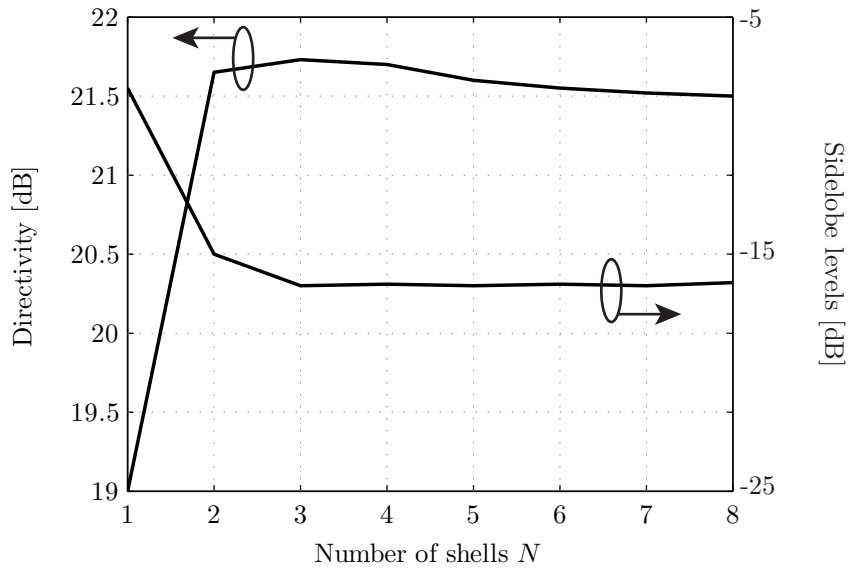
(b)

Figure 2.27.: Performance of $4\lambda_0$ diameter lens: (a)Influence of the number of shells on the distance between lens surface and feed $(F-R)$ between the waveguide and the lens; (b) Influence of the number of shells on the directivity and sidelobe levels

2.8.4. Preferred feeds for lenses: horns

The horn antenna can be considered a region of transition between two media where the EM wave is, respectively, guided and allowed to freely radiate. Metal horns (see a prototype realized for HAPS by [63] in Fig. 2.28) can be seen as a continuation of the waveguide where end walls are flared outwards to form a funnel-shaped structure. The design of the horn aperture is chosen for an appropriate field distribution thus for the desired radiation. A trade-off needs to be made between the occupied volume of the horn and the antenna performances, especially for HAPS antenna where the weight is an issue. A long transition between the waveguide and the antenna aperture yields low sidelobes and a shaped beam. Although in [63], horns have already been investigated standalone as HAPS antenna, horns are usually used just as feeders of a main aperture formed by a reflector or a lens.

Advantages: For HAPS, horn antennas could be advantageous because of the following properties:

- high power can be handled by this structure;

- each horn of a multi-beam antenna system can be customized to achieve the desired footprint. Rectangular, circular and elliptical horns have been already investigated for this purpose in [146, 147];

- horns are easily machined with high accuracy by using CNC process;

- mechanically robust;

- horn antennas are broadband and efficient also at mm-wave frequency.

Drawbacks: However, horn antennas have certain disadvantages for some HAPS antenna applications:

- volume occupied and weight of high directive horn antennas might be an issue;

- one horn generates one beam and a multi-beam antenna system based on horn antenna might be bulky and heavy.

Courtesy of CTU

Figure 2.28.: Horn antenna prototype for HAPS station working at 46 GHz.

2.9. Conclusion

Following the above discussions, it was found that the lens antenna was the choice best suited to our scenario. Moreover, for all the potential advantages of stratified lenses like Luneberg, it was decided to demonstrate the concept with an homogeneous lens, which was easily available in the laboratory.

References

[1] D. Grace, N. E. Daly, T. C. Tozer, and A. G. Burr, "LMDS from high altitude aeronautical platforms," *Proceedings IEEE GLOBECOM*, vol. 99, pp. 2625–2629, 1999.

[2] D. Grace, J. Thornton, G. P. Whire, C. Spillard, D. A. J. Pearce, M. Mohorčič, T. Javornik, E. Falleti, J. A. Delgado-Penín, and E. Bertran, "The European HeliNet broadband communications application - an update on progress," *The 4th Stratospheric Platform Systems Workshop*, Tokyo, Japan, 2003.

[3] S. Karapantazis and F. N. Pavlidou, "Broadband communications via high-altitude platforms: a survey," *IEEE Communications Surveys & Tutorialsn*, vol. 7, no. 1, pp. 2–31, 2005.

[4] T. Morisaki, "Overview of regulatory issues and technical standards on high altitude platform stations," *Proceedings of the International Workshop on High Altitude Platforms Systems, WHAPS 05*, Athens, Sept. 2005.

[5] J. Gavan, S. Tapuchi, and D. Grace, "Concepts and Main Applications of High-Altitude-Platform Radio Relays," *Radio Science Bulletin*, no. 330, Sep. 2009.

[6] "European Union contract FP6-IST-2003-506745, Communications from aerial platform networks delivering broadband communications for all," *6th Framework Programme, Priority 2, Information Society Technologies, Annex*, pp. 1–27, December 2003.

[7] D. Avagnina, "Wireless networks based on high platforms for the provision of integrated navigation/communication services," *IEEE Communications Magazine*, vol. 40, no. 2, pp. 119–125, 2002.

[8] S. Karapantazis and F. N. Pavlidou, "The role of high altitude platforms in beyond 3G Networks," *IEEE Wireless Communications*, pp. 33–41, 2005.

[9] A. Aragón-Zavala, J. Cuevas-Ruíz, and J. Delgado-Penín, *High-altitude platforms for wireless communications*. Wiley, 2008.

[10] J. D. Laurier, B. Gagnon, J. Wong, R. Williams, and C. Hayball, "Research on the technology of an airplane concept for a Stationary High Altitude Relay Platform (SHARP)," *32nd Annual General Meeting of the Canadian Aeronautics and Space Institute*, Montreal, Canada, May 1985.

[11] G. W. Jull, A. Lillemark, and R. M. Turner, "SHARP (Stationary High Altitude Relay Platform)telecommunications missions and systems," *IEEE Vehicular Technology Conference*, New Orleans, USA, Dec. 1985.

[12] Y. Lee and H. Ye, "Sky station stratospheric telecommunications system, a high speed low latency switched wireless network," *Proceedings of 17th AIAA International Communications and Satellite Systems Conference*, pp. 25–32, 1998.

[13] N. J. Colella, J. N. Martin, and I. F. Akyildiz, "The HALO network," *IEEE Communications Magazine*, vol. 38, pp. 142–148, Jun. 2000.

[14] J. Martin and N. Colella, "Broadband wireless services from high altitude long operation(HALO) aircraft," *SPIE International Symposium of Voice, Video, and Data Communications: Broadbanding for Multimedia Markets*, pp. 31–42, Dallas, TX, USA, Nov. 1997.

[15] "http://www.angelcorp.com/," Angel Technologies Corporation.

[16] "High Altitude Long Endurance (HALE), URL: http://www.lindstrand.co.uk/."

[17] T. C. Tozer, "European Union Contract FP6-2002-AERO-2 SSA Project-516081, High altitude aircraft and airships," *USE HAAS Activity Assessment Report, 6th Framework Programme*, pp. 1–20, URL:http://www.usehaas.org, 2007.

[18] "ESA-ESTEC contract 162372/02/NL/US, STRATOS: Stratospheric Platforms, a Definition Study for an ESA Platform," *Final Report*, pp. 1–34, Sept. 2005.

[19] R. Tafazolli, R. Wansch, C. Plenge, J. Horwath, and U. Apel, "Stratospheric services," *Technical Note of Stratospheric Platforms - a definition study for an ESA platform (TN1)*, 2004.

[20] T. C. Tozer, "Strategic Research Agenda, High altitude platforms for communications services," *European Civil Unmanned Aerial Vehicles Road map Report*, pp. 1–192, URL: http://www.uavnet.com, 2005.

[21] "www.capanina.org/."

[22] Y. Hase, R. Miura, and S. Ohmor, "A novel broadband all-wireless access network using stratospheric radio platform," *IEEE Vehicular Technology Conference*, vol. 98, pp. 98–105, May Ottawa, Canada, May 1998.

[23] ——, "European Union Contract IST-1999-11214, Network of stratospheric platforms for traffic monitoring, environmental surveillance and broadband services," *5th Framework Programme of European Community Activities in the Field of Research and Technological Development*, vol. 98, 1999.

[24] J. Thornton, D. Grace, C. Spillard, T. Konefal, and T. C. Tozer, "Broadband communications from a High-Altitude Platform - the European HeliNet programme," *IEE Electronic Communication Engineering journal*, vol. 13, pp. 138–144, Jun 2001.

[25] L. LoPresti, M. Mondin, S. Orsi, and M. Pent, "Heliplat as a GSM base station: a feasibility study," *Data Systems in Aerospace Conference, DASIA*, pp. 31–42, Lisbon, Portugal, May 1999.

[26] "European Union contract FP6-IST-2003-506745, Communications from aerial platform networks delivering broadband communications for all," *6th Framework Programme, Publish-able Executive Summary*, pp. –6, Mar. 2007.

[27] http://www.hapcos.org/, 2005.

[28] H. Lee, "Ku-bandlink budget analysis of UAV with atmospheric losses," *25th Digital Avionics Systems Conference, 2006 IEEE/AIAA*, 1-8, Oct. 2006.

[29] R. Miura, "Wireless system using high altitude platforms - R&D in Japan," *USE-HAAS Workshop*, Brussels, Belgium, July 2005.

[30] M. Oodo, H. Tsuji, R. Miura, M. Maruyama, M. Suzuki, Y. Nishi, and H. Sasamoto, "Experiments on IMT-2000 using unmanned solar powered aircraft at an altitude of 20 km," *IEEE Transactions Vehicular Technology*, vol. 54, no. 4, pp. 1278–1294, May 2005.

[31] J. M. Park, B. J. Ku, Y. S. Kim, and D. S. Ahn, "Technology development for wireless communications system using stratospheric platform in Korea," *Proceedings of the 13th IEEE International Symposium on Personal, Indoor and Mobile Radio Communications, PIMRC'02*, vol. 4, pp. 1577–1581, 2002.

[32] Y. Yokomaku, "Overview of stratospheric platform airship R&D Program in Japan," *Proceedings of the 2nd Stratospheric Platform Systems Workshop*, pp. 15–23, Feb. 2000.

[33] D. Grace, M. Mohorčič, M. H. Capstick, M. Bobbio-Pallavicini, and M. Fitch, "Integrating users into the wider broadband network via high altitude platforms," *IEEE Transactions on Wireless Communications*, vol. 12, no. 1, pp. 98–105, May 2005.

[34] M. Bourry, F. Tiezzi, and S. Vaccaro, "Omni-directional antenna for mobile satellite broadcasting applications," Patent US 20 090 027 294, January 29, 2009.

[35] "High Altitude Platforms for Communications and Other Services," COST 297, URL:http://www.hapcos.org, 2005.

[36] C. Oestges and D. Vanhoenacker-Janvier, "Coverage analysis of a stratospheric communication system," *IET Proceedings on Microwave, Antennas and Propagation*, vol. 148, no. 1, pp. 45–49, May 2001.

[37] "ITU Internet Report, Birth of Broadband," *International Telecommunication Union*, 1-200, Geneva, September, 2003.

[38] "Fixed Service Recommendation F.592-3, Vocabulary of terms for the fixed service," *International Telecommunication Union*, 1-10, Geneva, 2002.

[39] "High Altitude Platform Stations: An Opportunity to Close the Information Gap," *Question 9/2*, Report on ITU, Geneva, 1998.

[40] "Resolution 122: Whereby HAPS is allowed to operate within the fixed service in the band 47.2-47.5 GHz and 47.9-48.2 GHz," *World Radio Communications Conference*, 1997.

[41] "Fixed Service Recommendation F.1399-1, Vocabulary of Terms for Wireless Access," *International Telecommunication Union*, 1-14, Geneva, 2001.

[42] G. M. Djuknic, J. Freidenfelds, and Y. Okunev, "Establishing wireless communications services via high-altitude aeronautical platforms: a concept whose time has come?" *IEEE Communications Magazine*, pp. 128–135, Sept. 1997.

[43] S. D. Ilcev, "Global Mobile Satellite Communications for Maritime, Land and Aeronautical Applications," *IEEE Vehicular Technology Conference*, May Springer, Berlin, 441–460, 2005.

[44] J. Gavan and M. Haridim, "Stratospheric quasi-stationary platforms: can they replace communication satellite systems?" *Telecommunications and Space Journal*, vol. 4, pp. 275–282, 1997.

[45] J. Thornton, D. Grace, M. Capstick, and T. Tozer, "Optimizing an array of antennas for cellular coverage from a high altitude platform," *IEEE Transactions on Wireless Communications*, vol. 2, no. 3, pp. 484–492, May 2003.

[46] T. Wierzbanowski, "Unmanned aircraft systems will provide access to the stratosphere," *RF Design*, pp. 12–16, Feb. 2006.

[47] S. R. Saunders and A. Aragón-Zavala, "Antennas and propagation for wireless communication system," 2nd edn, Wiley,London, 2007.

[48] "Itu-r propagation recommendation p.676-3: Attenuation by atmospheric gases," *International Telecommunication Union*, Geneva, 1997.

[49] S. Haykin, *Communication systems*. John Wiley and Sons, New York, 2001.

[50] S. Y. Eom, S. H. Son, Y. B. Jung, S. I. Jeon, S. A. Ganin, A. G. Shubov, A. K. Tobolev, and A. V. Shishlov, "Design and test of a mobile antenna system with tri-band operation for broadband satellite communications and DBS reception," *IEEE Trans. Antennas Propagat.*, vol. 55, no. 11, pp. 3123–3133, Nov. 2007.

[51] F. Hules, G. Streelman, and H. Yen, "A direct broadcast satellite reception system for automotive OEMs," in *IEEE Antennas and Propagation Society International Symposium*, vol. vol. 1B, 2005, pp. 80–83.

[52] A. C. Densmore and V. Jamnejad, "A satellite-tracking K and Ka-band mobile vehicle antenna system," *IEEE Trans. Veh. Technol.*, vol. 42, no. 4, pp. 502–513, Nov. 1993.

[53] F. Hules, G. Streelman, and H. Yen, "A direct broadcast satellite reception system for automotive OEMs," in *IEEE Antennas and Propagation Society International Symposium*, vol. vol. 1B, 2005, pp. 80–83.

[54] H. Schantz, *The art and science of ultrawideband antennas*. Artech House, 2005.

[55] D. J. Daniels, *Ground penetrating radar*. 2nd ed. The Institution of Engineering and Technology, London, 2004.

[56] C. A. Balanis, *Antenna Theory: Analysis and Design*. John Wiley & Sons Inc., 1996.

[57] R. F. Harrington, "Effect of antenna size on gain, bandwidth and efficiency," *Journal of Research of the National Bureau of Standards-D Radio Propagation*, vol. 64-D, pp. 1–12, 1960.

[58] L. J. Chu, "Physical limitations of omni-directional antennas," *Journal of Applied Physics*, vol. 19, no. 12, pp. 1163–1175, 1948.

[59] H. Wheeler, "Fundamental limitations of small antennas," *Proceedings of the IRE*, vol. 35, no. 12, pp. 1479 – 1484, 1947.

[60] A. Henderson and J. James, "Low-cost flat-plate array with squinted beam for DBS reception," *Microwaves, Antennas and Propagation, IEE Proceedings H*, vol. 134, no. 6, pp. 509–514, 1987.

[61] ——, "Improved microstrip flat-plate array for domestic DBS reception," in *Antennas and Propagation Society International Symposium*, vol. 24, Jun. 1986, pp. 565–568.

[62] J. Huang, "Microstrip antennas for commercial applications," in *Microstrip Antennas. The Analysis and Design of Microstrip Antennas and Arrays*, D. M. Pozar and D. H. Schaubert, Eds. New York: IEEE Press., 1995, pp. pp. 371–379.

[63] "Report on steerable antenna architectures and critical RF circuits performance," *Deliverable Number D24, FP6-IST-2003-506745 CAPANINA*, pp. –6, Nov. 2006.

[64] R. C. Hansen, Ed., *Microwave scanning antennas.* Los Altos, Calif.: Peninsula Publishing, 1985.

[65] J. Kasemodel, C.-C. Chen, and J. Volakis, "Broadband planar wide-scan array employing tightly coupled elements and integrated balun," in *Phased Array Systems and Technology (ARRAY), 2010 IEEE International Symposium on*, oct. 2010, pp. 467 –472.

[66] B. Thors, H. Steyskal, and H. Holter, "Broad-band fragmented aperture phased array element design using genetic algorithms," *IEEE Trans. Antennas Propagat.*, vol. 53, no. 10, pp. 3280 – 3287, oct. 2005.

[67] P. Friedrich, L. Pringle, L. Fountain, P. Harms, D. Denison, E. Kuster, S. Blalock, G. Smith, J. Moloney, and M. Kesler, "A new class of broadband planar apertures," in *Allerton Antenna Applications Symposium*, Monticello, Illinois (USA), Sep. 2001.

[68] H. Holter, "Dual-polarized broadband array antenna with BOR-elements, mechanical design and measurements," *IEEE Trans. Antennas Propagat.*, vol. 55, no. 2, pp. 305 – 312, feb. 2007.

[69] B. Munk, R. Taylor, T. Durharn, W. Croswell, B. Pigon, R. Boozer, S. Brown, M. Jones, J. Pryor, S. Ortiz, J. Rawnick, K. Krebs, M. Vanstrum, G. Gothard, and D. Wiebelt, "A low-profile broadband phased array antenna," in *Antennas and Propagation Society International Symposium, 2003. IEEE*, vol. 2, june 2003, pp. 448 – 451.

[70] J. Shin and D. Schaubert, "A parameter study of stripline-fed vivaldi notch-antenna arrays," *IEEE Trans. Antennas Propagat.*, vol. 47, no. 5, pp. 879 – 886, may 1999.

[71] J. Thornton, "Properties of spherical lens antennas for high altitude platform communications," in *6th European Workshop on Mobile/Personal Satcoms and 2nd Advanced Satellite Mobile Systems (EMPS & ASMS), ESTEC, European Space Agency*, 2004.

[72] S.-M. Lin, Y.-Q. Wang, and P.-L. Shen, "Phase-only synthesis of the shaped beam patterns for the satellite planar array antenna," *Proc. IEEE*, pp.331-334, 2000.

[73] T. Koleck, "Active antenna coverage synthesis for GEO satellite using genetic algorithm," *in Proc. Int. Symp. on Antennas and Propagat.*, pp. 142-144, 2003.

[74] D. Popovic and Z. Popovic, "Multibeam antennas with polarization and angle diversity," *IEEE Trans. Antennas Propag.*, vol. 50, no. 5, pp. 651-657, Mai 2002.

[75] D. Popovic, "Constrained lens arrays for communications systems with polarization and angle diversity," *Ph.D. Thesis*, University of Colorado at Boulder, 2002.

[76] S. Rondineau, C. Dietlein, Z. Popovic, R. Lee, F. Miranda, R. Romanofsky, M. Ingram, W. Barott, J. Langley, and D. Mandl, "Ground stations of arrays to increase the LEO download capacity," 36th *European Microwave Conference*, Manchester, pp. 874-877, 10-15 Sept. 2006.

[77] R. F. Harrington, *Field Computation by Moment Methods.* MacMillan, 1968.

[78] A. Peterson, S. Ray, and R. Mittra, *Computational Methods for Electromagnetics.* IEEE Press/Oxford University Press, 1998.

[79] R. J. Mailloux, *Phased Array Antenna Handbook*, 2nd ed. London: Artech House, 2005.

[80] ——, *Phased Array Antenna Handbook*, 1st ed. London: Artech House, 1994.

[81] A. Ellgardt, "Wide-angle scanning wide-band phased array antennas," Ph.D. dissertation, KTH School of Electrical Engineering, Stockholm, Sweden, 2009.

[82] H. Wheeler, "The grating-lobe series for the impedance variation in a planar phased-array antenna," *IEEE Trans. Antennas Propagat.*, vol. 13, no. 5, pp. 825 – 827, sep 1965.

[83] D. M. Pozar, "Microstrip antennas," vol. 80, no. 1, Jan. 1992, pp. 79–91.

[84] K. R. Carver and J. W. Mink, "Microstrip antenna technology," *IEEE Trans. Antennas Propagat.*, vol. AP-29, pp. 2–24, Jan. 1981.

[85] D. M. and D. H. Schaubert, Eds., *Microstrip Antennas. The Analysis and Design of Microstrip Antennas and Arrays.* New York: IEEE Press., 1995.

[86] R. J. Mailloux, J. F. McIlvenna, and N. P. Kernweis, "Microstrip array technology," *IEEE Trans. Antennas Propagat.*, vol. AP-29, no. 1, pp. 25–37, Jan. 1981.

[87] J.-F. Zürcher and F. E. Gardiol, "The SSFIP: A global concept for high performance broadband planar antennas," *Electron. Lett.*, vol. 24, no. 23, pp. 1433–1435, Nov. 1988.

[88] ——, *Broadband patch antennas.* Boston: Artech House, 1995.

[89] T. Ismail and M. Dawoud, "Null steering in phased arrays by controlling," *IEEE Transactions on Antenna and Propagation*, vol. 39, no. 2, pp. 1561–1566, Nov. 1991.

[90] M. V. Ivashina, M. N. Kehn, P. Kildal, and R. Maaskant, "Decoupling efficiency of a wideband vivaldi focal plane array feeding a reflector antenna," *IEEE Transactions on Antenna and Propagation*, vol. 2, no. 2, pp. 373–382.

[91] W. K. Kahn, "Element efficiency: a unifying concept for array antennas," *IEEE Transactions on Antenna and Propagation*, vol. 49, no. 4, pp. 48–56, Aug. 2007.

[92] P. Hannan, "The element-gain paradox for a phased array antenna," *IEEE Trans. Antennas Propag.*, vol. 12, no. 4, 1999.

[93] M. N. Kehn, M. V. Ivashina, and R. M. P. Kildal, "Definition of unifying decoupling efficiency of different array antennas: Case study of dense focal plane array feed for parabolic reflector," *Int. J. Electron.*, Commun. (AEU), 2009, 10.1016/j.aeue.2009.02.011.

[94] J. H. P. Muhs and C. K. Watson, "Slot antenna with face mounted baffle," *U.S. Patent No. 4499474*, Feb. 1985.

[95] R. C. Hansen, *Phased Array Antennas.* John Wiley and Sons, New York, 1998.

[96] R. J. Mailloux, "On the use of metallized cavities in printed slot arrays with dielectric substrates," *IEEE Transactions on Antenna and Propagation*, vol. 35, no. 5, pp. 477–487, May 1987.

[97] R. Garg, P. Barthia, I. Bahl, and A. Ittipiboon, *Microstrip Antenna Design Handbook.* Boston: Artech House, 2001.

[98] M. Ettorre and R. Sauleau, "Dual-layer optimized pill-box antenna for applications in the millimeter-wave range," in *5th ESA Workshop on Millimetre Wave Technology and Applications & 31st ESA Antenna Workshop*, ESA/ESTEC, Noordwijk, The Netherlands, Jun. 2009.

[99] Y. J. Cheng, W. Hong, and K. Wu, "Millimeter-wave substrate integrated waveguide multibeam antenna based on the parabolic reflector principle," *IEEE Trans. Antennas Propagat.*, vol. 56, no. 9, pp. 3055–3058, Sept. 2008.

[100] S.-C. Gao, L.-W. Li, M.-S. Leong, and T.-S. Yeo, "Integrated multibeam dual-polarised planar array," in *IEE Proceedings in Microwaves, Antennas and Propagation*, vol. 148, no. 3, Jun. 2001, pp. 174–178.

[101] D. McGrath, "A three-dimensional beamformer with planar front and back faces," *IEEE Antennas and Propag. Symposium*, vol. 23, pp.463-465, Juin 1985.

[102] ——, "Planar three-dimensional constrained lenses," *IEEE Trans. Antennas Propag.*, vol. 34, no. 1, pp. 46-50, Jan. 1986.

[103] F. Averty, A. Louzir, J.-F. Pintos, P. Chambelin, C. Person, G. Landrac, and J.-P. Coupez, "Cost effective antenna for LEO satellites communication system using a homogeneous lens," *IEEE Antennas and Propag. Symposium, Monterey, CA.*, Jun 2004.

[104] C. Fernandes, "Shaped dielectric lenses for wireless millimeter-wave communications," *IEEE Antennas and Propag. Magazine*, vol. 41, no. 5, pp. 141-150, Oct 1999.

[105] X. Wu, G. Eleftheriades, and T. van Deventer-Perkins, "Design and characterization of a single- and multiple-beam mm-Wave circularly polarized substrate lens antennas for wireless communications," *IEEE Trans. Microwave Theory Tech.*, vol. 47, no. 6, pp. 732-737, Jun 1999.

[106] X. Wu and G. Eleftheriades, "Two-lens and lens-fed reflector antenna systems for mm-wave wireless communications," *IEEE Antennas and Propag. Symposium, Salt Lake City, UT.*, vol. 1, pp. 660-663, 16-21 Jul. 2000.

[107] C. Fernandes, "Performance of lens antennas un wireless indoor millimeter-wave applications," *IEEE Trans. Microwave Theory Tech.*, vol. 47, no. 6, pp. 732-737, Juin 1999.

[108] P. Ingerson, "The feasibility of Luneberg lenses for 20-30 GHz applications," *IEEE Int. Symp. Antennas and Propag.*, Atlanta, 1998.

[109] K. Chang, "Handbook of microwave and optical components," *vol. 1 Microwave passive and antenna components*, Wiley, New York, Chapitre 11, 1989.

[110] T. Cheston and E. Luoma, "Constant-K lenses," *Emerson & Cuming*, APL Technical Digest, Mar-Apr. 1963.

[111] S. Morgan, "General solution of the Luneburg lens problem," *J. Appl. Phys.*, vol. 29, pp. 1358-1368, 1958.

[112] M. A. Mitchell, J. R. Sanford, L. E. Corey, R. A. Moore, and V. P. Pusateri, "Antenna system providing hemispherical coverage," *ICAP*, no. 89, pp. 394–398, 1989.

[113] A. Greenwood and J.-M. Jin, "Finite-element analysis of complex axisymmetric radiating structures," *IEEE Trans. Antennas Propag.*, vol. 47, no. 8, pp. 1260-1266, Aug. 1999.

[114] P. Rozenfeld, "The electromagnetic theory of three-dimensional inhomogeneous lenses," *IEEE Trans. Antennas Propag.*, vol. 24, no. 3, pp. 365-370, May 1976.

[115] H. Rosu and M. Reyes, "Electromagnetic modes of the Maxwell fisheye lens," *Atomic, molecular and optical physics*, Apr. 1996.

[116] "A Luneberg-lens update," *IEEE Antennas Propag. Mag.*, vol. 37, no. 1, pp. 76-79, Feb. 1995.

[117] R. Luneburg, "Mathematical theory of optics," *Providence, Rhode Island*, Brown University Press, 1944.

[118] C. Walter, "Surface-wave Luneberg lens antennas," *IEEE Trans. Antennas Propag.*, vol. 8, no. 5, pp. 508-515, Sept. 1960.

[119] R. Luneburg, "Mathematical theory of optics," *Providence, Rhode Island*, Brown University Press, 1944.

[120] Y. Rahmat-Samii, H. Mosallaei, and Z. Li, "Luneburg lens antennas revisited: Design, optimization, and measurements," *IEEE Millennium Conference on Antennas and Propag.*, Davos, Switzerland, Avr. 9-14, 2000.

[121] A. Greenwood and J.-M. Jian-Ming, "A field picture of wave propagation in inhomogeneous dielectric lenses," *IEEE Antennas Propag. Mag.*, vol. 41, no. 5, pp. 9-18, Oct. 1999.

[122] P. Ingerson, K. Kim, and Y. Rahmat-Samii, "Spherical Luneburg lens antennas: engineering characterizations including air gap effects," *in Proc. IEEE AP-S URSI Meet.*, Atlanta, 1998.

[123] Zimmerman, "Luneberg lens and method of constructing same," U.S. Patent 5 677 796, Oct. 14, 1997.

[124] K. Sato and H. Ujiie, "A plate Luneberg lens with the permittivity distribution controlled by hole density," *Proc. Int. Symp. Antennas and Propagation*, Japan, 2000.

[125] P. Ingerson, K. Kim, and Y. Rahmat-Samii, "Luneberg lenses performance limitations due to fabrication process," *IEEE Int. Symp. Antennas and Propag.*, Montreal, 1997.

[126] P. Ingerson, "Luneberg lenses performance limitations due to fabrication process," *IEEE Int. Symp. Antennas and Propag.*, pp.862-865, 1997.

[127] H. Mosallaei and Y. Rahmat-Samii, "Non-uniform luneburg and 2-shell lens antennas: Radiation characteristics and design optimization," *IEEE Trans. Antennas Propag.*, vol. 49, no. 1, pp. 60-69, 2001.

[128] L. Xue and V. Fusco, "24 GHz automotive radar planar Luneburg lens," *IET Microwaves, Antennas and Propag.*, vol. 1, no. 3, pp.624-628, Jun. 2007.

[129] J. Eaton, "On spherically symmetric lenses," *IRE Trans. Antennas Propag.*, vol. 4, pp. 66-71, Déc. 1952.

[130] K. Kim and Y. Rahmat-Samii, "Spherical Luneburg lens antennas: engineering characterizations including air gap effects," *in Proc. IEEE AP-S URSI Meet.*, Atlanta, pp. 2062-2065.

[131] P. Ingerson, "The feasibility of Luneberg lenses for 20-30 GHz applications," *IEEE Int. Symp. Antennas and Propag.*, Atlanta, 1998.

[132] D. Cheng, "Modified Luneberg lens for defocused source," *IRE Trans. Antennas Propag.*, vol. 8, no. 1, pp. 110-111, Jan. 1960.

[133] C. Fernandes and L. Anunciada, "Constant flux illumination of square cells for millimetre-wave wireless communications," *IEEE Trans. Microwave Theory Tech.*, vol. 49, no. 11, pp. 2137-2141, Nov. 2001.

[134] G. Godi, R. Sauleau, and L. L. Coq, "A shaping technique of substrate lens antennas with genetic algorithm," 11th *Symposium on Antenna Technology and Applied Electromagnetics*, St Malo, France, pp. 162-163, 15-17 Juin 2005.

[135] H. Mosallaei and Y. Rahmat-Samii, "Non-uniform Luneburg lens antennas: a design approach based on genetic algorithms," *IEEE Int. Symp. Antennas and Propag.*, 1998.

[136] ——, "IEEE Int. Symp. Antennas and Propag." *IEEE Antennas Propag. Mag.*, vol. 1, Jul. 11-16, 1998, pp.434-437.

[137] ——, "Non-uniform luneburg and 2-shell lens antennas: Radiation characteristics and design optimization," *IEEE Antennas Propag.*, vol. 49, no. 1, pp. 60-69, Jan. 2001.

[138] G. Peeler and H. Coleman, "Microwave stepped-index Luneberg lenses," *IEEE Antennas Propag.*, vol. 6, no. 2, pp. 202-207, Apr. 1958.

[139] J. Sanford and Z. Sipus, "Sidelobe reduction with array fed spherical lenses," *IEEE AP-S Digest*, vol. 1, pp. 670-673, Jun 1995.

[140] B. Fuchs, S. Palud, S. Member, L. L. Coq, and O. Lafond, "Scattering of Spherically and Hemispherically Stratified Lenses Fed by Any Real Source," *IEEE Transactions on Antennas and Propagation*, vol. 56, no. 2, pp. 450–460, Feb. 2008.

[141] I. Gresham, N. Jain, T. Budka, A. Alexanian, N. Kinayman, B. Ziegner, S. Brown, and P. Staecker, "A compact manufacturable $76 - 77$ GHz radar module for commercial ACC applications," *IEEE Trans. Microwave Theory Tech.*, vol. 49, no. 1, pp. 44-58, Jan. 2001.

[142] R. Sauleau, C. A. Fernandes, and J. R. Costa, "Review of lens antenna design and technologies for mm-wave shaped-beam applications," *Invited paper to the 11th Int. Symp. Antenna Technology and Applied Electromagnetics*, Saint Malo, France, 15-17 Juin, 2005.

[143] G. Godi, R. Sauleau, and D. Thouroude, "Performance of reduced size substrate lens antennas for millimeter-wave communications," *IEEE Trans. Antennas Propag.*, vol. 53, no. 4, pp. 1278-1286, Apr. 2005.

[144] B. Schoenlinner, X. Wu, J. Ebling, G. Eleftheriades, and G. Rebeiz, "Wide-scan spherical-lens antennas for automotive radars," *IEEE Trans. Microwave Theory Tech.*, vol. 50, no. 9, pp. 2166-2175, Sept. 2002.

[145] B. Schoenlinner and G. Rebeiz, "Compact multibeam imaging antenna for automotive radars," *IEEE Microwave Theory Tech. Symposium*, Seattle, WA, pp. 1373-1376, Jun 2002.

[146] S. Rao, M. Tang, C.-C. Hsu, and J. Wang, "Advanced antenna technologies for satellite communication payloads," *1st European Conference on Antennas and Propagation*, 2006.

[147] N. J. G. Fonseca and J. Sombrin, "Multi-beam reflector antenna system combining beam hopping and size reduction of effectively used spots," *IEEE Trans. Antennas Propagat.*, vol. AP-54, pp. 88-99, Apr 2012.

3. Circularly polarized homogeneous lens antenna system providing multibeam radiation pattern for HAPS [*][†]

Contents

3.1. Introduction

This chapter addresses the original design, prototyping and characterization of a multibeam circularly polarized HAPS antenna.

In particular, the two main goals of this chapter are:

1. to present the scenario of the circularly polarized multibeam antenna for cellular based communication services delivered from the stratosphere. This comprises the set of the general requirements of the on-board antenna for the targeted stratospheric mission and the discussion of the investigated solutions. The two solutions presented in this chapter are both based on the use of an internal polarizer inserted in the feed and included in its design.

2. to provide an effective design for the proposed scenario.

Multibeam antennas are a standard in telecommunication satellites. They are currently being used to provide the downlink and uplink coverage for mobile communication satellites, direct broadcast satellites, and personal communication services. These antennas typically provide contiguous coverage over a specified area by using high-gain overlapping spot beams. For effective utilization of the frequency spectrum of these satellite systems, the frequency is reused on a number of beams. This is done by dividing the available bandwidth into a number of subbands, typically using either a three-cell or a four-cell frequency-reuse scheme [1]. The relevant point here is that these considerations are applicable not only to Low-Earth Orbit (LEO) satellites, but also to our High-Hltitude-Platform Stations (HAPS).

Among the possible solutions for multibeam antennas, here we have selected, for the reasons detailed in Chapter 2, the use of dielectric lenses as an alternative solution for HAPS [2, 3]. Indeed, a multibeam radiation pattern is easily achievable by feeding a dielectric lens with several apertures that will generate N spot beams on the ground [4].

Many wireless services, such as GPS and TV broadcasting, need circular polarization to reach high performance. Since these services can be supplied and improved by using HAPS, a circularly polarized antenna system is a basic onboard element. However, and to the knowledge of the authors, a functional prototype of a circularly polarized compact multibeam antenna, suitable for HAPS applications, has not yet been fully described in the literature. This chapter puts together well-known solutions for individual components (waveguide/horn feed, inner circular polarizer, dielectric lens). It presents the design, realization, and preliminary characterization of a Ka-band circularly polarized multibeam antenna for HAPS applications.

The proposed antenna system was achieved by feeding a lens with circular waveguides terminated by small horns. To reach the desired circular polarization, polarizers were

integrated into these feeds.

Although the practical demonstrator included only a reduced number of feeds (up to nineteen), all of the antenna technology and topology have been developed to easily allow the increasing of the number of beams without redesigning the full antenna system.

The chapter is organized as follows: after a presentation of the scenario in Section 3.2, the lens-feed design is described in Sections 3.3 and 3.4. Emphasis is placed on the two polarizer solutions in Sections 3.5. Sections 3.6 and 3.7 then discusses the dielectric lens design and the antenna performance. Section 3.8 shows the prototype realization, together with the first measurement results. Finally, Section 3.9 concludes and summarizes the chapter.

Designs suitable and frequently used for multibeam antennas include (a) a single-aperture design with a single feed element per beam, (b) a single aperture design with overlapping feed clusters, (c) a direct radiating array, and (d) a multiple-aperture design with a single element per beam. In the satellite realm, the apertures are usually offset-parabolic reflector antennas.

The original contribution of this chapter resides in the design of the fully operational antenna subsystem and on the optimization of its main components, like the internal septum polarizer. The obtained antenna subsystem will be used as a benchmark against any eventual improvement and any new concept (as those discussed in Chapter 4 and 5) must be tested.

3.2. Scenario

In this section, a set of antenna specifications is introduced based on a possible scenario suitable for wireless communications via HAPS. The selected challenge corresponds to a concept currently under investigation in Switzerland [5, 6]. It consists of a Ka-band (27.5-31.3 GHz) multibeam antenna, mounted on a balloon platform at the standard height of $H_{HAPS}=$ 21 km, and providing 19 spot beams on the ground [7]. This antenna should allow for multi-cell architecture and for spectrum reuse [8–11].

From global system considerations, it was determined that the spot beams should be arranged in an overlapping hexagonal grid, and that every beam should guarantee an effective ground coverage in the form of a circular cell cluster (Figure 3.1). Typical beam overlaps used for multibeam antenna designs are -3 dB for two adjacent beams, and -4 dB for three adjacent beams, as explained in [1]. Since in this scenario the beams were arranged in a hexagonal grid, the beam-overlap level was chosen to be -4 dB. The circular cell boundary on the ground therefore corresponded to a -4 dB beam aperture. The cell in the center of cluster should have a nominal diameter $2R_{cell,1}$=5 km and the center distance between adjacent cells should be then $d_{cell} = 2R_{cell,1} \cos 30^o = 4.33$ km to guarantee uniform coverage of the illuminated
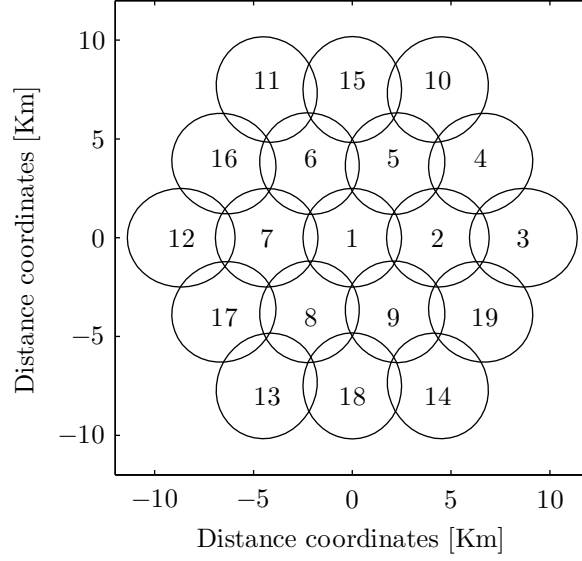
Figure 3.1.: Enumeration and arrangement of the ground power footprints.
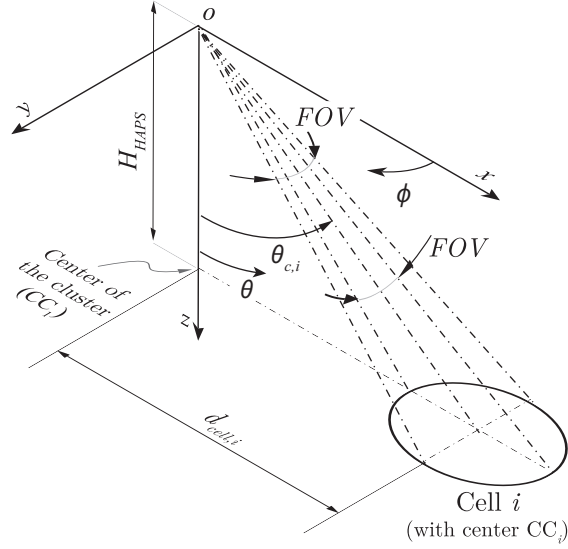
Figure 3.2.: Down-link geometry using symmetric beams.

area. From geometrical considerations (see also Figs. 3.1 and 3.2), if the cell in the center of the cluster is circular in shape, its radius $R_{cell,1}$ is associated to the -4dB angle (FOV) of the beam by:

$$FOV = 2 \arctan\left(\frac{R_{cell,1}}{H_{HAPS}}\right) = 13.6° \tag{3.1}$$

This value could also be considered to be an external specification for our antenna.

In this first stage, the Earth surface has been supposed flat and the elongation of the external cells of the cluster (due to high elevation angles) has been neglected. Under such hypothesis, the shape of the antenna beams can be considered identical for all the 19 beams. The cell elongation will be considered more in detail in Chapter 5, while this chapter will concentrate on the main design guidelines for the on-board antenna.

Finally, it must be recalled that as mentioned in chapter 1, global budget link considerations called for a minimum antenna gain of $G = 19$ dB in this scenario. (This last value must be considered as the transducer gain since it takes into account the antenna mismatch).

The feasibility of such a gain requirement from an antenna point of view can be very quickly checked. Standard antenna theory provides an upper value for the theoretical directivity of a antenna having a conical main beam with no sidelobes as (see also Chapter 2)

$$D_{max} = \frac{4\pi}{\Omega_{beam}},\tag{3.2}$$

where Ω_{beam} beam is the solid angle of the main beam. As mentioned in Chapter 2, this angle is usually estimated as

$$\Omega_{beam} = \left(\theta_{3dB}\right)^2,\tag{3.3}$$

where θ_{3dB} is the half-power beamwidth angle (radians) in any cut of the conical beam. From our specifications, the 4 dB angle is given, as it corresponds to the field-of-view angle (FOV in eqn. 3.1). The 3 dB angle is obviously a trifle smaller, and can be estimated with the usual cosine-squared assumption for the pattern, yielding

$$\theta_{3dB} = 0.88\theta_{4dB} = 0.88FOV\tag{3.4}$$

Introducing the value of $\theta_{3dB} = 12.0°\bar{0}.2094$ rad obtained from using eqn. 3.4 in eqn. 3.2 and 3.3, the maximum theoretical achievable directivity was found to be around 25.4 dBi. This gives a comfortable margin for including losses and efficiencies of real antennas, and still achieving the sought-after gain of 19 dB.

The specifications of the final link scenario are summarized in Table 3.1. Although those key parameters values are strictly connected to our specific antenna design, the proposed concept and the underlying strategies can successfully be applied in other different realistic scenarios.

Fig. 3.2 depicts the geometry considered here. The center of the antenna radiating element is the origin of the coordinate system. For each beam i, the boresight angle $\theta_{c,i}$, is then the angle formed by the center (CC_1) of the cluster, the antenna position and the center (CC_i)

Table 3.1.: *The HAPS link scenario. A more detailed scenario is given in Tables 1.1 and 1.2*

Frequency	27.5 - 31.3 GHz
Bandwidth	3.8 GHz ($\cong$13%)
R_{cell}	2.5 km
H_{HAPS}	21 km
FoV	13.6°
$G_{antenna}$HAPS	19 dB

of the cell i. Table 3.2 lists all the relevant information concerning the cluster geometry.

From geometrical considerations, the distance between the center of the cell i and the center of the cluster CC_1 is related with the boresight angle $\theta_{c,i}$ of each beam and with the platform altitude H_{HAPS} by:

$$\theta_{s,i} = \arctan\left(\frac{d_{cell,i}}{H_{HAPS}}\right) \tag{3.5}$$

3.2.1. Overview of the on-board antenna type

The proposed scenario requirements can be satisfied by an antenna system achieved by illuminating a dielectric lens with waveguide feeds. The choice of this antenna type for the selected scenario and the associated advantages and drawbacks has been motivated in Chapter 2.

In order to produce 19 cells on the ground (as shown in Fig. 5.1), 19 independent beams have to be radiated by the lens. By placing 19 feeds at the same distance from the surface of the lens, 19 identical beams are generated. Each feed radiates broadside and properly illuminates the lens. The lens focuses the radiation coming from every feed and shapes it into a directive beam. Each feed has to be positioned around the lens in such a way that each beam points to the corresponding cell center on the ground, and all the feed longitudinal axes intersect at the center of the lens.

A last word must be said about the ground shape of external cells. Obvious geometrical considerations demonstrate that the external cells of the cluster (cells number 2-19) are slightly deformed, and exhibit an elliptical shape. The correction of this ellipticity through a slight modification of the lens shape will be the subject of Chapter 5.

Table 3.2.: *Data for the 19 cells considered in Fig. 3.1.*

i	$\mathbf{CC}_i$ $(\mathbf{x}_i,\mathbf{y}_i)$ [km]	$\mathbf{d}_{cell,i}$ [km]	$\theta_{c,i}$ [deg]
1	(0,0)	0	0
2	(4.330,0)	4.330	11.65
3	(8.660,0)	8.660	22.41
4	(6.495,3.750)	7.500	19.65
5	(2.165,3.750)	4.330	11.65
6	(-2.165,3.750)	4.330	11.65
7	(-4.330,0)	4.330	11.65
8	(-2.165,-3.750)	4.330	11.65
9	(2.165,-3.750)	4.330	11.65
10	(4.330,7.500)	8.660	22.41
11	(-4.330,7.500)	8.660	22.41
12	(-8.660,0)	8.660	22.41
13	(-4.330,-7.500)	8.660	22.41
14	(4.330,-7.500)	8.660	22.41
15	(0,7.500)	7.500	19.65
16	(-6.495,3.750)	7.500	19.65
17	(-6.495,-3.750)	7.500	19.65
18	(0,-7.500)	7.500	19.65
19	(6.495,-3.750)	7.500	19.65

3.3. Feed design analysis

For many reasons, waveguide technology is indeed very appropriate for feeding the lens for HAPS applications [12–14].

- The use of waveguide feeds allows handling high power.

- Interaction with the lens can be controlled by designing a proper horn.

- By using waveguide technologies, each feed is mechanically independent from the others. This usually leads to a weak electromagnetic coupling between feeds (on the other hand, if printed feeds were used, they would typically share the same substrate, thus increasing the chances of mutual coupling, for instance through surface waves) [15–19].

- Waveguide feeds can be accurately and inexpensively produced in aluminum or brass by using digital milling machines

- Circular polarization can be easily achieved by combining a circular waveguide working on its dominant linearly polarized mode and an internal polarizer.

Although the basic theory of circular waveguide is well known [20, 21], here we report a few key concepts on the mode propagation inside such devices since the proper design of polarizers is based on the perturbation of the propagating mode. The typical coordinate system used to
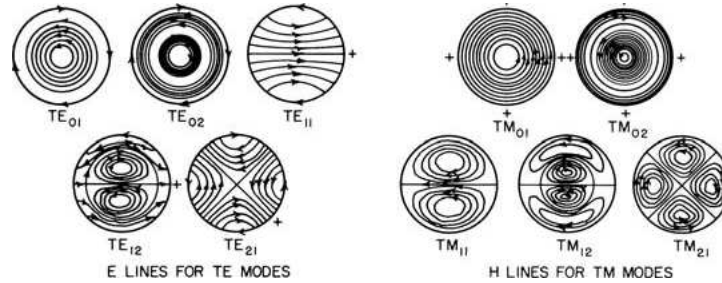
Figure 3.3.: Modes in circular waveguide [21].

describe a field in circular waveguide is ρ, θ, z, where ρ is the radial direction, θ is the angle, and z is the longitudinal direction. For TE_{mn} waves in circular waveguides, m denotes the number of axial planes along which the normal component of the electric field vanishes and n the number of cylinders including the boundary of the guide along which the tangential component of the electric field vanishes. The number m may take any integral value from 0 to infinity, and n may take any integral value from 1 to infinity. The dominant mode in circular waveguide is the TE_{11} [20]. For TM_{mn} waves, m denotes the number of axial planes along which the magnetic field vanishes and n the number of cylinders to which the electric field is normal. Of the circularly symmetrical waves, the TM_{01} has the lowest cutoff frequency. Field patterns for some of the simpler waves in circular guides are shown in Fig. 3.3 taken

from [21]. If the waveguide operating in a pure TE_{11} (dominant mode), the radiated field should be linear polarized with small cross-pol component which could be improved by adding some well selected higher-order modes. In order to achieve circular polarization in Ka-band, a convenient solution [22] envisages the use of two different orthogonal and in quadrature TE_{11} modes and thus a polarizer is needed.

Figure 3.4 is a schematic view of a circular waveguide feed that illuminates the lens. The coaxial-to-waveguide transition allows exciting the fundamental mode in the circular waveguide. This transition determines the bandwidth of not only the waveguide feed, but also of the whole lens antenna. Since the fundamental mode in a circular waveguide is linearly polarized, a polarizer is necessary to achieve circular polarization (section AB of Fig. 3.4). Finally, since the open end of the waveguide constitutes a strong discontinuity for the propagating waves, a horn is needed to provide a smooth transition to free space, matching the impedance while avoiding internal reflections [23–26]. Moreover, the horn helps to illuminate the lens properly.
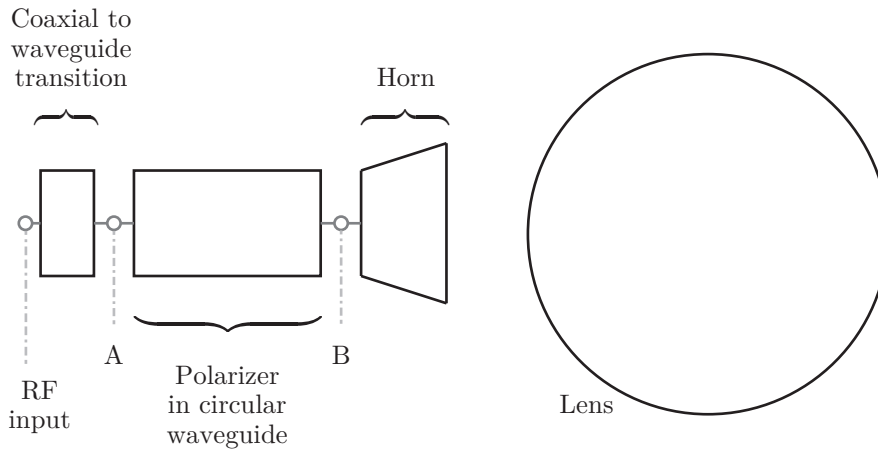
Figure 3.4.: The antenna system configuration

3.4. Coaxial to waveguide transition

The coaxial connector played an important role in the waveguide feed design. A 2.4 mm bulkhead connector assembly (see Fig. 3.5(a)) was used to feed the waveguide: it allowed good performance up to 60 GHz. The most efficient way to excite the fundamental mode in circular waveguides via a coaxial connector is shown in Fig. 3.5(b). The structure in Fig. 3.5 was modeled using CST Microwave Studio®. The dimensions T_M, W_d, and T_P were then optimized to work in Ka-band. With the optimized values in Table 3.3, a return loss lower than -25 dB was achieved over the whole frequency band (27.5 GHz - 31.3 GHz).

1.32 mm

∅ 0.6 mm

∅ 5.15 mm

1.83 mm

12.22 mm

∅ 2.42 mm

(a)

T_M

W_d

T_P

(b)
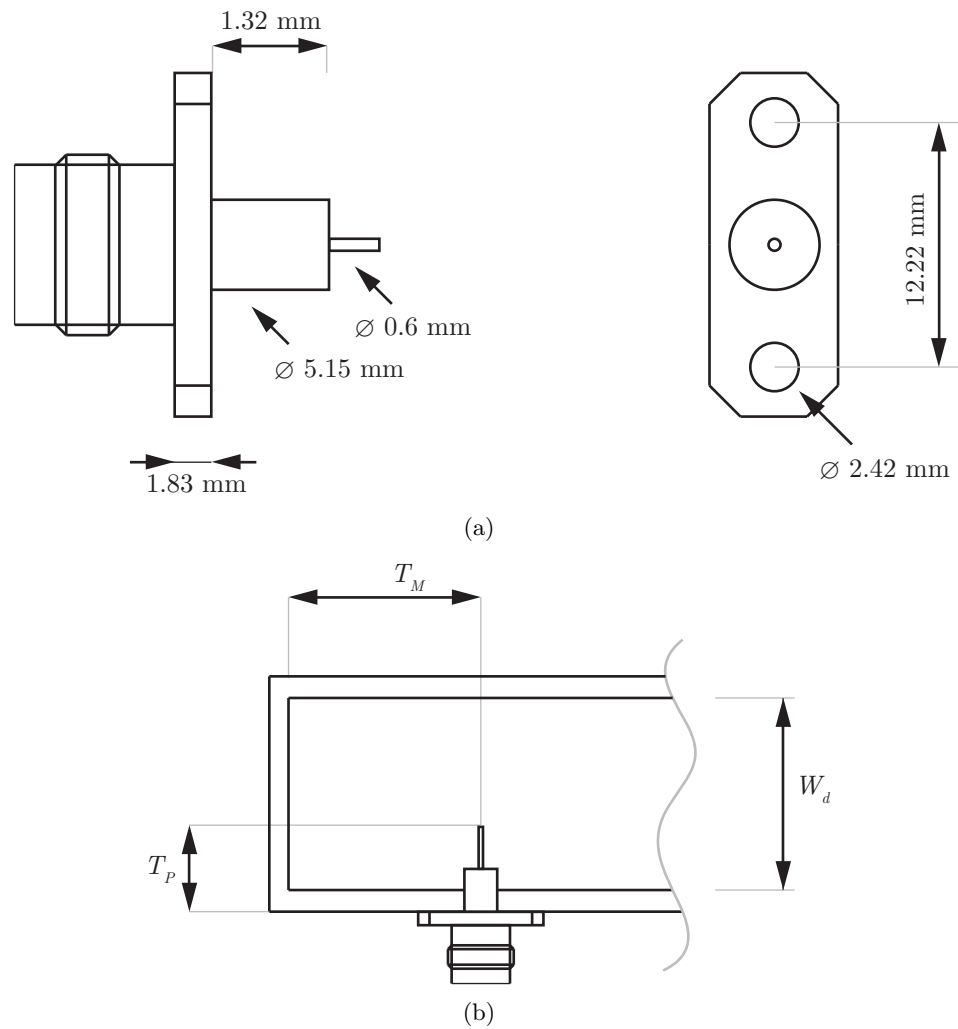
Figure 3.5.: (a) The dimensions of the coaxial connector and (b) the coaxial-to-waveguide transition.

Table 3.3.: *The dimensions of the coaxial-to-waveguide transition.*

T_M	3.72 mm
T_P	2.05 mm
W_d	7.30 mm

3.5. Polarizer in circular waveguide

A polarizer is needed to convert linear polarization into circular polarization. If wideband behavior is needed, an elliptical section waveguide polarizer or a dielectric septum polarizer are probably the best candidates [27, 27, 28]. These two solutions have been analyzed numerically and compared in this section.

A linearly polarized incident field, $\mathbf{E}_i$, must be excited at the input section of the polarizer. $\mathbf{E}_i$ is composed of two orthogonal components, $\mathbf{E}_h$ and $\mathbf{E}_v$. Originally (before reaching the waveguide region where the polarizer is located) $\mathbf{E}_h$ and $\mathbf{E}_v$ have value $\mathbf{E}_{h,o}$ and $\mathbf{E}_{v,o}$ with the same amplitude and phase (linear polarization).

The two components then propagate through the polarizer region with little reflection due to the discontinuity produced by the polarizer. In the polarizer region, the propagation constant of one component is strongly perturbed by the polarizer whereas, the propagation constant of the other component is weakly perturbed. Ideally, when the wave propagates through the polarizer region, one component is delayed by 90° with respect to the orthogonal one, while the same amplitude should be kept for both components, and thus the outgoing wave is circularly polarized. So the quality of the polarizer is defined by the differential phase shift $\Delta\Phi$ and by the amplitude ratio ΔM between the two components $S_{21,h}$ and $S_{21,v}$.

In order to compute these quantities, the structure has to be analyzed for both polarizations. From these two full-wave analyses, we recovered the scattering transmission parameters, $S_{21,h}$ and $S_{21,v}$, from which the differential phase, $\Delta\Phi$ was computed as $\Delta\Phi = \angle S_{21,h}$ - $\angle S_{21,v}$ and $\Delta M = |S_{21,h} - S_{21,v}|$. The polarizer design procedure started by considering the relevant specifications over the operating bandwidth, which, in this typical case, were

- the center frequency;

- the differential phase error with respect to 90° $\Delta\Phi$;

- the amplitude ratio between orthogonal components, ΔM

- the return-loss lower bound

3.5.1. Elliptical section waveguide polarizer

An elliptical sections waveguide polarizer can be designed [27, 28] by creating elliptical stretches in the section of a circular waveguide, as shown in Figs. 3.6 and 3.7. The ellipticity of each section of the polarizer can be characterized by the ratio between the longest axis length ($E_{a,i}$) of the stretch and the shortest one ($E_{b,i}$). The original linearly polarized incident field, E_i, is inclined 45° with respect to the shortest axis. Hence, the two orthogonal components, E_h and E_v of E_i have the same magnitude and phase and are respectively parallel and perpendicular to the shortest axis. The two components then propagate through the elliptical section region with little reflection due to the small discontinuity.

In the elliptical section region, the propagation constant of one component is strongly perturbed by the elliptical section because the electric field line is parallel to the longest axis of the elliptical section. On the other hand, the propagation constant of the other (orthogonal) component is weakly perturbed because the electric-field line is not disturbed by the discontinuity. Ideally, when the wave propagates through the elliptical sections, $\mathbf{E}_{h,o}$, (the horizontal component of the outgoing wave) is delayed by 90° with respect to $\mathbf{E}_{v,o}$, by passing through the polarizer, and thus the outgoing wave is circularly polarized. A right-hand circular polarization or a left-hand circular polarization is produced depending on the direction of the incident field, E_i, as illustrated in Figure 3.6.
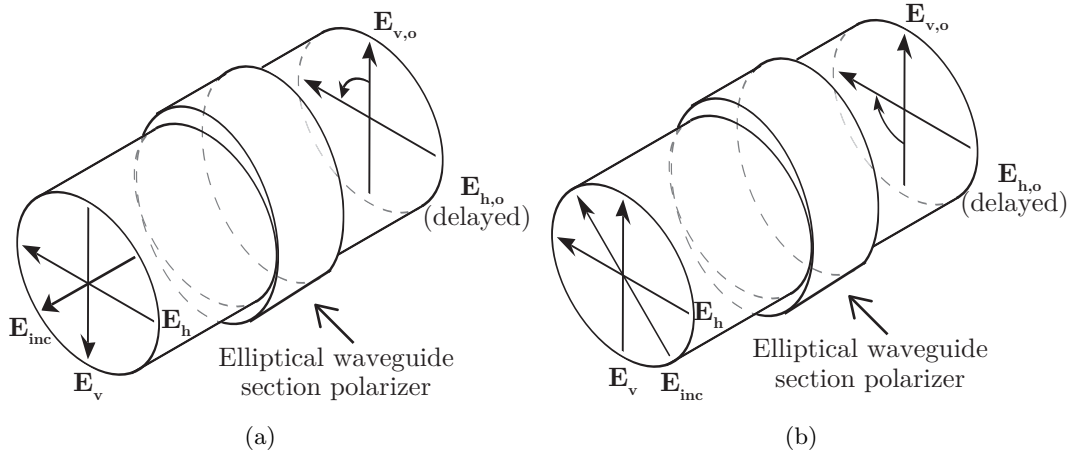
Figure 3.6.: A schematic representation of the elliptical section waveguide polarizer. (a) A left-hand circular polarization is produced after the polarizer, and (b) a right-hand circular polarization is produced after the polarizer.

In this type of polarizer, the number of stretches N influences the impedance matching of the device. To improve the reflection coefficient and to enlarge the bandwidth, more stretches are needed [6]. However, the electromagnetic performances do not improve linearly by increasing the number of stretches. Indeed, a high number of stretches implies more losses

in the discontinuity areas where the currents are important. Furthermore more sections mean also more length and weight.
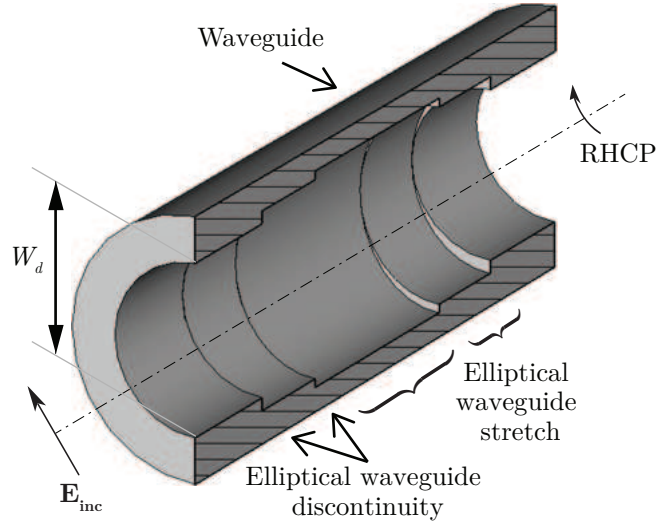
Figure 3.7.: The elliptical waveguide sections polarizer model.
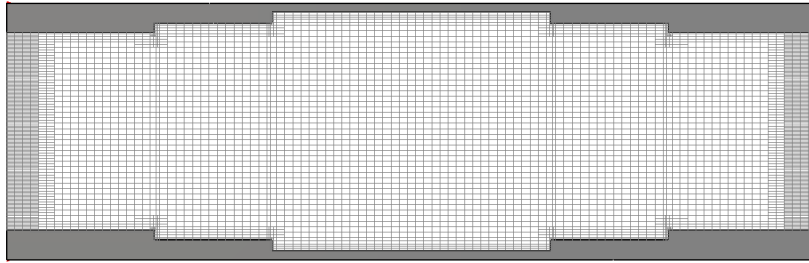
Figure 3.8.: A cross-sectional view of the elliptical sections waveguide polarizer and its mesh.

The following dimensions remained fixed during the polarizer-optimization design process:

- the waveguide diameter, W_D;

- the numer of septum stretches, S_W.

A convenient choice was to use the same shortest axis length for all of the waveguide's sections (including the end parts making the connections with the coaxial feed and with the horn). This avoided further step discontinuities, and simplifies the polarizer machining.

The relevant parameters for the optimization (see Fig. 3.7) were the length of the elliptical stretches, $E_{l,i}$, and their longest axis length, $E_{a,i}$. The index i is used here to indicate the stretches and ranges form 1 to N. The initial values and bounds of $E_{l,i}$ and $E_{a,i}$ were chosen according to the recommendations found in [28]. The stretch lengths, $E_{l,i}$, were taken to be in the range $[\lambda/8, \lambda/2]$, whereas the length of the stretches longest axis, $E_{a,i}$, was selected to be in the range $[W_d, 2W_d]$. An initial design was made with only a single elliptical stretch ($N = 1$). Although the optimized polarizer design was very compact and lightweight, with only one elliptical stretch, the polarization performances were too narrowband. The number of stretches has been then increased up to $N=5$ stretches and $E_{l,i}$ and $E_{a,i}$ were optimized in each case. By choosing $N \geq 3$, both the frequency center, return-loss and the polarization specifications were met [5, 6]. According to numerical simulations, the choice of $N=3$ yields the best performance of the device. Table 3.4 reports all of the final polarizer dimensions.

Table 3.4.: *The dimensions of the elliptical section waveguide polarizer.*

W_d	7.30 mm
$E_{l,1}$	1.40 mm $\approx \lambda_g/5$
$E_{a,1}$	8.03 mm
$E_{l,2}$	3.23 mm $\approx \lambda_g/2$
$E_{a,2}$	10.67 mm
$E_{l,3}$	1.40 mm $\approx \lambda_g/5$
$E_{a,3}$	8.03 mm

The magnitude difference ΔM in dB between $\mathbf{E}_{v,o}$ and $\mathbf{E}_{h,o}$ and the differential phase shift $\Delta\phi$, corresponding to these dimensions have been computed as function of the frequency using CST Microwave Studio®. The polarizer model has been discretized by using around 20 hexahedral mesh-cells per wavelength and the performances of the polarizer have been evaluated by the time domain solver. The transmission parameters match the requirements within the band of interest. The ΔM (Fig. 3.9) is lower than 1 dB within this band. The $\Delta\phi$ (Fig. 3.10) approaches the optimal value of 90°in the center of the band of interest.
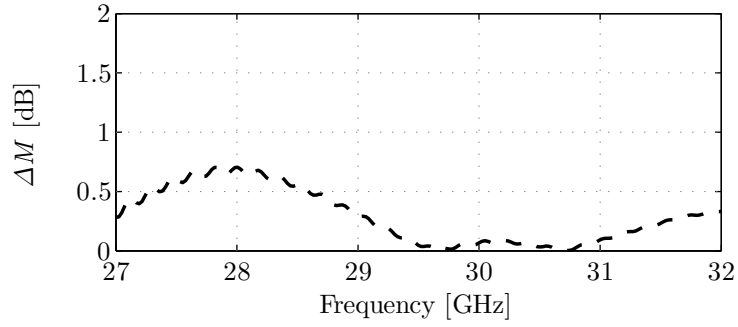
Figure 3.9.: Simulated magnitude difference between $\mathbf{E}_{h,o}$ and $\mathbf{E}_{v,o}$ for the elliptical sections waveguide polarizer.
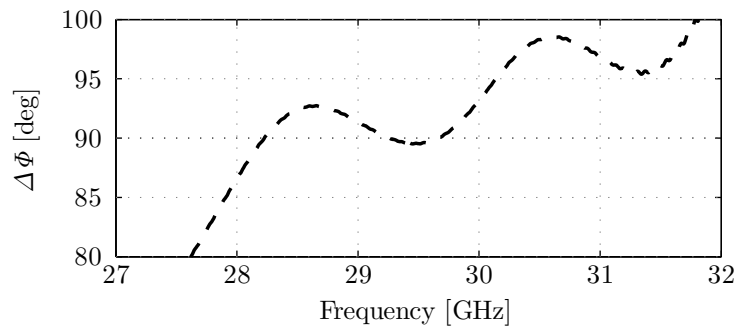
Figure 3.10.: Simulated phase shift between $\mathbf{E}_{h,o}$ and $\mathbf{E}_{v,o}$ for the elliptical sections waveguide polarizer.

3.5.2. Dielectric septum polarizer

A septum polarizer can be designed [29, 30] by placing a metallic or dielectric slab (septum) in the center plane of the waveguide where the electric fields are strongest. A typical circular polarizer with a dielectric septum is illustrated in Figure 3.11(a). The general strategy developed at the beginning of Section 3.5 can again be used here. A vertical incident field, E_i, which is inclined 45° with respect to the septum, is composed of two orthogonal components, $\mathbf{E}_h$ and $\mathbf{E}_v$. $\mathbf{E}_h$ and $\mathbf{E}_v$ have the same magnitude and phase, and are respectively parallel and perpendicular to the dielectric septum.

The two components then propagate through the septum region with little reflection due to the small septum discontinuity. In the septum region, the propagation constant of one component is strongly perturbed by the dielectric septum because the electric field line is parallel to the septum. On the other hand, propagation constant of other component is weakly perturbed because the electric-field line is perpendicular to the septum. Ideally, when the wave propagates through the septum region, $E_{h,o}$, (the horizontal component of the outgoing wave) is delayed by 90° with respect to $\mathbf{E}_{v,o}$, by passing through the polarizer, and thus the outgoing wave is circularly polarized. A right-hand circular polarization or a left-hand circular polarization is produced depending on the direction of the incident field, E_i, as illustrated in Figure 3.11.
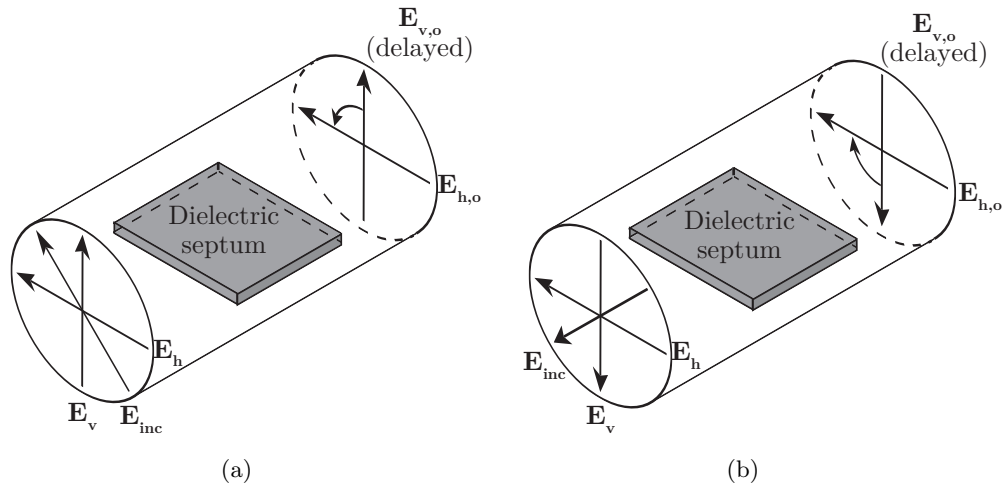
Figure 3.11.: A schematic representation of the dielectric-septum circular waveguide polarizer. (a) A left-hand circular polarization is produced after the polarizer, and (b) a right-hand circular polarization is produced after the polarizer.

To improve the impedance matching, the rectangular shaped dielectric septum of Fig. 3.11 was smoothly modified and transformed into the tapered shape shown in Fig. 3.12. The tapering at both ends of the dielectric septum was optimized for matching the impedance in

both polarization states.

CST Microwave Studio® has been used to accurately model and simulate the EM performances of the polarizer. The polarizer model (Fig. 3.13) was meshed with around 300 000 hexahedrals.
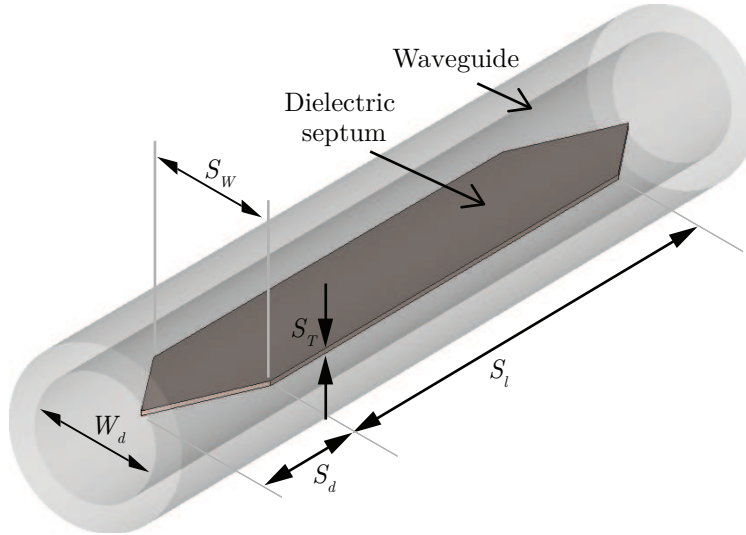
Figure 3.12.: The dielectric-septum polarizer model with the notation used for the design.
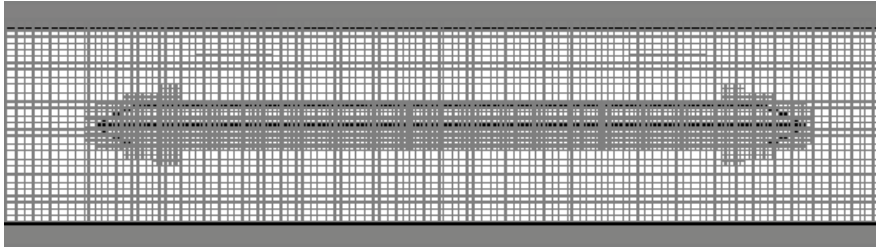
Figure 3.13.: A cross-sectional view of the waveguide feed in the polarizer proximity and its mesh.

The following dimensions remained fixed during the polarizer-optimization design process:

- the polarizer diameter, W_d;

- the septum width, S_W;

- the septum relative permittivity, ε_r;

- the septum thickness, S_T.

The obvious choice was to use the same diameter for all of the circular waveguide's sections (the central part containing the polarizer, and the end parts making the connections with the coaxial feed and with the horn). This avoided step discontinuities, and ensured a perfect surface continuity for the entire lens feed. For mechanical reasons, the septum had to touch the internal waveguide wall, so the septum width, S_W, remained constant during the design. A width $S_W = 7.20$ mm ensured good mechanical contact between septum and waveguide wall. Rogers RT5870 substrate $\varepsilon_r = 2.33$ and $\tan \delta = 0.0012$) was used to design the septum.

The relevant parameters for the optimization (see Fig. 3.12) were the dielectric septum length, S_l, and the dielectric septum end extension (taper length), S_d. The initial values and bounds of L and d were chosen according to the recommendations found in [28]. The septum length, S_l, was taken to be in the range $[\lambda/2, \lambda]$, whereas the dielectric septum end extension, S_d, was selected to be in the range $[\lambda/4, \lambda/2]$. The differential phase shift was controlled by adjusting the septum length, S_l. By optimizing S_d, both the frequency center and return-loss specifications were met. Table 3.5 reports all of the final polarizer dimensions.

Table 3.5.: *The dimensions of the polarizer.*

S_l	6.20 mm
S_d	10.67 mm
W_d	7.30 mm
S_T	1.02 mm
S_W	7.20 mm

The magnitude difference ΔM in dB between $\mathbf{E}_{v,o}$ and $\mathbf{E}_{h,o}$ and the differential phase shift $\Delta \phi$, corresponding to these dimensions, have been computed as function of the frequency using numerical simulator. The transmission parameters are very stable within the band of interest. The AR is lower than 0.4 dB within this band.
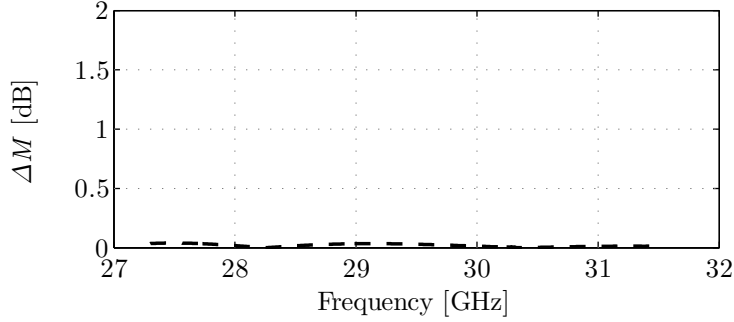
Figure 3.14.: Simulated magnitude difference between $\mathbf{E}_{h,o}$ and $\mathbf{E}_{v,o}$ for the dielectric septum polarizer.
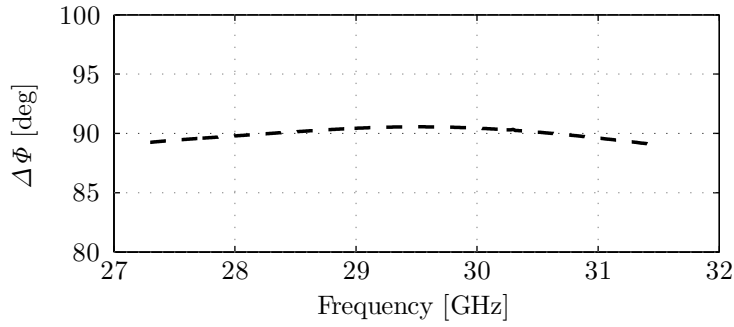
Figure 3.15.: Simulated phase shift between $\mathbf{E}_{h,o}$ and $\mathbf{E}_{v,o}$ for the dielectric septum polarizer.

3.5.3. The final choice of the internal polarizer

The choice of the polarizer type for the on-board antenna has to take into account three aspects.

Firstly, the performance of the device has to be considered. By comparing Figs. 3.9 and 3.14 with Figs.3.10 and 3.15, it is evident that dielectric septum polarizer performs better than the elliptical waveguide section polarizer. Furthermore, the performances of the septum polarizer are more stable within the band of interest.

A second important aspect to be considered is the manufacturing process of the two solutions. On one hand, the elliptical waveguide sections polarizer needs to be machined in several parts. Different strategies can be adopted to satisfy this purpose. A possible solution envisages the manufacturing of each waveguide stretch in a single piece whereas a second solution

envisages to machine the left-side of the polarizer and the right-side of the polarizer (with respect to the longitudinal plane) and assemble the different parts in a second stage. In both cases, the current distribution (see Fig 3.16) inside the polarizer would be strongly perturbed in proximity of the joined parts. This would excite secondary modes degrading the quality of the circular polarization. Furthermore, in Ka-band applications, the mechanical tolerances are crucial and an undesired misalignment among the different parts would certainly degrade the performance.

On the other hand, the septum polarizer based feed can be machined in one piece and the dielectric septum can be added afterwards. The mechanical imperfections of the septum will scarcely affect the performance of the feed since the polarizer is made by a dielectric material.

Finally, the tuning capability of the two polarizers has been considered. The elliptical waveguide section polarizer cannot be fine-tuned in the laboratory once it has been built. An eventual tuning can be performed only by re-machining the parts. This would delay the design process excessively. On the other hand, the septum polarizer can easily be tuned during the measurement campaign. If undesired effects occur, the septum polarizer can be rotated inside the feed (see picture 3.25) or easily re-machined.

After considering all these aspects, the septum based polarizer was chosen as best candidate for the on-board antenna.
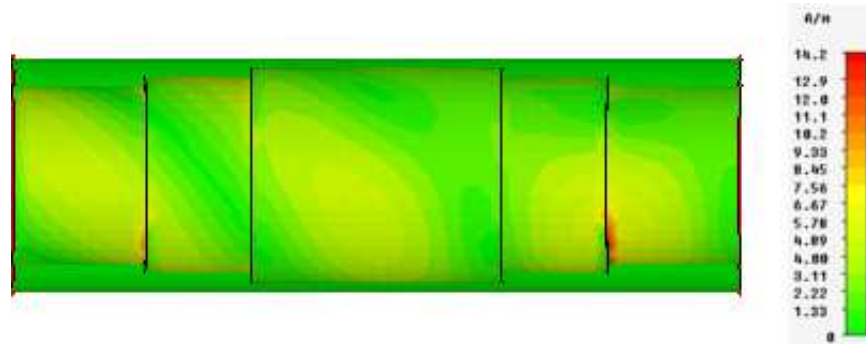
Figure 3.16.: A cross-sectional view of the elliptical waveguide polarizer. The current distribution. The current is very high in the discontinuity proximities.

3.6. Design procedure [31]

3.6.1. Complete feed design

The feed was completed by terminating the polarizer with a coaxial-to-waveguide transition (described in Section 3.4) and a small horn (see Fig. 3.17). The distance between the dielectric slab and the coaxial connector pin was optimized to improve the return loss while keeping the quality of the circular polarization. Since the polarizer was designed to work in mono-modal conditions, its distance to the coaxial pin had to be larger than $\lambda/4$, because obviously the fundamental mode TE_{11} was strongly perturbed around the coaxial pin.
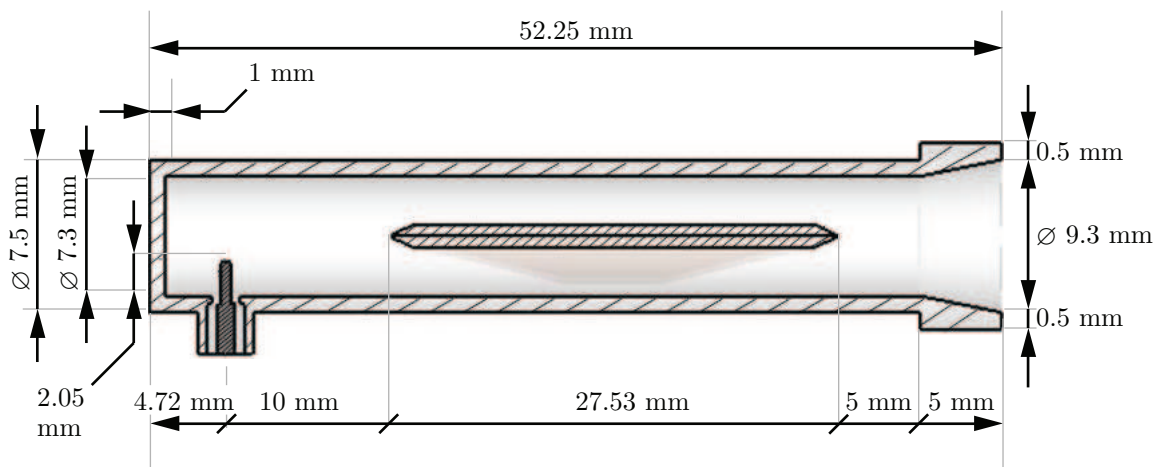
Figure 3.17.: A cross-sectional view of the feed model, and its dimensions.
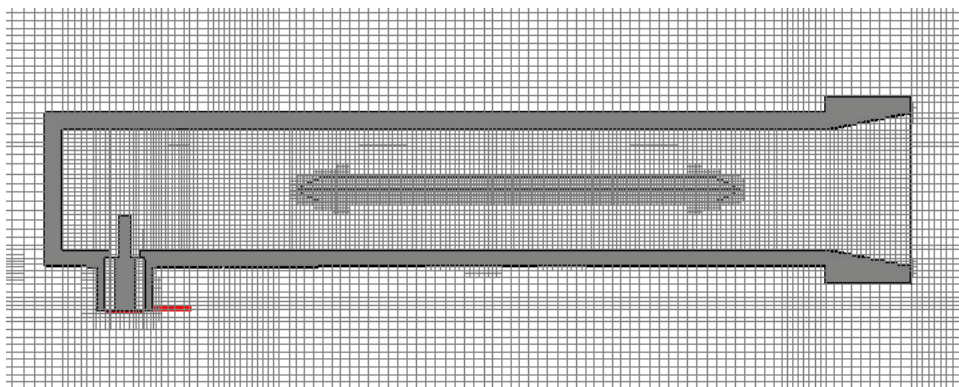
Figure 3.18.: A cross-sectional view of the feed model, and its mesh.

The aperture of the horn and its length were optimized with the Quasi-Newton algorithm

of CST Microwave Studio$^®$ to improve both the axial ratio and the reflection coefficient of the structure. With respect to the feed optimized values shown in Fig. 3.17, the magnitude difference ΔM and the differential phase shift $\Delta \phi$ between the vertical and horizontal component of the filed radiated by the feed have been computed as function of the frequency using CST$^®$. The value of the amplitude ratio ΔM (3.19) is lower than 1.5 dB within this band. The value of the differential phase shift $\Delta \phi$ (3.20) approaches the optimal value of 90° at 29.3 GHz and remain stable in the band of interest.
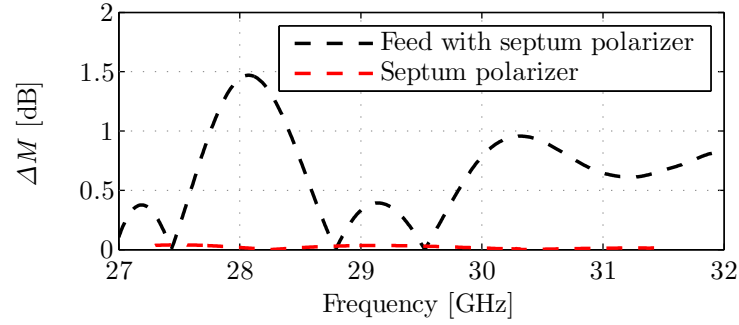
Figure 3.19.: Simulated magnitude difference between $\mathbf{E}_{h,o}$ and $\mathbf{E}_{v,o}$ for the feed
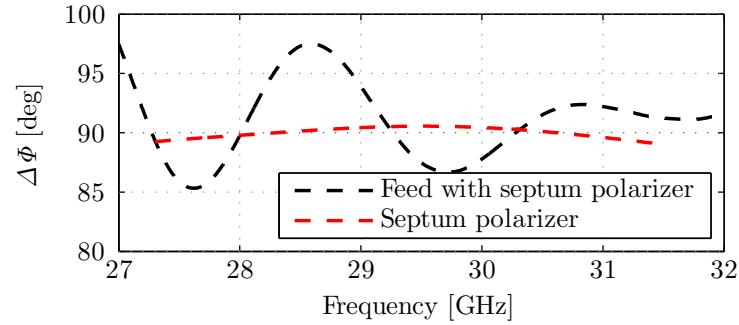
Figure 3.20.: Simulated phase difference between $\mathbf{E}_{h,o}$ and $\mathbf{E}_{v,o}$ for the feed.

A final word must be said about the feed termination. A larger aperture improves the matching between waveguide and free space, but also increases the feeds directivity. In a multi-feed scenario, large apertures would also result in restrictions concerning the angular distances between feeds. Moreover, the lens needs to be illuminated by a moderately directive primary source [24]. It was therefore not convenient to design a large, highly-directive horn aperture.

3.6.2. Homogeneous teflon lens fed by circular waveguide

To focus the radiation of the primary source designed in Section 3.3, a homogeneous Teflon spherical lens was selected. As shown in Chapter 2, spherical dielectric lenses indeed exhibit a good trade-off in performance, robustness, and ease of manufacturing.
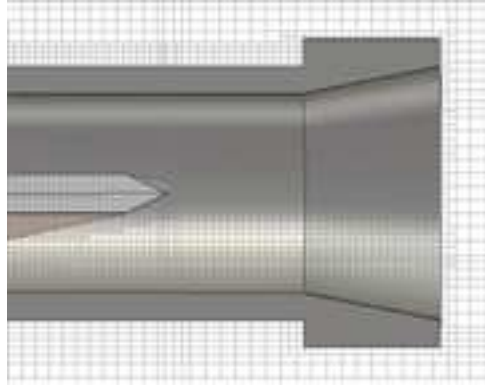
Figure 3.21.: A cross-sectional view of the feed model. The polarizer and the feed aperture have been modeled with a refined mesh.

The whole lens antenna structure was analyzed with CST Microwave Studio®. A refined mesh (see Figs. 3.21 and 3.23) was used to model the feed polarizer, in order to have enough accuracy for the circular polarization prediction, whereas a coarser mesh was used to model the homogeneous lens. The model of the whole structure (Fig. 3.24) was meshed with more than 6.2×10^6 hexahedrals, which took around 12 hours to be simulated using a 2.66 GHz quad-core CPU.

In order to efficiently design the lens antenna, the degree of complexity of the analyzed structure was increased step by step:

1. First, the waveguide aperture (horn only) was associated with the lens to roughly find the best lens diameter and the best feed-lens distance, looking at the farfield and the reflection coefficient. At this stage, only a linearly polarized source was considered.

2. The complete feed (with polarizer) and lens were then considered to compute the far field, the reflection coefficient, and the axial ratio.

3. Finally, a simplified multibeam arrangement of seven feeds and lens were simulated to determine the far field, the reflection coefficient, the axial ratio, and the coupling between feeds.

This number greatly simplifies both numerical simulations and prototype construction, while already providing all the required information about feed coupling, beam interaction and footprints on ground.

3.7. Single and multibeam operation

The lens radius, R, and the distance, F, between the center of the lens and the feed aperture, are obviously the most critical parameters influencing the beam pattern. They were optimized to find the best trade-off in maximum directivity, field of view, and the best reflection coefficient. F can be roughly approximated by the homogeneous dielectric lens focal-point distance, given by [32]:

$$F \approx \frac{nR}{2(n-1)}, \tag{3.6}$$

where n is the refractive index of the lens material ($n \approx 1.44$ for Teflon). This value was used as a starting point to speed up the numerical optimization, which finally yielded $F = 49$ mm and $R = 30$ mm as optimized values.

The complete feed and the lens were included in a global model (Fig. 3.22) that was numerically discretized. The performance of the full antenna system is described in the following sections.
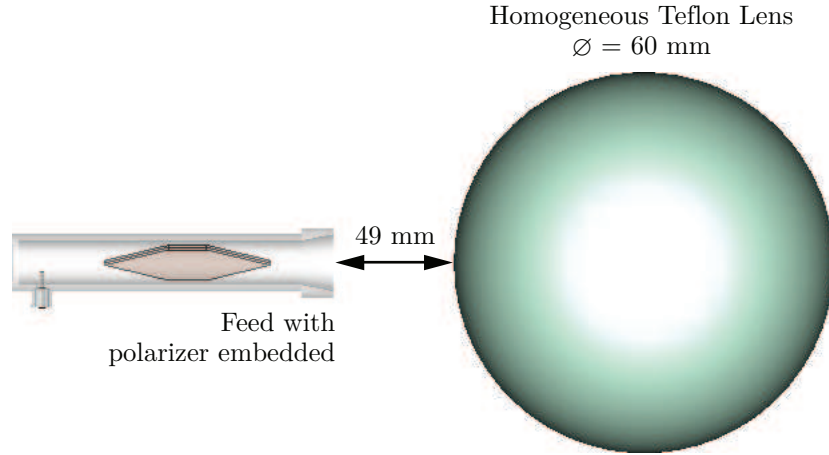
Figure 3.22.: The single-beam antenna model with relevant dimensions.

In the next step, the full multibeam antenna system was modeled by positioning seven feeds around the lens, as shown in Fig. 3.24. The angle between two adjacent beams was θ_s=12° as explained in Section 3.2. The distance between the center of the lens and each horn aperture was kept at 49 mm. The polarizers were positioned within each feed in order to radiate a right-hand-circular-polarized field.
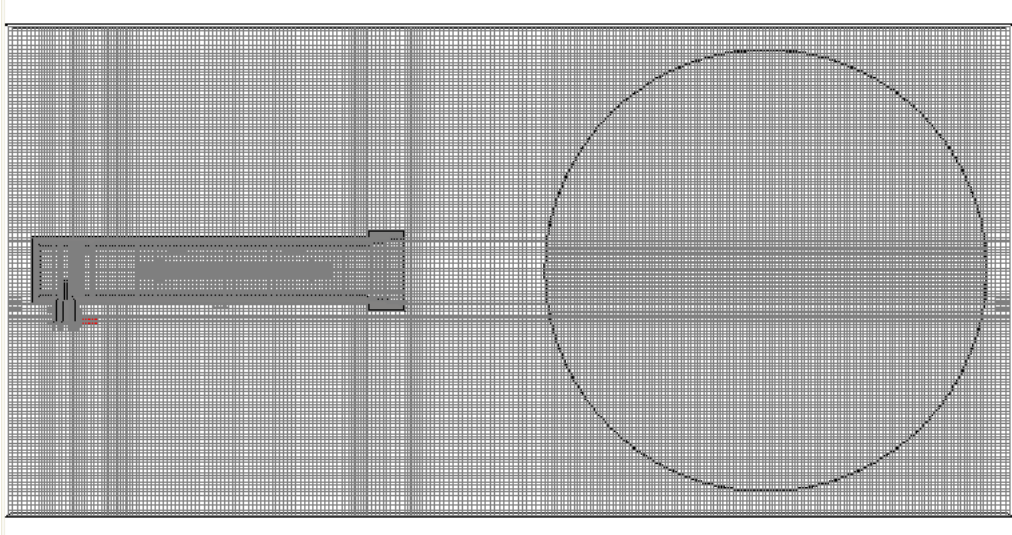
Figure 3.23.: A cross-sectional view of the lens antenna model.
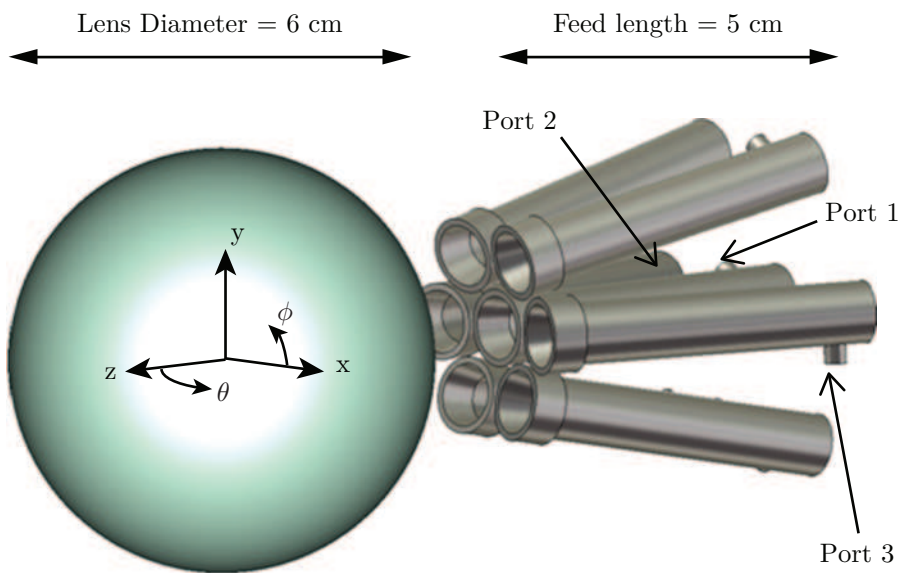
Figure 3.24.: The multibeam antenna model.

3.8. Prototypes and measurements [33]

Primary sources, dielectric polarizers, and Teflon lens were achieved by using milling-machine techniques with a nominal tolerance of 50 μm. A metal adjuster tool (Fig. 3.25) was machined to align the dielectric septum inside the waveguide before mounting the connector. Thanks to this tool, few operations were needed to change the antenna polarization. Fig. 3.26 is a picture of a single-feed prototype with a mounted coaxial connector. The dielectric-slab polarizer was inside the waveguide, and the horn shape was integrated into the inner profile of the waveguide. A plastic frame (Fig. 3.27) kept the lens and the feeds in place for anechoic-chamber measurements. The Axial Ratio (AR) has been measured using the spinning dipole method for different frequencies (between 26 and 33 GHz) and for different angles θ represented in Figs. 3.2 and 3.24 between 0° and 30°.
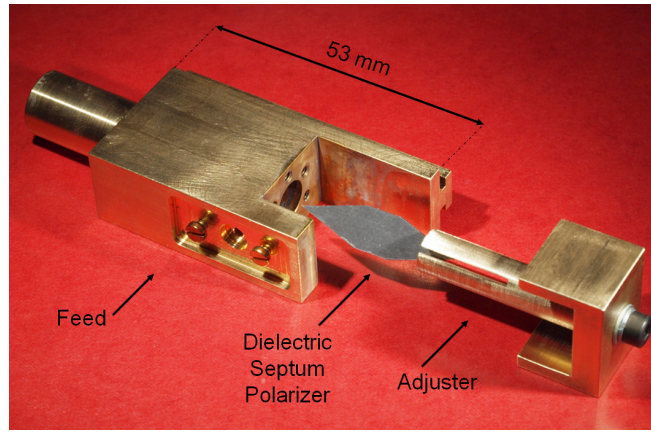
Figure 3.25.: A single feed realization: the dielectric polarizer was introduced into the waveguide structure by using a proper adjuster.

3.8.1. Feed prototype and measurements

Fig. 3.25 and 3.26 show a single feed with its septum polaizer and coaxial connector. Figures 3.28, 3.29 and 3.30 show the radiation patterns of the complete feed (no lens), and the excellent quality of the circular polarization achieved for different frequencies. The half-power beamwidth of the feed was about 60° and its radiation pattern was symmetric and stable within the frequency band of interest.
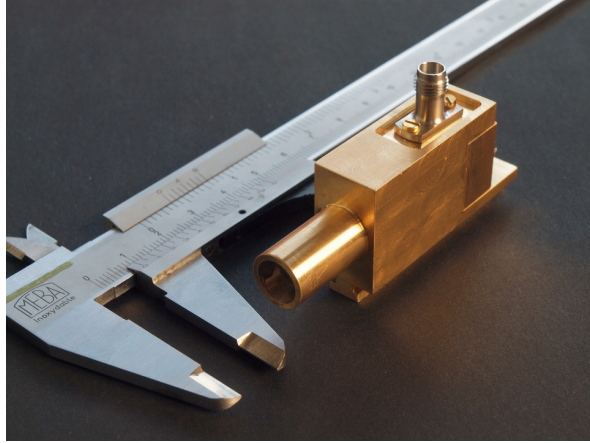
Figure 3.26.: The single feed prototype with a mounted coaxial connector: the dielectric slab polarizer was inside the waveguide, and the horn shape was integrated in the inner profile of the waveguide.
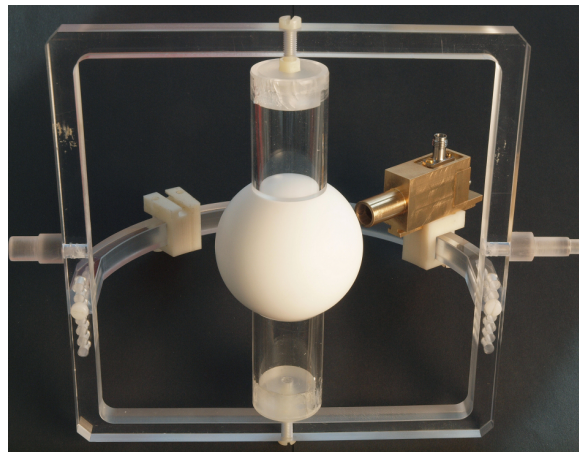
Figure 3.27.: The 60 cm diameter Teflon lens realization with the primary source.
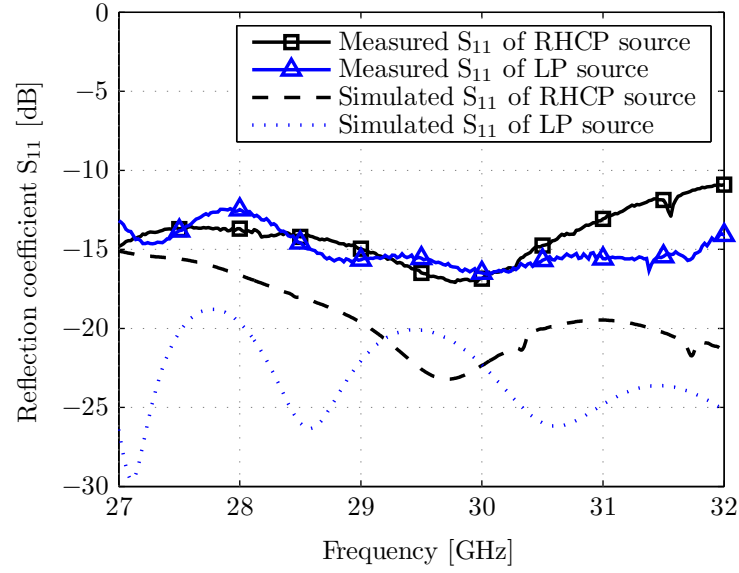
Figure 3.28.: The performance of the primary source alone. RHCP is achieved by introducing the dielectric septum inside the feed and LP is achieved without polarizer.
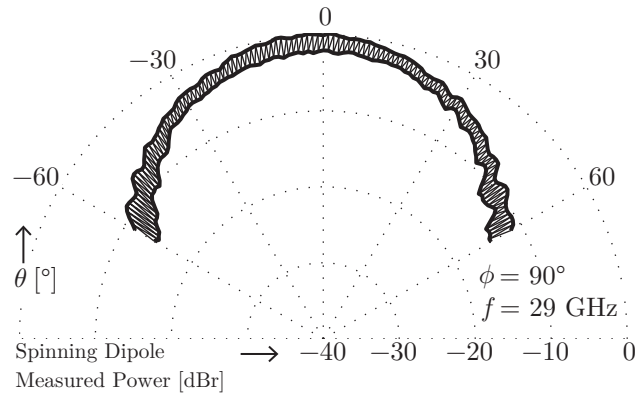
Figure 3.29.: The spinning dipole measurement of the primary source alone. The axial ratio is below 2dB within the range of θ: $-30^o \leq \theta \leq +30^o$.
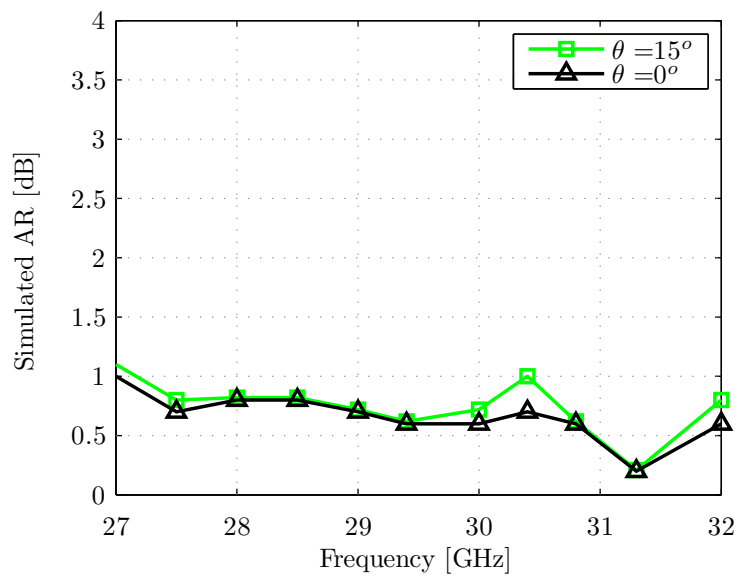
Figure 3.30.: Simulated axial ratio of the feed alone as a function of the frequency for 2 angular directions.

3.8.2. Lens antenna prototype and measurements [31, 33]

A dense mesh was used to model the feed polarizer, in order to guarantee enough accuracy for the circular-polarization prediction, whereas a coarser mesh was used to model the homogeneous lens. The model of the whole structure (Fig. 3.24) was meshed with more than 6.2×10^6 hexahedrals, which took around 12 hours to be simulated using a 2.66 GHz quad-core CPU.

The reflection coefficient was lower than -15 dB within the frequency band of interest (Fig. 3.30), and the antenna bandwidth was more than 13%. The feed worked in a mono-modal condition within 26.8 GHz and 32.5 GHz. The presence of the lens did not significantly alter the return loss of the feed.

The farfield patterns of the lens antenna are plotted in Figure 11 for frequencies of 27.5 GHz and 29.4 GHz. A directivity of 21 dB$_i$ was reached, and the main-beam half-power beamwidth was equal to $12°$ for a field of view of $13.4°$. The sidelobe level, SLL, was 18 dB. As expected, the pattern was identical for both the $\phi=0°$ and $\phi=90°$ planes. Furthermore, it was stable within the frequency band of interest. The lens increased the directivity of the feed alone by 10 dB.
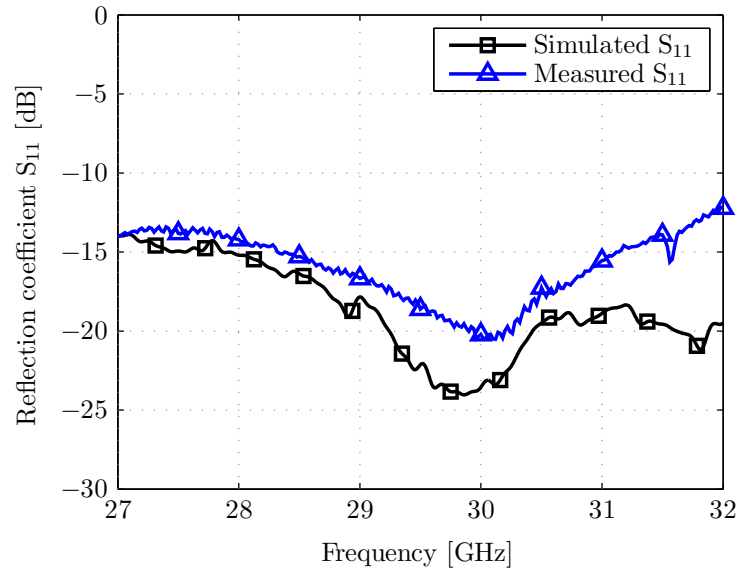
Figure 3.31.: The reflection coefficient of the lens antenna. Simulation and measurement.
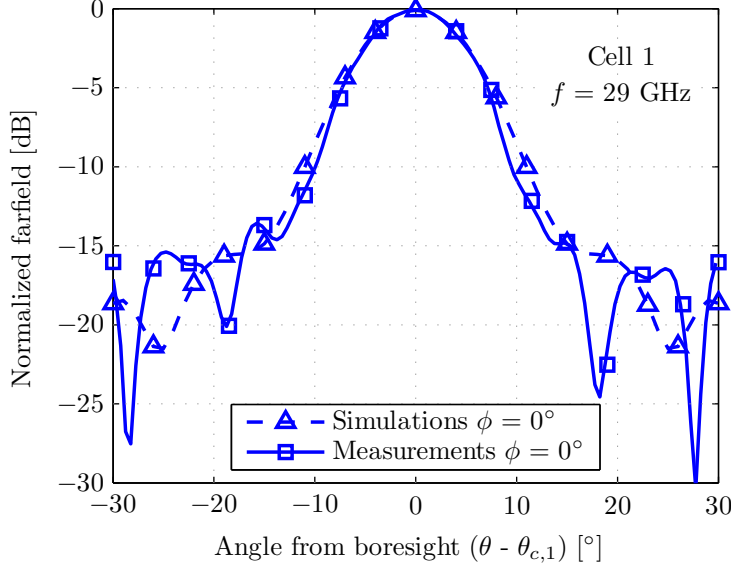
Figure 3.32.: Farfield radiation pattern of the lens fed by one primary source: comparison between simulation and measurements.

The aperture efficiency of a lens antenna is defined by [22]

$$\eta_{ap} = \frac{D}{D_{ap}}, \tag{3.7}$$

where D is the maximum directivity of the lens and D_{ap} is the directivity of a constant-field circular aperture with the same lens diameter, as recalled in Chapter 2. Since the lens directivity was computed to be 21 dB$_i$, we easily obtained an aperture efficiency given by

$$\eta_{ap} = \frac{10^{(21/10)}}{(2\pi R/\lambda)^2}, \tag{3.8}$$

Losses were not taken into account in eqn. 3.8. η_{ap} could be considered too low, but the design goal here was not to maximize the directivity, but rather to meet footprint and axial-ratio specifications. Indeed, the quality of the circular polarization is shown in Fig. 3.33 for different frequencies and for $\theta = 0°$ and $\theta = 15°$. The axial ratio of the complete antenna system (Fig. 3.22) was better than -2 dB. According to Figs. 3.30 and 3.33, the lens degraded the primary source polarization quality by only 0.8 dB in the worst case.

Simulations confirmed that the polarization of the antenna system shown in Fig. 3.22 could
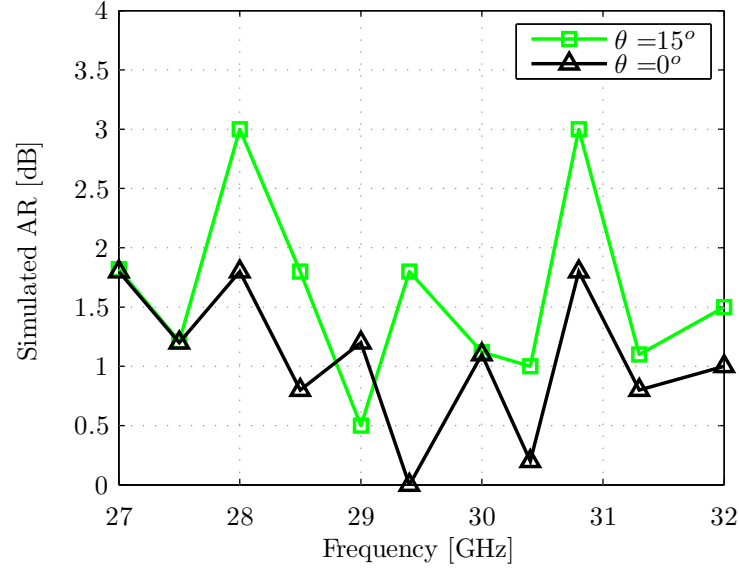
Figure 3.33.: Simulated axial ratio of the lens antenna as a function of the frequency for 2 angular directions.
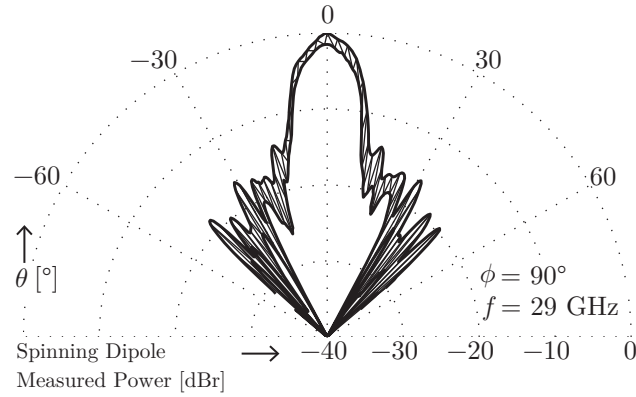
Figure 3.34.: The spinning dipole measurement of the lens antenna. The axial ratio is below 2.5dB within the range of θ: $-18^o \leq \theta \leq +18^o$.

be easily changed from right-hand circular polarization to left-hand circular polarization by rotating the polarizer septum by 90° along its major axis. The performance of the antenna for right-hand circular polarization and left-hand circular polarization was identical, as expected.
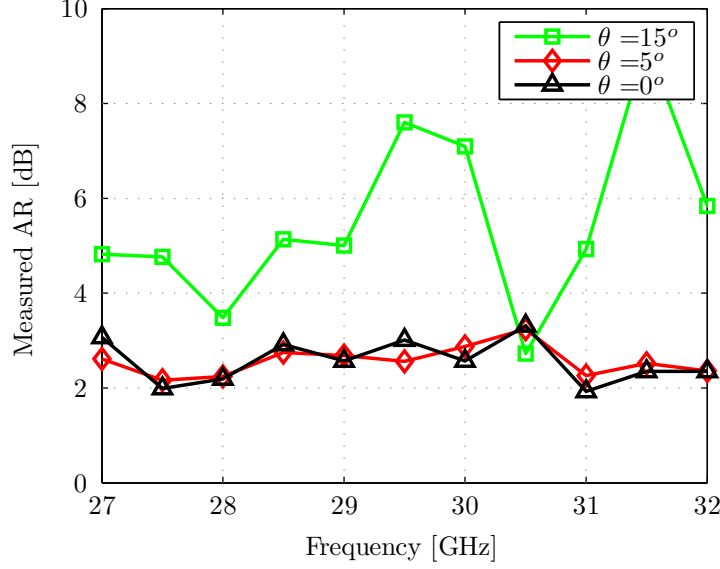
Figure 3.35.: Measured axial ratio as a function of the frequency for 3 angular directions.

With the proposed antenna, all the initial scenario specifications given in Table 3.1 were achieved. The antenna covered all the expected frequencies, and indeed showed a frequency bandwidth broader than required (19% instead of 13%). The directivity of 21 dB$_i$ gave a 2 dB margin to meet the gain requirement of 19 dB. This means that the ohmic and dielectric losses of the real antenna had to be lower than 2 dB. Both the sidelobe level and axial ratio were within the specifications.

3.8.3. Coupling between antenna feeds

The active reflection coefficient of the central feed in the presence of the other six (S_{11} in Fig. 3.37) was quite similar to that of the single-feed antenna (Figure 10). This anticipated weak coupling between feeds, and promised quite identical results for all the S_{ii} in the multi-feed simulation. Indeed, the coupling between adjacent feeds was lower than -32 dB within the working frequency band. This is shown in Fig. 3.37, where for symmetrical reasons only S_{21}, S_{23} and S_{73} are depicted. Ports 1, 2, and 3 were defined as in Figs. 3.2 and 3.24. Again, the single-beam radiation pattern (Figure 3.36) of the multibeam antenna (embedded radiation pattern) did not change significantly compared to the radiation pattern of the single-feed antenna (Fig. 3.33). Since the performance of one waveguide feed was not influenced by the presence of the others, the multibeam antenna could easily be designed focusing attention on only one feed.
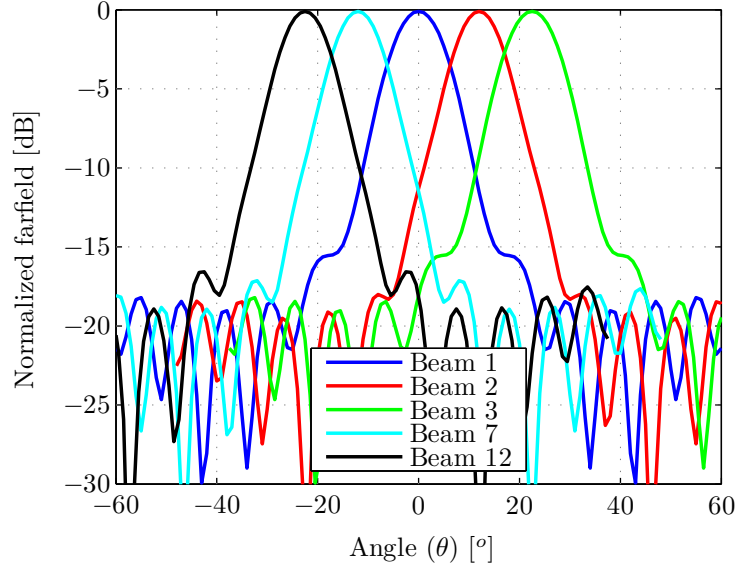
Figure 3.36.: Radiation pattern of beam 1,2,3,5,13 on the $\phi = 0^o$ plane.

Since in the proposed antenna system each radiated beam can have both right-hand circular polarization and left-hand circular polarization, depending on the position of the polarizer, the coupling between feed 1 and feed 2 (see Fig. 3.24) was compared for the two following cases:

- feeds 1 and 2 both radiated a right-hand circular polarization field;

- feed 1 radiated right-hand circular polarization and feed 2 radiated left-hand circular polarization.

Figs. 3.38 and 3.40 show that the coupling between adjacent feeds increased when the two primary sources radiated with opposite polarization. This phenomenon was probably due to partial reflections in the lens' surfaces, reversing the wave polarization. Although of minor relevance (the coupling increased from -32 dB to -25 dB at some frequencies), these considerations had to be taken into account when the performance of the cluster was evaluated.
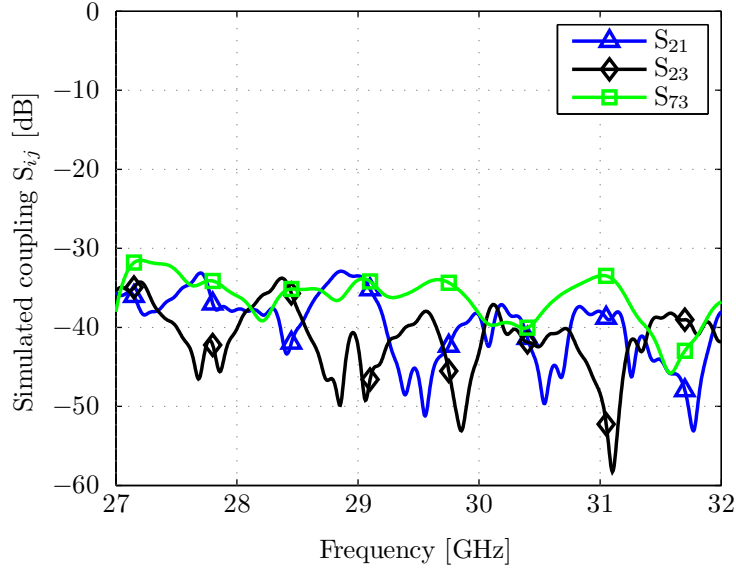
Figure 3.37.: Coupling between adjacent feeds. Most relevant cases.
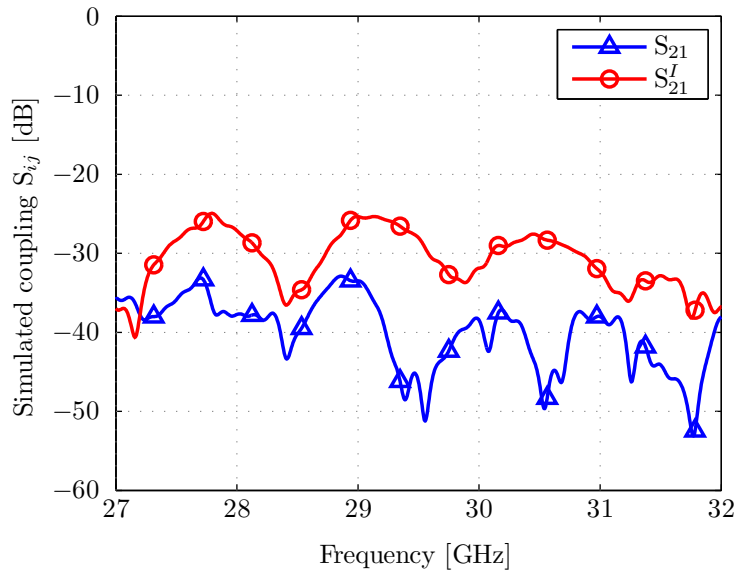
Figure 3.38.: Coupling between adjacent feeds. S_{21}^I: feed 1 radiated a right-hand circularly polarized field and feed 2 radiated a left-hand circularly polarized field. S_{21}: both feeds radiate right-hand circularly polarized fields.
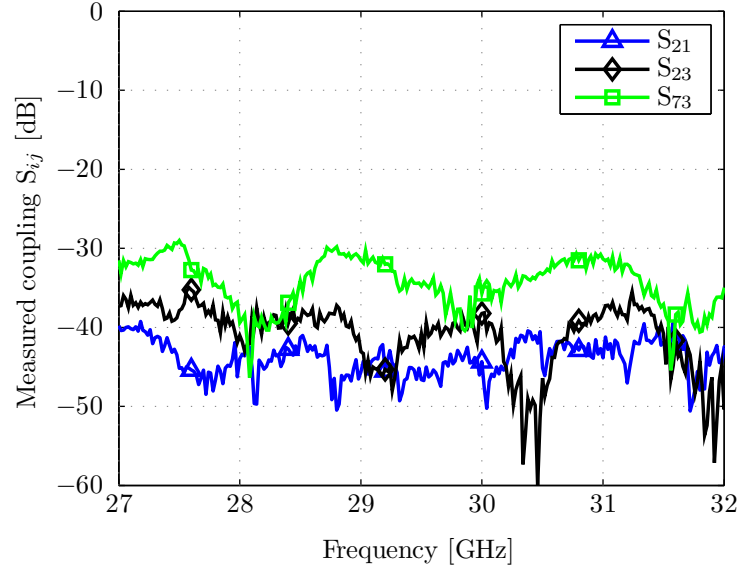
Figure 3.39.: Coupling between adjacent feeds. Most relevant cases.
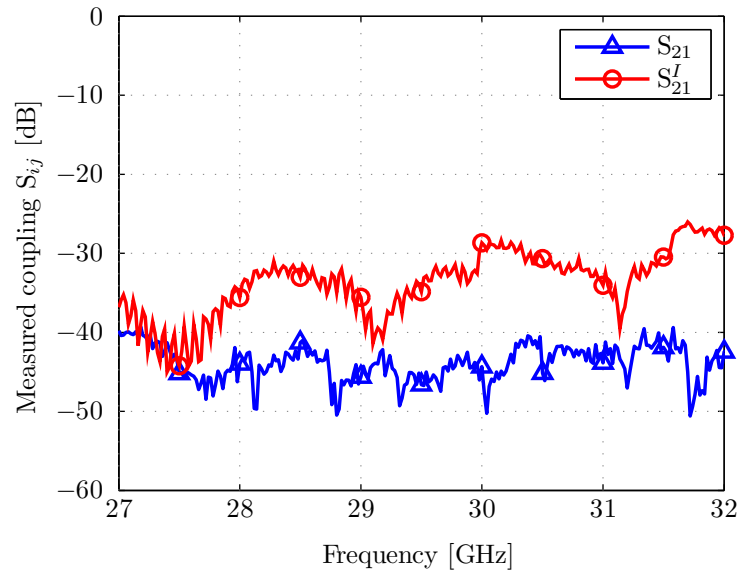
Figure 3.40.: Coupling between adjacent feeds. S_{21}^I: feed 1 radiated a right-hand circularly polarized field and feed 2 radiated a left-hand circularly polarized field. S_{21}: both feeds radiate right-hand circularly polarized fields.

3.9. Conclusion

This chapter has presented a Ka-band multibeam antenna suitable for HAPS wireless applications. A set of well-known elements (coaxial excitation, circular waveguide, septum polarizer, circular horn, and homogeneous dielectric lens) has been carefully optimized, in order to produce a functional concept, demonstrated by a *preliminary* prototype.

The antenna was based on 19 identical elementary radiators that feed a dielectric lens. Each elementary radiator consisted of a circular waveguide internally supporting a polarizer and terminated with a short horn. These elementary radiators can handle relatively high powers, while providing excellent circular polarization and a reasonable bandwidth meeting the system specifications. Moreover, computer simulations and measurements showed that the mutual coupling between adjacent elementary radiators (and hence, between adjacent beams) could be easily mastered and kept at low levels. With a relatively easy fabrication process and excellent mechanical robustness, these radiators are the best possible candidates for the antenna feed system.

To synthesize the circular polarization, two strategies have been proposed and compared. On one hand, a polarizer made of elliptical waveguide section is placed between the coaxial transition and the horn. On the other hand, a dielectric septum based polarizer is placed inside the feed. This second solution offered the best performance. The synthesized polarization is very good and the septum can easily be fine-tuned for the best working condition of the feed.

As motivated in Chapter 2, Teflon is an adequate material to build the lens. It is of relative low cost and mechanically robust. From the EM point of view, the relative dielectric constant of Teflon ($\varepsilon_r = 2.2$) allows low reflection on the lens surfaces and negligible aberration effects. The analysis of the complete antenna, including the lens, was also fully satisfatory. According to our measurements, the lens only slightly degraded (about 0.8 dB in the broadside direction, and 2 dB at 15° from the broadside direction) the good quality of the circular polarization of the feed (always below 3 dB within the aperture angle, lower than 2 dB in the main direction of the beam). The complete antenna showed excellent performances, with a symmetric radiation pattern stable across the 27 to 32 GHz frequency band. Return loss (lower than -12 dB within the working frequency band) and sidelobes (lower than -16 dB) also met the specifications. With overall dimensions of only 12 cm × 6 cm × 6 cm, this antenna concept is an excellent solution for wireless systems that require high RF power, circular polarization, high antenna gain, and multibeam behavior. With a relatively easy fabrication process and an excellent mechanical robustness, these radiators are good candidate for the antenna feed system.

This antenna subsystem thus provides a golden benchmark against which any future innovative modification must be compared.

References

[1] S. K. Rao, "Design and analysis of multiple-beam reflector antennas," *IEEE Transactions on Antennas and Propagation*, vol. 41, no. 4, pp. 53–54, Apr. 1999.

[2] J. Gavan, S. Tapuchi, and D. Grace, "Concepts and Main Applicat ions of High-Altitude-Platform Radio Relays," *Radio Science Bulletin*, no. 330, Sep. 2009.

[3] J. Thornton, D. Grace, M. Capstick, and T. Tozer, "Optimizing an array of antennas for cellular coverage from a high altitude platform," *IEEE Transactions on Wireless Communications*, vol. 2, no. 3, pp. 484–492, May 2003.

[4] D. Gray, D. Thornton, H. Tsuji, and Y. Fujinos, "Scalar Feeds for 8 Wavelength Diameter Homogeneous Lenses," *IEEE Transactions on Microwave Theory and Techniques, Charleston, USA*, 2009.

[5] M. B. Pallavicini, "Feasibility antenna Study FEASANT," *StratXX, Kaegiswil, Switzerland, Tech. Rep., 2009, Draft.*

[6] M. Letizia, "Feasibility antennas for High Altitude Platforms FEASANT," *LEMA (EPFL), Lausanne, Switzerland, Tech. Rep., Jun. 2009, Draft.*

[7] T. C. Tozer and D. Grace, "High-altitude platforms for wireless communications," *Electronics & Communication Engineering Journal*, pp. 127–137, June 2001.

[8] J. Thornton, "Properties of spherical lens antennas for high altitude platform communications," in *6th European Workshop on Mobile/Personal Satcoms and 2nd Advanced Satellite Mobile Systems (EMPS & ASMS), ESTEC, European Space Agency*, 2004.

[9] J. Thornton, D. Grace, C. Spillard, T. Konefal, and T. C. Tozer, "Broadband communications from a High-Altitude Platform - the European HeliNet programme," *IEE Electronic Communication Engineering journal*, vol. 13, pp. 138–144, Jun 2001.

[10] M. A. Mitchell, J. R. Sanford, L. E. Corey, R. A. Moore, and V. P. Pusateri, "Antenna system providing hemispherical coverage," *ICAP*, no. 89, pp. 394–398, 1989.

[11] J. Thornton, "Antenna technologies for communications services from stratospheric platforms," in *4th International air-ship convention and exhibition, Cambridge, UK, July*, 2002.

[12] J. Sanford and D. Schrank, "A Luneberg-Lens Update," *IEEE Transactions on Antennas and Propagation*, vol. 37, no. 1, pp. 76–79, Jan. 1995.

[13] J. R. Sanford, "Scattering by Spherically Stratified Microwave Lenses," *IEEE Transactions on Antennas and Propagation*, vol. 42, no. 5, pp. 690–698, May 1994.

[14] B. Fuchs, S. Palud, S. Member, L. L. Coq, and O. Lafond, "Scattering of Spherically and Hemispherically Stratified Lenses Fed by Any Real Source," *IEEE Transactions on Antennas and Propagation*, vol. 56, no. 2, pp. 450–460, Feb. 2008.

[15] W. K. Kahn, "Element efficiency: a unifying concept for array antennas," *IEEE Transactions on Antenna and Propagation*, vol. 49, no. 4, pp. 48–56, Aug. 2007.

[16] T. Ismail and M. Dawoud, "Null steering in phased arrays by controlling," *IEEE Transactions on Antenna and Propagation*, vol. 39, no. 2, pp. 1561–1566, Nov. 1991.

[17] P. Hannan, "The element-gain paradox for a phased array antenna," *IEEE Trans. Antennas Propag.*, vol. 12, no. 4, 1999.

[18] M. N. Kehn, M. V. Ivashina, and R. M. P. Kildal, "Definition of unifying decoupling efficiency of different array antennas: Case study of dense focal plane array feed for parabolic reflector," *Int. J. Electron.*, Commun. (AEU), 2009, 10.1016/j.aeue. 2009.02.011.

[19] M. V. Ivashina, M. N. Kehn, P. Kildal, and R. Maaskant, "Decoupling efficiency of a wideband vivaldi focal plane array feeding a reflector antenna," *IEEE Transactions on Antenna and Propagation*, vol. 2, no. 2, pp. 373–382.

[20] D. M. Pozar, "Microwave Engineering," *New York: John Wiley and Sons*, pp. 29-49, 208-211, 2nd Ed., 1998.

[21] N. Marcuvitz, "Waveguide Handbook," *Radiation Laboratories Series, McGraw-Hill Book Co., Inc., New York, N. Y.*, pp.28-33, 280-289, 1951.

[22] C. A. Balanis, *Antenna Theory: Analysis and Design.* John Wiley & Sons Inc., 1996.

[23] K. Chang, "Handbook of microwave and optical components," *vol. 1 Microwave passive and antenna components*, Wiley, New York, Chapitre 11, 1989.

[24] T. Cheston and E. Luoma, "Constant-K lenses," *Emerson & Cuming*, APL Technical Digest, Mar-Apr. 1963.

[25] B. Schoenlinner, X. Wu, J. Ebling, G. Eleftheriades, and G. Rebeiz, "Wide-scan spherical-lens antennas for automotive radars," *IEEE Trans. Microwave Theory Tech.*, vol. 50, no. 9, pp. 2166-2175, Sept. 2002.

[26] B. Schoenlinner and G. Rebeiz, "Compact multibeam imaging antenna for automotive radars," *IEEE Microwave Theory Tech. Symposium*, Seattle, WA, pp. 1373-1376, Jun 2002.

[27] S.-w. Wang, C.-h. Chien, C.-l. Wang, R.-b. Wu, and S. Member, "A Circular Polarizer Designed With a Dielectric Septum Loading," *IEEE Transactions on Microwave Theory and Techniques*, vol. 52, no. 7, pp. 1719–1723, 2004.

[28] T. Zhang and Y. Z., "A Ka Dual-Band Circular Waveguide Polarizer," *National Laboratory of Antennas and Microwave Technology, Xidian University, Xi'an, 710071, China (CIE).*

[29] J. Bornemann and V. Labay, "Ridge Waveguide Polarizer with Finite and Stepped-Thickness Septum," *IEEE Transactions on Microwave Theory and Techniques*, vol. 4352, pp. 1782–1787, 1995.

[30] J. Esteban and J. M. Rebollar, "Field theory cad of septum omt-polarizers," in *IEEE International Symposium on Antennas and Propagation Antennas and Propagation 2012*, 1992, pp. 2146–2149.

[31] M. Letizia, B. Fuchs, and J. R. M. A. Skrivervik, "Circularly polarized lens antenna system providing multibeam radiation pattern for HAPS," *Radio Science Bulletin*, no. 330, pp. 18-28, March 2010.

[32] B. Schoenlinner, S. Member, X. Wu, S. Member, J. P. Ebling, G. V. Eleftheriades, and G. M. Rebeiz, "Wide-Scan Spherical-Lens Antennas for Automotive Radars," *IEEE Transactions on Microwave Theory and Techniques*, vol. 50, no. 9, pp. 2166–2175, 2002.

[33] M. Letizia, J.-F. Zürcher, B. Fuchs, J. Mosig, and A. Skrivervik, "Circularly polarized lens antenna system for high altitude platforms (HAPS)," *proc. EuCAP 2011*, 5th European Conference on Antennas and Propagation, 2011.

4. Oblique incidence design of meander-line polarizers for dielectric lens antennas [*]

Contents

4.1. Introduction

†

This chapter addresses the design, prototyping and characterization of a planar multilayer meander-line (ML) polarizer for multi-beam lens antennas. In particular the three main goals of this chapter are:

1. investigate an alternative solution to polarize the beams generated by the on-board antenna. This solution consists in using a polarizer placed outside the antenna feeds, precisely behind the lens. Since, due to the antenna geometry, the wave impinging the polarizer comes from different directions, such a polarizer should be designed to operate optimally for any angle of incidence.

2. provide an effective design of this polarizer for the proposed scenario.

3. study the overall performances of the on-board antenna with this external polarizer when compared with the internal polarizer solution presented in Chapter 3.

Multilayered planar polarizers are convenient devices to transform the fields of a linearly polarized antenna into a circularly polarized wave at millimeter-wave frequencies [1–5]. A typical polarizer can be made of several stacked printed-meander-line sheets (the "grating" layer) separated by dielectric spacers. The principle of operation of this meander-line (ML) polarizer is well known [6] and results from the different action of the grating on the two orthogonal components of the incident field.

One of the useful characteristics of this type of polarizer is its independence from the antenna properties. Indeed, the polarizer may be thought an add-on that does not affect the performance parameters of the antenna [7].

The ML polarizer has been proposed in [6] and improved in [8]. Later, [9–12] gave analytical formulas to compute the phase delay and characterize the grating layer of the polarizer. Transmission line theory together with Method of Moments based algorithms have been used by [10, 13–15] to analyze the ML polarizer.

All these contributions were primarily focused on polarizers which are supposed to work with normally incident plane waves. However, it is clear from literature results [7, 13, 16, 17] that the performances of this type of polarizers gradually deteriorate for higher angles of incidence. This represents a limitation for multi-beam antenna systems in which oblique incidence is a ubiquitous situation.

---

†M. Letizia, J.-F. Zürcher, B. Fuchs, Carlos Zorraquino Gastón, Juan. R. Mosig, "Circularly Polarized Multi-Beam Lens Antenna System. Comparison Between 2 Polarizers," *proc. EuCAP 2012, 6th European Conference on Antennas and Propagation,*2012

In this chapter, we present a design approach for planar multilayered printed polarizers, intended to generate CP from a linearly polarized incident wave coming from a dielectric lens and impinging the polarizer at, possibly, an oblique angle.

After a presentation of the polarizer's working principle in Section 4.2, the method used to design the polarizer is explained in Section 4.3. Section 4.4 shows the synthesized performances of the optimized polarizers. The optimal working condition of the TL model is perturbed by including the effect of non-idealities (i.e. mechanical tolerances) in the model. This sensitivity analysis is presented in Section 4.5 whereas the performances of two prototypes are shown in Section 4.6. In Section 4.7, the septum polarizer presented in Chapter 3 is compared with the meander-line polarizer presented in this chapter. The method to design meander-line polarizers is generalized to arbitrary incidence in Section 4.8. Finally, Section 4.9 concludes and summarizes the chapter.

The original contributions of this chapter reside in the design procedure of a planar ML polarizer suitable for oblique incidence. This polarizer is intended to work as a component of an antenna subsystem including a dielectric lens antenna and Ka-band circular horns used as primary radiators. The chapter concentrates on the polarizer design since the other elements (elementary radiator, lens) have been described in Chapter 3 [18]. However, the polarizer performances are indirectly characterized through measurements of the global subsystem performances which, at the end of the day, are those of practical interest. The proposed method is inspired by [13], avoids the use of full-wave analysis to characterize the entire polarizer and it is based on the combination of Transmission Line (TL) model and unit cell full-wave analysis with periodic boundaries conditions. As a proof of concept, two prototypes are designed following the proposed procedure, built and measured. The first prototype is designed for normal incidence, whereas the second prototype is optimized for oblique incidence. The latest has been designed to work optimally for waves impinging its surface with an angle of θ_{inc}=25°, in order to satisfy the AR requirements on the boundary of the 19 cells cluster.

4.2. Meander Line (ML) polarizer

4.2.1. Working principle

The ML polarizer is a multilayer structure composed of different sections (Fig. 4.1). Each section is made by conducting meander lines which are etched on a dielectric substrate and separated by dielectric spacers.

Fig. 4.2 depicts the geometry considered here. The z-axis is defined as normal to the polarizer surface. For the sake of simplicity, we define the x-axis in such a way that the wave vector $\mathbf{k_{inc}}$ of the incident wave is located in the xz-plane. Thus, the angle of incidence θ_{inc} is customarily defined in the xz-plane as the angle between $\mathbf{k_{inc}}$ and the z-axis.

We consider now an incident wave generating an electric field $\mathbf{E_{inc}}$ along the y-axis (Fig. 4.2) and we place the metalizations in the xy-plane in such a way that the meander axes are all oriented at an angle Ψ in respect to the incident electric field. Ψ is known as the "polarizer orientation angle".

The incident electric field can now be decomposed into components parallel to the meander axes and perpendicular to it, respectively $\mathbf{E}_{||}$ and $\mathbf{E}_{\perp}$:

$$\mathbf{E_{inc}} = \mathbf{E}_{||} + \mathbf{E}_{\perp} = |\mathbf{E_{inc}}| \cos \Psi \widehat{\mathbf{e}}_{||} + |\mathbf{E_{inc}}| \sin \Psi \widehat{\mathbf{e}}_{\perp} \tag{4.1}$$

In a typical ML polarizer operation the polarizer's orientation angle takes the value $\Psi = 45°$, thus resulting in identical values for the components $\mathbf{E}_{||}$ and $\mathbf{E}_{\perp}$.

In the grating region, the propagation constant of these two components is differently perturbed by the meander-lines because the electric field line is parallel (for the $\mathbf{E}_{||}$ component) and perpendicular (for the $\mathbf{E}_{\perp}$ component) to the meander-axis. A CP wave can be obtained by designing a meander-line polarizer that introduces a differential phase shift of $90°$ between the components $\mathbf{E}_{||}$ and $\mathbf{E}_{\perp}$ while keeping their amplitudes identical [16]. A proper design will also ensure a reasonable CP axial ratio over a broad frequency bandwidth and for a wide range of incident angles [16]. Right-hand or left-hand circular polarizations can easily be obtained selecting the sign of the polarizer orientation angle Ψ ($\pm 45°$).

4.2.2. Transmission line model

The ML polarizer reacts differently to the parallel and perpendicular components of the incident field, thus it is electrically treated as a four-port device (see Fig. 4.3) in respect to these components. The grating is seen by $\mathbf{E}_{||}$ and $\mathbf{E}_{\perp}$ as, respectively, an inductive and a capacitive load [19]. Therefore, shunt admittances ($1/j\omega L_{eq}$ and $j\omega C_{eq}$) are chosen to model the grating for the two components of $\mathbf{E_{inc}}$ and transmission lines are used to model the
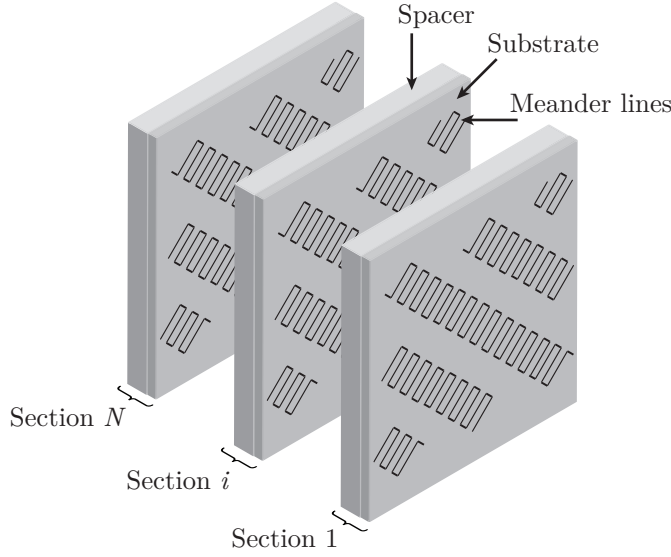
Figure 4.1.: Meander Line (ML) polarizer geometry. The polarizer is composed of N sections. For each section, the meander-line gratings are printed on dielectric substrate. The spacer separates the gratings of different sections.

dielectric materials between different gratings.

This is clearly depicted in the multiport transmission line model of Fig. 4.3, where the reference impedance for both the input and output ports is the free-space impedance $\eta_0=$ 377 Ω. The transmission line lengths $l^{(s)}$ and $l^{(d)}$ correspond, respectively, to the thicknesses of the spacer and of the dielectric layer supporting the meander lines. Snell's Law is used to compute the angle of incidence of the propagating wave in each section i of the polarizer both for the spacer (characterized by a relative permittivity $\varepsilon_{r,i}^{(s)}$) and for the dielectric substrate (characterized by a relative permittivity $\varepsilon_{r,i}^{(s)}$):

$$\sqrt{\varepsilon_{r,i}^{(s)}} \sin \theta_{inc,i}^{(s)} = \sqrt{\varepsilon_{r,i}^{(d)}} \sin \theta_{inc,i}^{(d)} = \sin \theta_{inc} \tag{4.2}$$

Since the incident field is always parallel to the dielectric surfaces of the polarizer (in all the sections and for any θ_{inc}), the propagation constants of transmission lines are given by [20]:

$$\beta_i^{(m)} = \frac{2\pi f_0 \sqrt{\varepsilon_{r,i}^{(m)}}}{c} \cos \theta_{inc,i}^{(d)}, \quad \text{for } m = \{s, d\} \tag{4.3}$$

where $m = s$ and $m = d$ indicate, respectively, the spacer and the dielectric substrate.
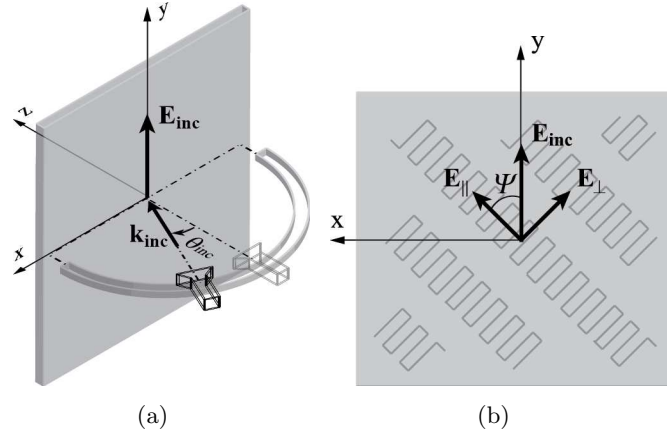
Figure 4.2.: Coordinate system. (a) θ_{inc} defines the direction of arrival of the incident wave and $\mathbf{k_{inc}}$ its pointing vector. (b) The polarizer grating and the electric field $\mathbf{E_{inc}}$ belong to the x-y plane. Ψ defines the angle between the meander-line axis and $\mathbf{E_{inc}}$ on the x-y plane.
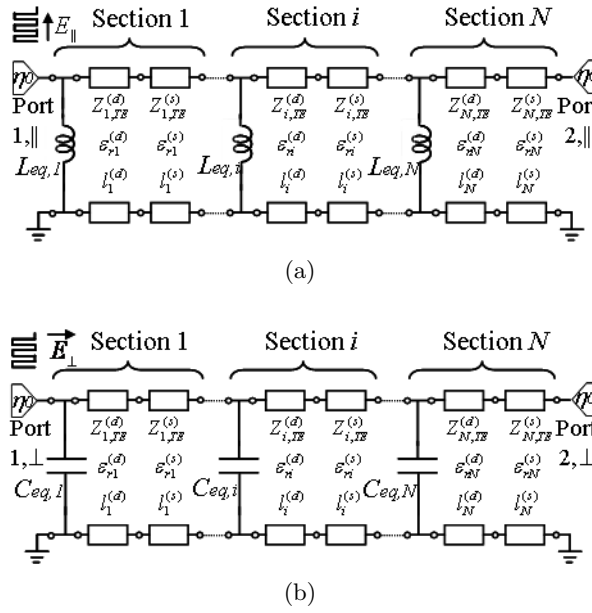
Figure 4.3.: Transmission line model of the meander-line polarizer (a) for the parallel component of the incident electric field and (b) for the perpendicular component of the incident electric field.

4.3. Polarizer design procedure

The design procedure aims to find the optimized dimensions of the polarizer. The approach for the solution of the problem is described in the flow-chart of Fig. 4.4. We first include the design input parameters (i.e. f_0, θ_{inc}, dielectric materials...) in the TL model. Then we solve this model to find the shunt components $L_{eq,i}$ and $C_{eq,i}$ which are not directly related to the input specification parameters of the polarizer. Once the TL model is properly characterized, the dimensions of the meander are optimized, for each layer, using a full-wave unit cell analysis.

4.3.1. Specifications and analyzed parameters (input parameters)

The design procedure starts by considering the relevant specifications and the input parameters that remain invariant during the polarizer design process:

- the center frequency f_0 ;

- the angle of incidence θ_{inc};

- the number of sections N of the polarizer;

- the relative permittivity and the thickness of the dielectric materials.

For the sake of clarity and without loss of generality, we consider a polarizer with $N=4$ sections, working at the central frequency $f_0 = 29$ GHz and oriented at the nominal angle $\Psi = 45°$ Since the angle Ψ and the substrate quantities are fixed before designing the polarizer, the phase shift between the components $\mathbf{E}_{||}$ and $\mathbf{E}_{\perp}$ after crossing the polarizer is the parameter that plays the most important role in controlling the polarizer optimization.

4.3.2. The transmission line analysis

The goal of the transmission line analysis is to characterize the phase shift accumulated by $\mathbf{E}_{||}$ and $\mathbf{E}_{\perp}$ during the propagation through the different sections of the polarizer, as well as their eventual amplitude mismatch.

T-matrix formulation is used to analyze the multilayered meander line structures. Each element of the two equivalent circuits is associated to its **T**-matrix. The **T**-matrix of the transmission lines of the i-th section is given by [20]:

$$\mathbf{T}_i^{(m)} = \begin{bmatrix} \cos\left(\beta_i^{(m)} l_i^{(m)}\right) & j\frac{\eta_0}{\sqrt{\varepsilon_{r,i}^{(m)}}\cos\theta_{inc,i}^{(m)}}\sin\left(\beta_i^{(m)} l_i^{(m)}\right) \\ j\frac{\sqrt{\varepsilon_{r,i}^{(m)}}\cos\theta_{inc,i}^{(m)}}{\eta_0}\sin\left(\beta_i^{(m)} l_i^{(m)}\right) & \cos\left(\beta_i^{(m)} l_i^{(m)}\right) \end{bmatrix} \quad (4.4)$$

for $m=s,d$.
The transmission matrices $\mathbf{T}_i^{\mathrm{L}}$ and $\mathbf{T}_i^{\mathrm{C}}$ of the shunt components of the i-th section are
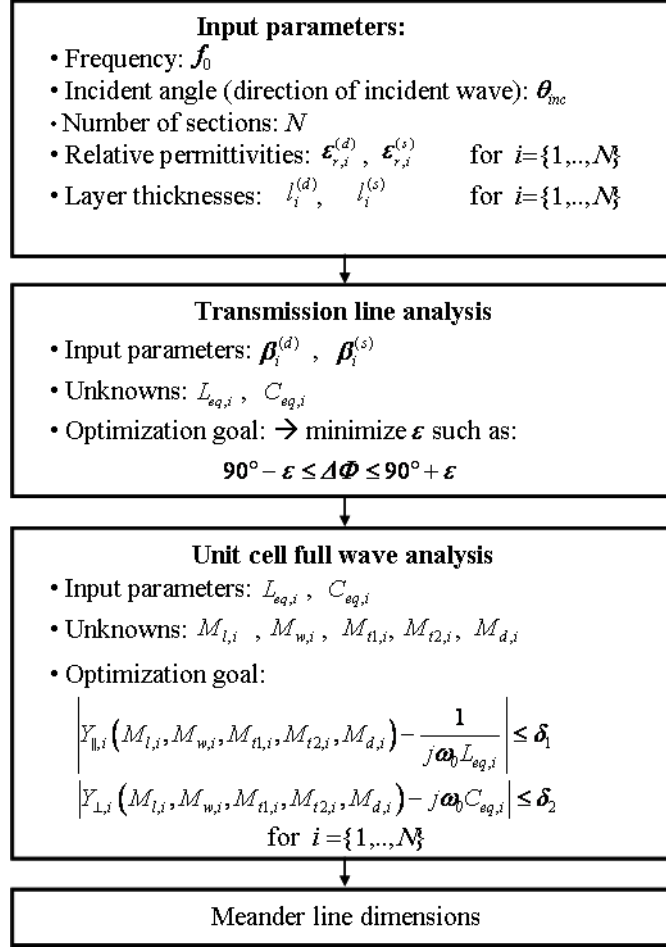
Figure 4.4.: Flow chart of the meander-line polarizer design procedure.

obviously given by:

$$\mathbf{T}_i^{\mathrm{L}} = \begin{bmatrix} 1 & 0 \\ \dfrac{1}{j\omega L_{eq,i}} & 1 \end{bmatrix} \tag{4.5}$$

$$\mathbf{T}_i^{\mathrm{C}} = \begin{bmatrix} 1 & 0 \\ j\omega C_{eq,i} & 1 \end{bmatrix} \tag{4.6}$$

By cascading the transmission matrices of each section of the equivalent circuit, we obtain the transmission matrices $\mathbf{T}_{\parallel}$ and $\mathbf{T}_{\perp}$ associated to the vertical and horizontal component respectively:

$$\mathbf{T}_{||} = \prod_{i=1}^{N=4} \mathbf{T}_i^{\mathrm{L}} \mathbf{T}_i^{\mathrm{d}} \mathbf{T}_i^{\mathrm{s}} \tag{4.7}$$

$$\mathbf{T}_{\perp} = \prod_{i=1}^{N=4} \mathbf{T}_i^{\mathrm{C}} \mathbf{T}_i^{\mathrm{d}} \mathbf{T}_i^{\mathrm{s}} \tag{4.8}$$

From these two analyses, we compute the scattering transmission parameters, $S_{21,||}$ and $S_{21,\perp}$, as explained in [20]. The differential phase shift $\Delta\Phi$ is computed as $\Delta\Phi = \angle S_{21,\perp}$ - $\angle S_{21,||}$ whereas the magnitude difference ΔM is computed as $\Delta M = |S_{21,\perp}|$ - $|S_{21,||}|$.

In this model, the shunt elements are optimized using a quasi-Newton algorithm in order to obtain a differential phase shift $\Delta\Phi$ as close as possible to $90°$.

As a final step, the AR performance of the polarizer is estimated by using transmission line theory [21] as:

$$AR = \left(\frac{\left|S_{21,||}\right|^2 + |S_{21,\perp}|^2 + \sqrt{a}}{\left|S_{21,||}\right|^2 + |S_{21,\perp}|^2 - \sqrt{a}} \right)^{\frac{1}{2}} \tag{4.9}$$

where $a = \left|S_{21,||}\right|^4 + |S_{21,\perp}|^4 + 2\left|S_{21,||}\right|^2 |S_{21,\perp}|^2 \cos\left(2\Delta\Phi\right)$

4.3.3. The unit cell full-wave analysis

The full-wave analysis of the unit cell aims to provide the physical dimensions of the meander-lines. Fig. 4.5 shows in detail the geometry of a single meander section. M_l is the meander section length and M_w the meander section width. The meander line shows two different widths M_{t1} and M_{t2} and M_d is the distance between adjacent meander-line axes. Due to the periodicity of the meander lines, the gratings are modeled by imposing periodic boundary conditions on the unit cell. This is easily implemented in modern FEM software [22]. The unit cell (Fig. 4.5) accommodates only one meander of the i-th layer. The electromagnetic source is modeled as a linearly polarized plane wave impinging on the meander inside the unit cell. The direction of the excitation is $\theta_{inc,i}$ (different for each layer according to the computed transmission line analysis). The unit cell is analyzed separately for the two components $\mathbf{E}_{||}$ and $\mathbf{E}_{\perp}$ and the admittances $Y_{||,i}$ and $Y_{\perp,i}$ are respectively computed. Both analyses need to be performed for the N sections of the polarizer.

The meander dimensions (M_l, M_w, M_{t1}, M_{t2}, M_d) are adjusted until the admittances $Y_{||,i}$ and $Y_{\perp,i}$ are close the values ($j\omega_0 C_{eq}$ and $1/j\omega_0 L_{eq}$) found in the equivalent circuit
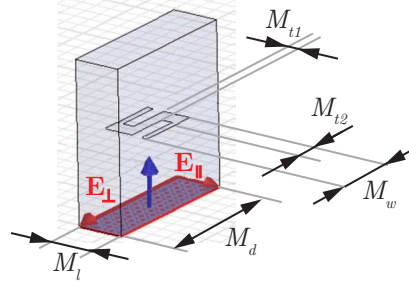
Figure 4.5.: Meander model used for the unit cell analysis. The parallel component ($\mathbf{E}_{||}$) excites the structure (The excitation is oriented along the meander-line axis). The perpendicular component ($\mathbf{E}_\perp$) excites the structure (The excitation is normal to the meander-line axis).

analysis. A quasi-Newton algorithm is used for the minimization of the absolute values of the differences between the numerically found admittances and their lumped-element counterparts until they pass below some threshold values δ_1 and δ_2 :

$$\left| Y_{||,i}\left(M_{l,i}, M_{w,i}, M_{t1,i}, M_{t2,i}, M_{d,i}\right) - \frac{1}{j\omega_0 L_{eq,i}} \right| \leq \delta_1 \tag{4.10}$$

$$\left| Y_{\perp,i}\left(M_{l,i}, M_{w,i}, M_{t1,i}, M_{t2,i}, M_{d,i}\right) - j\omega_0 C_{eq,i} \right| \leq \delta_2 \tag{4.11}$$

Although each layer of meander-line is analyzed separately for both excitations, the computational time is roughly two orders of magnitude lower than the one required for a full-wave simulation of the whole ML polarizer. The number of optimization cycles required to achieve the final design of the polarizer depends directly on the number of polarizer sections, but does not depend on the surface of the designed polarizer. The typical number of iterations for the equivalent transmission line circuit optimization is approximately 1000 while the number of iterations for the meander unit cell optimization is around 50. For the designs presented in the next section, the computer time is inferior to 1 hour using a 2.66 GHz quad-core CPU.

4.4. Synthesized polarizers

Two Ka-band ML polarizers have been designed following the proposed design procedure. One polarizer has been designed to work for normal incidence (θ_{inc}=0°), while the second one is optimized for obliquely incident plane waves (θ_{inc}=25°). This angle ensures that the radiation coming from a standard 19 horn-feeds will impinge on the polarizer with angle θ_{inc} lower than 25°. Both polarizers are composed of four sections and they are designed to operate in Ka-band (27.5-31.5 GHz). Kapton Polyimide ($\varepsilon_r = 3.2$) has been chosen as dielectric substrate because of its thin profile ($l^{(d)}$=100μm) while Rohacell ($\varepsilon_r = 1.07$ and variable $l^{(s)}$) has been chosen for the dielectric spacers.

4.4.1. ML polarizer optimized for normal incidence (θ_{inc}=0°)

The dimensions of the polarizer optimized for normal incidence are summarized in Table 4.1. The magnitude difference ΔM in dB between $\mathbf{E}_{||}$ and $\mathbf{E}_{\perp}$, the differential phase shift $\Delta\Phi$ and the axial ratio AR, corresponding to these dimensions have been computed as function of the frequency using our TL model (Fig. 4.6). The transmission parameters and the AR are very stable within the band of interest. The AR is lower than 0.4 dB within this band.

	Section 1	Section 2	Section 3	Section 4
L_{eq}[nH]	4.89	3.78	3.78	4.89
C_{eq}[fF]	3.52	6.06	6.06	3.52
M_l [mm]	0.970	1.440	1.440	0.970
M_w [mm]	1.480	1.960	1.960	1.480
M_{t1} [mm]	0.195	0.350	0.350	0.195
M_{t2} [mm]	0.140	0.470	0.470	0.140
M_d [mm]	4.385	5.455	5.455	4.385
$l^{(d)}$[mm]	0.100	0.100	0.100	0.100
$l^{(s)}$[mm]	1.700	1.350	1.350	1.700

Table 4.1.: Dimensions of polarizer designed for an incident angle θ_{inc}=0°.

4.4.2. ML polarizer optimized for oblique incidence (θ_{inc}=25°)

The dimensions of the polarizer optimized for oblique incidence are summarized in Table 4.2. Fig. 4.7 gives the results obtained for the magnitude difference between $\mathbf{E}_{||}$ and $\mathbf{E}_{\perp}$, the differential phase shift $\Delta\Phi$ and the AR as function of the frequency when these dimensions are introduced in our TL model. The transmission parameters and the AR are very stable within the band of interest and the AR is lower than 0.5 dB within this band.
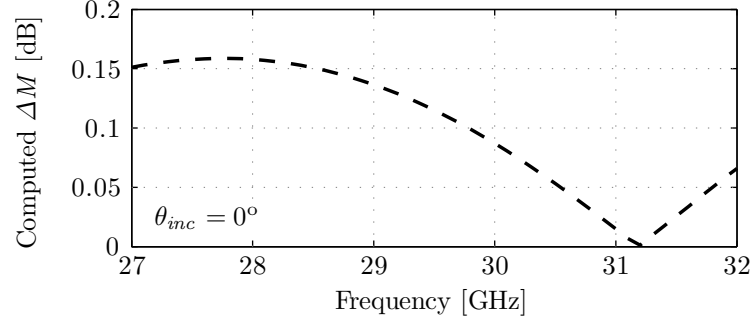
(a)
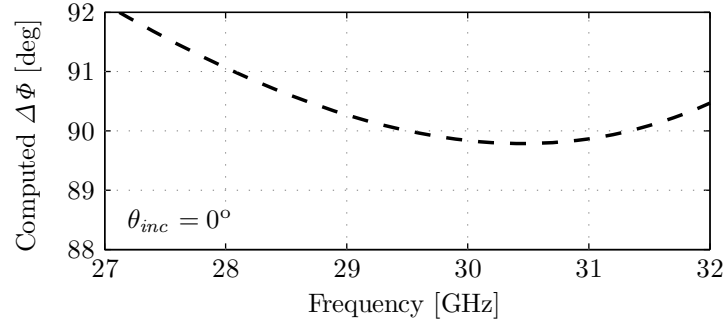
(b)
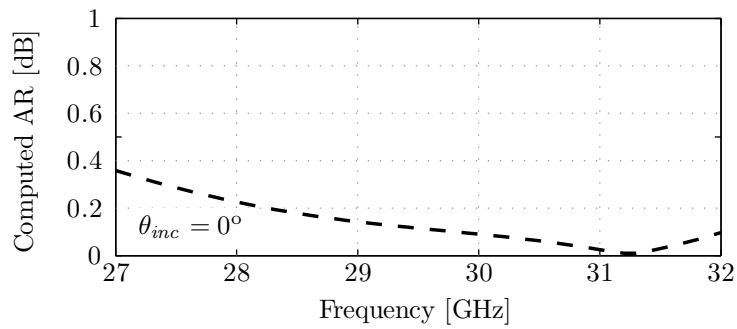
(c)

Figure 4.6.: Transmission performances of the synthesized polarizer computed by the equivalent transmission line model for θ_{inc}=0°. (a) Magnitude difference ΔM. (b) Phase shift $\Delta\Phi$. (c) Axial Ratio in dB.
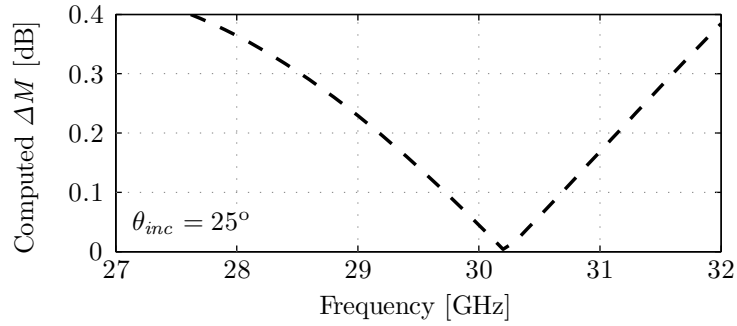
(a)
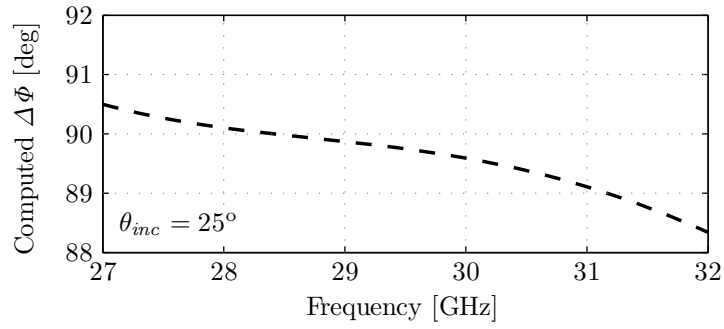
(b)
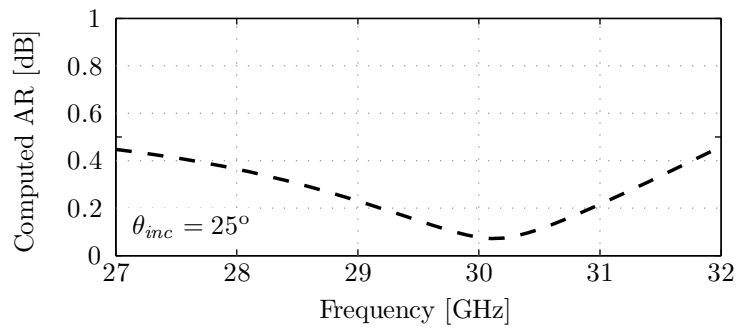
(c)

Figure 4.7.: Transmission performances of the synthesized polarizer computed by the equivalent transmission line model for θ_{inc}=25°. (a) Magnitude difference ΔM. (b) Phase shift $\Delta \Phi$. (c) Axial Ratio.

	Section 1	Section 2	Section 3	Section 4
L_{eq}[nH]	8.21	2.57	2.57	7.29
C_{eq}[fF]	5.62	3.37	3.37	5.62
M_l [mm]	1.480	1.480	1.480	1.480
M_w [mm]	2.120	1.390	1.390	2.120
M_{t1} [mm]	0.195	0.350	0.350	0.195
M_{t2} [mm]	0.140	0.465	0.465	0.140
M_d [mm]	8.070	5.300	5.300	7.800
$l^{(d)}$[mm]	0.100	0.100	0.100	0.100
$l^{(s)}$[mm]	1.700	1.350	1.350	1.700

Table 4.2.: Dimensions of polarizer designed for an incident angle θ_{inc}=25°.

4.5. Parametric studies and tolerance analysis

The goal of this Section is to show the robustness of the design method. With this purpose, a parametric study has been carried out. This parametric analysis is based on the perturbation of the optimal working condition of the TL model by including the effects on the transmission coefficients of our polarizer of: a) mechanical tolerances, b) non-purity of the linearly polarized field impinging the polarizer and c) non-perfect alignment of the incident field with respect to the meander-line axis. Furthermore, this analysis highlights the main qualitative relations between the constitutive parameters of the polarizer and its functionality.

4.5.1. Effect of mechanical tolerances

Here, the tolerances associated to the manufacturing process and the materials used for the assembly of the prototypes have been taken into account. This analysis involves both the unit cell and the TL models. The different dimensions of the meander modeled in the unit cell (Fig. 4.5) have been perturbed by a tolerance value *TOL* and the relative changes of the admittance have been monitored and included in the TL model. The AR has been computed as described in Section 4.3.2 for all the possible combinations of tolerance-affected dimensions. This results in a region in the AR vs. frequency diagram which corresponds to the predicted performance degradation of the polarizer due to a given value of the max mechanical tolerance in all the meander dimensions.

For a realistic value of TOL= ± 50 μm, Fig. 4.8 shows such a tolerance region depicted as a gray area where lower bound is the computed AR curve when using optimized nominal values for the meander dimensions. As it can easily be seen, the worst combination of dimensions with tolerances below 50 μm (upper boundary of the gray area) results in an AR degradation lower

than 1dB in the full frequency band. For the sake of simplicity, Fig. 4.8 only shows results for normal incidence. A similar degradation has been observed in the prototype optimized for oblique incidence.
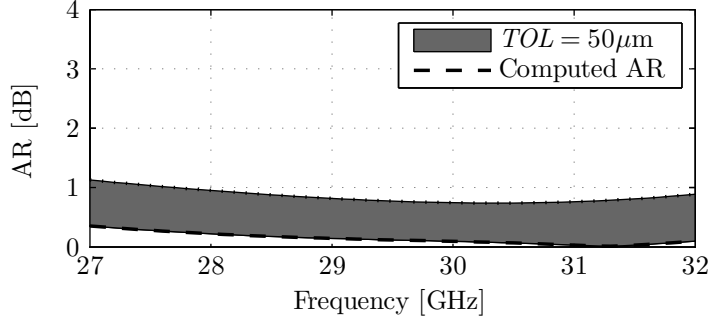
Figure 4.8.: Effect of mechanical tolerances on the Axial Ratio.

4.5.2. Effect of an imperfect linear polarization of the impinging field

Usually, polarizers are designed and optimized assuming a pure linearly polarized incident wave. Obviously, a more realistic scenario must consider an elliptically (quasi-linear) polarized incident wave, that will result in a degradation of the circular polarization emerging after the polarizer.

This effect can be modeled by adding a differential attenuation α_{LP} and a differential phase shift Φ_{LP} to one arm of the TL model, as depicted in Fig. 4.9. These two parameters are linked to the parallel $\mathbf{E}_{0,||}$ and perpendicular $\mathbf{E}_{0,\perp}$, components of the incident wave field by:

$$\alpha_{LP} = \frac{\left|\mathbf{E}_{0,||}\right|}{\left|\mathbf{E}_{0,\perp}\right|} \tag{4.12}$$

$$\Phi_{LP} = \angle\mathbf{E}_{0,||} - \angle\mathbf{E}_{0,\perp} \tag{4.13}$$

and are connected to the axial ratio of the incident wave AR_0 by the expression [21]:

$$AR_0 = \left(\frac{\alpha_{LP}^2 + 1 + \sqrt{\alpha_{LP}^4 + 2\alpha_{LP}^2 \cos\left(2\Phi_{LP}\right) + 1}}{\alpha_{LP}^2 + 1 - \sqrt{\alpha_{LP}^4 + 2\alpha_{LP}^2 \cos\left(2\Phi_{LP}\right) + 1}}\right)^{\frac{1}{2}} \tag{4.14}$$

Now, the scattering parameters of the modified model in Fig. 4.9 can be obtained and from them, the perturbed axial ratio AR of the field after the polarizer can be computed using (4.9).
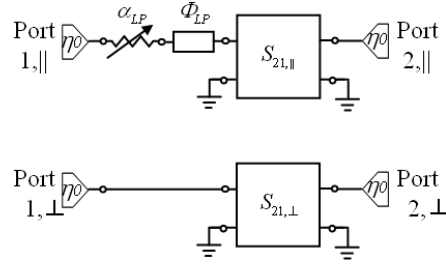
Figure 4.9.: Sensitivity analysis setup scheme. The purity of the linearly polarized incident wave is perturbated by adding a differential attenuation and a differential phase shift to the equivalent model of the polarizer.

As it could be expected, the ML polarizer is quite sensitive to the quality of the linear polarization of the incident wave. Figs. 4.10 and 4.11 refer to its performance when designed for normal incidence. For an initial linear polarized wave with AR_0 worse than 35dB, the circular polarization quality of the wave after the polarizer is unacceptable (AR>3dB). A similar degradation has been noted in the case of the polarizer optimized for oblique incidence.
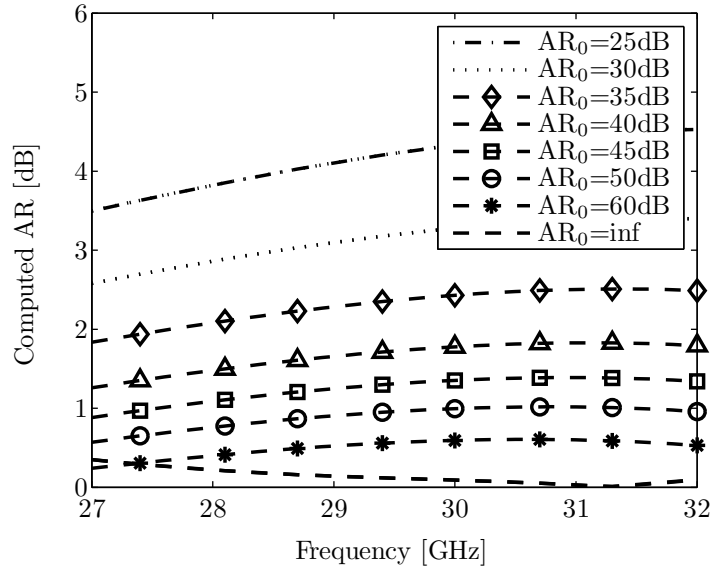
Figure 4.10.: Axial Ratio degradation computed for different AR_0.
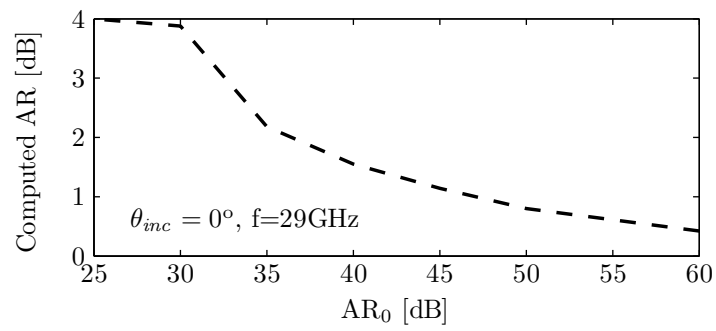
Figure 4.11.: Axial Ratio after the polarizer computed for different AR_0 at 29 GHz.

4.5.3. Effect of angular misalignment between the linearly polarized wave and the meander-line axis

The ML polarizer is obviously optimized for an incident field arriving at an angle Ψ=45°. The effect of an angular misalignment $\Delta\Psi$ of the linearly polarized source with the meander-line axis (see Fig. 4.2(b)) can degrade the polarization of the wave after the polarizer. This effect can also be easily quantified with our TL model by adding a differential attenuation α_{LP} such that:

$$\alpha_{LP} = \frac{\left|\mathbf{E_{0,\parallel}}\right|}{\left|\mathbf{E_{0,\perp}}\right|} = \tan\left(\Psi + \Delta\Psi\right) \tag{4.15}$$

The scheme shown in Fig. 4.9 can still be used in this section, keeping Φ=0 and introducing a value for α_{LP} given by eqn. (4.15).

Figs. 4.12 and 4.13 show the effect of the tilt $\Delta\Psi$ on the polarizer optimized for normal incidence. As it can be seen, the degradation is practically frequency independent and amounts approximately to 0.3 dB of AR deterioration for each degree of tilt. The same degradation is noted in the oblique incidence polarizer and when the tilt is directly applied to the linearly polarized horn.
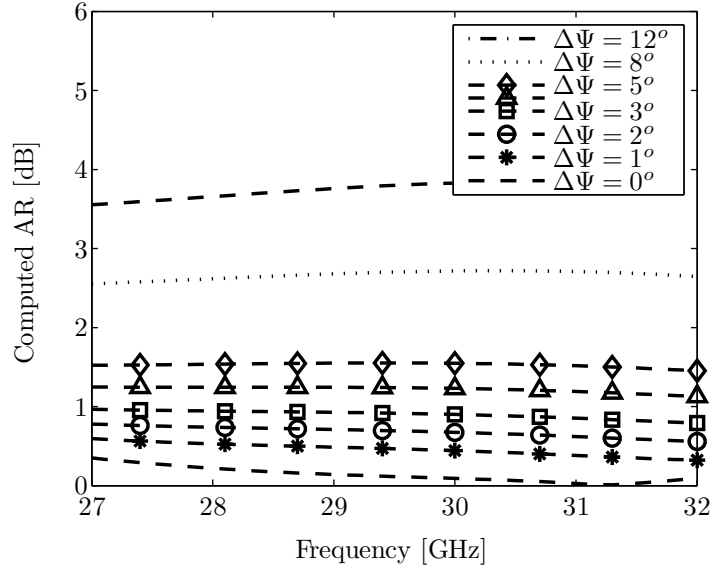
Figure 4.12.: Axial ratio degradation computed for different angular misalignments.
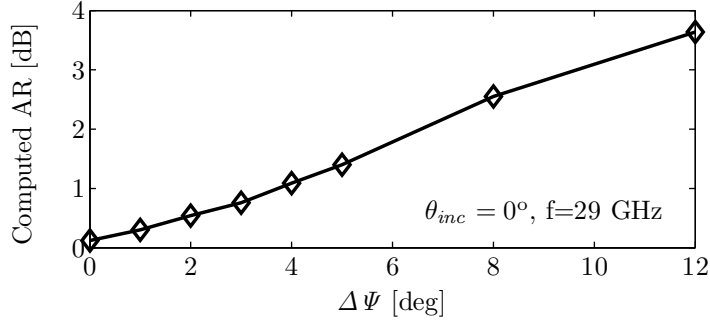
Figure 4.13.: Ratio degradation computed for different angular misalignments at 29 GHz.

4.5.4. Generalizing the sensitivity analyses

The previous parametric studies show that the proposed model is very well suited to perform a general sensitivity analysis, since it can predict the effect of any physical parameter with very low computational effort. Moreover, due to the linearity of the used models, the three effects studied and additional ones can easily be combined to predict the sensitivity of the polarizer performance to any combination of tolerances. This is done in the next section to ascertain the validity of tolerance-prone measurements.

4.6. Prototypes characterization

Two ML polarizers have been manufactured (see Figs. 4.14, 4.15, 4.17 and 4.18) following the proposed design procedure. Their dimensions are given in Table 4.1 and 4.2. The overall dimensions of the manufactured polarizers are $250 \times 250 \times 6$ mm and the metalization thickness used for realizing the printed meander lines is 0.1 mm.

The performance of the polarizers has been characterized in the anechoic chamber, through measurements of the AR using the spinning dipole technique. The antenna subsystem includes a linearly polarized horn and a 60 mm diameter Teflon lens which generates the linearly polarized plane wave on the polarizer surface [18, 23]. The ML polarizer under test is shown in Fig. 4.19. This measurement setup (see Fig. 4.20) ensures the test feasibility for beams impinging the polarizer surface within an angle range $-50° \leq \theta_{inc} \leq +50°$.
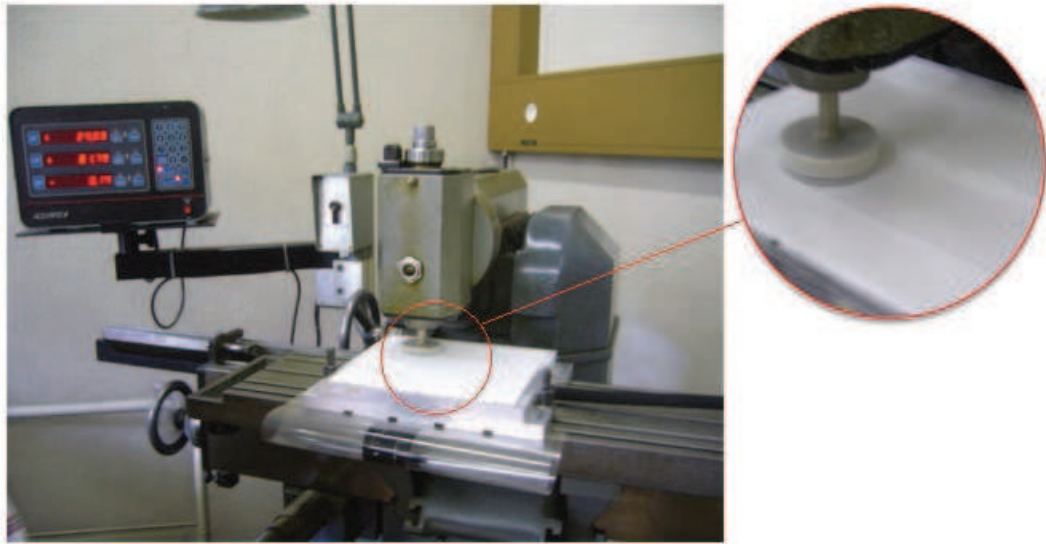
Figure 4.14.: Spacers milling process.

| (a) | (b) |
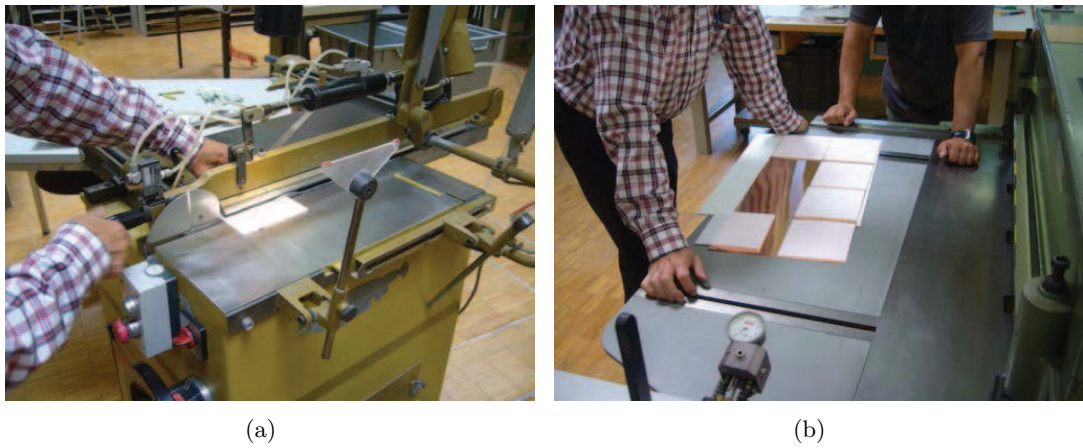
Figure 4.15.: Preparation of the foam spacers.(a) The foam spacers are cut and (b) prepared to be stacked.

(a) (b)
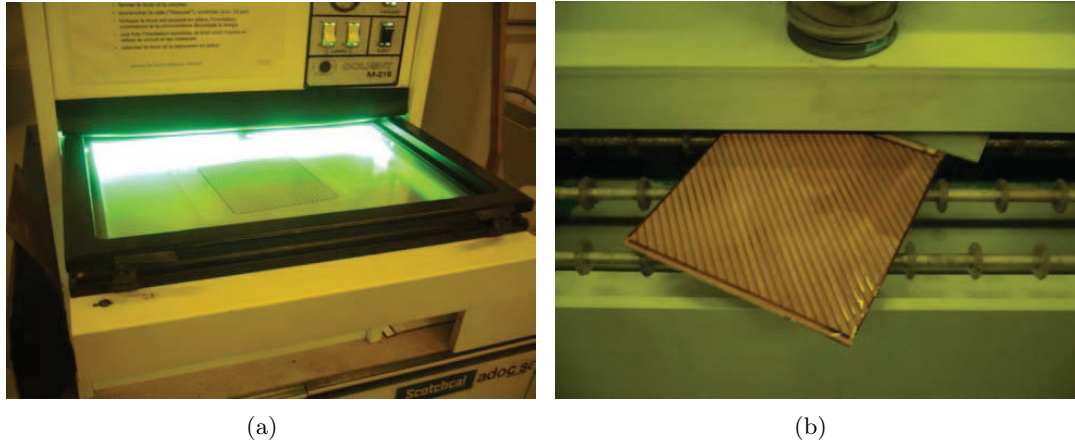
Figure 4.16.: Photo-etching process of the MLP. (a) Light exposure. (b) Acid development.

(a) (b)

Figure 4.17.: Assembling process. The different parts (a) have been aligned and glued (b). An aluminum clump has been manufactured for this purpose.

(a)   (b)
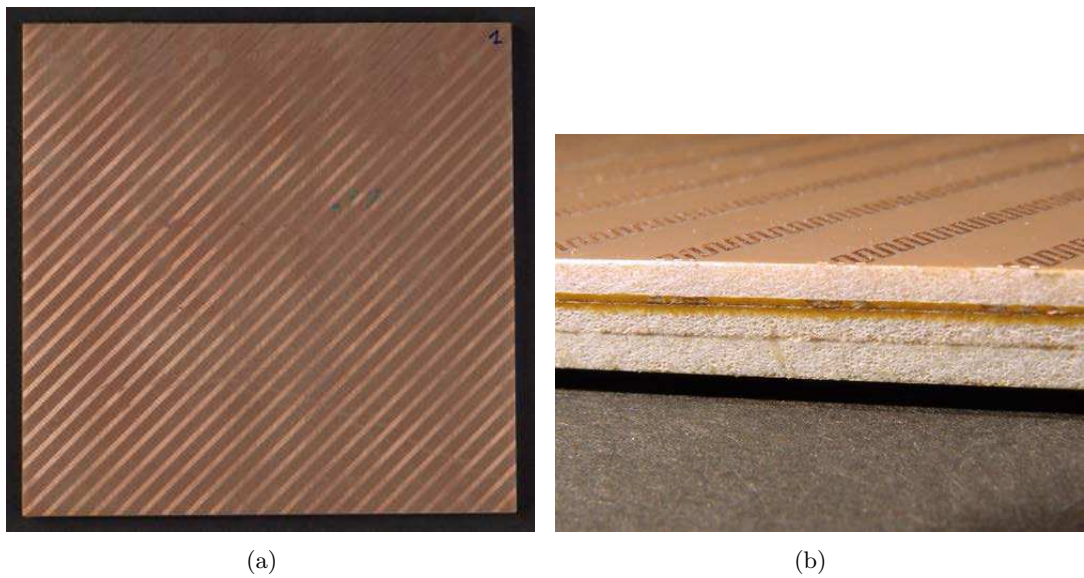
Figure 4.18.: Final prototype. Front view of (a) the meander-line polarizer and (b) details of the printed meanders.

(a) (b)
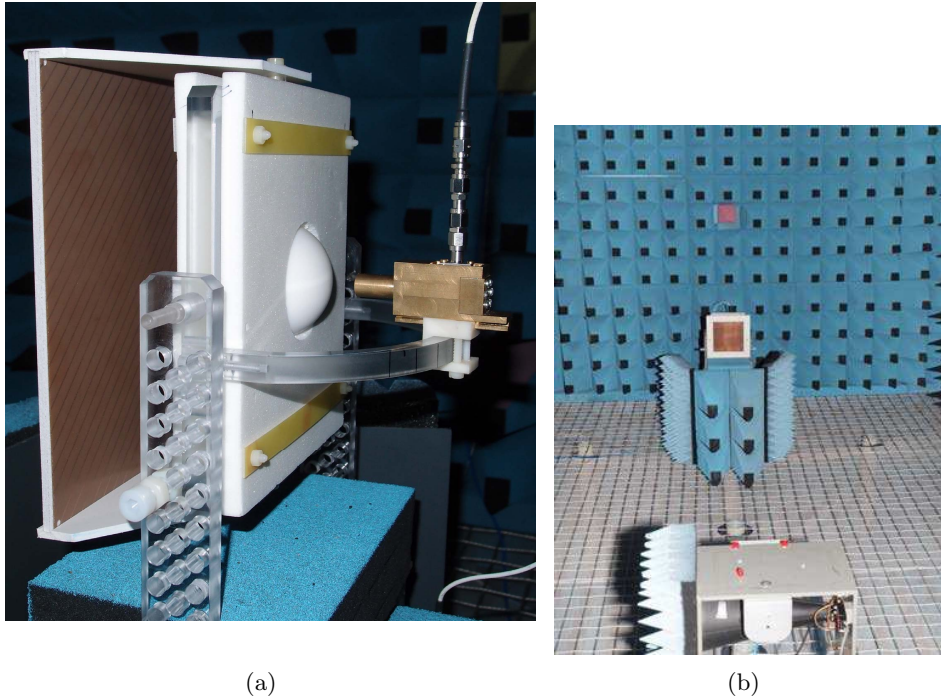
Figure 4.19.: Measurement setup.(a) Measurement setup with polarizer mounted beyond the lens. (b) The polarizer in the anechoic chamber.
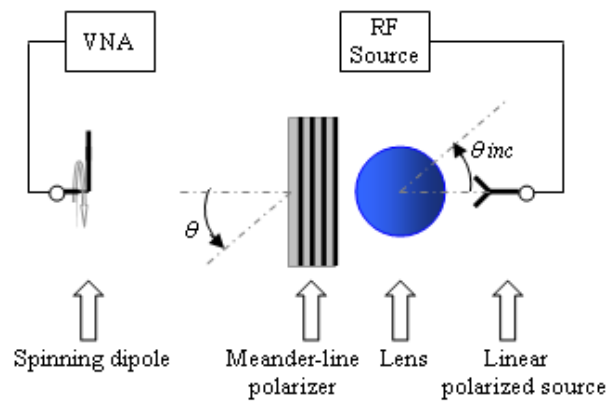
Figure 4.20.: Measurement setup scheme. A plane wave is created by illuminating a dielectric homogeneous Teflon lens with a linearly polarized horn. The polarizer changes the polarization of the lens outgoing wave. The polarization quality is measured by spinning dipole technique in the anechoic chamber.

4.6.1. Measurements of the polarizer optimized for normal incidence (θ_{inc}=0°)

Fig. 4.21 compares predicted and measured AR values for the polarizer optimized for normal incidence. In addition to the theoretical AR lower limit, a more realistic predicted range, combining three possible sources of error ($\Delta\Psi = 1°$, $AR_0 = 45$dB and $TOL = 50\mu$m), has been depicted. According to these numerical results, AR should remain around 2 dB within the design frequency band (27-32 GHz). Measurements are sensibly within the region predicted by the model and AR is always better than 3 dB, showing a trend to improve at higher frequencies.

The AR has also been measured for two different incident angles (θ_{inc}=0°and 12°) as function of the polar angle θ at frequency $f_0 = 29$ GHz. Fig. 4.22 shows that for normal incidence, the AR remains better than 2 dB within the range -12°$\leq \theta - \theta_{inc} \leq$ +12°. For a higher incidence angle ($\theta_{inc} \geq$12°) the AR still remains centered around the broadside direction $\theta = \theta_{inc}$ but its average value is higher (slightly above 3dB) and also deteriorates quickly outside the range -12°$\leq \theta - \theta_{inc} \leq$ +12°.

Indeed, a study at a fixed frequency f_0=29 GHz and in the broadside direction ($\theta=\theta_{inc}$) as a function of the planar-wave incident angle θ_{inc}, is given in Fig. 4.23. The measured polarization quality is very good for normal incidence (θ_{inc}= 0°) but deteriorates quickly when the incident angle θ_{inc} increases. The AR crosses the 3 dB line at around θ_{inc}= 12°. This clearly shows the need to redesign the polarizer for specific oblique incidence angles.
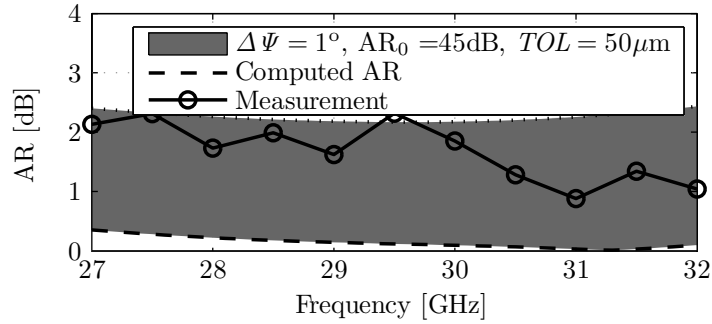
Figure 4.21.: Axial Ratio computed for $\Delta\Psi$=1°, AR_0=45dB. The region in gray includes the performance degradation due to mechanical tolerances.
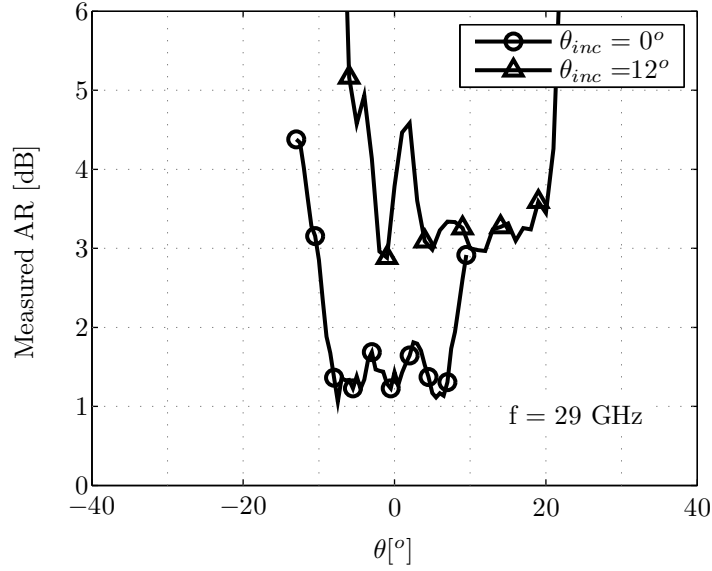
Figure 4.22.: Measured Axial Ratio of meander-line polarizer designed for normally incident plane wave. The direction of the incoming wave is θ_{inc}= 0° and θ_{inc}= 12°.
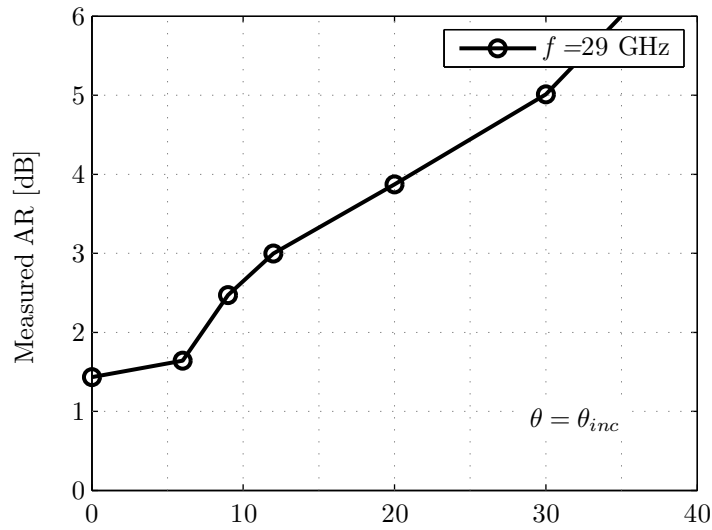
Figure 4.23.: Measured Axial Ratio of the meander-line polarizer designed for normally incident plane wave. The performances of the polarization quality degrade increasing θ_{inc}. The Axial Ratio becomes unacceptable for $\theta_{inc} \geq 12°$ and this justifies the design of a different polarizer for obliquely incident plane wave.

4.6.2. Measurements of the polarizer optimized for oblique incidence (θ_{inc}=25°)

When the polarizer is specifically designed for an oblique incidence angle, a measured value of the AR lower than 3 dB is recovered within the full 28-31.5 GHz band (Fig. 4.24). Again, the measured values are within the tolerance range corresponding to the combination ($\Delta\Psi$=1°, AR$_0$ =45dB and TOL =50μm).

In Fig. 4.25, the AR has been measured for different incident angles (0°$\leq \theta_{inc} \leq$40°) at two different frequencies, 29 and 31 GHz. The AR behavior remains centered broadside and acceptable in the range of -12°$\leq \theta - \theta_{inc} \leq$ +12°.

In Fig. 4.26, the planar-wave incident angle θ_{inc} is varied, while keeping the measurements in the broadside direction ($\theta=\theta_{inc}$). The incidence angle sweep has been performed at two frequencies 29 and 31 GHz. Results show that the oblique design is clearly successful, allowing to improve the AR performances for a large range of oblique incident angles (12°$\leq \theta_{inc} \leq$ 30°), while showing only a very minor reduction of the frequency band (28-31.5 GHz). This validates the proposed one-step design procedure even though additional improvements are still possible through fine tuning and further iterations.
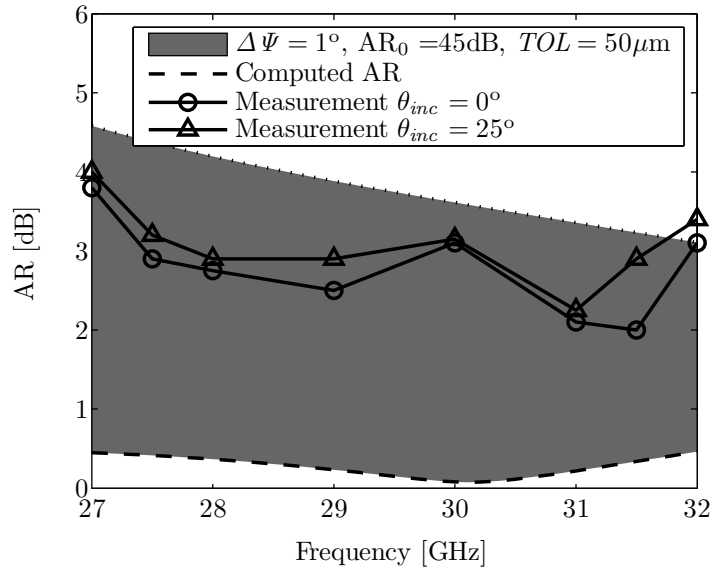
Figure 4.24.: Axial Ratio computed for $\Delta\Psi$=1°, AR$_0$ =45dB. The region in gray includes the performance degradation due to mechanical tolerances.

4.6.3. Towards a more precise design

It is expected that an even better agreement between the computed and the measured AR could be obtained if several improvements are introduced in both the mathematical model and the measurement procedures. On the modeling side, the obvious improvements would be:

- The meander-lines are assumed to be infinitely thin in the TL model. This typically produces a frequency shift of the predicted electrical response [24].

- The mutual coupling between the $\mathbf{E}_{||}$ and $\mathbf{E}_{\perp}$ components into the polarizer has not been included in the TL model. For waves with oblique incident angle, this coupling effect is more pronounced.

- The presence of higher order modes between the polarizer layers has not been included in this analysis. Although those modes are evanescent, they contribute to increase the insertion losses differently for the $\mathbf{E}_{||}$ and $\mathbf{E}_{\perp}$ components, influencing the performances of the whole polarizer. For waves with oblique incident angle, this effect is more pronounced.

- Obviously, more accurate results could be obtained if a full-wave model is used, including coupling between parallel and perpendicular polarizations and the effect of higher order modes [25–29]. However, computer time for complete analysis using full-wave models is prohibitive and partial implementation done at normal incidence shows no significant change from TL predictions. Moreover, the dispersion due to tolerances as shown in figures 4.21 and 4.24 is certainly larger than the discrepancies between the two models.

Measurements could also be improved if the following effects are mitigated or fully eliminated:

- The ML polarizer surface is not infinite and the effect of the plated edges impacts on the quality of the measured AR. An absorbing frame could be introduced.

- The incident wave on the ML polarizer is not uniform. A homogeneous Teflon lens ($\oslash$=60mm$\approx 6\lambda_0$) is used to generate the plane-wave and its measured gain is 20 dB in Ka-band [30–33]. A higher gain lens might improve the uniformity of the plane wave impinging into the polarizer. Furthermore, the quality of the plane wave is influenced by the distance between lens and polarizer. Ideally, the polarizer should be in the lens far-field. But it must be close enough to be seen by the lens as having very large transverse dimensions and reduce diffraction edge effect. So in practice a trade-off has to be made.

- The manufacturing tolerances of the prototyped polarizer and the undesired misalignments between horn, lens, polarizer and receiver should be reduced as much as possible.
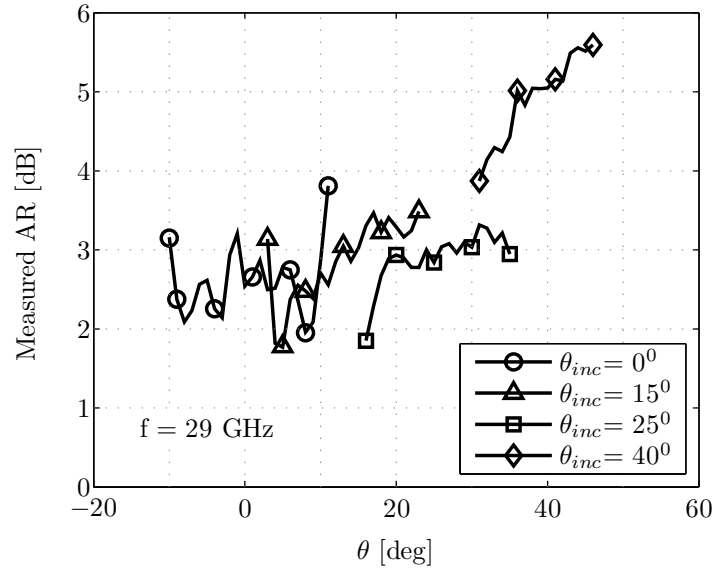
(a)
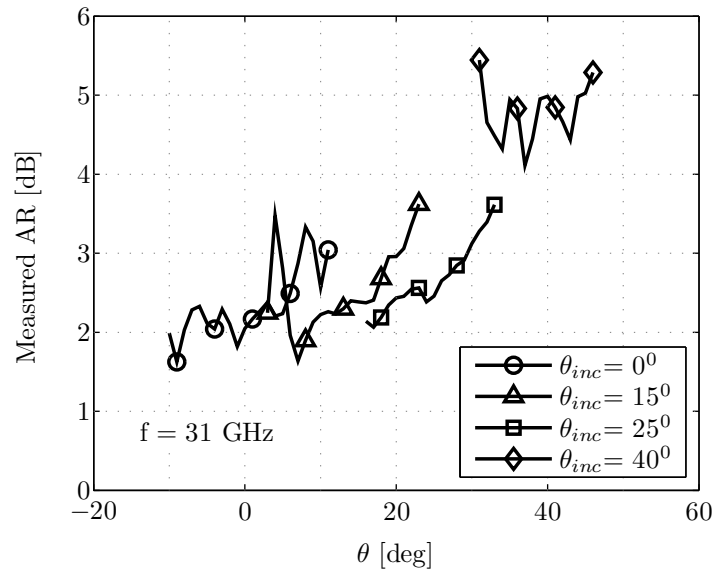
(b)

Figure 4.25.: Measured Axial Ratio of meander-line polarizer designed for obliquely incident plane
wave. The polarizer works for oblique angles of incidence. (a) at 29 GHz. (b) 31 GHz.
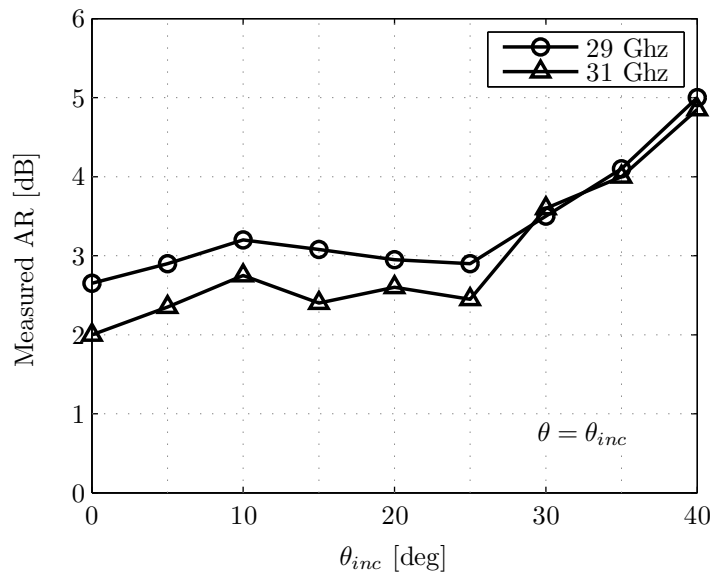
Figure 4.26.: Measured Axial Ratio of meander-line polarizer designed for obliquely incident plane wave. The Axial Ratio becomes unacceptable for $\theta_{inc} \geq 30°$.

4.7. Comparison between septum (internal) polarizer and meander-line (external) polarizer

Internal polarizer

With the internal polarizer designed in Chapter 3, the AR is lower than 3 dB in the broadside direction (θ_{inc}=0°) for all measured frequencies. Moreover, it remains acceptable within the range -10°$\leq \theta \leq$10°(see Fig. 4.27). For symmetry reasons, the radiation performances of this antenna do not depend on the angle of the main beam θ_{inc}. Hence, this polarizer can be used both for 7, 19 and 121 cells scenarios without introducing any degradation on the AR performances of the external cells.

Consequentially, the internal polarizer can be considered a benchmark against which any other polarizer design must be compared.

External polarizer

The obvious initial idea when using an external polarizer, the one developed in this chapter, is to optimize it for normal incidence $\theta_{inc} = 0°$. Then, a quite good AR (better than 2 dB) is found as expected in the broadside direction. The AR remains acceptable within the range -10°$\leq \theta \leq$10°, but it quickly degrades when the beam tilt angle θ_{inc} increases and it is higher than 3 dB for $|\theta_{inc}| \leq 10°$. Hence, this meander line polarizer, due to its limited range of operation, cannot satisfy the AR requirements of the beam directed to the boundary of the cluster (cell 3,4,10-19).

This motivated the investigation of an external polarizer tailored for an oblique angle of incidence. For instance, we can optimize the external polarizer for an angle (θ_{inc}=25°), which largely covers the operation angle of a 19-beam antenna. The good news is that not only the AR is lower than 3 dB in the broadside direction (θ_{inc}=25°) but it also remains acceptable within the range -10°$\leq \theta \leq$10°(see Fig. 4.28). However, the AR quickly degrades, when the beam tilt angle θ_{inc} increases and it is already higher than 3 dB for $|\theta_{inc}| \leq 28°$.

4.7.1. Comparison and final assessment [34, 35]

The above considerations fully demonstrate that an external polarizer is a perfectly acceptable solution in scenario up to 19 beams. External polarizers are simpler to built than internal ones and use low cost materials. In addition, a unique polarizer works for all the beams and fine tuning can easily be applied. The internal polarizer cannot compete in these aspects and moreover, most lenses behave better under linear polarization, while a CP wave can easily deteriorate when traversing a complex lens (the horizontal and vertical components of the field exibit different propagation inside a stratified lens yelding a degradation of the polarization quality beyond the lens). However, external polarizers suffer several drawbacks. First of all, mechanical constraints could simply prevent their use. Then, despite all the sophisticated optimization tools, it is hard to extend their validity to the larger angle required by scenarios with a larger number of beams (i.e. 121). The external polarizer should be then realized with

still more layers to have a chance to obtain a decent operation at all possible incidence angle and within the requested bandwidth. Last but not least, the incidence problem becomes truly 3D one (ϕ=0°) and the effect of beams impinging the polarizer at arbitrary direction (θ, ϕ) should be evaluated carefully.
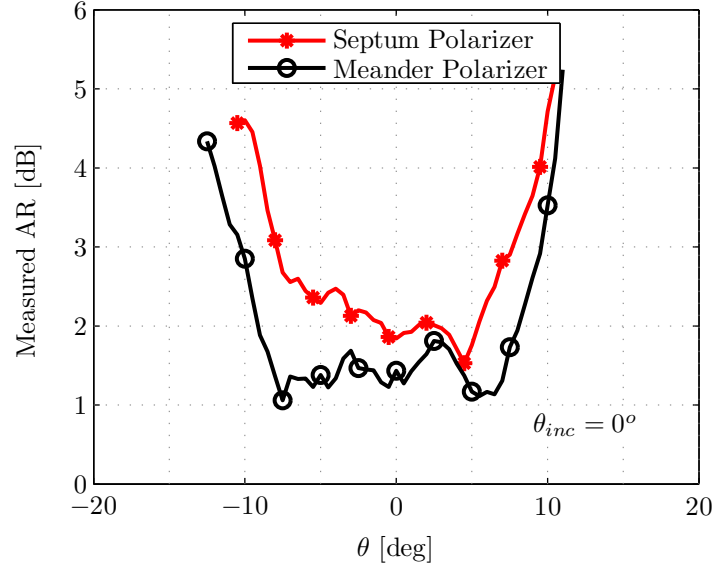
(a)
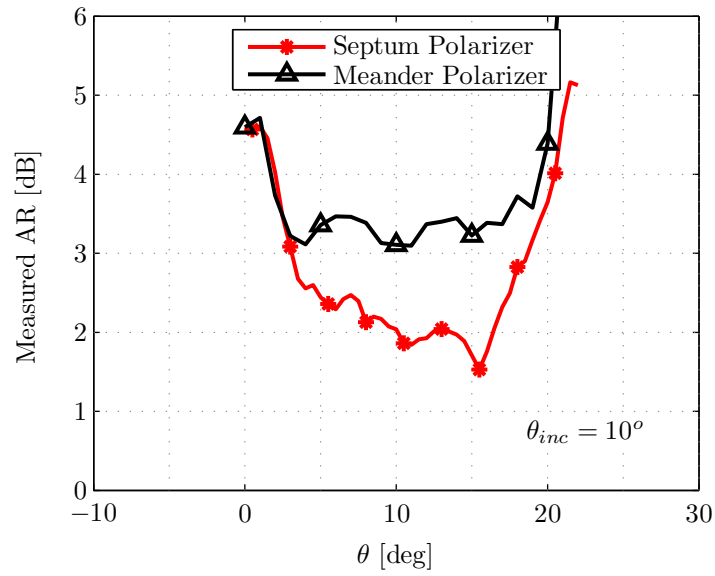
(b)

Figure 4.27.: Axial ratio measured at 29 GHz. Polarizer optimized for orthogonal incidence. Comparison between internal septum and external meander polarizers for two different incident angles θ_{inc}. (a) $\theta_{inc} =0°$. (b) $\theta_{inc} =10°$

(a)

(b)
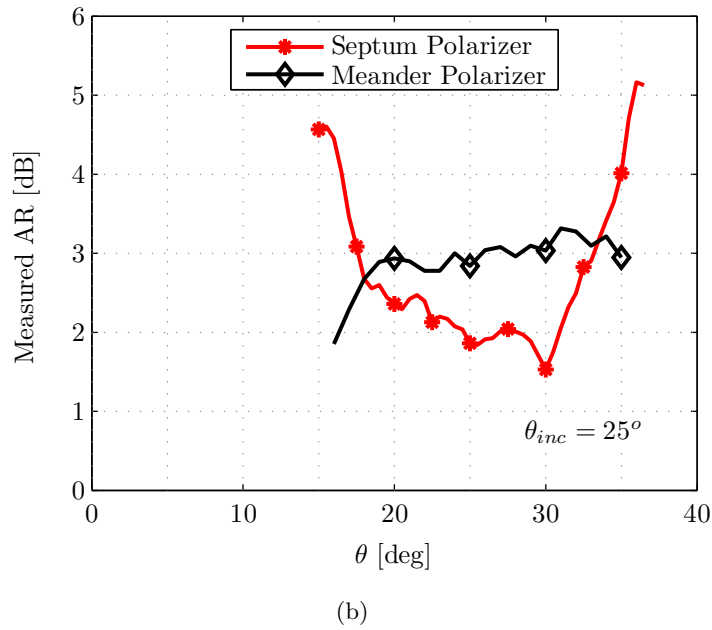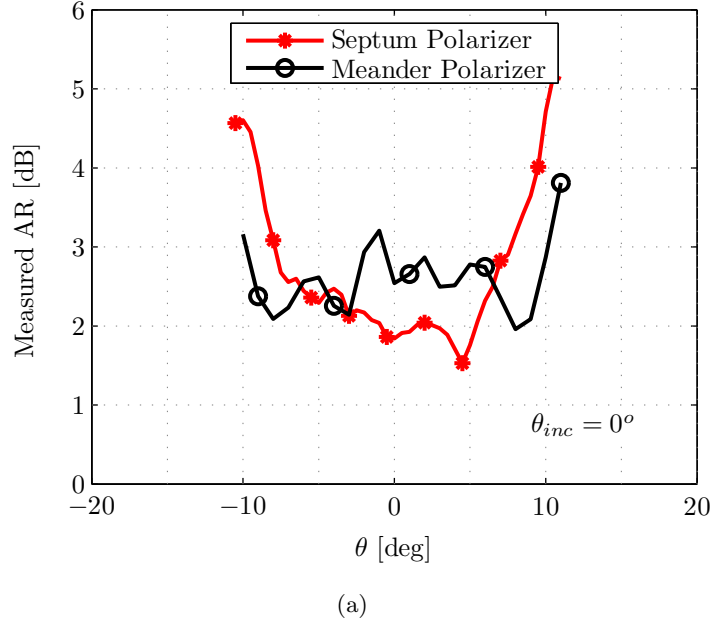
Figure 4.28.: Axial ratio measured at 29 GHz. Polarizer optiized for oblique incidence. Comparison between internal septum and external meander polarizers for two different incident angles θ_{inc}. (a) θ_{inc} =0°. (b) θ_{inc} =25°

4.8. Generalization to arbitrary incidence in a 3D-Space

The method presented in Section 4.3 is valid for the standard situation when the incident field $\mathbf{E_{inc}}$ belongs to the polarizer plane (xy-plane). In this case, a spherical coordinate system can be always selected respect to the polarizer orientation in such a way that, only the angle θ_{inc} is necessary to characterize the direction of incidence (Fig. 4.2(a)). However, there are situations in which it is not always possible to adjust the polarizer and the feed orientations to obtain an incident field purely tangential to the polarizer surface and $\mathbf{E_{inc}}$ also has a component along the z-axis. In this case, an additional angle ϕ_{inc} is necessary to characterize the direction of incidence, as shown in Fig. 4.29.
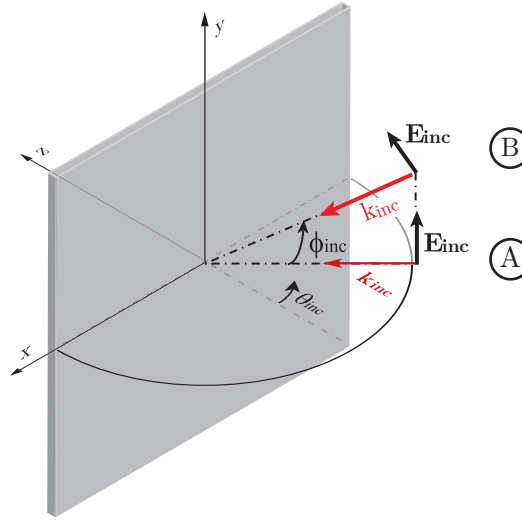
Figure 4.29.: Arbitrary incidence on the polarizer. In situation A, the incident electric field is parallel to the polarizer plane and can be separated into two components $\mathbf{E_{||}}$ and $\mathbf{E_{\perp}}$ along the diagonals of the plane xy (meander directions). In situation B, the incident electric field also has a z-component and an additional angle ϕ_{inc} is needed to describe the direction of incidence.

Following the same principles used for the parallel and perpendicular components, a logical idea is to accept that, in respect to the z component of $\mathbf{E_{inc}}$, the behavior of the polarizer can be modeled by the circuit shown in Fig. 4.30, where the meanders appear as a series of capacitances.

The analysis can now proceed along the standard lines.

The $\mathbf{T}$-matrix of the transmission lines of the i-th section is given by [20]:
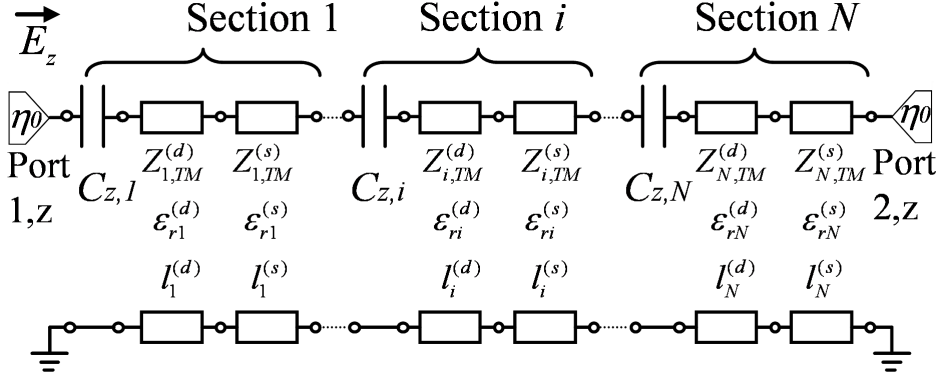
Figure 4.30.: Transmission line model of the meander-line polarizer for the z component of the incident electric field.

$$\mathbf{T}_i^{(m)} = \begin{bmatrix} \cos\left(\beta_i^{(m)} l_i^{(m)}\right) & j\dfrac{\eta_0 \cos\phi_{inc,i}^{(m)}}{\sqrt{\varepsilon_{r,i}^{(m)}}} \sin\left(\beta_i^{(m)} l_i^{(m)}\right) \\ j\dfrac{\sqrt{\varepsilon_{r,i}^{(m)}}}{\eta_0 \cos\phi_{inc,i}^{(m)}} \sin\left(\beta_i^{(m)} l_i^{(m)}\right) & \cos\left(\beta_i^{(m)} l_i^{(m)}\right) \end{bmatrix} \tag{4.16}$$

for $m=s,d$. The angle $\phi_{inc,i}^{(m)}$ is computed according with the Snell lows as in eqn. (4.2). The transmission matrices $\mathbf{T}_i^{C,z}$ of the shunt component of the i-th section are obviously given by:

$$\mathbf{T}_i^{C,z} = \begin{bmatrix} 1 & 1/j\omega C_{z,i} \\ 0 & 1 \end{bmatrix} \tag{4.17}$$

the circuit can be solved by cascading such matrices (as shown by eqn. (4.7) and (4.8)) and the z component field after the polarizer,$\mathbf{E_{o,z}}$, can be computed. The total field after the polarizer is given by:

$$\mathbf{E_o} = \mathbf{E_{||,o}} + \mathbf{E_{\perp,o}} + \mathbf{E_{z,o}} \tag{4.18}$$

where $\mathbf{E_{||}}$ and $\mathbf{E_{\perp}}$ are computed solving the circuits of Fig. 4.3 exactly as presented in Section 4.2.2. The AR can be computed from $\mathbf{E_o}$.

The lumped elements ($L_{eq,i}, C_{eq,i}$ and $C_{z,i}$) would have now to be optimized numerically in order to obtain an AR as close as possible to 0 dB. By the same token, the unit cells full-wave analysis would need to also include the z component of the field propagating in the different polarizer sections and, similarly to the case explained in Section 4.3.3, the physical dimensions ($M_{l,i}, M_{w,i}, M_{t1,i}, M_{t2,i}, M_{d,i}$) of the meander-lines would be adjusted separately

for each grating section and for the three orthogonal components of the incident field to match the admittances found in the equivalent circuit analysis.

The above procedure has been outlined as logical generalization of the simplified situation considered in this thesis. Obviously, its range of validity and the degree of accuracy that this simplified model would provide in the generalized geometry of Fig. 4.29 should be checked by exhaustive comparisons with full-wave software predictions and along with careful measurements. This was beyond the scope of this thesis where all the theoretical and empirical developments where restricted to the simple geometry of Fig. 4.2.

4.8.1. Tapered meander-line polarizer for multiple beam antenna systems

The method proposed in this chapter makes for an optimized design of a polarizer for a given arbitrary angle of incidence, not necessarily a normal one. This fact has been validated by characterizing two polarizers with two different optimal directions of incidence ($\theta_{inc} = 0°$ and $\theta_{inc} = 25°$). As it should be expected, the performances of such polarizers deteriorate due to waves impinging its surface with a direction different from the optimal one. In complex multibeam antenna systems, the orientation of the different antenna beams might range widely (-80° $\div$ +80°) both in azimuth and in elevation and a polarizer optimized for a unique angle of incidence might not satisfy the polarization requirements in the whole space. A possible solution to overcome this problem could be the use of a multifacet polarizer of polyhedric shape, every face of the polyhedron taking care of a feed. But a more elegant solution, also valid for sources generating large beams, would be to consider a meander contour where dimensions could vary continuously with the incidence angle, thus providing optimized values at any angle (the so-called tapered meander). A more realistic approach would consist in optimizing different regions of the polarizer for the relevant angles of incidence. This way, a flat polarizer could still be designed with the method developed in this thesis and each beam would impinge a specific area of the polarizer, which would be specially tailored for it. The polarizer surface would be *discretized* into different regions with different meander dimensions in each one. Hence, a smooth transition will be needed to guarantee the continuity of the meander lines. This concept is illustrated in Fig. 4.31 and is strongly suggested for further investigations and experimental check.
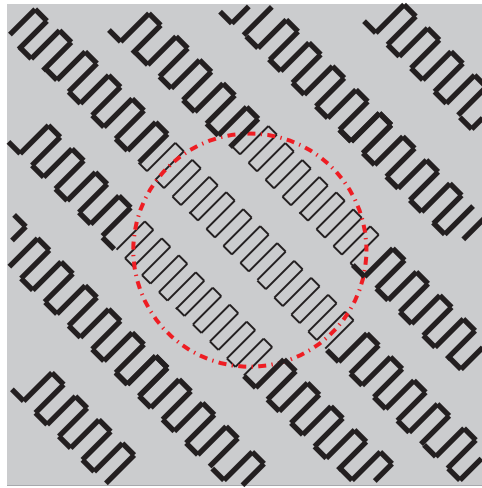
Figure 4.31.: Meander-line layer with regions optimized for different angles of incidence. Qualitative drawing.

4.9. Conclusion

This chapter has presented a simple method combing a TL model and a full-wave unit-cell analysis for the efficient design of ML polarizers operating with waves impinging on its surface with its incident field E_{inc} parallel to the polarizer surface and at an arbitrary oblique incidence angle. This is the situation most currently encountered in lens antenna subsystems.

The design procedure has been validated with measured data and, besides significantly reducing the development cycle, it also has introduced the possibility of designing ML polarizers for plane waves impinging its surface obliquely. Sensitivity analysis has been introduced in this work to give a quantitative insight on the effect of any tolerance on the optimal working condition of the polarizers.

To demonstrate the polarizer design method, two prototypes working in Ka-band have been designed, built and measured. The first prototype has been optimized for the easiest geometry, normal incidence. The AR is lower than 3 dB within the frequency band (28-31.5 GHz) and within the range of -10°$\leq \theta \leq$+10°. But it quickly degrades with the angle and this prototype could not be used beyond $\theta = +10°$. Hence only small multibeam systems (7-beams) could be considered with this polarizer.

Consequently, a second prototype has been optimized for waves impinging on its surface obliquely with a much larger incident angle θ_{inc}=25°. Although the circular polarization quality of this polarizer is, on average, not as good as the one designed for normal incidence, it still provides accetable values and this polarizer can be used for a plane-wave impinging its surface with a broader angle range (within 0°$\leq \theta_{inc} \leq$30°). This opens the door to the use of an external polarizer with a larger (i.e. 19) number of beams.

Overall, this chapter demonstrated the possibility of using external polarizers, which, through adequate design can provide performances comparable (and in some cases superior) to our benchmark design using internal polarizers. Therefore, external polarizers have become an interesting alternative not to be ignored.

The theory presented in this chapter is valid for any angle of incidence θ_{inc}. However in more complex scenarios where a higher number of beams (i.e. 121) is required, a more elaborated polarizer (made of more layers) could be needed for proper operation. This polarizer might be difficult to be accurately realized and despite the high number of beams, internal polarizers could be the only viable solution.

Last but not least, the effect of the beams impinging the meander-line polarizer with $\phi \neq 0$ and the possibility of variable-dimension meanders are generalizations that should be carefully considered.

References

[1] Y. Qu, G. S. Liao, S. Q. Zhu, and X. Y. Liu, "Pattern synthesis of planar antenna array via convex optimization for airbone forward looking radar," *Progress in Electromagnetics Research*, PIER 84, 1-10, 2008.

[2] F. Costa and A. Monarchio, "Design of subwavelength tunable and steerable fabry-perot/leaky wave antennas," *Progress in Electromagnetics Research*, PIER 111, 467-481, 2011.

[3] G. Exposito-Dominguez, J. M. Fernandez-Gonzalez, P. Padilla, and M. Sierra-Castner, "Dual circular polarized steering antenna for satellite communications in X band," *Progress in Electromagnetics Research*, PIER 122, 61-76, 2012.

[4] A. L. Peebles, "A Dielectric bifocal lens for multibeam antenna applications," *IEEE Antennas and Propagation*, vol. 36, 1988, pp. 599-606.

[5] J. F. Zürcher, "A meander-line polarizer covering the full E-band (60-90 GHz)," *Microwave Opt. Technol. Lett.*, vol. 18, pp. 320-323, Aug. 1998.

[6] L. Young, L. A. Robinson, and C. A. Hacking, "Meander-Line Polarizer," *IEEE Trans. Antennas Propagat.*, vol. AP-21, pp. 376-378, May 1973.

[7] R. A. Marino, "Accurate and efficient modeling of meanderline polarizers," *Microw. J.*, vol. 41, no. 11, pp. 22-34, Nov. 1998.

[8] J. J. Epis, "Broadband Antenna Polarizers," *U.S Patent*, No. 3,754,271, August 1973.

[9] T. L. Blackney, J. R. Burnett, and S. B. Cohn, "A design method for meander-line circular polarizers," *presented at 22nd Ann. Antenna Symp.*, pp. 1-5, Oct. 1972.

[10] C. Terret, J. R. Level, and K. Mahdjoubi, "Susceptance computation of a meander-line polarizer layer," *IEEE Trans. Antennas Propagat.*, vol. AP-21, pp. 1007-1011, Sept. 1984.

[11] S. W. Lee and G. Zarrilo, "Simple formulas for transmission through periodic metal grids or plates," *presented at 1983 Antenna Application Sym.*, Univ. Illinois, Urbana, IL, sponsored by RADC (EEA) Electromagn. Sci. Div., Hanscom AFB.

[12] A. K. Bhattacharyya and T. J. Chwalek, "Analysis of Multilayered Meander Line Polarizer," *IInt. J. of Microwave and Millimeter-Wave Computer-Aided Eng.*, pp. 442-454, 1997.

[13] M.-A. Joyal and J.-J. Laurin, "Analysis and design of thin circular polarizers based on meander lines," *IEEE Trans. Antennas Propagat.*, vol. AP-60, pp. 3007-3011, Sept. 2012.

[14] C. C. Chen, "Scattering by a two-dimensional periodic array of conducting plates," *IEEE Trans. Antennas Propagat.*, vol. AP-18, pp. 660-665, May 1970.

[15] R. S. Chu and K. M. Lee, "Radiation impedance of a dipole printed on periodic dielectric slabs protruding over a ground plane in an infinite phased array," *IEEE Trans. Antennas Propagat.*, vol. AP-35, pp. 13-25, Jan. 1987.

[16] ——, "Analytical model of a multilayered meander line polarizer plate with normal and oblique plane-wave incidence," *IEEE Trans. Antennas Propagat.*, vol. AP-35, pp. 652-661, June 1987.

[17] B. A. Munk, "Finite Antenna Arrays and FSS," *John Wiley and Sons*, pp. 306-326, 2003.

[18] M. Letizia, B. Fuchs, and J. R. M. A. Skrivervik, "Circularly polarized lens antenna system providing multibeam radiation pattern for HAPS," *Radio Science Bulletin*, no. 330, pp. 18-28, March 2010.

[19] N. Marcuvitz, "Waveguide Handbook," *Radiation Laboratories Series, McGraw-Hill Book Co., Inc., New York, N. Y.*, pp.28-33, 280-289, 1951.

[20] D. M. Pozar, "Microwave Engineering," *New York: John Wiley and Sons*, pp. 29-49, 208-211, 2nd Ed., 1998.

[21] C. A. Balanis, "Antenna Theory," *New York: John Wiley and Sons*, pp. 66-68, 2nd Ed., 1997.

[22] "www.ansoft.com."

[23] M. Letizia, J.-F. Zürcher, B. Fuchs, J. Mosig, and A. Skrivervik, "Circularly polarized lens antenna system for high altitude platforms (HAPS)," *proc. EuCAP 2011*, 5th European Conference on Antennas and Propagation, 2011.

[24] K. K. Chan, T. W. Ang, T. H. Chio, and T. S. Yeo, "Accurate analysis of meanderline polarizers with finite thicknesses using mode matching," *IEEE Trans. Antennas Propagat.*, vol. AP-56, pp. 3580-3585, Nov. 2008.

[25] W. K. Kahn, "Element efficiency: a unifying concept for array antennas," *IEEE Transactions on Antenna and Propagation*, vol. 49, no. 4, pp. 48–56, Aug. 2007.

[26] M. V. Ivashina, M. N. Kehn, P. Kildal, and R. Maaskant, "Decoupling efficiency of a wideband vivaldi focal plane array feeding a reflector antenna," *IEEE Transactions on Antenna and Propagation*, vol. 2, no. 2, pp. 373–382.

[27] T. Ismail and M. Dawoud, "Null steering in phased arrays by controlling," *IEEE Transactions on Antenna and Propagation*, vol. 39, no. 2, pp. 1561–1566, Nov. 1991.

[28] M. N. Kehn, M. V. Ivashina, and R. M. P. Kildal, "Definition of unifying decoupling efficiency of different array antennas: Case study of dense focal plane array feed for parabolic reflector," *Int. J. Electron.*, Commun. (AEU), 2009, 10.1016/j.aeue. 2009.02.011.

[29] P. Hannan, "The element-gain paradox for a phased array antenna," *IEEE Trans. Antennas Propag.*, vol. 12, no. 4, 1999.

[30] K. Chang, "Handbook of microwave and optical components," *vol. 1 Microwave passive and antenna components*, Wiley, New York, Chapitre 11, 1989.

[31] T. Cheston and E. Luoma, "Constant-K lenses," *Emerson & Cuming*, APL Technical Digest, Mar-Apr. 1963.

[32] B. Schoenlinner, X. Wu, J. Ebling, G. Eleftheriades, and G. Rebeiz, "Wide-scan spherical-lens antennas for automotive radars," *IEEE Trans. Microwave Theory Tech.*, vol. 50, no. 9, pp. 2166-2175, Sept. 2002.

[33] B. Schoenlinner and G. Rebeiz, "Compact multibeam imaging antenna for automotive radars," *IEEE Microwave Theory Tech. Symposium*, Seattle, WA, pp. 1373-1376, Jun 2002.

[34] M. Letizia, J.-F. Zürcher, B. Fuchs, C. Z. Gastón, and J. Mosig, "Circularly polarized multi-beam lens antenna system. Comparison between 2 polarizers," *proc. EuCAP 2012*, 6th European Conference on Antennas and Propagation, 2012.

[35] M. Letizia, B. Fuchs, C. Zorraquino, J. F. Zürcher, and J. R. Mosig, "Oblique incidence design of meander-line polarizers for dielectric lens antennas," *Progress in Electromangeics Research*, PIER 45, 309-335, 2012.

5. Prolate ellipsoidal lens for antenna systems providing multiple asymmetric beams[*]

Contents

5.1. Introduction

It is a basic fact of geometry that the intersection of a cone and a plane is a circle only if the plane is perpendicular to the cone axis. Slight deviations from this perfect orientation will produce ellipses of increasing eccentricity. Therefore, a multibeam antenna system, generating several identical conical beams, will typically produce a circular footprint only in the cell covered by the central beam while all the other footprints will be elliptical.

This situation will not change if a spherical lens is used to improve the directivity of the beams, where symmetry will not be affected by the lens if the axes pass through the lens center.

One possible solution to this problem is to change the shape of the lens. The new lens should

---

[*]M. Letizia, J. F. Zürcher and Juan R. Mosig, "Prolate ellipsoidal lens for antenna system providing multiple asymmetric beams," *Progress in Electromagnetics Research*, PIER 48, 289-312, 2013

modify the symmetry of the beams in such a way that, beyond the lens, the beam cross section can result in a circular footprint when impinging obliquely on the ground.

In this chapter, we propose a Ka-band multi-beam dielectric lens antenna design in which the beam symmetry is perturbed by acting on the lens shape, with the goal of generating circular footprints in the whole covered area. Such radiation characteristics are useful not only for HAPS, but also in scenarios where the antenna system is mounted on platforms flying above Earth and, in general, in any application where the shape of the footprints has to be carefully controlled for different elevation angles.

To the best of our knowledge, optimized dielectric lenses were considered in the past to generate single shaped-beams but they have never been studied to produce multiple beams, able to guarantee equal and circular ground footprints for communications from aerial stations. Such lenses would also be very interesting and efficient for applications where the antenna beams need to be shaped in the two radiating planes.

Controlling the beam patterns of a multi-beam antenna system is often a key issue of the design. For instance, the link budget and the geographic coverage of a system are both strongly influenced by the gain, the aperture, and the shape of the beams [1–3]. If used on an aerial station [4–9], circular and symmetric multi-beams would produce a circular footprint in the cell just below the antenna but elliptical footprints in all the remaining cells. The elongation of such footprints increases with the azimuth/polar angle, degrading the performance of the communication system [10–12]. However, circular footprints are highly desirable in such systems, providing better geographic coverage and more uniform link budgets across the coverage area [13]. For an aerial station to generate equal and circular footprints, asymmetric antenna beams are the obvious solution.

Synthesis and characterization of asymmetric beams have been addressed in previous publications [14–16]. These contributions were primarily focused on printed antenna arrays, which are not well-suited for Ka-band [17, 18], since it is well-known [19–21] that the total efficiency of printed arrays including the associated printed feeding networks quickly deteriorates at mm-wave frequencies. Lens antennas are considered an attractive alternative to generate shaped beams at mm-waves [13], as witnessed by many recently published papers proposing optimized lens shapes to produce various kinds of patterns. See for instance [22–29].

In typical LEO-satellites and HAPS scenarios, circular polarization is a required feature. This does not interfere with the proposed design, as circular polarization is easily achieved either by using circularly polarized primary sources or with the help of external polarizers [30].

Summarizing, the two main goals of this chapter are:

- to improve the power footprint generated by the spherical lens antenna designed in

Chapter 3 through the use of an ellipsoidal lens able to generate asymmetric beams.

- to provide and characterize an effective lens design for the proposed scenario.

The proposed method uses a full-wave time-domain software tool to optimize the lens. The usually prohibitive computer effort is greatly reduced here thanks to a set of design guidelines that suggest convenient initial values of the optimization parameters. As proof of concept, a lens prototype is designed following the proposed procedure, built and measured.

The chapter is organized as follows. After considering the effects of the antenna beams on the shape of the cluster in Section 5.2, the method used to compute the footprints generated by the antenna beams is explained in Section 5.3. Section 5.4 shows the lens antenna concept used to fulfill the scenario requirements. The antenna design procedure is presented in Section 5.5 whereas the performances of the prototype are shown in Section 5.6. Finally, Section 5.7 concludes and summarizes the chapter.

5.2. Antenna beams and shape of the cells in the cluster

The investigated scenario has been introduced in Section 3.2. The associated antenna performance, as discussed in Section 3.8, are now considered as benchmark to improve the ground footprint.

5.2.1. Scenario with 19 identical symmetric beams

Beams with the same beam aperture generate a cluster with elliptical cell shapes. From geometrical considerations, the cell in the center of the cluster has a circular shape and its radius $R_{cell,1}$ is associated to the -4 dB angle (FOV) of the beam simply by (5.1):

$$FOV = 2\arctan\left(\frac{R_{cell,1}}{H_{HAPS}}\right) \tag{5.1}$$

Furthermore, the other cells ($i=2,...,19$) of the cluster are elliptical (see Fig. 5.1 and 5.2), and they are characterized by a cell axial ratio (CAR) that depends on the boresight angle $\theta_{c,i}$ of each beam as (5.2):

$$CAR_i = \frac{H_{HAPS}\left[\tan\left(\theta_{c,i} + \frac{FOV}{2}\right) - \tan\left(\theta_{c,i} - \frac{FOV}{2}\right)\right]}{2H_{HAPS}\tan\left(\frac{FOV}{2}\right)\frac{1}{\cos\theta s,i}} \quad \text{for } i = 2,...,19 \tag{5.2}$$

In (5.2), the nominator is the longest semi-axis of the ellipse (CLA_i) whereas the denominator is the shortest (CSA_i) and their expression can be deduced from Fig. 5.2 with simple trigonometric considerations.

In this scenario, beams characterized by a $FOV = 13.6°$: produce a cell in the center of the cluster of circular shape ($R_{cell,1}$=2.5 km) and 18 asymmetric external cells. The cell
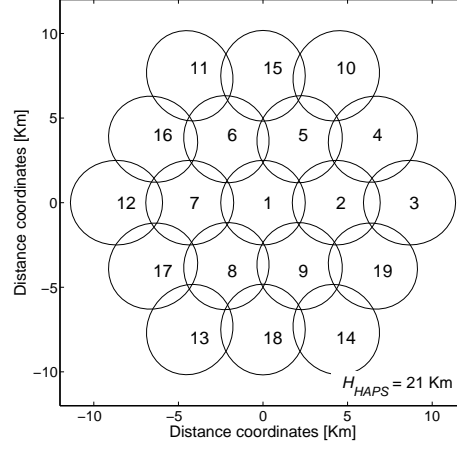
Figure 5.1.: Enumeration and arrangement of the ground power footprints.
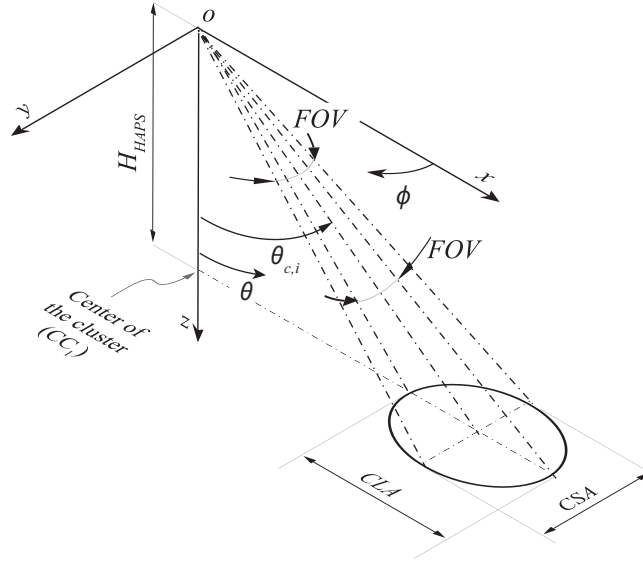
Figure 5.2.: Down-link geometry using symmetric beams.

centers and the associated boresight angles and cell axial ratios (CAR) are given in Table 1. CAR is frequently given as a percent deviation in respect the perfect circular case. The cells surrounding the central cell # 1 (i=2,5-9) are characterized by an axial ratio of 1.022 (i.e. 2.2% deviation in respect to the circular case) while the most external cells (i=5,10-14) are characterized by an axial ratio of 1.084 (8.4%), and the remaining intermediate cells (i=4,15-19) are characterized by an axial ratio of 1.064 (6.4%).

Table 5.1.: *Data for the 19 cells considered in Fig. 5.1.*

i	CC_i (x_i, y_i) [km]	d_i [km]	$\theta_{c,i}$ [deg]	CAR
1	(0,0)	0	0	1
2	(4.330,0)	4.330	11.65	1.022
3	(8.660,0)	8.660	22.41	1.084
4	(6.495,3.750)	7.500	19.65	1.064
5	(2.165,3.750)	4.330	11.65	1.022
6	(-2.165,3.750)	4.330	11.65	1.022
7	(-4.330,0)	4.330	11.65	1.022
8	(-2.165,-3.750)	4.330	11.65	1.022
9	(2.165,-3.750)	4.330	11.65	1.022
10	(4.330,7.500)	8.660	22.41	1.084
11	(-4.330,7.500)	8.660	22.41	1.084
12	(-8.660,0)	8.660	22.41	1.084
13	(-4.330,-7.500)	8.660	22.41	1.084
14	(4.330,-7.500)	8.660	22.41	1.084
15	(0,7.500)	7.500	19.65	1.064
16	(-6.495,3.750)	7.500	19.65	1.064
17	(-6.495,-3.750)	7.500	19.65	1.064
18	(0,-7.500)	7.500	19.65	1.064
19	(6.495,-3.750)	7.500	19.65	1.064

5.2.2. Scenario with asymmetrical beams and identical cells.

A cluster with all the cells identical and circular with radius R_{cell}, can be synthesized by using beams that are asymmetric in respect to their boresight axis. In such a case, the beam aperture angle is not the same for all the beams of the cluster and three angles are needed to characterize the beam shape. These angles are connected to three points $P_{A,i}$, $P_{B,i}$ and $P_{C,i}$ on the border of the i-th cell number as shown in Fig. 5.3. $P_{A,i}$ is the cell boundary point closest to the center of the cluster and $P_{C,i}$ is the opposite point to $P_{A,i}$ in respect to center CC_i of the cell. Point $P_{B,i}$ is easily obtained by considering the cell diameter perpendicular to $P_{A,i}$ - $P_{C,i}$ (Fig. 5.3). Then, $\beta_{A,i}$, $\beta_{B,i}$ and $\beta_{C,i}$ are the angles between the center of the cell, the antenna and $P_{A,i}$, $P_{B,i}$ and $P_{C,i}$, respectively. The values of $\beta_{A,i}$, $\beta_{B,i}$ and $\beta_{C,i}$ can

be deduced from Fig. 5.3 as follows:

$$\beta_{A,i} = \theta_{s,i} - \arctan\left(\frac{d_i - R_{cell}}{H_{HAPS}}\right) for \ i = 2, ..., 19 \tag{5.3}$$

$$\beta_{B,i} = \arctan\left(\frac{R_{cell}\cos\theta_{c,i}}{H_{HAPS}}\right) for \ i = 2, ..., 19 \tag{5.4}$$

$$\beta_{C,i} = \arctan\left(\frac{d_i + R_{cell}}{H_{HAPS}}\right) for \ i = 2, ..., 19 \tag{5.5}$$

$$\beta_{A,i} = \beta_{B,i} = \beta_{C,i} = \arctan\left(\frac{R_{cell}}{H_{HAPS}}\right) \tag{5.6}$$

where d_i is the distance between the center of the cell i and the center of the cluster. In scenarios like the proposed one, in which the antenna is above the center of the cluster, the following relation is always valid: $\beta_{A,i} \leq \beta_{B,i} \leq \beta_{C,i}$. This motivates the necessity of asymmetric beams to achieve the desired cell shapes. These angles are used to set up initial constraints on the -4dB beam aperture, in order to synthesize asymmetric beams generating circular cell footprints.
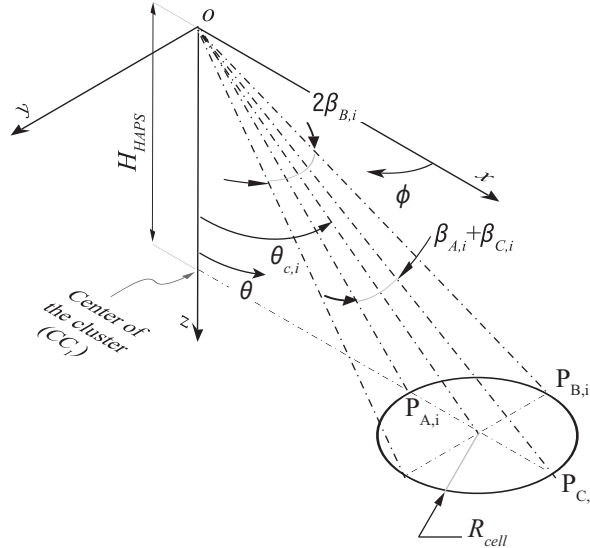
Figure 5.3.: Down-link geometry using asymmetric beams to produce circular cells.

5.3. Computation of ground power footprints and optimal beam patterns

The distribution of the power transmitted by each beam to its corresponding cell on ground can be computed using the Friis equation normalized to the transmitted power [31]. The free space path-loss between the antenna and the cell boundary has been taken into account in this work, since it strongly affects the cell shape.

The ground area covered by the footprints was discretized with a square grid of 10m size. For each point on the grid P(x, y), the power received from the i-th beam $P_{r,i}(x, y)$ was computed as:

$$P_{r,i}(x, y) = G_i(\theta, \phi) \left(\frac{\lambda}{4\pi \sqrt{x^2 + y^2 + H_{HAPS}^2}} \right)^2 \tag{5.7}$$

where $G_i(\theta, \phi)$ is the radiation diagram of the i-th beam and λ is the wavelength in free-space ($\lambda = 10.3$mm at $f = 29$GHz) of the transmitted signal. The involved angles θ and ϕ are obtained from the point coordinates P(x, y) as follows:

$$\theta = \arctan \left(\frac{\sqrt{x^2 + y^2}}{H_{HAPS}} \right) \tag{5.8}$$

$$\phi = \arg(x, y) \tag{5.9}$$

In (5.7), both the radiation diagram of the beam and the free-space path loss contribute in determining the shape of the cell on the ground.

In general, the same amount of power is sought-after in each cell. Hence, when all the cells have the same circular shape, the desired optimal power distribution in each cell is just the ground power footprint generated by the beam 1 ($P_{r,1}(x, y)$), translated at the center of the other cells. Therefore, the optimal beam radiation pattern $G_i^{th}(\theta, \phi)$ that guarantees the desired footprint can be directly obtained from eqn. (5.7) as:

$$G_i^{th}(\theta, \phi) = \frac{P_{r,i}(x - x_i, y - y_i)}{\left(\frac{\lambda}{4\pi \sqrt{x^2 + y^2 + H_{HAPS}^2}} \right)^2} \tag{5.10}$$

5.4. Lens antenna concept for the proposed scenarios

In this section, the antenna properties are determined according to the scenario specifications shown in Chapter 1. The antenna system was selected as a homogeneous Teflon lens excited by a set of circular waveguide feeds. This choice has been motivated in [32, 33] and fully discussed in [34], where a design suitable for 7 cells cluster has been characterized. The extension of such an idea to a cluster with 19 cells is quite straightforward if every beam is produced independently by its corresponding feed. The 19 feed radiating apertures are placed in such a way that their radiation is optimally focalized by the lens (Fig. 5.4). Moreover, all the feed longitudinal axes intersect at the center of the lens and each feed points to the center of its cell. The feeds numbering scheme follows that used for the cells exactly.

5.4.1. Antenna system based on spherical lens

A spherical lens focuses the radiation of the feeds, thus producing directive and symmetric beams [35]. Provided that the distance of all the feed apertures from the lens surface is the same, the beams focalized by this lens exhibit the same radiation pattern [36–39]. The theoretical directivity D_{th} of a circular radiating aperture that has a main beam with no sidelobes, is linked with the beam aperture Ω_{beam} (solid angle) and with the radius of the aperture R_{ap} by [33]:

$$R_{ap} = \frac{\lambda\sqrt{D_{th}}}{2\pi} = \frac{\lambda\sqrt{\frac{4\pi}{\Omega_{beam}}}}{2\pi} \tag{5.11}$$

Although a homogeneous Teflon lens always exhibits sidelobes [35, 40] and their level essentially depends on the feed radiation and on the lens material, eqn. (5.11) can still be used to correctly estimated the aperture of a directive beam generated by a lens with radius, as demonstrated in [33]. Hence, eqn. (5.11) has been used here to figure out the lens dimensions for a needed beam aperture. The half power beam-width angle θ_{3dB} can be estimated by the -4 dB angle of the beam aperture (FOV) by using the usual cosine-square assumption for the pattern [33], yielding:

$$\theta_{3dB} = 0.88 FOV \tag{5.12}$$

so eqn. (5.11) can be transformed as:

$$R_{lens} = \frac{\lambda\sqrt{\frac{4\pi}{\theta_{3dB}^2}}}{2\pi} = \frac{\lambda\sqrt{\frac{4\pi}{(0.88 FOV)^2}}}{2\pi} \tag{5.13}$$

Note that (5.1) and (5.11) provide a model to link the geometry of the scenario (R_{cell}, H_{HAPS}) with the lens dimension (R_{lens}). Due to the lens symmetry and to the fact that in this design the adjacent waveguide feeds couple very weakly even in the close vicinity of the lens [33, 34], the 19 patterned beams generated by the lens antenna system modeled in Fig.5.4 are identical and symmetric (see the simulated and measured radiation patterns in Fig. 5.5). These beam

patterns have been used to compute the cell power footprints according to eqn. 5.7. Figs. 5.6 and 5.7 show the power ground footprint of cells 1 and 3 predicted by using the simulated radiation pattern. Cell 1 is circular with a radius of 2.5 km, whereas cell 3 exhibits 8.8% of CAR. The same analysis has been performed for cell 2 and 4, yielding $CAR_2 = 2.8\%$ and $CAR_4 = 6.9\%$, in line with the values geometrical vales computed with (5.2). Figs. 5.8 and 5.9 depict the power footprints obtained by using the measured radiation patterns. The agreement between the footprint values corresponding to simulated and measured radiation patterns is reasonably good in terms of shape, size and levels. The footprint of cell 3 is quite elongated along the x-axis, indicating power spreading in this direction, as clearly shown in Fig. 5.9 by the -4dB, -8dB and -12dB contours.
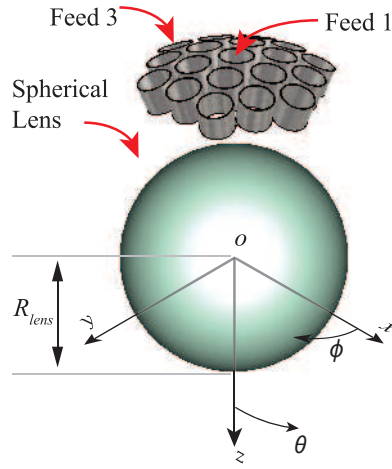
Figure 5.4.: Model of the 3-D spherical dielectric lens antenna system.
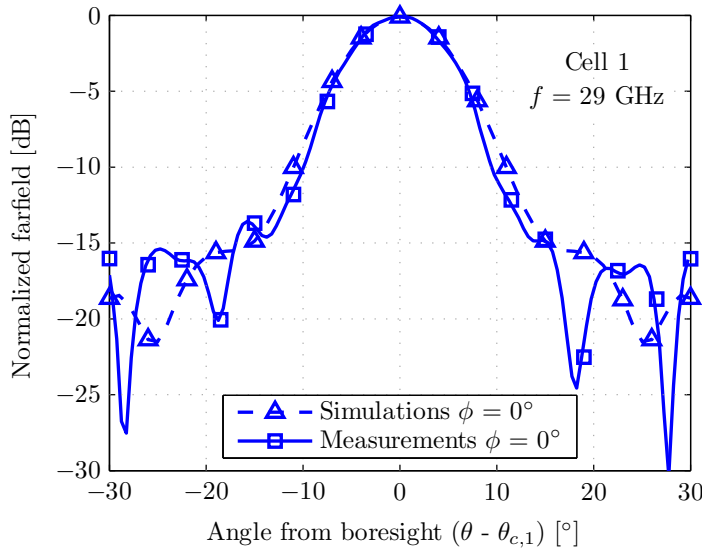
Figure 5.5.: Farfield radiation pattern of the spherical lens.

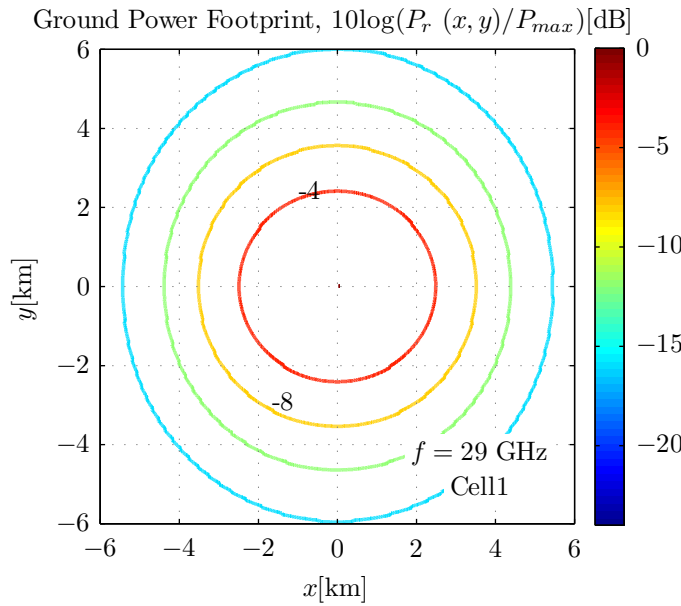Ground Power Footprint, $10\log(P_r\ (x,y)/P_{max})$[dB]
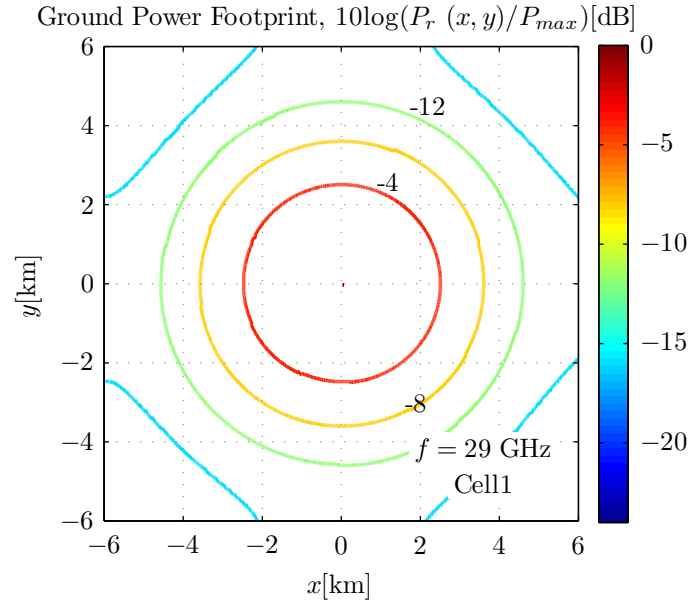
Figure 5.6.: Footprint of cell 1 achieved with the spherical lens by using the simulated radiation pattern of beam 1. The cell boundary is a circle of 2.5 km radius.

Ground Power Footprint, $10\log(P_r\ (x,y)/P_{max})$[dB]
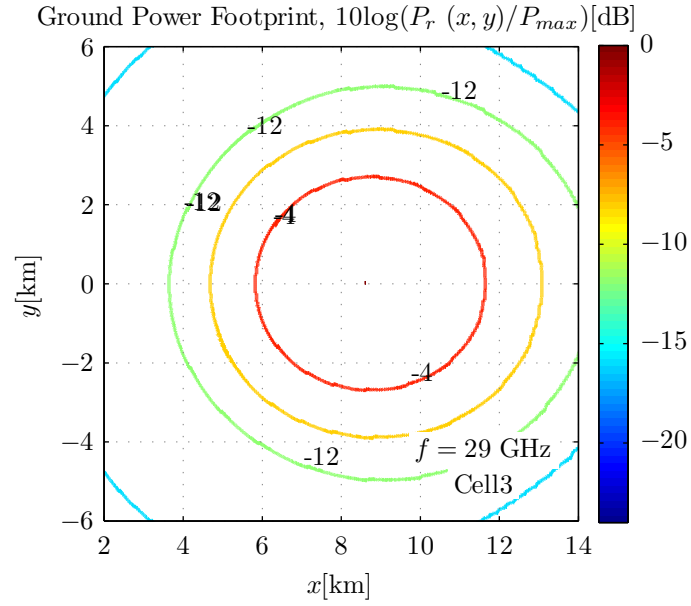
Figure 5.7.: Footprint of cell 3 achieved with the spherical lens by using the simulated radiation pattern of beam 3. The cell boundary is an ellipse. The -8dB and the -12dB contour are also elongated.
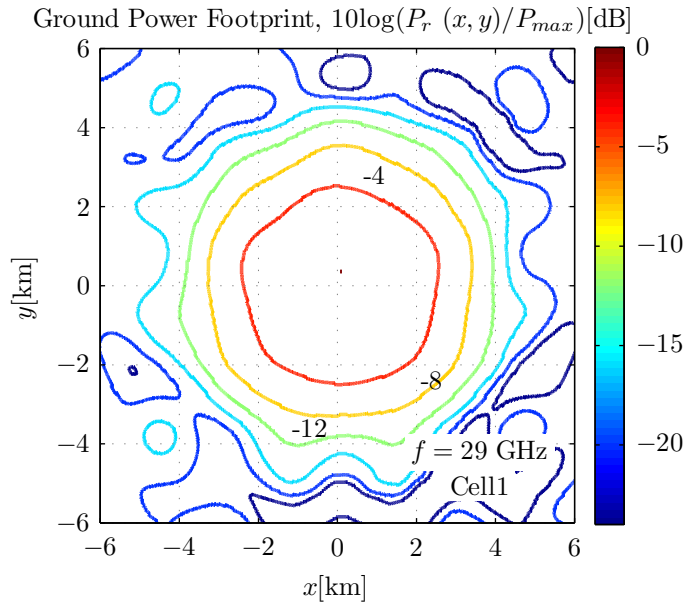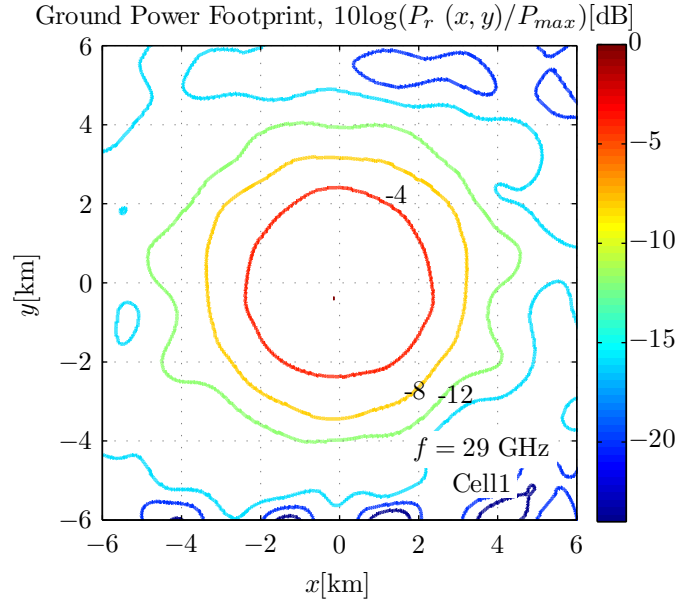
Figure 5.8.: Footprint of cell 1 achieved with the spherical lens by using the measured radiation pattern of beam 1.
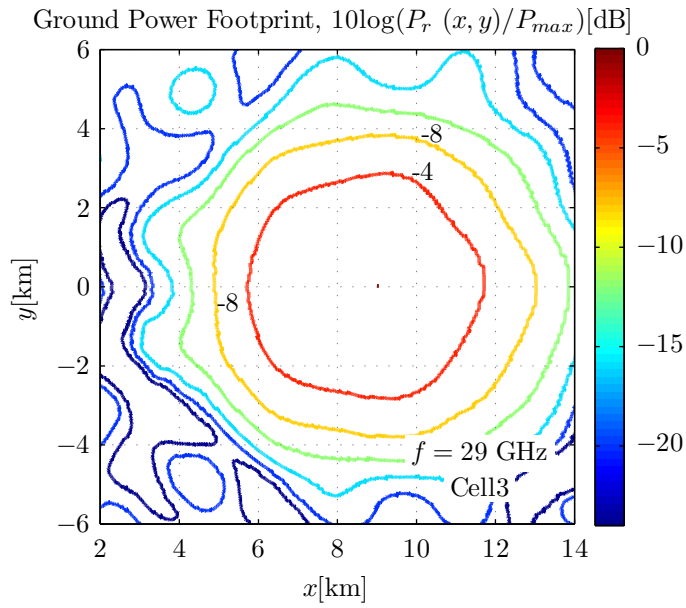
Figure 5.9.: Footprint of cell 3 achieved with the spherical lens by using the measured radiation pattern of beam 3. The -4dB, -8dB and the -12dB contours are elongated in respect to cell 1.

5.4.2. Antenna system based on prolate ellipsoidal lens

In the previous section, we used the approximate analytical formulas (5.1) and (5.13) to design the spherical lens and to obtain the cell dimensions. Here we consider an enhanced design in which the lens shape is slightly modified to take into account the beam asymmetry needed to satisfy the exact requirements in terms of beam aperture angles ($\beta_{A,i}$, $\beta_{B,i}$, $\beta_{C,i}$).

First, we note that the values of aperture angles $\beta_{A,i} + \beta_{C,i}$ and $2\beta_{B,i}$ of Fig. 5.3 are very close to the value of FOV of Fig. 5.2. Hence, we expect only minor modifications in the lens geometry in respect to the spherical case. Now, according to (5.13), a smaller beam aperture angle is achievable with a bigger lens dimension and vice versa. Since $\beta_{A,i} + \beta_{C,i}$ is smaller than $2^* \beta_{B,i}$ for all the external cells of the cluster and considering the rotational symmetry of the cluster in respect to the z-axis, we expect that the resulting lens shape is a prolate ellipsoid with two identical axes on the x-y plane and the longer axis on the z-axis (see Fig. 5.10). The equation of such ellipsoidal lens normalized to the shortest semi-axes is:

$$x^2 + y^2 + \frac{z^2}{LAR^2} = 1 \tag{5.14}$$

where LAR is the Lens Axial Ratio defined as the ratio between the longest (LLA) and the shortest (SLA) axis of the ellipsoid.
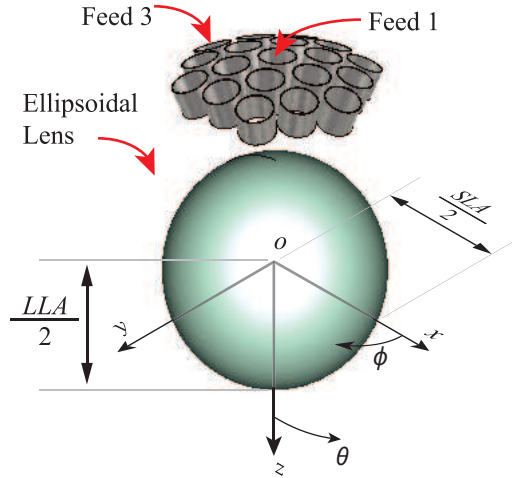
Figure 5.10.: Model of the 3-D elipsoidal (revolved around z-axis) dielectric lens antenna system. This antenna system generates 19 directive beams with asymmetric main-lobe.

As in the spherical lens case, an initial estimation of the lens dimensions (LLA and SLA) can be obtained using (5.13). But now, instead of FOV the beam aperture angles $\beta_{A,i} + \beta_{C,i}$ and $2^*\beta_{B,i}$ are used to compute LLA and SLA respectively, yielding:

$$LLA_i = \frac{\lambda \sqrt{\frac{4\pi}{(0.88(2\beta_{A,i}))^2}}}{2\pi} + \frac{\lambda \sqrt{\frac{4\pi}{(0.88(2\beta_{C,i}))^2}}}{2\pi} \tag{5.15}$$

$$SLA_i = \frac{\lambda \sqrt{\frac{4\pi}{\left(0.88(2\beta_{B,i})\right)^2}}}{\pi} \tag{5.16}$$

The lens axial ratio (see eqn. (5.17)) is directly obtained dividing (5.15) by (5.16). The value of LAR of the cells situated at the same distance from the center of the cluster is identical:

$$LAR_i = \frac{LLA_i}{SLA_i} = \frac{\frac{1}{\beta_{A,i}} + \frac{1}{\beta_{C,i}}}{\frac{1}{\beta_{B,i}}} \approx \frac{1}{\cos\theta_{c,i}} \; for \; i = 2, ..., 19 \tag{5.17}$$

where the value $1/\cos\theta_{c,i}$ has been found numerically (see Fig. 5.11). For practical reasons, only one value of LAR has to be chosen to perform the design of the lens so, following the procedure adopted in this chapter, it is not possible to fully compensate the ellipticity of all the cells of the cluster at the same time (see section 5.5). The system specifications associated to this research called for an optimization of the lens shape providing circular shapes in the most external cells of the cluster (cell 3, 10-14), where the ellipticity produced by using a spherical lens would have been more evident. The lens symmetry guarantees the circularity of cell 1 whereas SLA fixes its dimension. By ensuring the circularity of the shape of cell 1 and of the external cells of the cluster, we also logically expect a reduction of the ellipticity of the remaining cells (cell 4, 15-19, 2, 5-9) in respect to the spherical lens case. However, the shape of these intermediate cells can not be fully controlled by the simple lens design procedure proposed here.

A final consideration concerns the solution of equations (5.2) and (5.17). The cell axial ratio and the lens axial ratio have been computed for different θ_c within the angle range $0° \leq \theta_c \leq 50°$. Fig. 5.11 graphically proves that the function $1/\cos\theta_c$ is an excellent approximation for the solution of equation (5.17) and for $\theta_c \leq 30°$ it can also be considered a good approximation of eq. (5.2). This comparison highlights the fact that to compensate the axial ratio of a cell produced by a symmetric beam pointing in the θ_c direction, an ellipsoidal lens with $LAR = 1/\cos\theta_c$ is a good initial candidate. Thus, we can use the relation $CAR_i = LAR_i = 1/\cos\theta_c$ to initiate a design of an ellipsoidal lens for the scenario depicted in Fig. 5.3. The full ellipsoidal lens design procedure is given in the next Section.
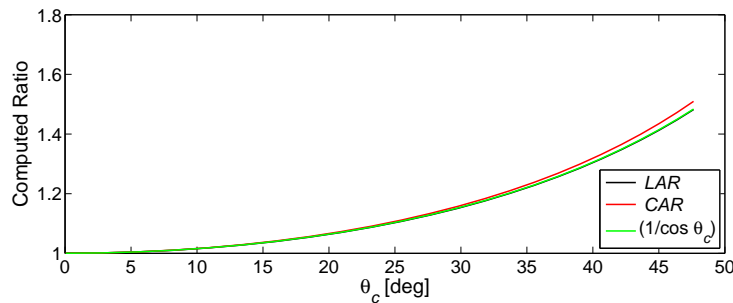
Figure 5.11.: Computed lens axial ratio and cell axial ratio for different value of θ_c. The two curves are compared with $1/\cos\theta_c$.

5.5. Ellipsoidal lens design procedure

The complete ellipsoidal lens design procedure is based on full-wave optimization. The analyzed geometry is depicted in Fig. 5.10. Because of the symmetry of the cluster, we optimize the lens activating only feeds 1 and 3 in the analysis. This simplifies the design process and, at the same time, makes it possible to optimize both the dimensions and the shape of the cells of the cluster.

Before starting the optimization process, the optimal radiation pattern $G_1^{th}(\theta, \phi)$ and $G_3^{th}(\theta, \phi)$ are computed with (5.10). Indeed these optimal patterns guarantee the desired circular contour for cells 1 and 3, adequately compensating the effect of the free-space path-loss.

The two parameters of the lens to be optimized are SLA and LAR. Eqns. (5.16) and (5.17) give the initial value of SLA and LAR, respectively. In our case $SLA=SLA_1=60$ mm and, since we are interested in minimizing th axial ratio of the most external cells, $LAR=LAR_3 = 1/\cos\theta_{c,3} = 1.082$.

For every combination of the two parameters, the radiation patterns of beams 1 and 3 were computed by full-wave analysis (CST Microwave Studio $^{\copyright}$ [41]) and compared with the sought-after optimal patterns. The optimization cost function was set up classically in terms of some threshold values (δ_1, δ_2, ...) for the differences between the computed and optimal radiation pattern. In this process, the use of the pre-computed optimal patterns ($G_1^{th}(\theta, \phi)$ and $G_3^{th}(\theta, \phi)$) avoids the calculation of the ground power footprint at the end of each iteration, thus accelerating the optimization.

In order to speed up the optimization procedure and, at the same time, maintain a reliable output, the radiation patterns are evaluated only in some reference angle values (see eqn. (5.18-5.21)). Such values correspond to the most relevant directions of the cells boundary (i.e. the directions singled out by the segments, $\overline{OA}, \overline{OB}$ and $\overline{OC}$ in Fig. 5.3).

$$\left| G_1(\theta, \phi)\big|_{\theta=FOV/2, \phi=0} - G_1^{th}(\theta, \phi)\Big|_{\theta=FOV/2, \phi=0} \right| \leq \delta_1 \qquad (5.18)$$

and similarly, for beam 3:

$$\left| G_3(\theta - \theta_{c,3}, \phi)\big|_{\theta=\beta_{C,3}, \phi=0} - G_3^{th}(\theta - \theta_{c,3}, \phi)\Big|_{\theta=\beta_{C,3}, \phi=0} \right| \leq \delta_2 \qquad (5.19)$$

$$\left| G_3(\theta - \theta_{c,3}, \phi)\big|_{\theta=\beta_{B,3}, \phi=90} - G_3^{th}(\theta - \theta_{c,3}, \phi)\Big|_{\theta=\beta_{B,3}, \phi=90} \right| \leq \delta_3 \qquad (5.20)$$

$$\left| G_3(\theta - \theta_{c,3}, \phi) \big|_{\theta=\beta_{A,3}, \phi=180} - G_3^{th}(\theta - \theta_{c,3}, \phi) \Big|_{\theta=\beta_{A,3}, \phi=180} \right| \leq \delta_4 \qquad (5.21)$$

The constraint on the boresight direction of each beam has been relaxed because preliminary full-wave simulations demonstrated that for the cases considered here, the steering of the beam due to the ellipsoidal lens can be neglected (less than 0.1 degrees).

A final word must be spent on the lens focal distance. which obviously changes with any modification of the lens geometry. Therefore, the feeds have to be moved to the new focal points to maximize the radiation performances and reduce the side-lobe levels. At a first glance, this appears to be a drawback in this method since it would slow down the whole optimization process. But, thanks to the accurate initial values used in the optimization process, only a few iterations are necessary to find the optimal geometry.

5.6. Characterization of the ellipsoidal lens prototype

The optimal patterns $G_1^{th}(\theta, \phi)$ and $G_3^{th}(\theta, \phi)$ for the critical beams #1 and #3 have been computed using eqn. (5.10). They are shown in Fig. 5.12 and 5.13, respectively. The radiation pattern of beam #1 is symmetric in respect to its boresight direction. The half-power beamwidth of this beam is 11.9°, the beamwidth at -4 dB is 13.5° and the sidelobe level is lower than -15 dB, as expected from [33]. The radiation pattern of beam #3 is asymmetric, being more directive in the $\phi = 0°$ plane than in the $\phi = 90°$ plane, as expected by the relation $\beta_{A,i} + \beta_{C,i} < 2\beta_{B,i}$ discussed in section 4.2. Furthermore, in the $\phi = 0°$ plane, beam #3 presents an asymmetry between its right ($\theta - \theta_{C.3} > 0°$) and left ($\theta - \theta_{C,3} < 0°$) sides. This is also expected due to the fact that in Fig. 5.3 the circular shape of the cell 3 is guaranteed by using $\beta_{C,i} ¡ \beta_{A,i}$.

An ellipsoidal lens has been designed following the designed procedure proposed in Section 5. The optimal values of LAR and SLA achieved at the end of the optimization are 1.08 and 57.8 mm, respectively. The radiation patterns of beams 1 and 3 achieved by full-wave simulation and the optimal patterns $G_1^{th}(\theta, \phi)$ and $G_3^{th}(\theta, \phi)$ are in very good accordance (Figs. 5.12 and 5.13) confirming that our optimization process yields a lens design that satisfies our optimization goal. It is interesting to note that the initial values of SLA and LAR computed before the optimization process by eqn. (5.16) and (5.17) are very close to those optimized, demonstrating the robustness of our design approach. Furthermore, only three iterations have been performed to conclude the optimization procedure.

The ellipsoidal lens prototype has been produced through milling machine techniques with a nominal tolerance of 50μm to guarantee the best shape accuracy. Fig. 5.14 shows the lens prototype during the machining process. Metal clumps have been machined to align the lens accurately during its realization. A digital micrometer has been used to verify the quality and dimensions of the final machined prototype which is shown in Fig. 5.15.
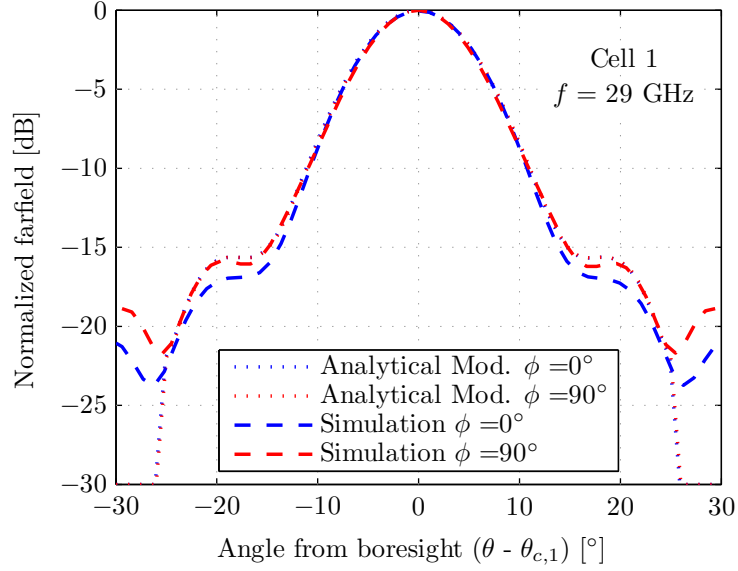
Figure 5.12.: Farfield radiation pattern of beam # 1. Comparison of optimal and simulated patterns for cuts ϕ=0° and ϕ=90°. The symmetry of beam #1 is readily apparent.
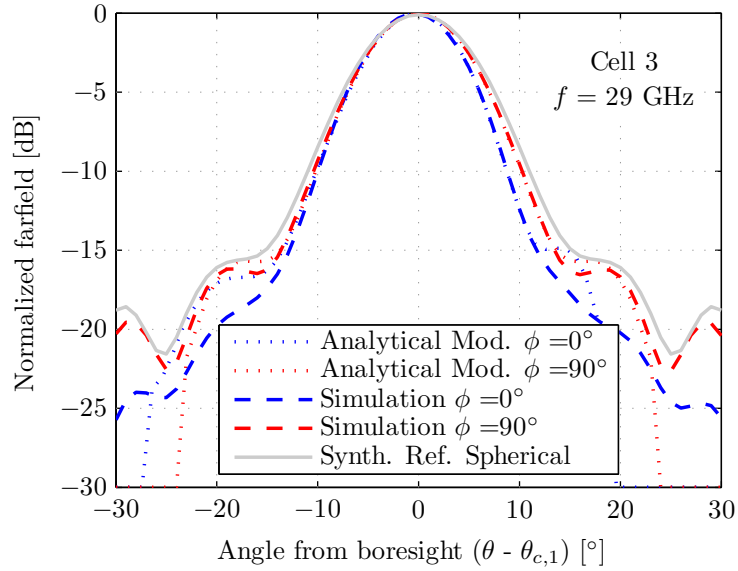
Figure 5.13.: Farfield radiation pattern of beam #3. Comparison of optimal and simulated patterns for cuts ϕ=0° and ϕ=90°. Beam #3 is asymmetric and more directive than beam #1. Beam #3 is asymmetric and more directive than beam #1.

<div align="center">(a)   (b)</div>
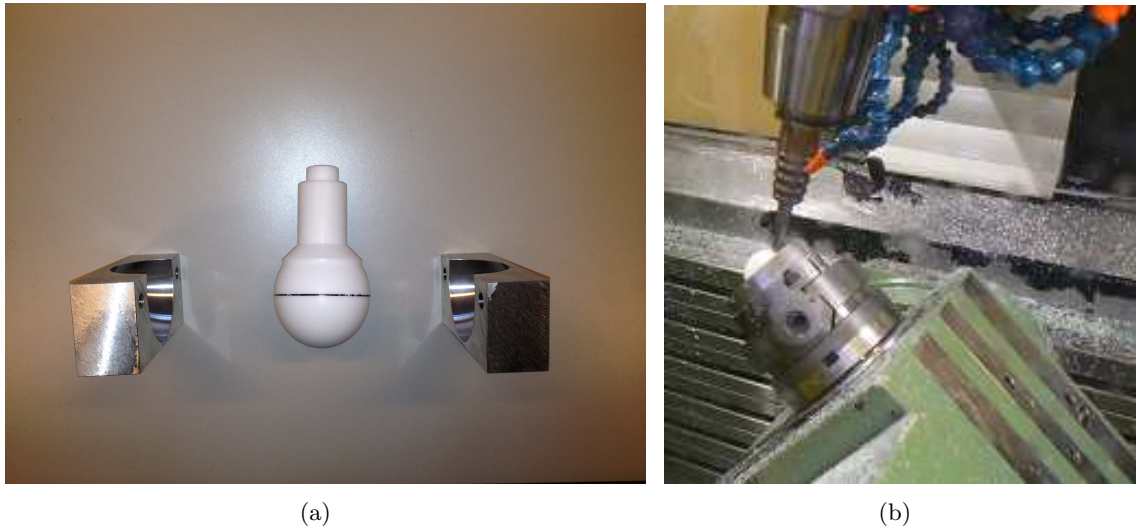
Figure 5.14.: Ellipsoidal lens prototype under machining. (a) the lens alignment during the machining process is guaranteed by metal clumps. (b) the CNC machine manufactures the lens surface.

<div align="center">
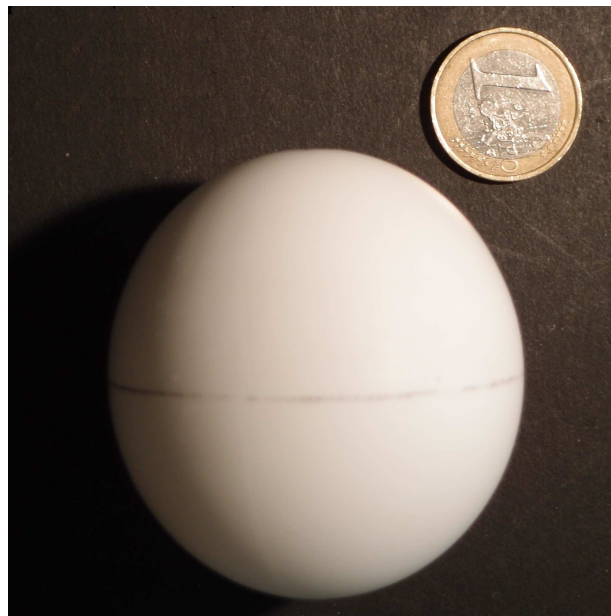
Figure 5.15.: Ellipsoidal lens prototype.

</div>
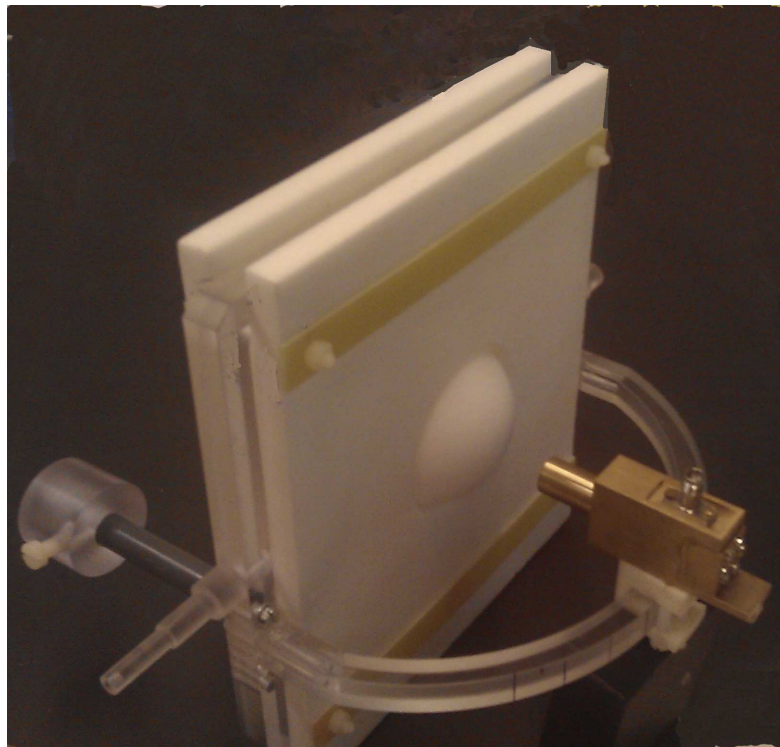
Figure 5.16.: Ellipsoidal lens prototype with a waveguide feed.

5.6.1. 2D radiation pattern measurements

The performance of the lens has been characterized through measurements of the radiation pattern in the anechoic chamber. In addition to the lens, the antenna subsystem includes a linearly polarized primary source kept in place with a plastic frame [21, 30, 33], which also allows a fine control of the relative position between the waveguide feed and the lens. The test set-up is shown in Fig. 5.16.

The required optimal patterns $G_1^{th}(\theta, \phi)$ and $G_3^{th}(\theta, \phi)$ predicted by our theory, have been compared with the measurement data for the two main cut planes $\phi = 0°$ and $\phi = 90°$. The farfield patterns of the ellipsoidal lens antenna (only one feed is active at any one time) are plotted in Figs. 5.17 and 5.18. The accordance between theory and measurements is good, especially within the angle range $|\theta - \theta_{c,i}| \leq 10°$ where the pattern is determinant for the right cell shape.
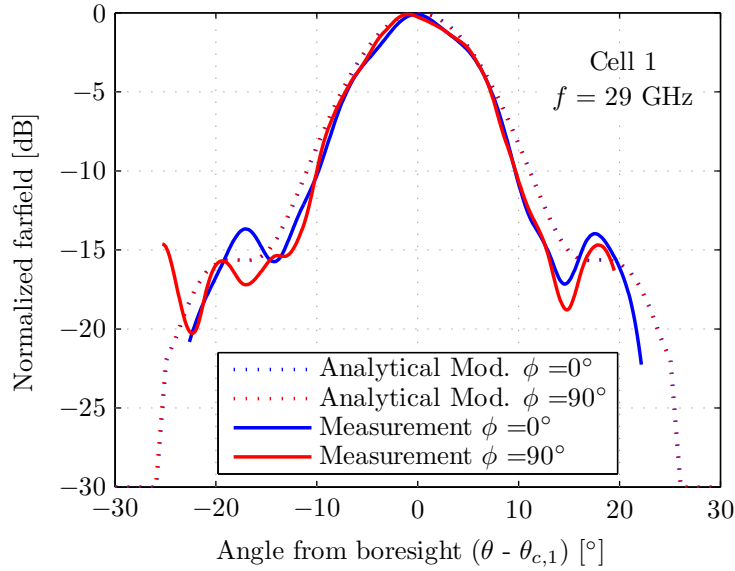
Figure 5.17.: Farfield radiation pattern of beam 1. Comparison of optimal and measured patterns. Good agreement is observed.
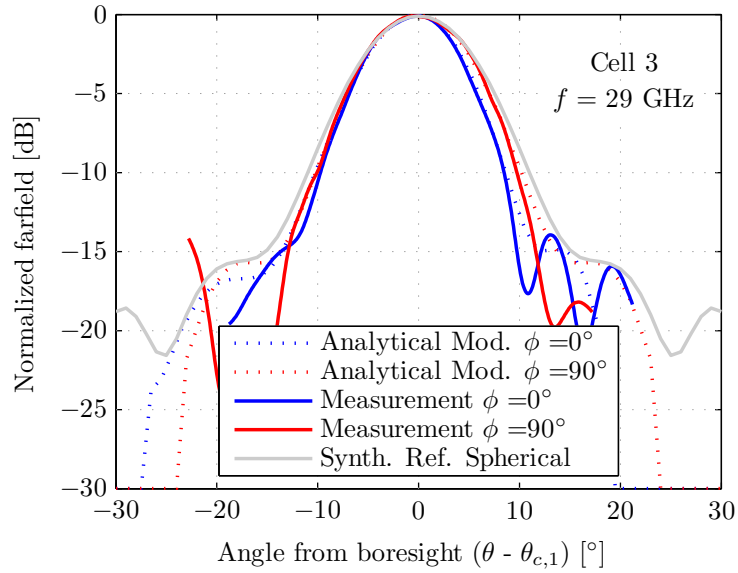
Figure 5.18.: Farfield radiation pattern of beam 3. Comparison of optimal and measured patterns. Good agreement is observed. Beam 3 is asymmetric and more directive than beam 1.

5.6.2. Ground power footprint generated by the simulated and measured data

Simulated and measured radiation patterns of the ellipsoidal lens have been used to compute the ground power footprints.

Figs. 5.19 and 5.20 show the footprint of cell 1 achieved with, respectively, the simulated and measured radiation pattern. Good agreement between simulations and measurements can also be observed in this case. The contour at -4dB (that delimits the cell boundary) is circular and its diameter is 4.95 km, closely approaching the scenario requirements.

Figure 5.19.: Footprint of cell 1 achieved with the ellipsoidal lens by using the simulated radiation pattern of beam 1. The cell boundary is a circle with 2.475 km radius.

Figs. 5.21 and 5.22 show the footprint of cell 3 achieved with the simulated and measured radiation pattern respectively. A good agreement between simulations and measurements can also be observed in this case. The footprint contour at -4dB is again circular and its diameter is 5.01 km. Fig. 5.21 clearly shows that the elliptical cell shape produced by a symmetric beam (as shown in Fig. 5.7) is fully compensated with the designed lens. Furthermore, the cell is centered in the position expected by Table 1 confirming that in this scenario the ellipsoidal lens has a negligible influence in steering the beam radiated by the primary source.

Figs. 5.19-5.22 also show globally that out of the -12 dB contour the footprint quality degrades in general. This is probably due to the presence of sidelobes, but is of only slight concern here since the region where the shape should be controlled is within the cell boundary.

For the sake of completeness, the shape of the footprints has also been characterized for intermediate cells 2 and 4 (not directly controlled by the optimization process) in order to

Ground Power Footprint, $10\log(P_r\ (x,y)/P_{max})$[dB]

Figure 5.20.: Footprint of cell 1 achieved with the ellipsoidal lens by using the measured radiation pattern of beam 1.

Ground Power Footprint, $10\log(P_r\ (x,y)/P_{max})$[dB]
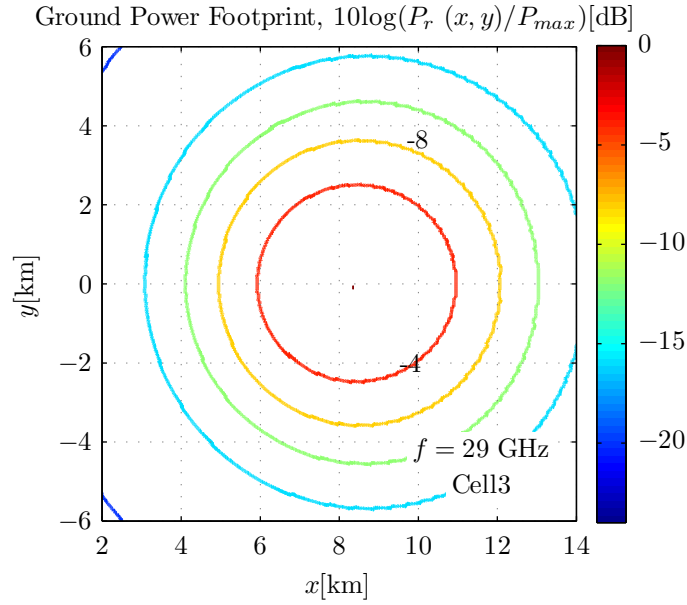
Figure 5.21.: Footprint of cell 3 achieved with the ellipsoidal lens by using the simulated radiation pattern of beam 3. The cell boundary is a circle with 2.505 km radius.

investigate the validity of the proposed strategy. Table 2 summarizes the results for the relevant cells #1 to #4. All the cells now have practically circular footprints and even in the worst-case (cells #2 and #4) the improvement of the axial ratio is evident.

Ground Power Footprint, $10\log(P_r\ (x,y)/P_{max})$[dB]
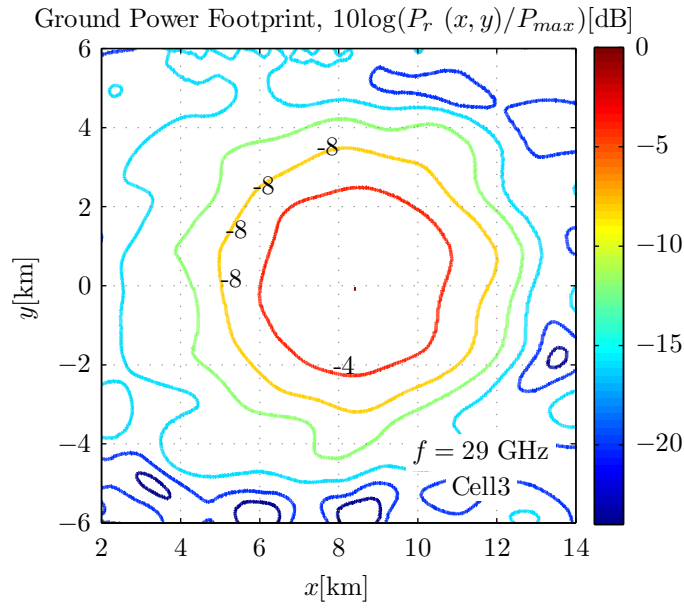
Figure 5.22.: Footprint of cell 3 achieved with the ellipsoidal lens by using the measured radiation pattern of beam 3.

Table 5.2.: *Properties of the most relevant cells.*

i	CAR Spherical	CAR Ellipsoidal	CLA, CSA Spherical [km]	$(\text{P}_{C,i}$ - $\text{P}_{A,i})$, $2(\text{P}_{B,i}\text{-CC}_i)$ Ellipsoidal [km]
1	1	1	5, 5	4.95, 4.95
2	1.022	0.985	5.11, 5.22	4.93, 5
3	1.084	1	5.42, 5.88	5.01, 5.01
4	1.064	0.990	5.32, 5.66	4.95, 5

5.6.3. Application to more demanding scenarios [42]

As witnessed in table 1 the scenario that originally motivated this chapter implies footprints that deviate only slightly from a circular shape (max axial ratio to be corrected 8.4%) and are therefore not very challenging. In this section, we show the capabilities of the prolate ellipsoidal lens design procedure developed in this chapter to deal with much more elongated cells. To this purpose, we select a scenario in which the antenna operates at 12 km altitude (instead of 21 km) and the most critical cells are characterized by a lower elevation angle θ_c = 33.7°. This corresponds to cells which are 8 km offset from the center of the cluster. Fig. 5.23 shows the ground footprint achieved when a spherical Teflon lens of 60 mm diameter is used. The cell boundary is characterized by an ellipticity of 23%. According to the procedure presented in Section 5, a prolate ellipsoidal lens with $LAR = 1/\cos\theta_c = 1.120$ should correct this cell ellipticity by generating asymmetric beams. Fig. 5.24 shows the cell shape achieved with such a modified lens. Despite the high zenith angle, the cell shape is now practically circular with a percent CAR lower than 0.5%. In this particularly extreme situation, a slight beam steering, apparent in Fig. 5.24, is introduced by the elliptical lens. However this small value (around 1 degree) can easily be compensated by a mechanical repositioning of the corresponding feed.
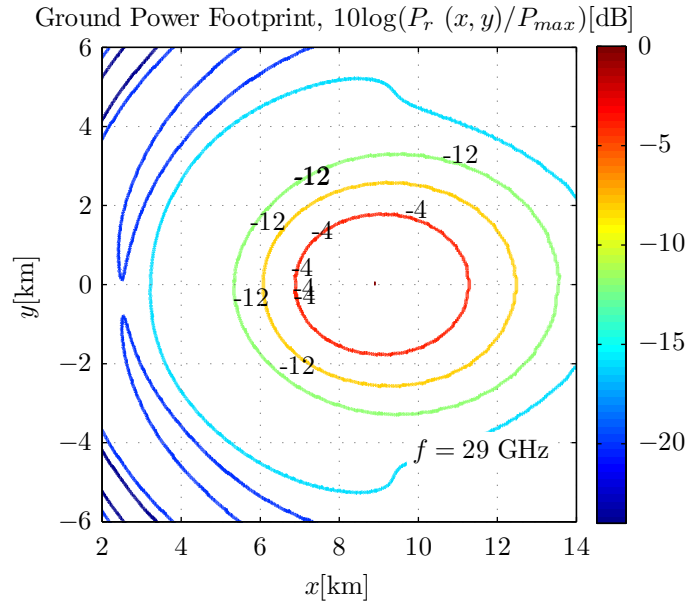
Figure 5.23.: Original footprint for the very low elevation angle considered in the scenario of section 4.1 spherical lens produced a very elongated -4 dB footprint with an ellipticity of 1.230.

Ground Power Footprint, $10\log(P_r\,(x,y)/P_{max})$[dB]
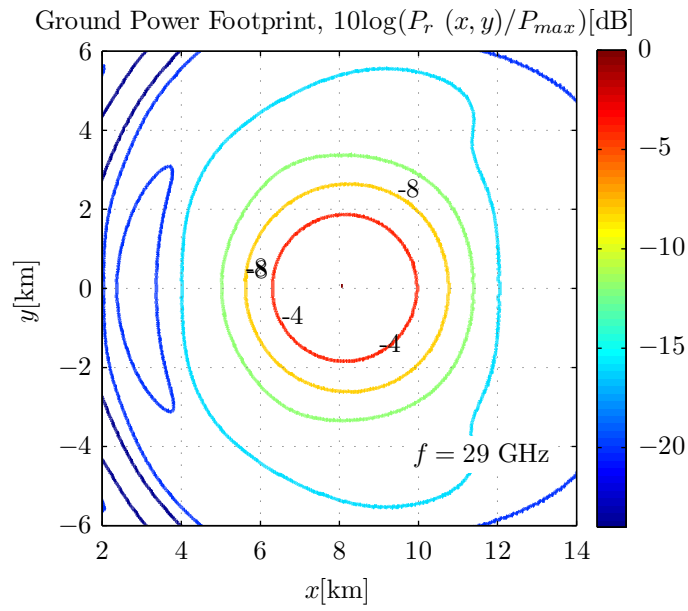
Figure 5.24.: Improved footprint for the very low elevation angle considered in the scenario of section 4. The new prolate ellipsoidal lens produces an almost circular -4 dB footprint with an ellipticity of 1.005.

5.7. Conclusion

The capabilities of a Ka-band prolate ellipsoidal shaped dielectric lens antenna for generating asymmetric beams producing circular ground footprints have been investigated. Our analysis revealed that the problem of elongated footprints generated by spherical lenses located in traditional aerial platforms can be solved via the optimization of the lens shape. The new ellipsoidal shape is obtained with a set of simple analytical design equations, eventually to be enhanced by full-wave optimizations. A properly designed prolate ellipsoidal lens can simultaneously and efficiently focus beams radiated by several independent waveguide feeds adequately placed around its surface. The comparison between the ellipsoidal lens and the spherical lens (both optimized to operate properly in the same scenario) has shown that the ellipsoidal lens improves the circularity of all the beam footprints generated by the antenna, which is of particular interest in airborne-based communication systems.

The proposed lens design procedure can be applied for both small and quite large values of the footprint cell elongation. Moreover, the use of prolate ellipsoid lenses does not increase the technological complexity nor the required computational resources during the antenna design process.

Minor collateral effects of the ellipsoidal lens are a small beam steering (but only at very low elevation angles), easily compensated by adjusting the feed angle, a slight change in focal distances and the deformation of the footprints for lower power levels outside the -4dB boundary. This last effect is probably due to the lens sidelobes. It could be reduced eventually by using a stratified lens and by adding a matching layer, which would also increase the lens efficiency [43–45]. These questions are out of the scope of this thesis but should be in that of further research.

References

[1] K. Katzis and D. Grace, "Inter-high-altitude-platform handoff for communications systemswith directional antennas," *Radio Science Bulletin*, no. 330, pp. 29-38, March 2010.

[2] I. R. Palma-Lazgare and J. A. Delgado-Penín, "WiMAX HAPS-based downlink performances employing geometrical and statistical propagation-channel characteristics," *Radio Science Bulletin*, no. 330, pp. 50-60, March 2010.

[3] C. Abella, J. Peces, M. Mariín, J. Martinez, and K. Markus, "Development of a compact antenna for global earth coverage," *in Proc. 23rd Eur. Microwave Conf.*, Madrid, Spain, pp. 906-908, Oct. 1993.

[4] E. Carrasco, M. Arrebola, J. A. Encinar, and M. Barba, "Demonstration of a shaped beam reflectarray using aperture-coupled delay lines for LMDS central station antenna," *IEEE Trans. Antennas Propagat.*, vol. AP-56, pp. 3103-3111, Oct 2008.

[5] G. L. Charvat, L. C. Kempel, E. J. Rothwell, C. M. Coleman, and E. L. Mokole, "An ultrawideband (UWB) switched-antenna-array radar imaging system," *presented at IEEE Int. Symp. on Phased Array Systems and Technology (ARRAY)*, pp. 543-550, Oct 2010.

[6] S. Rao, M. Tang, C.-C. Hsu, and J. Wang, "Advanced antenna technologies for satellite communication payloads," *1st European Conference on Antennas and Propagation*, 2006.

[7] F. Averty, A. Louzir, J. F. Pintos, P. Chambelin, C. Person, G. Landrac, and J. P. Coupez, "Cost effective antenna for LEO-satellites communication system using a homogeneous lens," *Antennas and Propagation Society International Symp., 2004 IEEE*, vol.1, pp. 671-674, June 2004.

[8] Z. Xu, G. White, and Y. Zakharov, "Optimization of beam pattern of high-altitude platform antenna using conventional beamforming," *Proc. IEE*, vol. 153, no.6, pp.865-870, Dec. 2006.

[9] N. J. G. Fonseca and J. Sombrin, "Multi-beam reflector antenna system combining beam hopping and size reduction of effectively used spots," *IEEE Trans. Antennas Propagat.*, vol. AP-54, pp. 88-99, Apr 2012.

[10] S.-M. Lin, Y.-Q. Wang, and P.-L. Shen, "Phase-only synthesis of the shaped beam patterns for the satellite planar array antenna," *Proc. IEEE*, pp.331-334, 2000.

[11] J. Martínez-Lorenzo, "A shaped and reconfigurable reflector antenna with sectorial beams for LMDS base station," *IEEE Trans. Antennas Propag.*, vol. 54, no. 4, Apr. 2006.

[12] T. Koleck, "Active antenna coverage synthesis for GEO satellite using genetic algorithm," *in Proc. Int. Symp. on Antennas and Propagat.*, pp. 142-144, 2003.

[13] J. Thornton, "A low sidelobe asymmetric beam antenna for high altitude platform communications," *IEEE Microw. Wireless Comp. Lett.*, vol. 14, no. 2, pp. 59-61, Feb. 2004.

[14] F. J. Villegas, "Parallel genetic-algorithm optimization of shaped beam coverage areas using planar 2-D phased arrays," *IEEE Trans. Antennas Propagat.*, vol. AP-58, pp. 604-608, Feb. 2010.

[15] J. Córcoles, J. Rubio, and M. . González, "Spherical-wave-based shaped-beam field synthesis for planar arrays including the mutual coupling effects," *IEEE Trans. Antennas Propagat.*, vol. AP-59, pp. 2872-2881, Aug. 2011.

[16] Y. Liu, Q. H. Liu, and Z. Nie, "Reducing the number of elements in the synthesis of shaped-beam patterns by the forward-backward matrix pencil method," *IEEE Trans. Antennas Propagat.*, vol. AP-55, pp. 1745-1753, June 2007.

[17] J. R. Costa, E. B. Lima, and C. A. Fernandes, "Compact beam-steerable lens antenna for 60-GHz wireless communications," *IEEE Trans. Antennas Propagat.*, vol. AP-57, pp. 2926-2933, Oct. 2009.

[18] H. Chreim, R. Chantalat, M. Thévenot, U. Naeem, S. Bila, T. Monédière, B. Palacin, Y. Cailloce, G. Caille, and P. D. Maagt, "An enhanced Ka-band reflector focal-plane array using a multifeed EBG structure," *IEEE Antennas and Wireless Propagat Lett.*, vol. 9, pp. 1152-1156, 2010.

[19] P. F. M. Smulders, "Exploiting the 60 GHz band for local wireless multimedia access: Prospects and future directions," *IEEE Commun. Mag.*, vol. 40, no. 1, pp. 140-147, Jan. 2002.

[20] J. R. Costa, C. A. Fernandes, G. Godi, R. Sauleau, L. L. Coq, and H. Legay, "Compact Ka-band lens antennas for LEO satellites," *IEEE Trans. Antennas Propag.*, vol. 56, pp. 1251-1258, May 2008.

[21] M. Letizia, J.-F. Zürcher, B. Fuchs, C. Z. Gastón, and J. Mosig, "Circularly polarized multi-beam lens antenna system. Comparison between 2 polarizers," *proc. EuCAP 2012*, 6th European Conference on Antennas and Propagation, 2012.

[22] R. Sauleau and B. Barès, "A complete procedure for the design and optimization of arbitrarily-shaped integrated lens antennas," *IEEE Trans. Antennas Propagat.*, vol. 54, no. 4, pp. 1122-1133, Apr. 2006.

[23] A. Rolland, R. Sauleau, and L. L. Coq, "Flat-shaped dielectric lens antenna for 60-GHz applications," *IEEE Trans. Antennas Propagat.*, vol. 59, no. 11, pp. 4041-4048, Nov. 2011.

[24] G. Godi, R. Sauleau, L. L. Coq, and D. Thouroude, "Design and optimization of three-dimensional integrated lens antenna with genetic algorithm," *IEEE Trans. Antennas Propagat.*, vol. 55, no. 3, pp. 770-775, Mar. 2008.

[25] N.-T. Nguyen, R. Sauleau, and L. L. Coq, "Reduced-size double-shell lens antenna with flat-top radiation pattern for indoor communications at millimeter waves," *IEEE Trans. Antennas Propagat.*, vol. 59, no. 6, pp. 2424-2429, Jun. 2011.

[26] C. A. Fernandes, "Shaped dielectric lenses for wireless millimeterwave communications," *IEEE Trans. Antennas Propagat.*, vol. 41, no. 5, pp. 141-150, Oct. 1999.

[27] J. R. Costa, C. A. Fernandes, G. Godi, R. Sauleau, L. L. Coq, and H. Legay, "Compact Ka-band lens antennas for LEO satellites," *IEEE Trans. Antennas Propagat.*, vol. 56, no. 5, pp. 1251-1258, May 2008.

[28] B. Chantraine-Barès, R. Sauleau, L. L. Coq, and K. Mahdjoubi, "A new accurate design method for millimeter-wave homogeneous dielectric substrate lens antennas of arbitrary shape," *IEEE Trans. Antennas Propagat.*, vol. 53, no. 3, pp. 1069-1082, Mar. 2005.

[29] T. Komljenovic, R. Sauleau, Z. Sipus, and L. L. Coq, "Layered circular-cylindrical dielectric lens antennas-Synthesis and height reduction technique," *IEEE Trans. Antennas Propagat.*, vol. 58, no. 5, pp. 1783-1788, May 2010.

[30] M. Letizia, B. Fuchs, C. Zorraquino, J. F. Zürcher, and J. R. Mosig, "Oblique incidence design of meander-line polarizers for dielectric lens antennas," *Progress in Electromangeics Research*, PIER 45, 309-335, 2012.

[31] S. Haykin, "Communication Systems," *4th Ed., John Wiley and Sons*, pp. 518-522, 2001.

[32] A. Aragon-Zavala, J. L. Cuevas-Ruiz, and J. A. Delgado-Penin, "High-Altitude Platforms for Wireless Communications," *John Wiley and Sons*, pp. 5-15, 2008.

[33] M. Letizia, B. Fuchs, A. Skrivervik, and J. Mosig, "Circularly Polarized Lens Antenna System Providing Multibeam Radiation Pattern for HAPS," *Radio Science Bulletin*, no. 330, pp. 18-28, March 2010.

[34] M. Letizia, J.-F. Zürcher, B. Fuchs, J. Mosig, and A. Skrivervik, "Circularly Polarized Lens Antenna System for High Altitude Platforms (HAPS)," *proc. EuCAP 2011*, 5th European Conference on Antennas and Propagation, 2011.

[35] C. A. Balanis, "Antenna theory," *New York: John Wiley and Sons*, pp. 45-86, 575-560, 2nd Ed., 1997.

[36] K. Chang, "Handbook of microwave and optical components," *vol. 1 Microwave passive and antenna components*, Wiley, New York, Chapitre 11, 1989.

[37] T. Cheston and E. Luoma, "Constant-K lenses," *Emerson & Cuming*, APL Technical Digest, Mar-Apr. 1963.

[38] B. Schoenlinner, X. Wu, J. Ebling, G. Eleftheriades, and G. Rebeiz, "Wide-scan spherical-lens antennas for automotive radars," *IEEE Trans. Microwave Theory Tech.*, vol. 50, no. 9, pp. 2166-2175, Sept. 2002.

[39] B. Schoenlinner and G. Rebeiz, "Compact multibeam imaging antenna for automotive radars," *IEEE Microwave Theory Tech. Symposium*, Seattle, WA, pp. 1373-1376, Jun 2002.

[40] J. Sanford, "Scattering by spherically stratified microwave lens antennas," *IEEE Trans. Antennas Propagat.*, vol. 42, no. 5, pp. 690-698, 1994.

[41] "www.cst.com."

[42] M. Letizia, J. F. Zürcher, and J. R. Mosig, "Prolate ellipsoidal lens for antenna systems providing multiple asymmetric beams ," *Progress in Electromangeics Research*, PIER 48, 289-312, 2013.

[43] I. Gresham, N. Jain, T. Budka, A. Alexanian, N. Kinayman, B. Ziegner, S. Brown, and P. Staecker, "A compact manufacturable $76 - 77$ GHz radar module for commercial ACC applications," *IEEE Trans. Microwave Theory Tech.*, vol. 49, no. 1, pp. 44-58, Jan. 2001.

[44] R. Sauleau, C. A. Fernandes, and J. R. Costa, "Review of lens antenna design and technologies for mm-wave shaped-beam applications," *Invited paper to the 11th Int. Symp. Antenna Technology and Applied Electromagnetics*, Saint Malo, France, 15-17 Juin, 2005.

[45] G. Godi, R. Sauleau, and D. Thouroude, "Performance of reduced size substrate lens antennas for millimeter-wave communications," *IEEE Trans. Antennas Propag.*, vol. 53, no. 4, pp. 1278-1286, Apr. 2005.

6. Conclusion and perspectives

The last decade has been characterized by a growing interest in high altitude platform stations (HAPS) and their related telecommunication systems. The strategy behind HAPS envisages the use of such platforms as complementary systems that would increase the capacity of existing telecommunication infrastructures (e.g. terrestrial network and satellites). From the frequency point of view, the migration towards higher frequencies, providing larger bandwidths and hence higher channel capacities, is a continuous trend and perfectly matches the HAPS concept. Nowadays, the Ka-band is considered very promising for this type of application since it provides a non-congested spectrum segment, in which broadband services can be delivered by HAPS from the stratosphere.

From the antenna payload point of view, typical HAPS communication systems scenarios require the use of high gain circularly polarized multi-beam antennas. Multiple beams allow for switching between different antenna footprints while increasing the capacity of the communication channel. On the other hand, circular polarization is the standard solution to overcome misalignments between transmitter and receiver and to mitigate multipath problems. Further challenges are posed by the coupling between different antenna elements and the high power level needed in such communications. Since the antenna is supposed to fly on quasi stationary platforms, the antenna weight and its mechanical design are issues that cannot be ignored.

Despite the great academic and industrial interest in this subject, an on-board antenna design for HAPS had not been developed before now. The Swiss-CTI project FEASANT (involving the company StratXX, the research institute Centre Suisse d'Electronique et Microtechnique SA (CSEM) and the Laboratory of Electromagnetics and Acoustics (EPFL-LEMA)) offered our laboratory the possibility to design, prototype and test an on-board antenna for HAPS. This is the main driver of the thesis research.

6.1. Thesis achievements

Among the salient aspects of HAPS communication systems and the associated antenna topics, identified in Chapter 2, the achievements of this thesis can be summarized as follows:

- The benchmark circularly polarized multibeam antenna design for HAPS (Chapter 3).

- The use of an external polarizer for multibeam antenna systems (Chapter 4).

187

- The use of prolate ellipsoidal lens to tailor the ground power footprint generated by the on-board antenna (Chapter 5).

Each of these aspects has resulted in a paper being published in a leading peer-reviewed technical journal. These achievements are briefly assessed and discussed here below.

The benchmark circularly polarized multibeam antenna design for HAPS

Chapter 3 describes the design of the on-board antenna system and explains the proposed solution. The antenna system consists of a dielectric lens illuminated by identical radiators. Each radiator comprises of a circular waveguide terminated with a short horn and supporting a polarizer internally. Although the antenna solution investigated in this chapter is based on a set of well-known elements (dielectric lens, circular horn, septum polarizer, circular waveguide), the proposed combination constitutes a novelty in this domain and no similar antenna design for HAPS communications was previously available in literature.

The use of an external polarizer for multibeam antenna systems

The antenna system proposed in Chapter 3 is fully operational and it has been considered a benchmark in this work. Chapter 4 presents an antenna system design for HAPS based on the use of an external polarizer. The strategy to generate multiple beams is identical to that proposed in Chapter 2, but the polarizer is placed outside the feed, more precisely after the lens (see Fig. 4.19). The two polarizer solutions (that with septum polarizers located inside the feeds and that with a meander-line polarizer placed after the lens) have been compared. The innovation in this chapter also resides in the proposed method to design the meander-line (external) polarizer. This method combines a transmission line model and a full wave unit-cell analysis for the efficient design of meander-line polarizers operating with waves impinging on its surface with an incident field θ_{inc} parallel to the polarizer surface and at an arbitrary oblique incidence angle. This is the situation most currently encountered in lens antenna subsystems and in many multi-beam antenna systems, and the proposed approach leads to rapid optimization and parametric studies of these antennas.

The use of prolate ellipsoidal lens to tailor the ground power footprint generated by the on-board antenna

Controlling the beam patterns of a multi-beam antenna system is often a key issue of the design. In Chapter 5, we propose a multi-beam lens antenna design in which the beam symmetry is controlled by acting on the lens shape, with the goal of generating circular footprints in the entire area covered. Indeed, traditional symmetric beams launched from aerial stations would produce elliptical ground footprints in the external areas of the cluster

where the azimuth angle is important. With the proposed lens prototype, the natural elongation of the beam footprints, can be mastered and kept at low level. The proposed method uses a full-wave time-domain software tool to optimize the lens. The usually prohibitive computer effort is greatly reduced here, thanks to a set of design guidelines that suggest convenient initial values of the optimization parameters. As proof of concept, a lens prototype was designed following the proposed procedure, built and measured. The original procedure introduced in this chapter is an innovation in the lens antenna domain and is also applicable to many other lens antenna subsystems and scenarios.

6.2. Perspectives

This thesis has proposed several innovative solutions for the implementation of on-board antenna systems for HAPS, useful for industrial and scientific applications. The development of these solutions suggested new ideas, opened issues and potential improvements that are discussed in this section and should, hopefully, inspire further research activities.

From the theoretical point of view, potential improvements might be assessed considering the following aspects:

- The method introduced in Chapter 4 to design meander-line polarizers works properly for cases in which the wave impinges the polarizer surface obliquely with its incident field parallel to the polarizer surface. However, in more complex scenarios, the field impinging the polarizer might have a component orthogonal to the polarizer surface and the proposed method must be modified to also include this aspect.

- The method used to design the prolate ellipsoidal lens has been validated with a homogeneous lens which should be extended to work with stratified lenses.

From the antenna design point of view, potential improvements might be assessed considering the following aspects:

- The antenna matching is extremely important especially when the antenna requirements call for high power and circular polarization. The axial ratio can indeed be improved by acting on the coaxial-to-waveguide transition (i.e., adding waveguide posts in the transition proximity) in order to fine-tune the mode launched in the waveguide feed.

- The antenna efficiency could be improved if reflections on the lens surface are reduced. This could be achieved by adding a matching (quarter-wavelength) layer around the lens. However, the presence of this layer must be compatible with the arrangement of feeds in the lens proximity. Furthermore, the eventual benefit that this layer, in terms of EM performances of the antenna, should also be evaluated from the mechanical point of view. Indeed, at mm-waves, this layer is very thin (≈ 0.25 mm) and very soft (a foam-like material must be used to keep the dielectric constant around $\epsilon_r \approx 1.45$).

- The use of a conformal external polarizer might improve the circular polarization of the antenna beams characterized by a high azimuth angle (obliquely impinging to the polarizer surface). Mechanical issues might rise when assembling the diverse layers of the polarizer, since the alignment of all the parts is an issue and, mechanical tolerances in Ka-band are critical.

Appendices

A. Geometries of the investigated antenna system

For the sake of completeness, there is a collection of technical drawings and pictures pertaining to the construction of the lens antenna subsystem and of its measurement setup in this appendix.
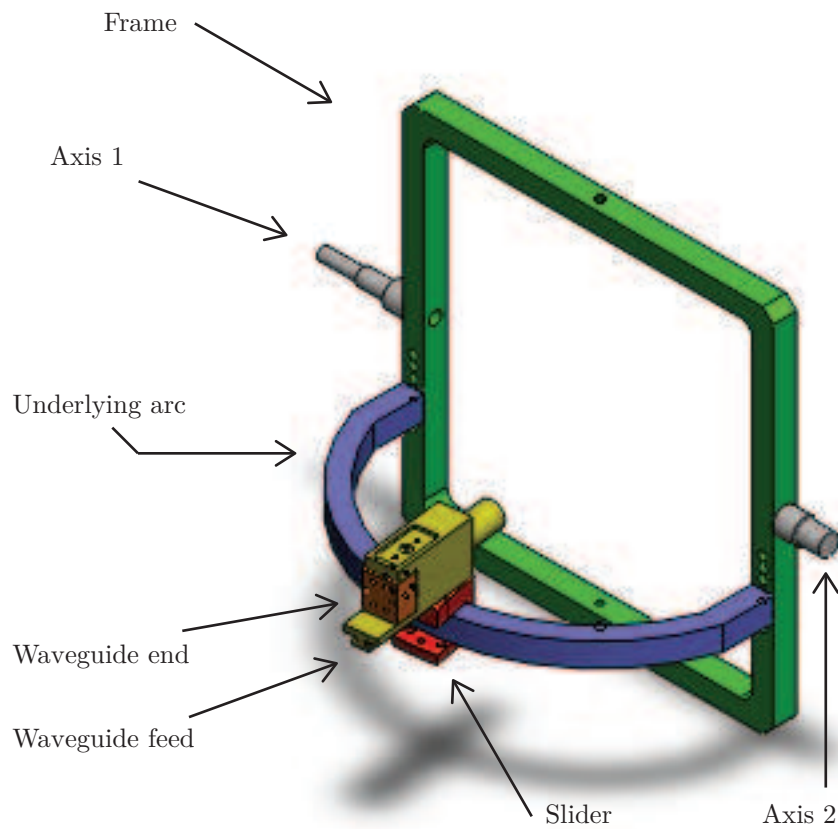
Figure A.1.: Lens frame assembly.
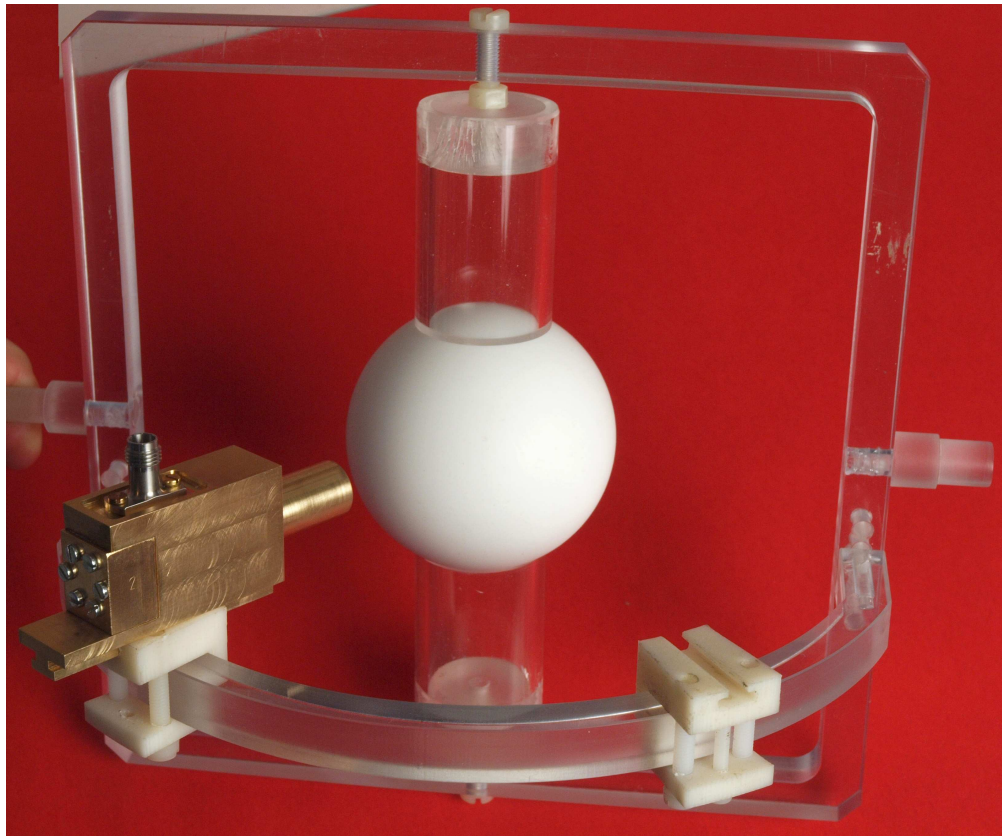
Figure A.2.: Lens frame assembly.
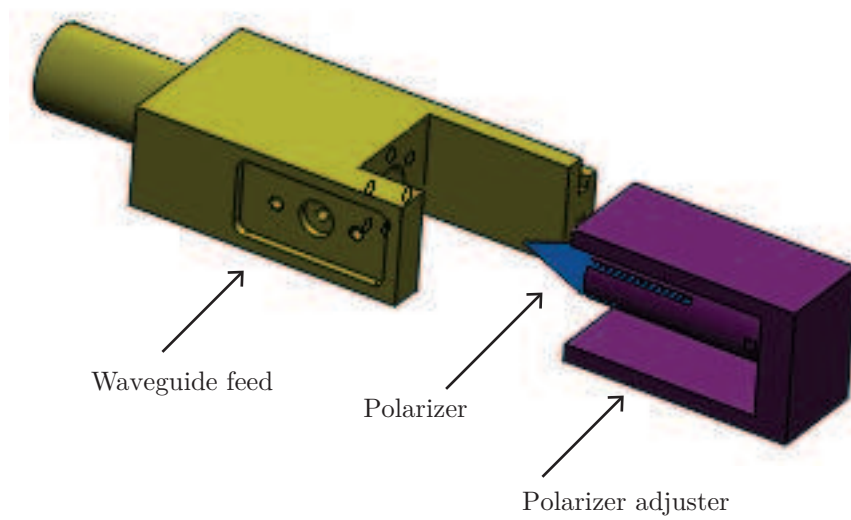
Figure A.3.: Polarizer and adjuster tool.
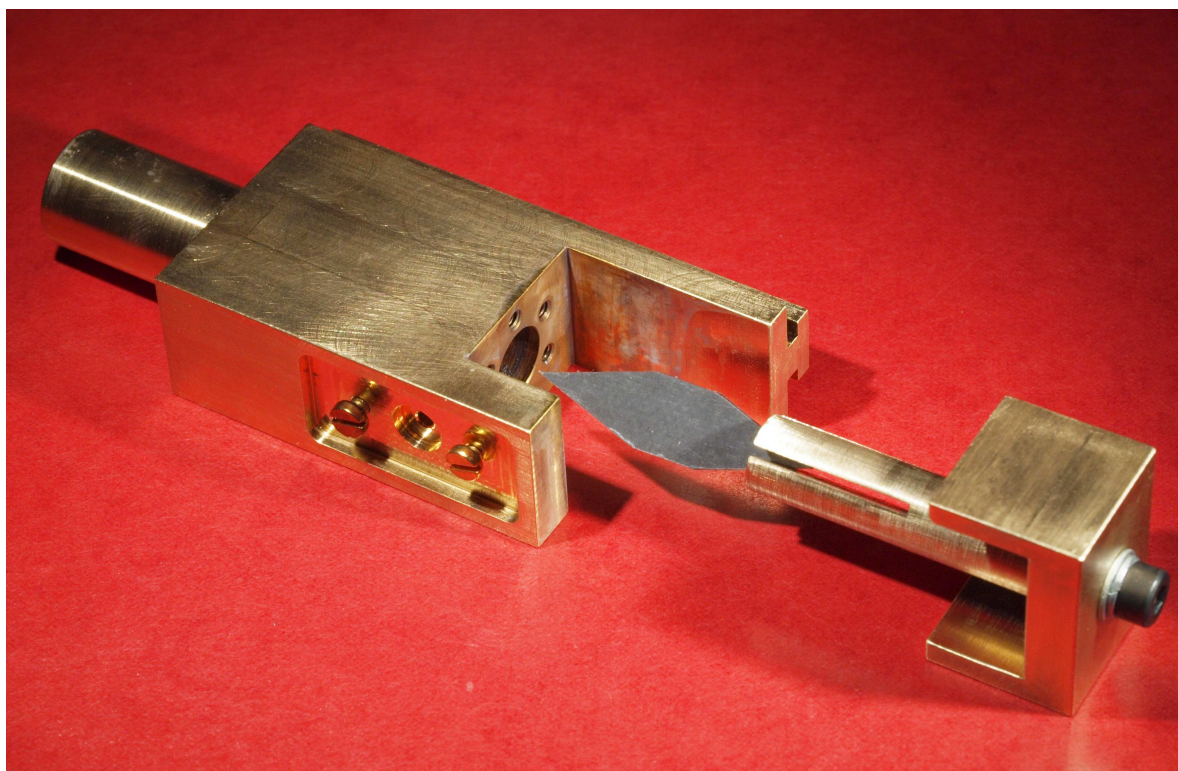
Figure A.4.: Polarizer and adjuster tool.
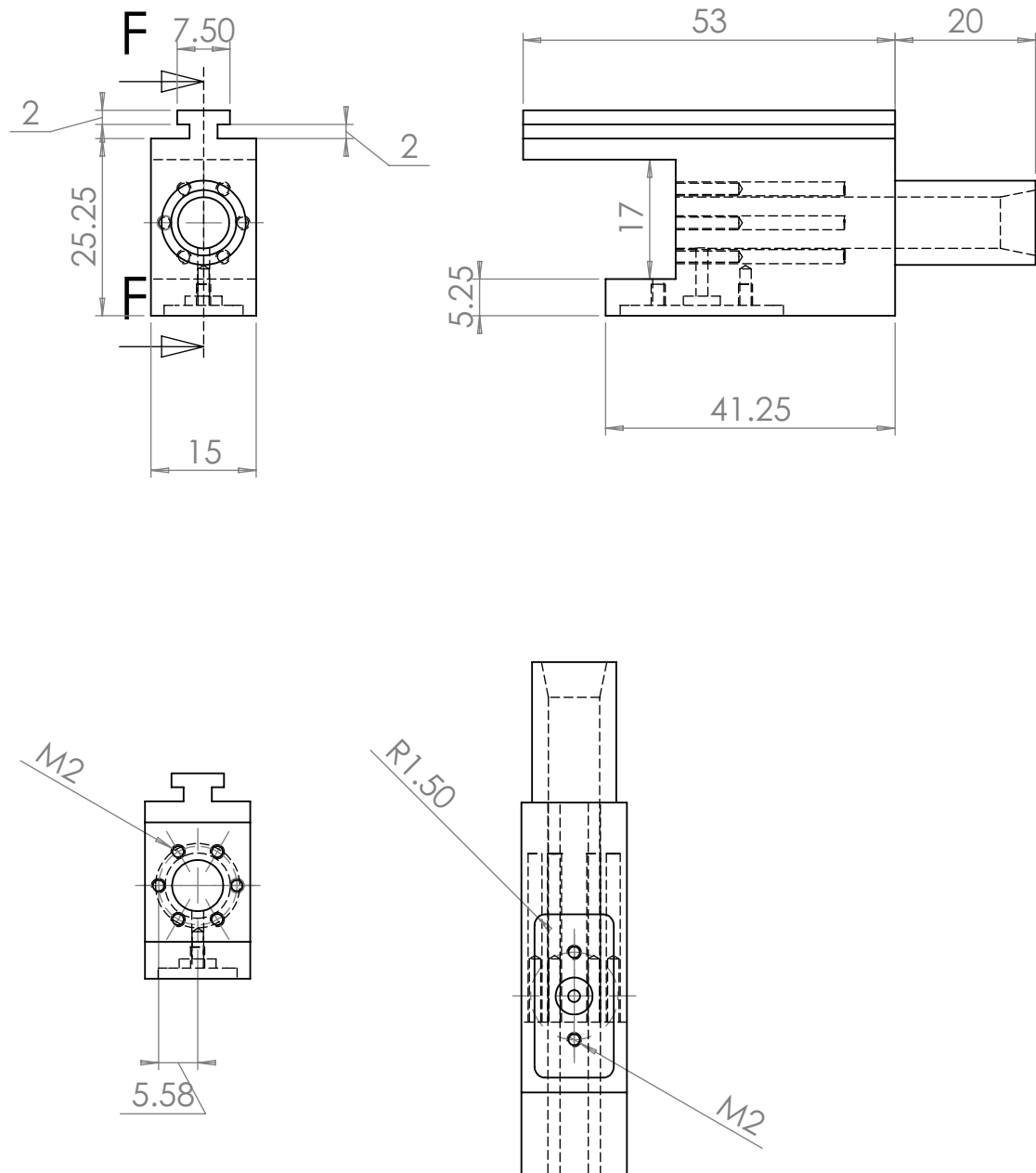
Figure A.5.: Waveguide feed.
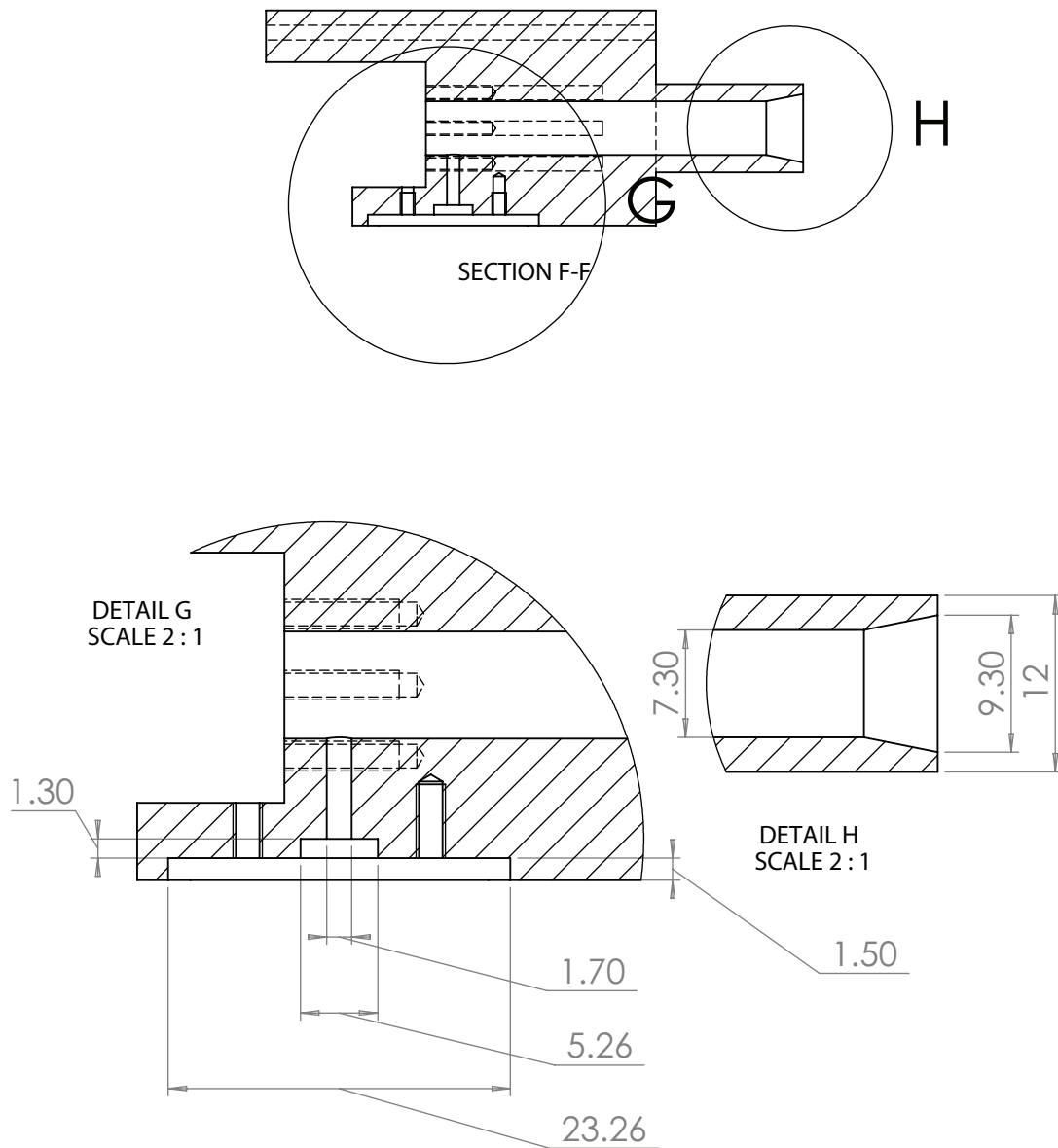
Figure A.6.: Waveguide feed. Cutview
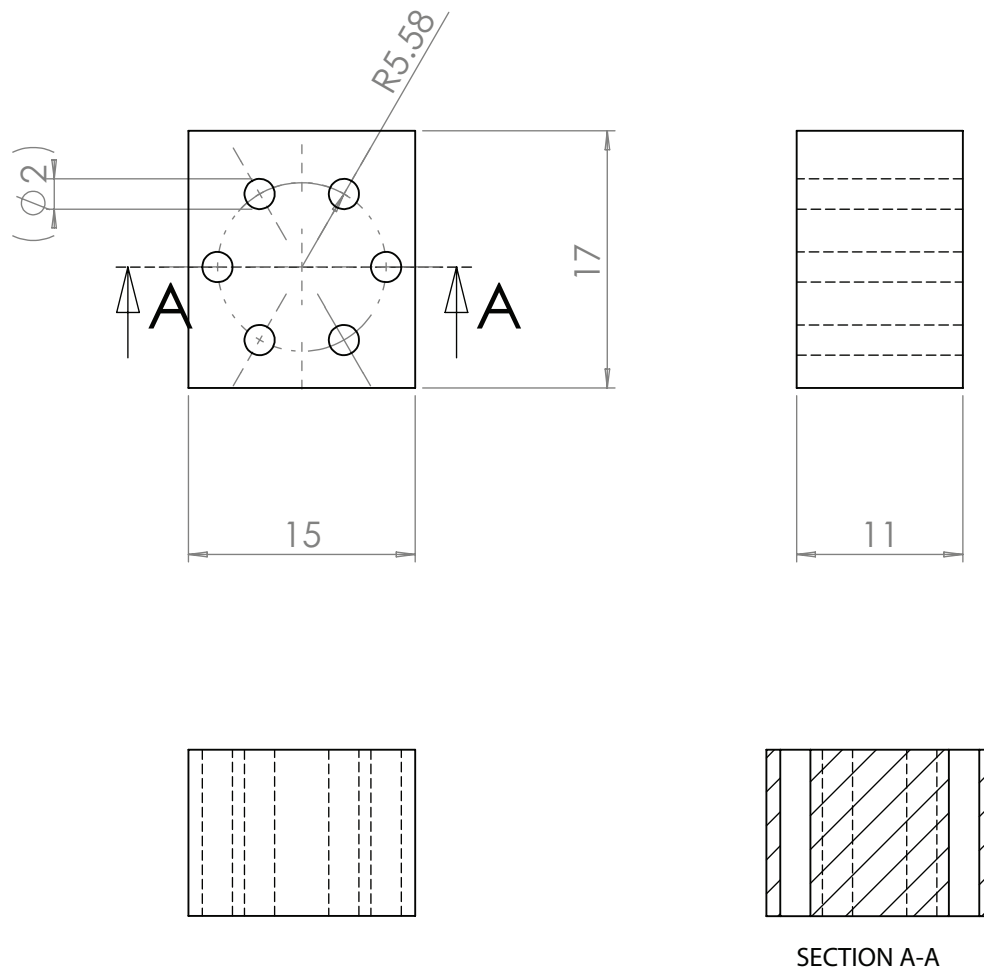
Figure A.7.: Waveguide end.
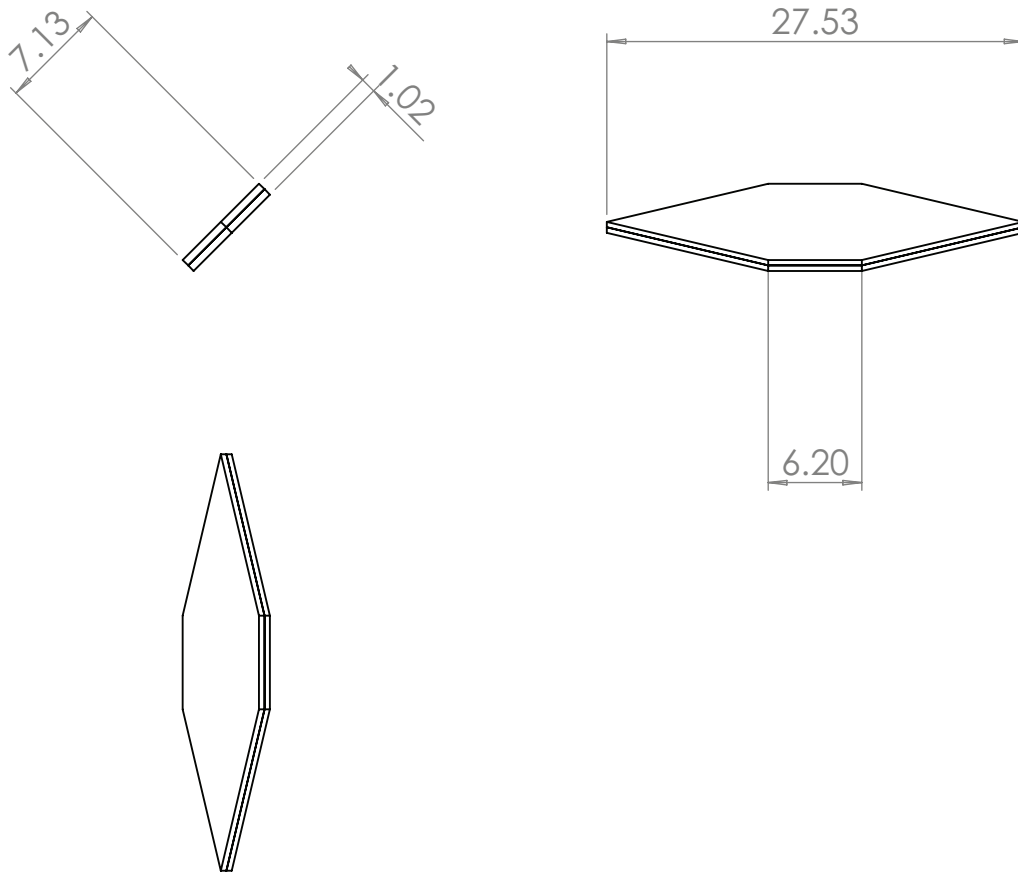
Figure A.8.: Internal septum polarizer used in the lens waveguide feed. See also Fig. A.1.
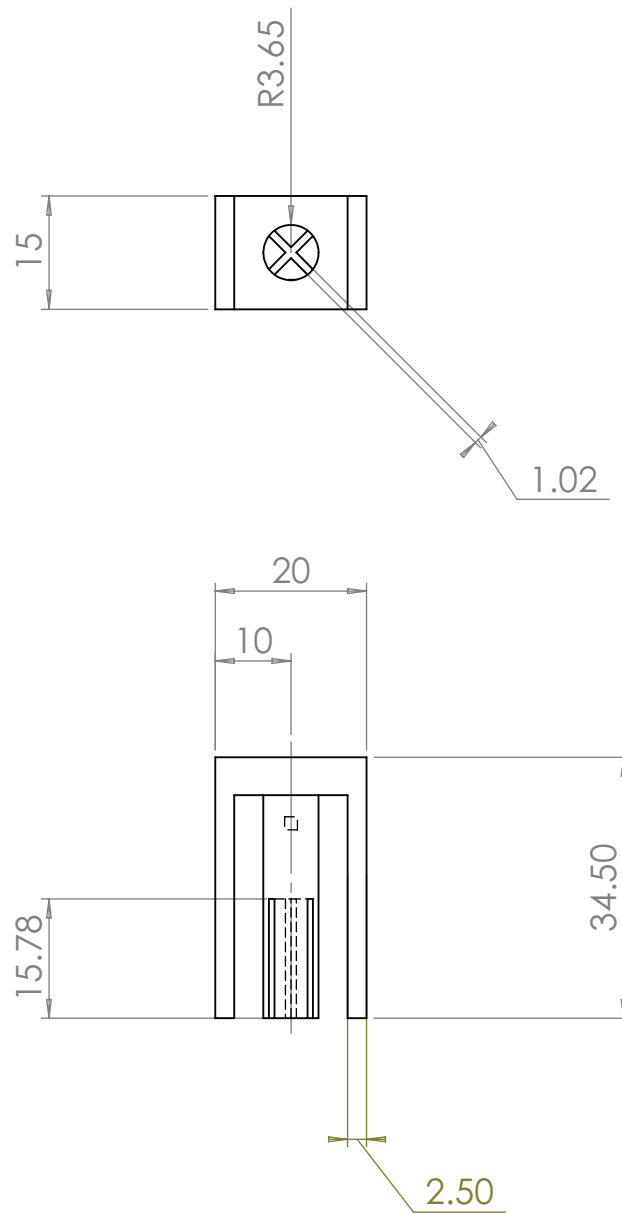
Figure A.9.: Polarizer adjuster tool. This tool is used to adjust the septum polarizer inside the waveguide feed. See Fig.A.4
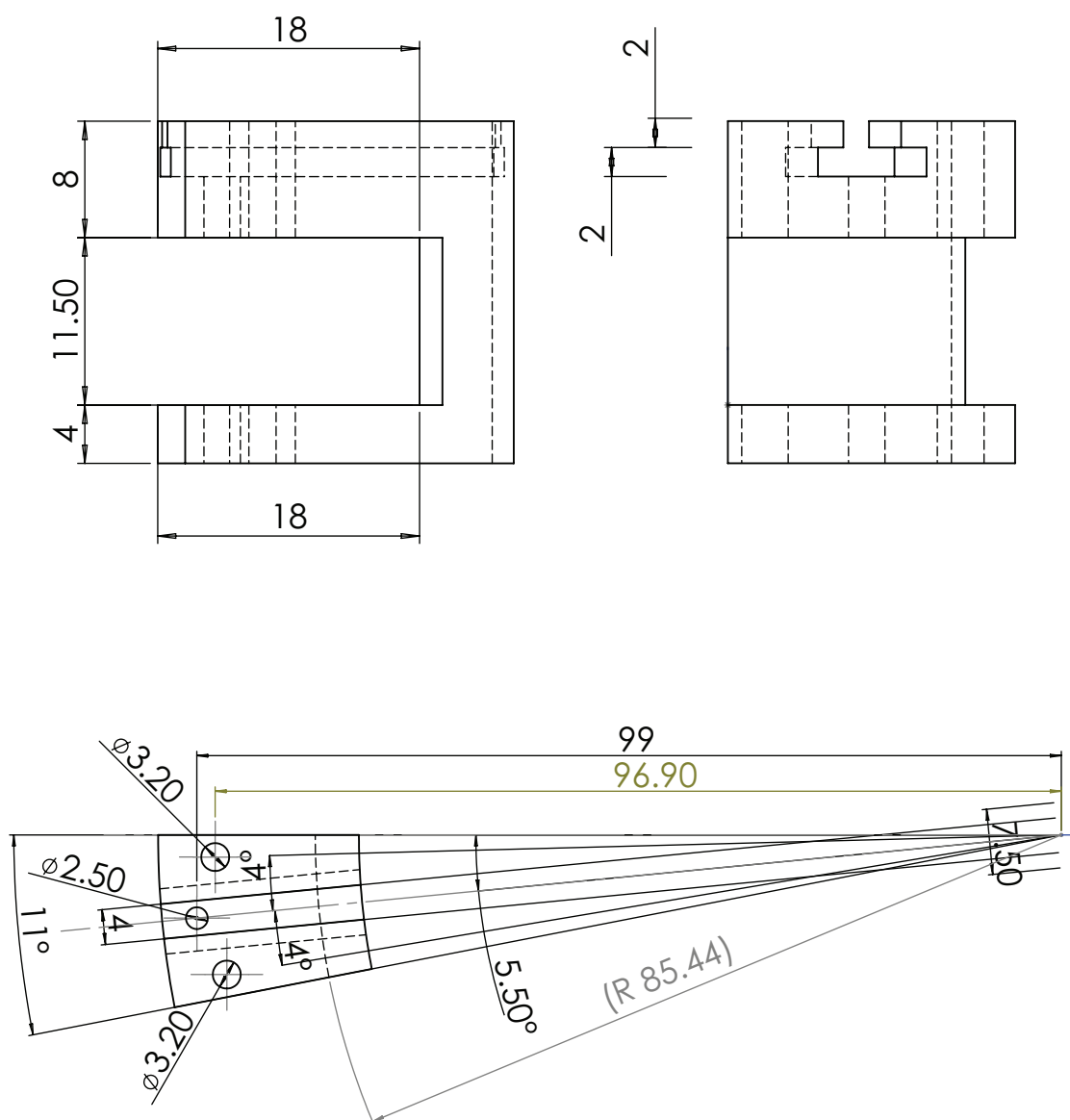
Figure A.10.: Slider. This tool allows for movements of the feed around the lens. See also Fig. A.1.
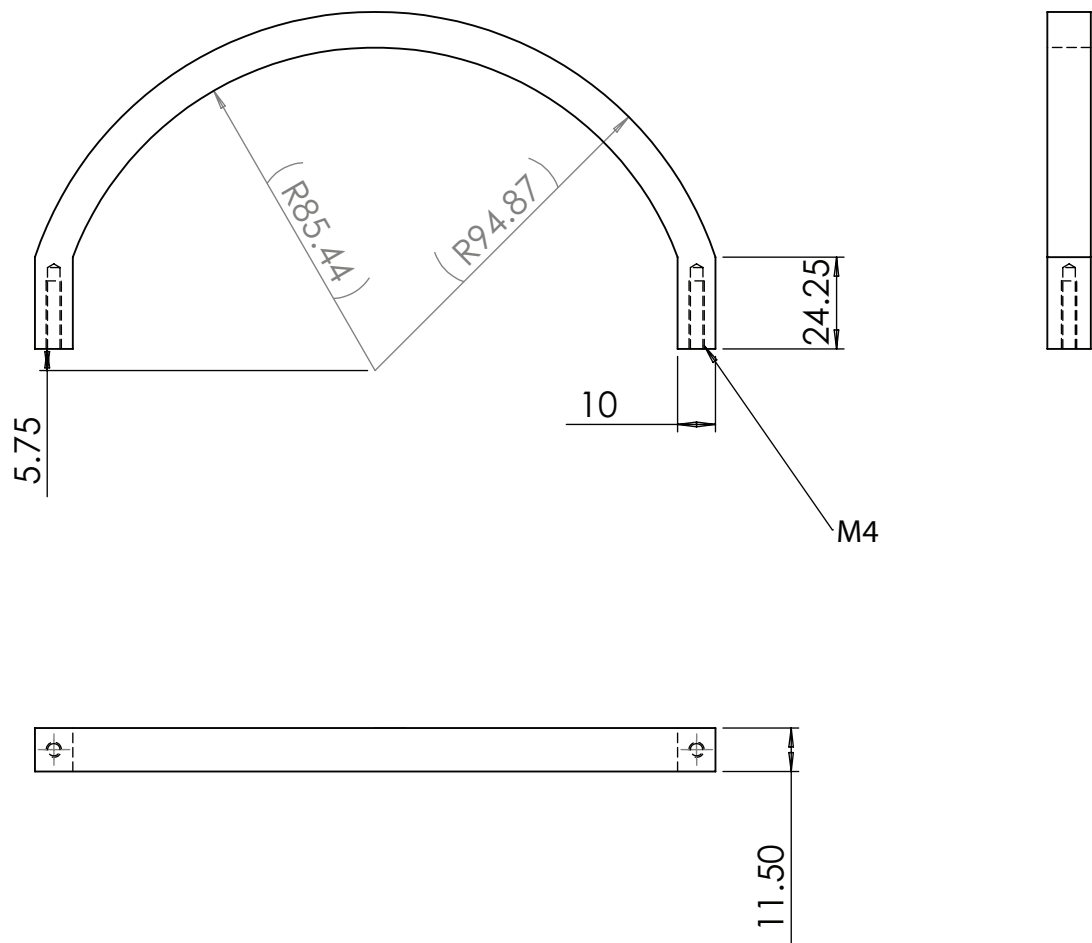
Figure A.11.: Underlying arc. This tool allows for movements of the feed around the lens. See also Fig. A.1
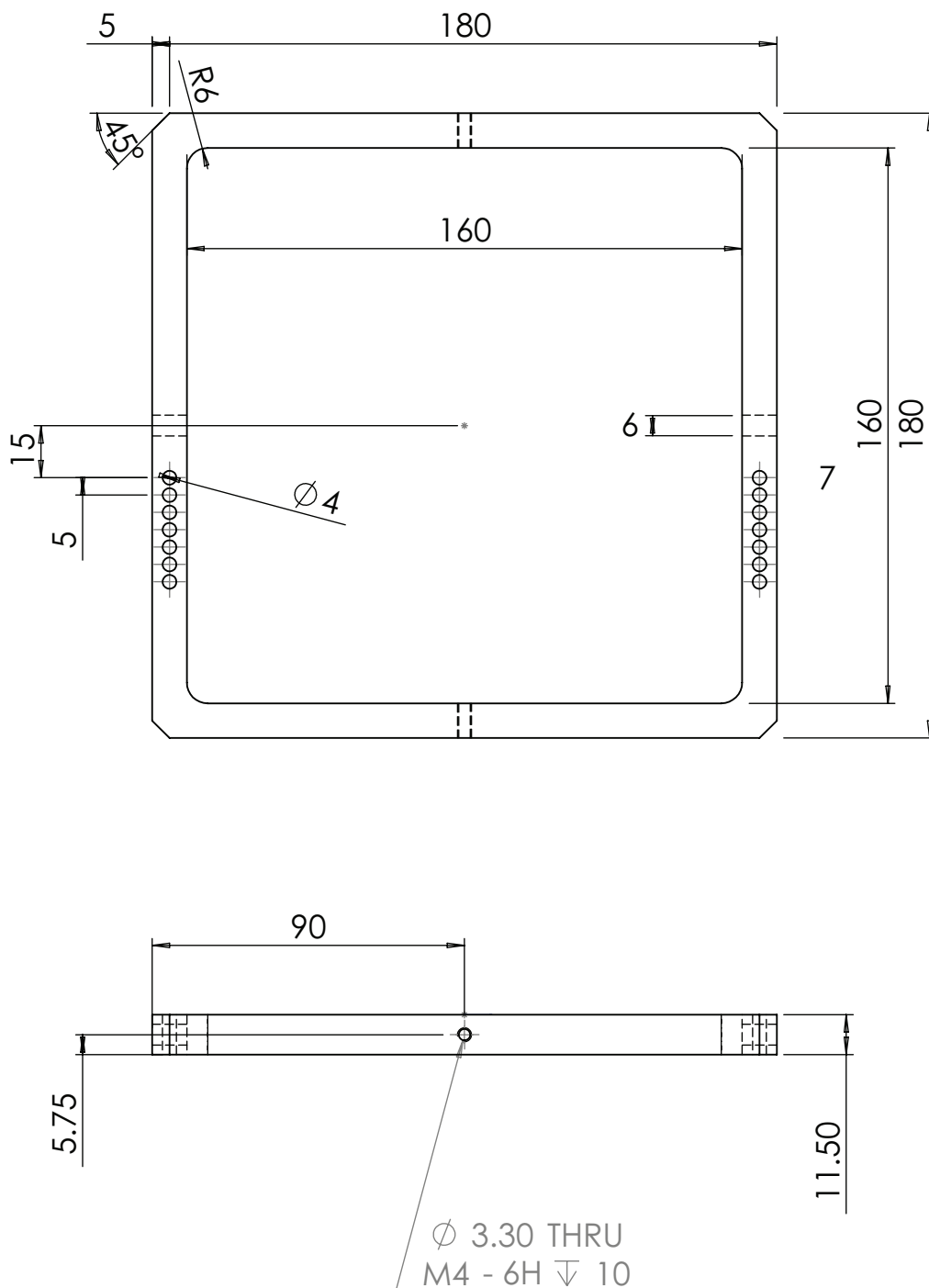
Figure A.12.: Frame of the lens assembly. See also Fig. A.1
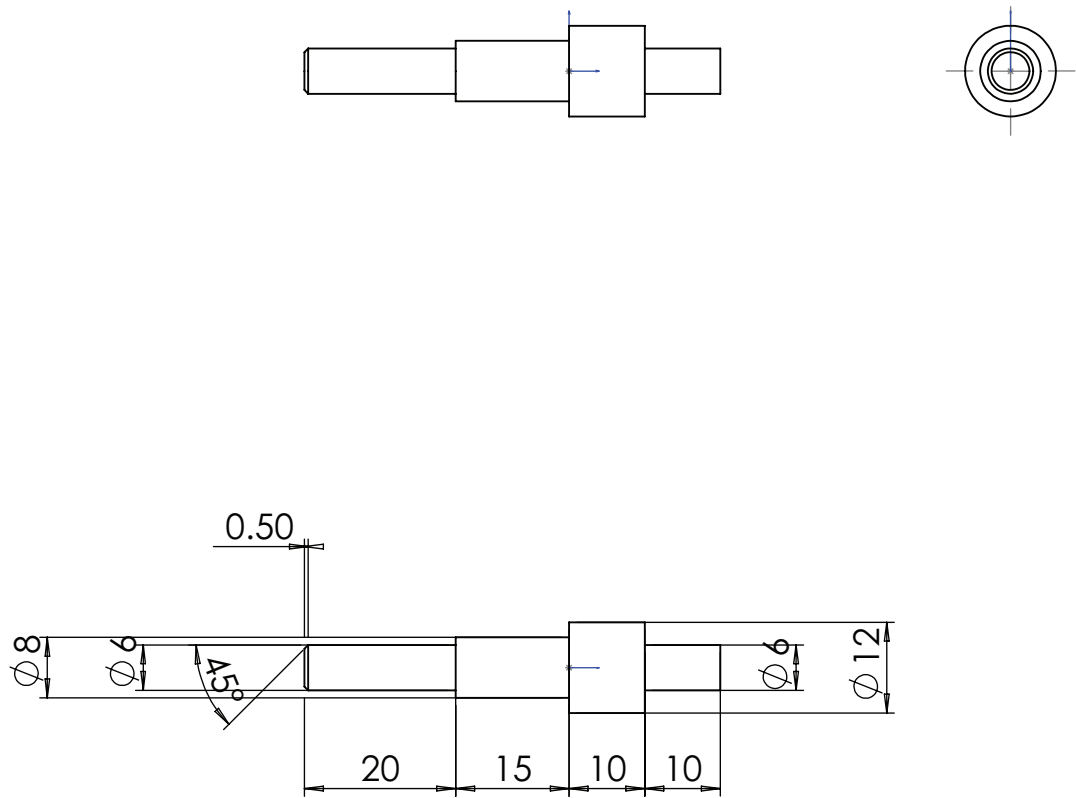
Figure A.13.: Axis 1 in the lens frame assembly of Fig.A.1.
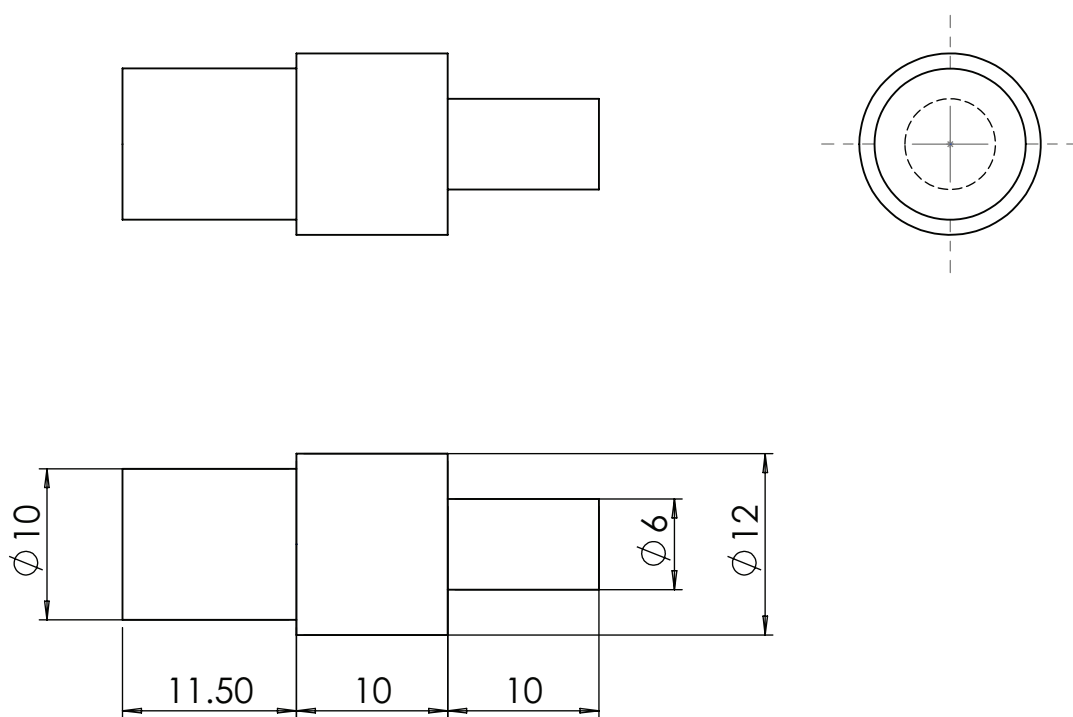
Figure A.14.: Axis 2 in the lens frame assembly of Fig.A.1.

Glossary

CLA	Cell longest axis
CSA	Cell shortest axis
D	Directivity
E_a	Elliptical section axis
E_l	Elliptical section lenght
F	Focal distance
FOV	Field of view
f	Frequency
G	Gain
H_{HAPS}	Station altitude
LAR	Lens axial ratio
LLR	Lens longest axis
LSR	Lens shortest axis
M_l	Meander length
M_w	Meander width
n	Refractive index
P_r	Received power
R	Lens radius
R_{cell}	Cell radius
S_d	Septum tapered end lenght
S_l	Septum length
S_T	Septum tickness
S_w	Septum width
W_d	Waveguide diameter

List of Acronyms

AR	Axial Ratio
BW	Bandwidth
CIR	Carrier to Interference Ratio
CNC	Computer Numerical Control
CP	Circular Polarization
EIRP	Effective Isotropic Radiated Power
FSPL	Free Space Path Loss
GEO	Geostationary Earth Orbit
HAPS	High Altitude Platform Station
HPBW	Half Power Beamwidth
ITU	International Communication Union
LEO	Low Earth Orbit
LHCP	Left-Hand Circular Polarization
LOS	Line Of Sight
LP	Linear Polarization
ML	Meander-Line
RF	Radio Frequency
RHCP	Right-Hand Circular Polarization
RP	Radiation Pattern
Rx	Receiver
SLL	Sidelobe Level
SNR	Signal to Noise Ratio
Tx	Transmitter
VNA	Vector Network Analyzer

List of Figures

List of Tables

219

CV

Marco Letizia was born on November the 22th, 1983 in Italy. He was awarded the Masters degree in Telecommunication Engineering from the Politecnico di Milano in 2008. From June to December 2007 he was working as trainee at the European Space Agency (ESA), in the Microwave Department. He was involved in the design of tuning mechanisms for microwave filters for Space applications.

In August 2008, he started his PhD studies at the Laboratory of Electromagnetics and Acoustics (LEMA) of the École Polytechnique Fédérale de Lausanne (EPFL), where he is currently a researcher and assistant lecturer. As a research assistant in LEMA, he has been involved in the following projects:

FEASANT[*], founded by the **Commission for Technology and Innovation (CTI)**, in collaboration with **StratXX** and **CSEM**, Switzerland.
The main objective of this project was to develop an antenna system for high-altitude-platforms.

CHAPS[†], founded by the **Commission for Technology and Innovation (CTI)**, in collaboration with **StratXX**, Switzerland.
The main objective of this project was to develop two antenna systems for ground users involved in HAPS communications.

OFCOM[‡], founded by the **OFCOM**.
The main objective of this project was to develop a ray-tracing algorithm to predict the field level in urban areas in the presence of modern base stations.

He was assistant lecturer for the courses of Electromagnetics I and II, and co-supervisor of nine students project activities.
During his PhD, he attended the certified courses of Industrial Antenna Design (European School of Antennas, ESoA), Antenna Project Management (ESoA).

---

[*]Feasibility antenna study for HAPS
[†]Communication subsystems for High Altitude Platforms
[‡]Radio system planning

Publications

Journal publications

M. Letizia, B. Fuchs, A. Skrivervik, Juan. R. Mosig, "Circularly Polarized Lens Antenna System Providing Multibeam Radiation Pattern for HAPS", *Radio Science Bulletin*, March 2010.

M. Letizia, B. Fuchs, C. Zorraquino, J. F. Zürcher and Juan R. Mosig, "Oblique Incidence Design of Meander-Line Polarizers for Dielectric Lens Antennas", *Progress in Electromagnetics Research*, PIER 45, 309-335, 2012.

M. Letizia, J. F. Zürcher and Juan R. Mosig, "Prolate ellipsoidal lens for antenna system providing multiple asymmetric beams", *Progress in Electromagnetics Research*, PIER 48, 289-312, 2013.

Conference publications

M. Letizia, J.-F. Zürcher, B. Fuchs, A. Skrivervik, Juan. R. Mosig, "Circularly Polarized Multi-beam Lens Antenna System for High Altitude Platform (HAPS)", *proc. EuCAP 2011, 5th European Conference on Antennas and Propagation*, 2011.

M. Letizia, J.-F. Zürcher, B. Fuchs, Carlos Zorraquino Gastón, Juan. R. Mosig, "Circularly Polarized Multi-Beam Lens Antenna System. Comparison Between 2 Polarizers", *proc. EuCAP 2012, 6th European Conference on Antennas and Propagation*, 2012.

N. Pires, **M. Letizia**, A. Maisenbacher, "Design of an Ultra Wideband Universal Serial Bus device mounted antenna", *Antenna Technology (iWAT), 2010 International Workshop on*, vol., no., pp.1-4, 1-3 March 2010.

N. Pires, **M. Letizia**, S. Boyesz, Y. Luz, Y. Huangz, A. Skriverviky, A. A. Moreira, "Improved Design of an Ultra Wideband Universal Serial Bus Device Mounted Antenna Based on Comparative Radiation Efficiency Measurements", *proc. EuCAP 2011, 5th European Conference on Antennas and Propagation*, 2011.

D. Denti, **M. Letizia**, "Design Considerations of Bandwidth Reconfigurable Input Multiplexers", *proc. EMC 2011, 38th European Microwave Conference*, 2008.

Technical reports

M. Letizia, "Feasibility antennas for High Altitude Platforms FEASANT", *LEMA (EPFL), Lausanne, Switzerland, Tech. Rep.*, Jun. 2009.